QCD Interactions in Hadrons

Dissertation

zur Erlangung des Doktorgrades der Naturwissenschaften
Dr. rer. nat.

Stephan Hagel[1,2]

Institut für Theoretische Physik
Justus-Liebig-Universität Gießen
April 2026

[1]stephan.hagel@physik.uni-giessen.de
[2]physics@sthagel.site

Erstgutachter:	Prof. Dr. Christian S. Fischer
Zweitgutachter:	Prof. Dr. Lorenz von Smekal

Anmerkung: Die hier präsentierten Forschungsarbeiten sind zu Teilen vor der Fertigstellung dieser Dissertation veröffentlicht worden. Hierbei sind die in der Veröffentlichung enthaltenden Arbeiten in Zusammenarbeit mit Dritten entstanden. Eine genaue Trennung und Zuordnung der wissenschaftlichen Beiträge erfolgt an den entsprechenden Stellen dieser Dissertation. Die dazugehörigen Veröffentlichungen sind unter [1, 2] zu finden. Die Herleitung der Kernel-First Trunkierung in Abschnitt 4.3.4 ist reproduziert aus [3] mit Genehmigung der Autoren.

Remark: Some of the work and results presented in this work has been published before finishing this thesis. The work contained in these publications has been done in collaboration with co-authors. Attribution of contribution of individuals is given at the corresponding sections. The related publications can be found under [1, 2]. The derivation of the kernel-first truncation in Sec. 4.3.4 is reproduced from [3] with permission by the authors.

Abstract

In this work, we use functional methods, namely the formalism of Dyson-Schwinger and Bethe-Salpeter equations (DSEs and BSEs) and the n-particle irreducible effective action formalism, to describe properties of quarks and mesons as bound states of quarks and antiquarks. We explore how truncations of these equations relate to the phenomenon of dynamical chiral symmetry breaking in quantum chromodynamics (QCD). Within the rainbow-ladder truncation, we explore, how different effective running couplings give rise to interaction potentials and how they relate to Regge behaviour in the resulting meson spectra. In particular, we explore spectra of light mesons, kaons, $s\bar{s}$-states, charmonia and bottomonia with total angular momenta up to $J \leq 5$ within this truncation.

Furthermore, we use a universal kernel-first truncation to construct a quark self-energy from a quark-antiquark scattering kernel, such that the axialvector Ward-Takahashi identity and thus the effects of dynamical chiral symmetry breaking are conserved. In this truncation we solve the equations of motion for the quark propagator and quark-photon vertex to investigate, whether the vector Ward-Takahashi identity is fulfilled. Starting from a three particle irreducible effective action, we use this method to extract exploratory spectra of light mesons, kaons and $s\bar{s}$-states with total angular momentum up to $J \leq 4$ and sketch a way to expand this framework to heavier quarkonia and heavy-light mesons.

Kurzzusammenfassung

In dieser Arbeit nutzen wir funktionale Methoden, genauer den Formalismus der Dyson-Schwinger und Bethe-Salpeter Gleichungen (DSEs und BSEs), sowie den Formalismus der n-Teilchen irreduziblen effektiven Wirkung, um Eigenschaften von Quarks und Mesonen als gebundene Zustände von Quarks und Antiquarks zu beschreiben. Wir untersuchen, wie Trunkierungen dieser Gleichungen mit dem Phänomen der spontanen chiralen Symmetriebrechung in der Quantenchromodynamik (QCD) in Verbindung stehen. Innerhalb der Regenbogen-Leiter Trunkierung extrahieren wir aus verschiedenen effektiven laufenden Kopplungen Wechselwirkungspotentiale und untersuchen, wie diese mit Regge Verhalten der entstehenden Mesonenspektren zusammenhängen. Insbesondere betrachten wir innerhalb dieser Trunkierung die Spektren leichter Mesonen, Kaonen, $s\bar{s}$ Zuständen, sowie Charmonia und Bottomonia mit Gesamtdrehimpuls bis zu $J \leq 5$.

Des weiteren nutzen wir eine kernel-first Trunkierung, um aus einem Quark-Antiquark Streukern einen Ausdruck für eine Quarkselbstenergie herzuleiten, sodass die Axialvektor Ward-Takahashi Identität und somit die Effekte der spontanen chiralen Symmetriebrechung erhalten bleiben. Innerhalb dieser Trunkierung lösen wir die Bewegungsgleichungen für den Quarkpropagator und den Quark-Photon Vertex, um zu untersuchen, ob die Vektor Ward-Takahashi Identität erfüllt ist. Ausgehend von einer dreiteilchenirreduzieblen effektiven Wirkung nutzen wir diese Methode, um explorative Spektren von leichten Mesonen, Kaonen und $s\bar{s}$ Zuständen mit Gesamtdrehimpuls bis zu $J \leq 4$ zu erhalten, und skizzieren einen Weg um die Methode auf schwere Quarkonia und Heavy-Light Mesonen zu erweitern.

Contents

1. Introduction **8**
1.1. The standard model of particle physics 8
1.2. Quarks, gluons and hadrons 9
1.3. Motivation 10
1.4. Theoretical and experimental status 13
1.5. Outline of this work 19

2. Theoretical background **20**
2.1. Aspects of quantum chromodynamics 20
2.2. Continuous symmetries of QCD 29
2.3. Spontaneous chiral symmetry breaking 33

3. Dyson-Schwinger equations and functional methods **38**
3.1. Dyson-Schwinger equations 38
3.2. n-particle irreducible effective action 46
3.3. Dyson-Schwinger equations of the Yang-Mills sector 52
3.4. Dyson-Schwinger equation of the quark propagator 54
3.5. Dyson-Schwinger equation of the quark-gluon-vertex 56

4. QCD bound states and the Bethe-Salpeter equation **62**
4.1. Bound states and resonances 62
4.2. The Bethe-Salpeter equation 68
4.3. Truncation schemes 81

5. Results - QCD correlation functions **92**
5.1. Quark-gluon vertex 92
5.2. Quark propagator 94
5.3. Quark-photon vertex 96

6. Results - Meson properties **101**
6.1. Interaction potentials 101
6.2. Gell-Mann-Oakes-Renner relation 104
6.3. Pion decay constant 105
6.4. Meson spectra 107

7. Concluding remarks **120**

A. Conventions **122**
A.1. Euclidean conventions 122
A.2. Gamma matrices 123
A.3. Natural units 125
A.4. Hyperspherical coordinates 125
A.5. Quark propagator dressing functions 127

B. Derivations **129**
B.1. Chiral limit relations between dressing functions 129
B.2. Derivation of the quark DSE 130

C. Technical details **132**
C.1. Extrapolation of eigenvalue curves 132
C.2. Evaluating the quark propagator in the complex plane 134
C.3. Level-crossing in eigenvalue curves 135
C.4. Numerically solving the quark-photon vertex BSE 138
C.5. Axialvector WTI in the rainbow-ladder truncation 140
C.6. Transforming between different tensor bases 140
C.7. Explicit meson tensor bases 145
C.8. Tabulated results for meson spectra 149

D. Numerical methods **153**
D.1. Numerical integration 153
D.2. Root finding 154

E. Technical toolkit **155**
E.1. Feynman diagrams 155
E.2. The Rust programming language 155
E.3. FORM 155
E.4. Plotting and Typesetting 156

1. Introduction

1.1. The standard model of particle physics

The search for the smallest structures that make up our universe is a question that dates back at least to the philosophers of Ancient Greece, possibly even longer. For the longest time, this search was only of philosophical nature. Only in the early 19th century evidence of the existence of elementary particles in the form of atoms arose. Throughout the past two centuries, a plethora of new discoveries has deepened our understanding of the smallest scales known to mankind significantly.

As of today, the best model for elementary particle physics is the so-called standard model of particle physics, or standard model for short. It describes the particles, that make up the visible matter in our universe, as fermions, namely quarks and leptons, which interact by exchange of vector bosons. These bosons mediate three of nature's fundamental forces, the strong interaction, weak interaction and electromagnetism. The standard model fails to explain certain phenomena, the most important one being the force of gravitation, which motivates many searches, both theoretical and experimental, for physics beyond the standard model. Still, it has proven to be a very reliable tool for explaining many aspects of particle physics both qualitatively and quantitatively.

The mathematical language, in which the forces of the standard model are formulated, are quantum field theories (QFTs). The interaction between charged particles by exchange of photons is described by the QFT of quantum electrodynamics (QED). Since the coupling constant of QED is sufficiently small for all practical applications, it can be treated perturbatively to great precision.

The part of the standard model, that describes the strong interaction, is the QFT of quantum chromodynamics (QCD). A prominent feature of QCD is that the coupling constant becomes large at small momenta (or large distances respectively). This makes it impossible to extract meaningful results in those regimes via perturbation theory and necessitates the development of non-perturbative methods.

1.2. Quarks, gluons and hadrons

In this work, we focus on the strong interaction, more precisely on the theory of QCD. The fundamental particles of QCD are quarks and gluons. Quarks are fermionic particles with spin $\frac{1}{2}$, which come in six different flavours (up, down, strange, charm, bottom, top) with masses ranging from a few MeV[1] for the lightest quarks up to roughly 172.5 GeV for the top quark [4]. Similar to QED, which describes interactions between particles with an electric charge, the fundamental particles of QCD possess a so-called colour charge, which is described by an underlying SU(3) gauge symmetry group. The non-Abelian nature of this group means that gluons, the exchange bosons of QCD, can directly interact with each other, which is a crucial difference to the photons in QED.

While the fundamental particles in the standard model are quarks and gluons, to this day no free quark or gluon has ever been observed [4]. Instead, we can only see bound states of (anti-)quarks as asymptotic particles in experiments. The reason behind this is twofold; first, the requirement, that asymptotic states are gauge invariant, forbids particles with a net-colour charge to propagate freely. Second, the potential energy between two quarks in a colourless state increases linearly when the quarks are pulled apart up to a point, where quark-antiquark production happens and again two colourless states are formed. This phenomenon is generally known as confinement, and we will talk some more about it in Section 2.1.6.

From the properties of the underlying SU(3) gauge symmetry one can derive, what possible constituents can make up a colourless state. The two easiest and most well-understood combinations are (anti-)baryons, which are composed of three (anti-)quarks ($qqq/\overline{qqq}$), and mesons which are bound states of a quark and an antiquark ($q\overline{q}$). These are however not the only colourless combinations one can form. The self-interacting nature of the gluon allows for states, which are purely made up of two or more valence gluons (gg, ggg, ...) and are commonly called glueballs. Since gluons also carry a colour charge, one can construct colourless states from two (anti-)quarks and a valence gluon ($q\overline{q}g$). Such states are referred to as hybrid mesons, or hybrids for short. By combining the conventional $q\overline{q}$ and $qqq/\overline{qqq}$ combinations[2], one can construct colourless states with more than three (anti-)quarks in them, the most prominent ones being tetraquarks ($qq\overline{qq}$) and pentaquarks ($qqqq\overline{q}$). These states are commonly called “exotic” hadrons and are topic of ongoing research, both from the theoretical and experimental side.

[1] Using natural units, i.e. $\hbar = c = 1$. For more information about the conventions used, Appendix A can be consulted.

[2] Note, that only the combined state has to be colourless. This means, one can for example construct a $q\overline{q}$ state with net colour charge can combine it with another $q\overline{q}$ state with opposite colour charge to construct a colourless tetraquark.

1.3. Motivation

Light and strange meson spectroscopy

The discovery of the first light meson, the charged pion, dates back all the way to 1947 [5] and the field has advanced drastically in the past decades. Yet, there are still open questions even in light mesons and kaons. While many of the well known mesons, such as the pion and the ρ meson, can be well understood as bound states of a quark and an antiquark, other states superficially look like mesons but at closer inspection defy expectations one might have about $q\overline{q}$ states.

These include the light scalar mesons with a mass of below 1 GeV. The level ordering of the masses of those particles cannot be explained in a $q\overline{q}$ picture. A potential solution to this puzzle has been proposed in the 70s and suggests, that the light scalar mesons are in fact tetraquarks ($qq\overline{q}\overline{q}$ states) [6]. Modern day numerical calculations support this viewpoint [7], meaning there is good reason to believe, that these states are in fact tetraquarks.

Also, within the light meson spectrum states with quantum numbers that cannot be explained in a non-relativistic constituent quark model have been discovered. The most prominent example is the $\pi_1(1600)$ meson with quantum numbers of $J^{PC} = 1^{-+}$ [8]. In a non-relativistic view, a $q\overline{q}$ state can have quantum numbers of 1^{--} or $1^{+\pm}$, but no combination of spin and orbital angular momentum can be combined to form the quantum numbers 1^{-+}. This makes the appearance of the $\pi_1(1600)$ very puzzling. A commonly suggested solution to this puzzle is that this state could in fact be a hybrid meson.

When handling such states in theoretical descriptions, quantum effects lead to mixing between different constituent contents with identical quantum numbers. This already happens in conventional mesons, such as the π_0, which is a superposition of $u\overline{u}$ and $d\overline{d}$ components, and the η and η' mesons, which additionally have sizeable $s\overline{s}$ components. As a consequence, a full theoretical description of exotic states also needs to incorporate mixing between $q\overline{q}$ components and other constituent components, such as tetraquark or glueball components. Even states with exotic quantum numbers like the $\pi_1(1600)$ may have $q\overline{q}$ components, since in a relativistic picture exotic quantum numbers are not forbidden. It is then an interesting question to ask which of those components dominate a given physical state. Experimentally, this is often determined via the preferred decay channels of a state, while some theoretical frameworks can differentiate between contributions from different constituents and determine the dominant ones. While some work has been done to theoretically describe mixing between conventional $q\overline{q}$ components and exotic components in some frameworks, there are still many open questions, and it is still topic of ongoing research. In any case, in order to fully understand exotic states, a thorough understanding of the meson spectrum is a prerequisite.

Despite being known experimentally for a long time, light meson spectroscopy is a challenging task for many theoretical approaches to this day. Lattice QCD becomes increasingly computationally expensive at low pion masses, making calculations at physical pion masses difficult to achieve. Non-relativistic treatments of QCD, such as quark models, also struggle with light mesons, since the effective velocities of light constituent quarks are at relativistic scales. Functional methods also have their advantages and disadvantages in this regard, which we will cover more extensively throughout this work.

Heavy meson spectroscopy

Due to the higher mass of charm and bottom quarks, bound states containing them are typically produced less abundantly in experiments. Thus, less is known about charmonium ($c\bar{c}$) and bottomonium ($b\bar{b}$) states than about light mesons and kaons. For instance, there are a number of states in the bottomonium spectrum, which have already been measured in the 1980s but still need confirmation on their quantum numbers [9].

They are however particularly interesting in modern hadron spectroscopy, since in the past decade a plethora of exotic states, known as X-, Y- and Z-states, have been discovered. Some of them have since been identified as tetraquark states [4]. The exact nature of their inner structure may vary from state to state and is topic of ongoing research. As with light and strange mesons, a thorough understanding and accurate predictions of pure $q\bar{q}$ states are essential in order to identify states as potentially exotic.

In some theoretical frameworks such as lattice QCD, non-relativistic QCD and quark models, heavy mesons are easier to handle and better predictions can be made using those methods compared to the light quark sector. This makes them a good playing field for comparison between different theoretical approaches. Additionally, the approximately non-relativistic nature of bound bottom quarks (and to a lesser extent charm quarks) makes it possible to extract effective potentials for those quarks, which can provide insights in the underlying interactions of QCD.

Large angular momenta

Since the abundance of states with angular momentum J in particle collisions usually decreases drastically as J increases, very little is known about states with large angular momentum. There are a number of established states with $J = 2$, but there are currently only three established states with $J = 3$ and $J = 4$ respectively[3] across light unflavoured mesons, kaons, charmonium and bottomonium [4]. A few other states with up to $J = 6$ have been seen in individual experiments, but they still need confirmation [10–12]. New experiments like AMBER at CERN or PANDA at FAIR promise to bring new insights into some of those states and states with large angular momenta in general, which facilitates the need for reliable predictions in those parts of the meson spectrum.

The search for exotic states also requires as broad of a spectrum of states as possible, including states with large angular momentum. Especially the experimental search for glueballs requires a thorough understanding of mesonic spectra. In order to unambiguously identify a glueball, one needs both reliable predictions for $q\bar{q}$ and glueball spectra over a variety of quantum numbers and for their decays, ideally including the mixing between both. While such predictions of glueball spectra exist [13–15], they have been obtained in approximations such as quenched QCD. Better calculations closer to full QCD are a topic of ongoing research.

Besides concrete predictions for experiment, knowing the mass of states with different values for J makes it possible to study Regge behaviour in those states. Knowing whether the Regge trajectories of states predicted by calculations in a certain framework or model are linear can give insights into the underlying interactions.

Understanding of QCD interactions

Besides reproducing and predicting hadron spectra and decays, the goal of theoretical hadron physics is also to get a deeper understanding of the underlying QCD interactions, which cause bound states and resonances to form in the first place. A unique strength of theoretical calculations is, that one can vary physical parameters, such as bare quark masses and coupling constants and see what impact these changes have on the results. Within some approaches, one can also systematically turn individual parts of the interactions on and off at will and define models for interactions and investigate their behaviour.

A thorough understanding of the underlying interactions is particularly important for calculations of states with lots of gluonic interactions in them, such as glueballs and hybrids. In order to fully understand them and get reliable results for their spectra and decays including mixing with conventional mesons, a thorough understanding of the gluonic Yang-Mills sector of QCD is necessary. From there, it is still a challenging task to "unquench" the theory by including interactions between quarks and gluons and thus couple the Yang-Mills sector of QCD to the quark sector.

The insights obtained from hadron physics can in turn give insights to other aspects of QCD. For instance, the phenomenon of confinement in QCD is believed to be directly correlated to the interaction potential between two static quarks.

[3] The PDG also lists the $\psi_3(3842)$ with $J^{PC} = 3^{--}$ as established state, but its quantum numbers still need confirmation [4].

1.4. Theoretical and experimental status

The central goal of both experimental and theoretical hadron physics is to gain knowledge about the structure of hadronic matter and the underlying fundamental interactions. The task of modern experimental hadron physics and particle physics in general is to plan and conduct experiments at particle accelerator facilities, while theoretical physics is concerned with developing models and theories to reproduce experimental findings and make predictions, which can be verified or falsified by experiments later on. Theoretical predictions are also useful when designing new experiments, e.g. by suggesting energy scales at which potential undiscovered hadronic states may lie. This mutual interplay between experimental discoveries and theoretical descriptions thereof is vital for developing a full understanding of hadron physics.

1.4.1. Theoretical frameworks

In the following, a few selected theoretical approaches to deal with hadrons as bound states and resonances are briefly introduced. We will start with more phenomenologically based quark models and then move on to approaches derived from QCD. This section is only meant to serve as a short, non-technical overview of commonly used methods. More detailed summaries of multiple approaches are given in [16–18]. Additionally, references to relevant articles and reviews about the mentioned methods are given in their respective section.

Quark models

Quark model calculations treat hadrons as being composed of constituents quarks with an effective mass to formulate and solve mostly non-relativistic Schrödinger equations with effective potentials, including spin-spin interactions. This notable does not include phenomena like dynamical chiral symmetry breaking (DχSB) or relativistic effects. Instead, some of the emergent effects such as a dynamically generated quark mass are encoded in model parameters like the constituent quark mass. Quark models have been around for a long time by now and have been a good phenomenological tool to reproduce and predict many hadronic states on the basis of symmetries and group theory. Especially for heavy quarks, where non-relativistic approximations are justified, i.e. in the bottomonium sector and to a lesser extent in the charmonium sector, quark models see widespread use even to this day and can even be applied to calculations of exotic states by extension of the models by constituent gluons or (anti-)diquarks as effective degrees of freedom [19–22].

Lattice QCD

Lattice QCD is one of the most widespread approaches to a non-perturbative treatment of QCD. For reviews on the technique see [23–25], for a more comprehensive introductory textbook see [26]. The idea behind lattice QCD is to discretize spacetime to a 3+1 dimensional grid with finite lattice spacing and a finite volume. One then restricts the quarks to exist only on these discrete spacetime points called sites and the gluons exist on the links between those sites. This discretization naturally introduces a cutoff in momentum space acting as a regulator for the ultraviolet divergences of the theory. One can then explicitly simulate the dynamics of the full theory using on the lattice using Monte-Carlo methods. Once the configuration is thermalized, it is possible to directly calculate expectation values of operators in this configuration. Lattice QCD is as of today the only widely used ab-initio method for non-perturbative calculations within QCD. It also has the distinct advantage of being able to provide well-defined statistical error estimates.

However, this framework does not come without its unique challenges. The discretization to a typically hypercubic lattice explicitly breaks Poincaré invariance, which makes it difficult to extract properties of hadronic states with well-defined quantum numbers. Additionally, the computational cost of lattice simulations can be very high, especially if one is interested in the continuum limit, where the lattice spacing goes to zero and the number of lattice sites goes to infinity. Simulations with light quarks pose another great challenge, as the computational cost drastically increases when going to physical pion masses (and thus physical up and down quark masses). Recent technical developments such as GPU accelerated computations and constant improvements in numerical methodology have improved our capabilities to do such computations [27–30]. Nevertheless, its ab-initio nature and the fact, that no truncations or approximations to the fundamental interactions of QCD are needed on the lattice, make it an invaluable tool for comparison between theoretical frameworks and with experiment.

Dyson-Schwinger equations and functional methods

The Dyson-Schwinger framework, or functional methods in general, are a functional approach to derive equations of motion for the one-particle irreducible Green's functions from the effective action of QCD. The Dyson-Schwinger equations (DSEs) are a set of coupled integral equations for the Green's functions and in principle include the full dynamics of QCD in a fixed gauge. In general, these equations form an infinite tower of equations and thus require the use of suitable truncations to render the set of equations finite and solvable. When combined with the formalism of Bethe-Salpeter equations (BSEs), which are derived from full N-point Green's functions, DSEs and BSEs form a framework which has proven to be useful for extracting information about bound states and resonances [31–33], electromagnetic properties of hadrons [34–38] and even exotic hadrons [39–43]. The major challenge of this framework is the fact, that it is difficult to estimate the systematic error introduced into the calculations by the truncations and models used and exact solutions to the full tower of equations can only be obtained in certain limits [44]. For reviews on the methodology, cf. [18, 45–50].

Functional renormalization group

The functional renormalization group (FRG) framework is used in quantum field theories, especially strongly coupled ones, such as QCD. The main idea behind it is to use the effective action Γ of the theory and introduce a regulator R_k at an infrared scale k to obtain a scale-dependent effective action Γ_k. One then derives a differential equation for the full quark propagator by taking the partial derivative of Γ_k with respect to k and successively integrate out momentum shells from high to low energies. This equation is known as the Wetterich equation and its diagrammatic form is given by [51]

$$\frac{\partial}{\partial t}\Gamma_k = \frac{1}{2}$$

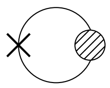

$$\times = \frac{\partial}{\partial t}R_k \tag{1.1}$$

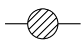

= full k-dependent propagator.

The equations of motion for the propagators and N-point functions of a theory obtained in the FRG framework are similar to the ones obtained within the Dyson-Schwinger framework. In principle, both functional frameworks are exact, but their resummation schemes differ in the presence of approximations. This makes studying both frameworks interesting with possible synergies between the two, as comparing the differences in the equations and their results can provide valuable insights into the nature of the underlying interactions [44, 52–55].

The FRG framework has been used for a variety of applications over the years, for reviews on the topic, cf. [56–58]. In recent years it has also been applied to provide insights into the quark-gluon vertex beyond the rainbow-ladder truncation and first results in hadron spectroscopy have been produced [59–61]. The current state-of-the-art tools for conducting hadron research within the FRG framework include dynamic hadronisation and emergent composites [62] as well as directly resolving the quark four point functions [63, 64]. For more reference of these methods being applied to hadron physics, cf. [65, 66].

Other approaches

Besides the frameworks outlined above, there are a number of other approaches to hadron spectroscopy. These include effective chiral Lagrangians, Hamiltonian approaches, or QCD sum rules. For a broader overview and guide for further reading on those topics, Reference [67] may be consulted.

1.4.2. Experiments

Over the past decades, many large particle physics experiments have been conducted, which have provided insights into the meson spectrum. Due to practical constraints, no single experiment will be perfect for all applications. Instead, each experiment comes with its advantages and disadvantages and specific areas of research they excel at. This section will briefly go over several big and relevant experiments for hadron spectroscopy in chronological order of their first runs and a modern analysis method for experimental data. For further details on the topics, the given references may be consulted.

Belle / Belle II

Belle and its successor Belle II are experiments at the SuperKEKB accelerator in Tsukuba, Japan. They study e^+e^- collisions at energy ranges suitable for bottom meson and bottomonium studies, especially at the $\Upsilon(4s)$ energy [68]. The Belle experiment discovered the first tetraquark candidate in 2003 in the $\chi_{c1}(3872)$ [69] (initially known as $X(3872)$). Belle II utilizes the high luminosity available at the SuperKEKB accelerator to improve upon the statistics of Belle's dataset and aims to eliminate statistical uncertainties, which limited some analyses of Belle [70].

COMPASS

The **Co**mmon **M**uon **P**roton **A**pparatus for **S**tructure and **S**pectroscopy experiment (COMPASS) is a fixed target experiment at the M2 beam-line of the **S**uper **P**roton **S**ynchrotron (SPS) at CERN. It has been running from the early 2000s until 2022 and has provided insights into many different parts of the meson spectrum. These include measurements of the $\pi_1(1600)$ state with exotic quantum numbers of $J^{PC} = 1^{-+}$ [8, 71, 72], measurements of high angular momentum states, such as the $a_4(1970)$ [8, 71, 73], or investigations on the effects of dynamical chiral symmetry breaking and the chiral anomaly [74]. More recent data gathered at COMPASS promises to give insights into even more states with angular momentum of up to $J = 6$ [75] as well as the kaon spectrum [76]. For an overview of recent results, cf. [72], for a broader review of the experiment, cf. [77].

BES III

The **Be**ijing **S**pectrometer III (BESIII) is an experiment at the **B**eijing **E**lectron-**P**ositron **C**ollider II (BEPC II), which utilizes an e^+e^- beam to study charmed hadrons, charmonium and light hadron decays and to search for physics beyond the standard model [78, 79]. The electron-positron nature of the beam as well as its high luminosity make it a good tool for investigating highly exited charmonia with quantum number $J^{PC} = 1^{--}$, such as the $\psi(4415)$ and the $\psi(4660)$ [80, 81]. It also has made contributions to the discovery of mesons with large angular momenta, such as the $K_4^*(2045)$ [82] or the $\rho_3(2250)$ state[4] [83]. Furthermore, the research conducted at BESIII is of particular interest for the search of exotic hadrons, as it allows investigation of radiative decays of J/ψ mesons into η_c, which further decays into $h\bar{h}$ intermediate states in an energy region, where the lightest glueballs are predicted and even recently discovered more glueball candidate states [84, 85].

LHCb

The **L**arge **H**adron **C**ollider **b**eauty (LHCb) experiment is one of the four main detectors at the **L**arge **H**adron **C**ollider (LHC) at CERN. It focuses mainly on the investigation of hadrons with heavy quarks (charm and bottom) and their decays via production of $b\bar{b}$ pairs, hence the name [86]. Within the past two decades it has contributed greatly to hadron physics through discoveries of tetraquark [87–90] and pentaquark states [91], determining the quantum numbers of the $\chi_{c1}(3872)$ (formerly $X(3872)$) for the first time [92], and discovering CP-violations in several mesonic [93, 94] and even baryonic systems [95]. Notably, it also discovered the $\psi_3(3842)$ [96], a $c\bar{c}$ state for which quark models predict quantum numbers of $J^{PC} = 3^{--}$, which still need confirmation though.

GlueX

GlueX is a particle physics experiment located at the Thomas Jefferson National Accelerator Facility (JLab) in Newport News, Virgina, USA. It uses electrons with an energy of 12 GeV to generate a linearly polarized photon beam with the coherent bremsstrahlung technique. This beam is scattered on nucleons to probe the light meson spectrum as well as properties of baryons and hadronic electromagnetic structure [97, 98]. Its primary goal is to search for and study exotic mesons, such as hybrid mesons like the $\pi_1(1600)$ [99]. For a summary on recent results, cf. [100].

[4] This state is not yet considered an established state by the PDG [4].

AMBER

The **A**pparatus for **M**eson and **B**aryon **E**xperimental **R**esearch (AMBER) is a fixed target experiment at the M2 beam-line of the **S**uper **P**roton **S**ynchrotron (SPS) at CERN. It is a newly formed collaboration following the COMPASS collaboration using the same beam-line. It will implement new state-of-the-art read out technology to allow for faster taking of data. It uses a wide variety of beams, such as muon, proton, pion and kaon beams of both charges with energies ranging from 50 GeV up to 280 GeV to probe several hadronic properties. These include production cross-sections for antiprotons off Helium targets using proton beams, the proton charge radius, pion and kaon parton distribution functions. Additionally, in AMBER Phase-2, the light and strange meson spectrum is planned to be probed in detail. For strange meson spectroscopy a high intensity Kaon beam will be used to include strangeness in the initial state of the collisions. The experiment aims at creating a world leading data set in this field, aiming to improve the sample size by a factor of 25 compared to existing data sets [101–103].

PANDA

The Anti**p**roton **An**nihilation in **Da**rmstadt (PANDA) experiment is a detector under construction at the **F**acility for **A**ntiproton and **I**on **R**esearch (FAIR). PANDA will be unique in that it will use proton-antiproton collisions to study the strong interaction, granting the opportunity the strong interaction in collisions with zero net baryon number [104–106]. Thus, it will be particularly important for studies of exotic states like tetraquarks, hybrids and glueballs, especially glueballs with large angular momentum. Some of its proposed goals include precision studies of the $\chi_{c1}(3872)$ state to see, whether it is a compact state or a hadronic molecule [107] and investigations of time-like proton electromagnetic formfactors [108].

Amplitude Analysis

Besides the challenge to design and build experiments for hadron physics, the analysis of the produced data is an essential part of the process. A common methodology to extract information about bound states and resonances, especially for hadrons of energies below 2 GeV, from experimental data such as their mass and quantum numbers is called amplitude analysis [109]. Its goal is to reconstruct the scattering amplitude in the complex plane and find poles, branch cuts and other analytic structures and extract hadron properties from them [110]. There are different formalisms to perform an amplitude analysis such as the helicity formalism [111] and covariant tensor formalisms [112–115], which have their unique advantages and disadvantages in different applications [116, 117].

1.5. Outline of this work

This work is structured as follows; in Chapter 2 we will introduce QCD as a quantum field theory and discuss some of its most important aspects, including spontaneous chiral symmetry breaking in Section 2.3.

In Chapter 3 we will introduce the framework of Dyson-Schwinger equations. We will discuss how they produce an infinite tower of coupled equations and talk about truncation schemes in general in Section 3.1.4. Furthermore, we will talk about the related framework of n-particle irreducible effective actions in Section 3.2 and discuss the resulting equations of motion in Sections 3.4 through 3.5.

Chapter 4 is dedicated to the study of bound states. Section 4.1 gives a general overview of QCD bound states, Section 4.2 is about the Bethe-Salpeter equation, which is used to describe hadrons in the functional methods framework, and Section 4.3 goes into detail on two truncation schemes, which we will use to calculate meson spectra.

Results for QCD correlation functions will be presented in Chapter 5, including the quark propagator, quark-gluon vertex and quark-photon vertex. Results for meson properties will be presented in Chapter 6. A concluding summary of this work is given in Chapter 7. Appendices A through E contain complementary information and lengthy derivations.

2. Theoretical background

2.1. Aspects of quantum chromodynamics

In the following, we will investigate the Lagrangian and thus the classical action of quantum chromodynamics (QCD) and discuss some of its most important features and non-trivial properties. Note, that not all aspects can be discussed in full detail here. Instead, one may consult existing literature and textbooks about these topics for further insights into these topics. The symmetries of the QCD Action are an essential cornerstone of this work, which is why an entire section is dedicated to them in Section 2.2 and to how they can be broken in Section 2.3.

2.1.1. The QCD Lagrangian

The central object of a quantum field theory is its Lagrangian density or equivalently its (classical) action, which is obtained by performing a spacetime integral over the Lagrangian. For QCD, the Lagrangian is the simplest local SU(3) gauge theory with fermions one can write down. In 4-dimensional Euclidean spacetime it is given by [118]

$$\begin{gathered}\mathscr{L}_{\mathrm{QCD}} = \sum_{i=1}^{N_f} \overline{\psi}_i \left(\not{D} + m_i\right) \psi_i + \frac{1}{2}\,\mathrm{tr}\left(F^{\mu\nu}F^{\mu\nu}\right), \quad S_{\mathrm{QCD}} = \int \mathrm{d}^4x\, \mathscr{L}_{\mathrm{QCD}}, \\ D^\mu = \partial^\mu + igA^\mu, \quad F^{\mu\nu} = \partial^\mu A^\nu - \partial^\nu A^\mu + ig\left[A^\mu A^\nu\right]\end{gathered} \tag{2.1}$$

where ψ_i and $\overline{\psi}_i = \psi_i^\dagger \gamma^0$ are the quark and antiquark fields with the sum going over all $N_f$quark flavours in the theory, D^μ is the covariant derivative and $F^{\mu\nu}$ is the gluon field strength tensor. The gluon fields A^μ are elements of the Lie-algebra $\mathfrak{su}(3)$ and can be expanded in terms of Gell-Mann matrices

$$A^\mu = A_a^\mu \lambda_a. \tag{2.2}$$

The latter part of the Lagrangian, which only depends on the gluon fields and their derivatives, is the Lagrangian of what is commonly referred to as Yang-Mills theory. By using eq. (2.2) and the structure constants f_{abc} of the Lie-algebra, the Yang-Mills Lagrangian can be written explicitly as

$$
\begin{aligned}
\mathscr{L}_{\mathrm{YM}} = &-\frac{1}{2} A_a^\mu (\Box \eta^{\mu\nu} - \partial^\mu \partial^\nu) A_a^\nu \\
&- \frac{g}{2} f_{abc} (\partial^\mu A_a^\nu - \partial^\nu A_a^\mu) A_b^\mu A_c^\nu \\
&+ \frac{g^2}{4} f_{abe} f_{cde} A_a^\mu A_b^\nu A_c^\mu A_d^\nu,
\end{aligned}
\tag{2.3}
$$

where $\eta^{\mu\nu}$ is the Euclidean spacetime metric, see Appendix A.1 for details. From this expression one can read off the three main components of the Yang-Mills Lagrangian, which combined with the quark sector lead to five main components of QCD:

- The quark kinetic term ($\sim \overline{\psi}(\partial + m)\psi$)
- The gluon kinetic term ($\sim A(\Box\eta - \partial\partial)A$)
- The quark-gluon interaction ($\sim \overline{\psi} A \psi$)
- The three-gluon interaction ($\sim [\partial, A]AA$)
- The four-gluon interaction ($\sim AAAA$)

The existence of the latter two is a consequence of the non-Abelian nature of the underlying gauge theory, and they are a central difference to Abelian gauge theories, like QED which has the Abelian gauge group U(1). When writing down Feynman diagrams for QCD, these five components correspond to tree-level expressions for the quark- and gluon propagators, as well as quark-gluon-, three-gluon- and four-gluon vertices.

2.1.2. CP-symmetry

The QCD Lagrangian as defined in (2.1) is symmetric under simultaneous charge- and parity transformations. In principle, one can also add CP-symmetry violating terms to the QCD Lagrangian, such as a CP violating mass term or a Theta vacuum term

$$
\begin{aligned}
\mathscr{L}_{\mathrm{CP}} &= -\sum_{i=1}^{N_f} \overline{\psi}_i m_i \mathrm{e}^{i\theta' \gamma_5} \psi_i, \\
\mathscr{L}_\theta &= \theta \left(\frac{g^2}{16\pi^2} \right) \varepsilon_{\mu\nu\rho\sigma} F_a^{\mu\nu} F_b^{\rho\sigma} \operatorname{tr} \lambda_a \lambda_b.
\end{aligned}
\tag{2.4}
$$

One can redefine the quark fields via a chiral rotation

$$\psi(x) \to \mathrm{e}^{i\theta'\gamma_5/2}\psi(x) \tag{2.5}$$

and a corresponding transformation to the antiquark fields to eliminate the CP-violating mass term, which in turn modifies the CP violating theta angle to be $\theta \to \theta + \theta'$. If one also includes the quark masses in the standard model via Yukawa matrices Y_u and Y_d, the CP violating angle is $\overline{\theta} = \theta - \arg\det\left(Y_u Y_d\right)$, a non-zero value of which would give rise to an electric dipole moment of the neutron [119]. The current experimental status suggests an upper bound on the dipole moment of the neutron of $1.8 \cdot 10^{-26}\, e\,\mathrm{cm}$ [4, 120], which requires $\overline{\theta} \lesssim 10^{-10}$.

Since $\overline{\theta}$ is the difference of two seemingly independent parameters of the standard model, and it is so close to zero, this poses a fine-tuning problem. A multitude of solutions have been proposed for it in the past, including the existence of axions as new particles [121, 122]. However, this problem is still not fully resolved yet and is topic of ongoing research [123, 124].

2.1.3. Gauge fixing and Faddeev-Popov Ghosts

The QCD Lagrangian (2.1) is constructed to be invariant under a local SU(3) gauge transformation, i.e. a simultaneous transformation of the quark- and gluon fields of the form

$$\begin{aligned} \psi(x) &\to U(x)\psi(x) \\ A^\mu(x) &\to U(x)A^\mu(x)U^\dagger(x) + \frac{i}{g}U(x)\partial^\mu U^\dagger(x), \end{aligned} \tag{2.6}$$

where $U(x)$ is an SU(3) matrix, which generally depends on the spacetime variable x. When calculating the partition function of QCD via the path integral formalism, i.e.

$$Z = \int \mathscr{D}A\,\mathscr{D}\psi\,\mathscr{D}\overline{\psi}\,\mathrm{e}^{-S_{\mathrm{QCD}}[A,\psi,\overline{\psi}]}, \tag{2.7}$$

the path integral for the gluons $\int \mathscr{D}A$ integrates over all possible values of A^μ, including gauge equivalent configurations. This also includes configurations, where the Fourier transform of the kinetic term for the gluons has zero modes

$$\left(k^2\eta^{\mu\nu} - k^\mu k^\nu\right) A^\mu(k) = 0. \tag{2.8}$$

This renders the kinetic term non-invertible and thus makes it impossible to have a well-defined gluon propagator. One example of such a configuration is $A^\mu = k^\mu \alpha(k)$, where $\alpha(k)$ is an arbitrary smooth function of the gluon momentum. Notably, this configuration is “pure gauge”, i.e. gauge equivalent to $A^\mu \equiv 0$.

This problem necessitates a gauge fixing procedure. One can define a gauge orbit as an equivalence class of field configurations which are related via a gauge transformation. This means a gauge orbit for gluons looks like

$$[A^\mu(x)] \coloneqq \left\{ A^{\mu\prime}(x) : A^{\mu\prime}(x) = U(x)A^\mu(x)U^\dagger(x) + U(x)\partial^\mu U^\dagger(x) \right\}. \tag{2.9}$$

With this definition at hand, gauge fixing is the procedure of choosing one representative $A^\mu(x)$ per each gauge orbit.[1]Gauge fixing of non-Abelian quantum field theories like QCD is a hugely non-trivial problem, which we can only scratch the surface of. For more thorough treatments of the problem, cf. [50, 125].

The typical procedure to do gauge fixing is the Faddeev-Popov procedure [127]. The idea behind it is to introduce a one into the path integral by using the relation [128]

$$1 = \int \mathscr{D}\alpha \, \delta\left(F\left(A^\alpha\right)\right) \left|\det\left(\frac{\delta F\left(A^\alpha\right)}{\delta\alpha}\right)\right|, \tag{2.10}$$

where the rightmost expression is called the Faddeev-Popov determinant. By inserting this expression into the path integral for the partition function (2.7), using a clever choice for $F(A^\alpha)$ and rewriting the Faddeev-Popov determinant as a path integral over two scalar Grassmann fields c and $\overline{c}$, one obtains

$$Z = \int \mathscr{D}\left\{A, \psi, \overline{\psi}, c, \overline{c}\right\} \exp\left(-S_{\mathrm{QCD}} - \int \mathrm{d}^4x \left[\frac{\left(\partial_\mu A^\mu\right)^2}{2\xi} + \overline{c}^a\left(-\partial^\mu D_\mu^{ab}\right)c^b\right]\right), \tag{2.11}$$

where the path integral measure is a shorthand for $\mathscr{D}A\mathscr{D}\psi\ldots$, and we suppressed the field dependence of the QCD action. The two new terms appearing in the argument of the exponential are a gauge fixing term with gauge parameter ξ and the Faddeev-Popov operator. The two newly introduced fields c and $\overline{c}$ are called Faddeev-Popov (anti-)ghosts, or just (anti-)ghosts for short. In Abelian gauge theories, they decouple from the other fields and thus do not appear in practical calculations. Due to the non-Abelian nature of QCD, they couple to the gluon field via a ghost-gluon vertex and thus need to be handled explicitly when working in a gauge-fixed setting.

By making a choice for the gauge parameter ξ, one can fix the gauge of the theory. Common choices are the Feynman gauge, where $\xi = 1$, the Yennie gauge with $\xi = 3$ and the Landau gauge, which we will use throughout this work, in which on performs the limit $\xi \to 0$ after the theory has been quantized, which entails $\partial^\mu A_\mu = 0$.

[1] In more mathematical terms, gauge fixing means choosing a section of a fibre bundle [126].

The Gribov problem

When using the Faddeev-Popov procedure to go to Landau gauge, one has to make two assumptions:

- The Faddeev-Popov determinant is positive definite, i.e. $\det(-\partial^\mu D_\mu) > 0$.
- There exists only one solution to the equation $\partial^\mu A_\mu = 0$.

It turns out, that the second condition is not true. The multiple solutions to $\partial^\mu A_\mu = 0$ are referred to as Gribov copies. One can restrict the path integral measure to the first Gribov region i.e. the subset of all field configurations A^μ, such that $\partial^\mu A_\mu = 0$ holds and $\det(-\partial^\mu D_\mu) \geq 0$, which is intersected by each gauge orbit at least once and contains $A^\mu = 0$. However, it turns out that even within the first Gribov region there are still Gribov copies.

To mitigate this problem, one needs to restrict the path integral to the Fundamental Modular Region, which is a subset of the Gribov region that contains exactly one intersection with each gauge orbit, contains $A^\mu \equiv 0$ and has a common boundary with the Gribov region. This endeavour is very difficult to implement in practice. There are some approaches, which try to solve this problem, such as the Gribov-Zwanziger framework [129, 130] or the Kugo-Ojima scenario [131], but it still poses an open problem.

However, lattice studies of gluon and ghost propagators indicate, that the impact of Gribov copies are negligible in energy regions relevant for hadron spectroscopy [132, 133]. Thus, they are usually ignored in practical calculations. Likewise, we will also ignore their appearance and work in Landau gauge throughout this work.

2.1.4. Renormalization

As is common in quantum field theories, loop diagrams in QCD introduce divergent integrals which have to be dealt with via regularization and renormalization. Here we will only take a brief look at the most important aspects of renormalization of QCD. More exhaustive treatments of renormalization can be found in most textbooks on quantum field theory, cf. [134].

When writing down the QCD Lagrangian in eq. (2.1), we have stated it in terms of bare fields, masses and couplings. They are related to their renormalized counterparts through multiplicative renormalization constants, i.e.

$$\begin{aligned}
\psi(\Lambda^2) &= Z_2^{1/2}(\mu^2,\Lambda^2)\,\psi_\mathrm{R}(\mu^2),\\
A^\mu(\Lambda^2) &= Z_3^{1/2}(\mu^2,\Lambda^2)\,A^\mu_\mathrm{R}(\mu^2),\\
m(\Lambda^2) &= Z_m(\mu^2,\Lambda^2)\,m_\mathrm{R}(\mu^2),\\
g(\Lambda^2) &= Z_g(\mu^2,\Lambda^2)\,g_\mathrm{R}(\mu^2).
\end{aligned} \tag{2.12}$$

The renormalized quantities no longer depend on the regularization cutoff Λ, but on the renormalization scale μ, while the cutoff dependence has been absorbed into the renormalization constants. One can also introduce renormalization constants on the level of propagators and vertices. The quark propagator $S(p)$, ghost propagator $G(p)$, gluon propagator $D(p)$, quark-gluon vertex Γ^μ_qg, ghost-gluon vertex Γ^μ_ghg, three-gluon vertex $\Gamma^{\mu\nu\rho}$ and four-gluon vertex $\Gamma^{\mu\nu\rho\sigma}$ are renormalized via [135]

$$\begin{aligned}
S(p,\Lambda^2) &= Z_2(\mu^2,\Lambda^2)\,S_\mathrm{R}(p,\mu^2),\\
G(p,\Lambda^2) &= \tilde{Z}_3(\mu^2,\Lambda^2)\,G_\mathrm{R}(p,\mu^2),\\
D^{\mu\nu}(p,\Lambda^2) &= Z_3(\mu^2,\Lambda^2)\,D^{\mu\nu}_\mathrm{R}(p,\mu^2),\\
\Gamma^\mu_\mathrm{qg}(p_i,\Lambda^2) &= Z_{1f}^{-1}(\mu^2,\Lambda^2)\,\Gamma^\mu_\mathrm{qg,R}(p_i,\mu^2),\\
\Gamma^\mu_\mathrm{ghg}(p_i,\Lambda^2) &= \tilde{Z}_1^{-1}(\mu^2,\Lambda^2)\,\Gamma^\mu_\mathrm{ghg,R}(p_i,\mu^2),\\
\Gamma^{\mu\nu\rho}_\mathrm{3g}(p_i,\Lambda^2) &= Z_1^{-1}(\mu^2,\Lambda^2)\,\Gamma^{\mu\nu\rho}_\mathrm{3g,R}(p_i,\mu^2),\\
\Gamma^{\mu\nu\rho\sigma}_\mathrm{4g}(p_i,\Lambda^2) &= Z_4^{-1}(\mu^2,\Lambda^2)\,\Gamma^{\mu\nu\rho\sigma}_\mathrm{4g,R}(p_i,\mu^2).
\end{aligned} \tag{2.13}$$

Throughout the rest of this work, we will always work with the renormalized quantities and thus supress the "R" subscript as well as the cutoff and renormalization point dependencies.

Note, that the renormalization constants introduced in eqs. (2.12) and (2.13) are not all independent, but instead are related to each other via Slavnov-Taylor identities (STIs) [136]

$$Z_1 = Z_g Z_3^{3/2}, \quad \tilde{Z}_1 = Z_g \tilde{Z}_3 Z_3^{1/2}, \quad Z_{1f} = Z_g Z_3^{1/2} Z_2, \quad Z_4 = Z_g^2 Z_3^2. \tag{2.14}$$

While in principle the renormalization constants are divergent in the limit $\Lambda \to \infty$ and the STIs are exact relations, in numerical calculations the renormalization constants are finite. The STIs also need not be exact in numerical calculations and can serve as a way to gauge the quality of the numerical methods used [137, 138].

2.1.5. Running Coupling and asymptotic freedom

As with any quantum field theory, one can employ the renormalization group formalism and evaluate the Feynman diagrams of the theory to obtain an expression

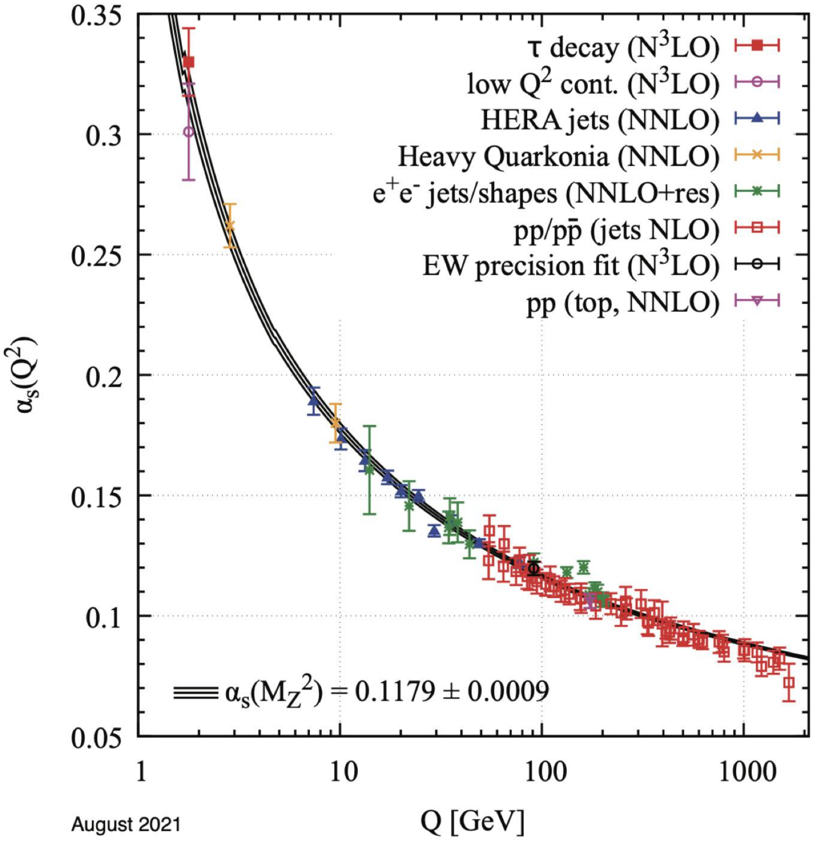

Figure 2.1.: Summary of α_s determinations from the year 2021 compared to the QCD prediction of the running coupling. The figure is taken from [139].

for the coupling strength as a function of the renormalization point. This behaviour is encoded in the renormalization group equation [118]

$$\mu \frac{\partial g}{\partial \mu} = \beta(g), \tag{2.15}$$

where g is the coupling and $\beta(g)$ is the beta function of the theory. It is customary to rephrase the beta function in terms of the squared coupling $\alpha_s = g^2/4\pi$. To one-loop order, the beta function of QCD is given by

$$\beta(\alpha_s) = -\left(11 - \frac{2}{3}N_f\right)\frac{\alpha_s^2}{2\pi}. \tag{2.16}$$

Thus, α_s obeys the differential equation

$$\mu \frac{\partial \alpha_s}{\partial \mu} = -\left(11 - \frac{2}{3}N_f\right)\frac{\alpha_s^2}{2\pi}, \tag{2.17}$$

which in turn has the solution

$$\alpha_s(\mu^2) = \frac{4\pi}{\beta_0 \ln\left(\mu^2/\Lambda_{\mathrm{QCD}}^2\right)} \tag{2.18}$$

with $\beta_0 = \left(11 - \frac{2}{3}N_f\right)$ and the parameter $\Lambda_{\mathrm{QCD}} \approx 230\,\mathrm{MeV}$ being a characteristic scale of the theory. From the sign of the beta function one can read off, that for $N_f \leq 16$ the coupling constant must get weaker at high energies and stronger at low energies, which is a concept known as asymptotic freedom. This implies, that at low energies, in particular energies below Λ_{QCD}, perturbation theory is no longer a useful tool for extracting meaningful results from QCD, which necessitates the use of non-perturbative methods.

This behaviour can even be investigated experimentally [139, 140], the results of which match up very well with theoretical predictions, as can be seen in Fig. 2.1.

2.1.6. Confinement

One phenomenon of QCD, respectively quark and hadron physics in general, is the concept of confinement. While most people working in the field have somewhat of an understanding of what confinement is, it can be hard to define it rigorously and there are many open questions surrounding the topic [141]. Confinement is a notoriously difficult problem and a lot of research about it has been conducted in the past so we can only scratch the surface of it here. For a general overview of the topic, references [23, 142] can be consulted.

Over the years, several attempts at defining confinement have been made. One of the first properties historically labelled as confinement is the fact, that no free quarks and gluons can be observed in experiment. More generally, only colourless states can be seen as asymptotic states in experiment. While this conception of "colour confinement" may be an intuitive way to define confinement, it is less a consequence of confinement than it is of gauge invariance. Quarks and gluons, as well as all other states with net colour charge, are not gauge-invariant objects and thus are not physical in the sense that they cannot appear as asymptotic particles. In a similar vein, electrons cannot appear as "bare" particles, as a single electron is not a gauge invariant state, but it has to be surrounded by a photon cloud. Moreover, the asymptotic states of a gauge-Higgs theory, where the forces are all Yukawa-like and the dynamics similar to the weak interaction are also colour singlet states, meaning such theories are also confining by that definition [142].

Other attempts at defining confinement include the Kugo-Ojima confinement criterion, which is derived from the notion, that the expectation value of a colour charge operator in any physical state has to vanish. As a consequence, the propagator of the Faddeev-Popov ghosts is more singular than a simple pole at $p^2 = 0$, while the gluon propagator is less singular [143]. There have been a number of works investigating whether the Kugo-Ojima scenario is a necessary and sufficient condition for confinement or whether it needs refinements in its description. For details see [144–146] and references therein.

Another property commonly associated with confinement is the emergence of a linearly rising potential between two static quarks. This is closely related to the Wilson loop of the theory falling of with an area-law behaviour rather than a circumference-law [23]. Motivated by the picture of the colourelectric field between two quarks, generated by gluons, being shaped into a fluxtube, one expects the static quark potential to be linearly rising at large distances while being Coloumb-like at small distances due to asymptotic freedom. This ideal potential is known as Cornell potential [147]

$$V(\vec{r}) = -\frac{4}{3}\frac{\alpha_s}{r} + \sigma(r)\,r + V_0, \tag{2.19}$$

with strong coupling constant parameter α_s and string tension σ. Such a potential implies, that the energy needed to separate two quarks is unbounded. In QCD, where quarks are dynamic and have finite mass, this means that eventually a new quark-antiquark pair can be created from the vacuum, causing the quarks to form bound states yet again. This effect is known as string breaking, and it has the consequence that a potential obtained from full QCD will not be linearly rising indefinitely, but become constant above a certain string breaking scale [148]. This in turn means, that by this definition QCD is not strictly a confining theory but Yang-Mills theory is.

Some consequences of the linearly rising static quark potential can be seen in the spectrum of hadrons [149]. In particular, we will later see, that linearly rising potentials give rise to Regge trajectories, which are a certain relation between meson mass and angular momentum. We will discuss them in more detail in Section 4.1.3.

It is also worth noting, that Yang-Mills theories and QCD are not the only theories which exhibit some form of confinement. Other confining theories include the Schwinger model [23] and quantum electrodynamics in 2+1 dimensions (QED_{2+1}) [46, 47, 150]. Confinement is not only interesting to be studied for its own sake, but there are also hints, that it may be related to other aspects of QCD, such as gauge fixing and the Gribov problem [151] as well as dynamical chiral symmetry breaking [152]. The latter is of utmost importance for hadron spectroscopy, especially for the light meson spectrum, which is why we will talk about it in more detail in Section 2.3.

Deconfinement

On a final note about confinement, it is believed that confinement only emerges in some parts of the QCD phase diagram. At high temperatures and high baryochemical potential, models and lattice QCD suggest that there may be a transition from a confined to a deconfined phase, in which a quark-gluon plasma dominates the dynamics instead of hadronic matter [153]. It is also commonly believed, that this transition is related to the transition between a phase with DχSB and a phase in which chiral symmetry is restored [154, 155]. Whether these transitions coincide and in which way they are related is still topic of ongoing research.

2.2. Continuous symmetries of QCD

Other than the local SU(3) gauge symmetry, the QCD Lagrangian has a number of other continuous and discrete symmetries related to the (anti-)quark fields. In this section, we will talk about the most important continuous ones and discuss their implications on hadron phenomenology and meson spectroscopy in particular.

2.2.1. Vector U(1) symmetry

First of all, the QCD Lagrangian is invariant under a global $\mathrm{U}(1)_V$ transformation of the quark fields

$$\psi_i(x) \to \mathrm{e}^{i\theta}\psi_i(x), \tag{2.20}$$

where θ is a real parameter. One can use Noether's theorem to find that the corresponding conserved current and charge are

$$j^\mu_{\mathrm{U}(1)_V}(x) = \sum_{i=1}^{N_f} \overline{\psi}_i(x)\gamma^\mu\psi_i(x), \quad \hat{Q}_{\mathrm{U}(1)_V} = \sum_{i=1}^{N_f} \int \mathrm{d}^3x\, \psi_i^\dagger(x)\psi_i(x), \tag{2.21}$$

which implies Baryon number conservation. This symmetry is the most robust of the ones we will talk about, as it is unbroken even in the full quantum field theory and independent of the quark masses. It is even conserved in the full standard model and while there is ongoing research to find violations in Baryon number conservation as signs of physics beyond the standard model, e.g. by the means of proton decay [156, 157], no significant evidence of Baryon number violation has been found yet [4].

2.2.2. Axial U(1) symmetry

Consider the transformation

$$\psi_i(x) \to \mathrm{e}^{i\theta\gamma_5}\psi_i(x). \tag{2.22}$$

It differs from (2.20) by the insertion of an additional γ_5 matrix in the argument of the exponential function. It is not a symmetry of the full QCD Lagrangian, as the mass term explicitly breaks it, but it is a symmetry of the Lagrangian for massless quarks, i.e. when $m_i = 0$. One can again consult Noether's theorem to construct a corresponding current and charge

$$j^\mu_{\mathrm{U}(1)_A}(x) = \sum_{i=1}^{N_f} \overline{\psi}_i(x)\gamma^\mu\gamma_5\psi_i(x), \quad \hat{Q}_{\mathrm{U}(1)_A} = \sum_{i=1}^{N_f} \int \mathrm{d}^3x\, \psi_i^\dagger(x)\gamma_5\psi_i(x). \tag{2.23}$$

Noether's theorem leads us to expect this current to be conserved, i.e. $\partial_\mu\, j^\mu_{\mathrm{U}(1)_A} = 0$. However, if one calculates the divergence of this current in the full quantum field theory, one obtains [158]

$$\partial_\mu\, j^\mu_{\mathrm{U}(1)_A}(x) = 2im\overline{\psi}\gamma_5\psi + \left(\frac{g^2}{16\pi^2}\right)\varepsilon_{\mu\nu\rho\sigma}F_a^{\mu\nu}F_b^{\rho\sigma}\,\mathrm{tr}\left(\lambda_a\lambda_b\right). \tag{2.24}$$

Here, we also included the mass-dependent term from the explicitly broken symmetry. The second term is independent of the mass and also present in the massless theory. One can think of it as a remnant of the theory's quantization. This is because ultraviolet divergences in loop diagrams demand the introduction of a UV-regulator, such as a Pauli-Villars regulator, which breaks the $\mathrm{U}(1)_A$ symmetry. The symmetry is not restored, even if the theory is properly renormalized and the regulator is removed. This phenomenon is known as anomalous symmetry breaking and is independent of the choice of regulator. This also cannot be circumvented by utilizing dimensional regularization, since the γ_5 matrix (or its equivalent in higher dimensions) is only well-defined, if the spacetime dimension is an even integer.

This phenomenon is known as chiral anomaly and is not just of purely theoretical interest, but has measurable consequences on the meson spectrum. A SU(3) symmetric quark model with up, down and strange quarks predicts the states [159]

$$\eta_1 = \frac{1}{\sqrt{3}}\left(u\overline{u} + d\overline{d} + s\overline{s}\right), \quad \eta_8 = \frac{1}{\sqrt{6}}\left(u\overline{u} + d\overline{d} - 2s\overline{s}\right). \tag{2.25}$$

The electroweak interaction causes them to mix into the physical states known as η and η' with a mixing angle of $\theta_\mathrm{P} \approx -17°$ [4, 160], with the η being close to the η_8 and the η' being close to the η_1. Since their quark content is very similar, the quark model predicts them to have almost the same mass. Experiments have shown though, that the mass gap is indeed sizeable, with the η' being roughly 75% more massive [4]. By now, more sophisticated theoretical analysis has shown, that the $\eta - \eta'$ gap is indeed a consequence of the chiral $\mathrm{U}(1)_A$ anomaly [161–167].

2.2.3. Vector SU(N_f) symmetry

For many practical applications, the difference between the masses of up and down quarks is so small, that it is often a justified approximation to assume that they are equal. Under this assumption, the QCD Lagrangian has another continuous symmetry. To phrase it more generally, if there are N_f flavours with equal masses, the Lagrangian is symmetric under the transformation

$$\psi(x) \to U_V\, \psi(x) \tag{2.26}$$

with $U_V = \exp\left(i\theta_a \frac{\tau_a}{2}\right)$ being a vector $\mathrm{SU}(N_f)$ matrix, τ_a being the generators of the $\mathfrak{su}(N_f)$ Lie algebra and θ_a the corresponding parameters. The conserved current and charge of this symmetry are

$$j^{\mu}_{\mathrm{SU}(N_f)_V,\,a}(x) = \overline{\psi}(x)\gamma^{\mu}\frac{\tau_a}{2}\psi(x), \quad \hat{Q}_{\mathrm{SU}(N_f)_V,\,a} = \int \mathrm{d}^3x\psi^{\dagger}(x)\frac{\tau_a}{2}\psi(x). \tag{2.27}$$

In the most prominent case, where one assumes that the masses of up and down quarks are the same and thus $N_f = 2$, the generators $\tau_a/2$ are the Pauli matrices and the symmetry is called isospin symmetry. In the case of $N_f = 3$ equal quark masses, the generators are the Gell-Mann matrices. Due to the same underlying symmetry group, isospin shares many properties with “regular” spin. Up and down quarks can be said to have total isospin of $I = 1/2$ and a third component of the isospin of $I_3 = \pm 1/2$ with the plus sign corresponding to up and the minus sign to down quarks. Isospins can also be added analogously to angular momenta, which makes it possible to define an isospin for hadrons as well.

Unequal masses in the QCD Lagrangian explicitly break this symmetry, leading to a non-zero divergence of the current defined in (2.27)

$$\partial_{\mu}\, j^{\mu}_{\mathrm{SU}(N_f)_V,\,a} = i\overline{\psi}\left[\mathbf{m}, \frac{\tau_a}{2}\right]_{-}\psi \tag{2.28}$$

where $\mathbf{m}$ is the quark mass matrix. For diagonal generator matrices τ_a, i.e. σ_3 in the case of $N_f = 2$ or λ_3 and λ_8 in the case of $N_f = 3$, the commutator with the diagonal mass matrix still vanishes, indicating that baryon number, third isospin component and hypercharge are still good quantum numbers even for explicitly broken isospin symmetry [45].

This again has consequences for hadron spectroscopy. For instance, $q\bar{q}$ states, where $q \in \{u, d\}$, can combine either to a total isospin of 0 or 1. Isoscalar states, i.e. states with total isospin 0, can mix with $s\bar{s}$ states, which is the case for the η meson among others, while states with total isospin 1 are prohibited to mix with $s\bar{s}$ states due to the difference in quantum numbers.

An instance where isospin has an impact on baryon physics is the difference in mass and lifetime between the isospin-1 Σ^0 state and the isospin-0 Λ^0 state, which otherwise have the same quark content and quantum numbers [4, 168]. Another case, which highlights the importance of isospin symmetry, is the decay of the $\rho(770)$ and $\omega(782)$ mesons. While both mesons consist of up and down quarks and have the same quantum numbers of angular momentum, parity and charge conjugation ($J^{PC} = 1^{--}$), they differ in their isospin quantum numbers, with the ρ having $I^G = 1^+$ and the ω having $I^G = 0^-$. This allows the ρ meson to decay into two π mesons (pions), while the ω meson decays predominantly into a final state of three pions [4].

2.2.4. Axial SU(N_f) symmetry

Lastly, we will talk about the symmetry, which is most important to the methods used in this work and also has a big impact on the light meson spectrum. If we assume the up and down quarks, or more generally speaking N_f flavours, to not only have the same mass, but also assume that mass to be zero, the QCD Lagrangian is symmetric under the transformation

$$\psi(x) \to U_A \psi(x) \tag{2.29}$$

with $U_A = \exp\left(i\gamma_5\theta_a\frac{\tau_a}{2}\right)$ being an axial SU(N_f) matrix and τ_a and θ_a again being the $\mathfrak{su}(N_f)$ generators and corresponding parameters. The conserved current and charge of this symmetry are

$$j^\mu_{\mathrm{SU}(N_f)_A,\,a}(x) = \overline{\psi}(x)\gamma^\mu\gamma_5\frac{\tau_a}{2}\psi(x), \quad \hat{Q}_{\mathrm{SU}(N_f)_A,\,a} = \int \mathrm{d}^3x\,\psi^\dagger(x)\gamma_5\frac{\tau_a}{2}\psi(x). \tag{2.30}$$

This symmetry is often referred to as chiral symmetry. To see why, let us define the projectors

$$P_\pm = \frac{1}{2}\left(1 \pm \gamma_5\right). \tag{2.31}$$

They form a complete set of projectors, as they obey the relations $P_\pm^2 = P_\pm$ and $P_+ + P_- = \mathbb{1}$. When acting on the quark fields, they project onto parts with positive or negative chirality respectively[2] [128]

[2]We omit the flavour index in the following equations for better readability.

$$P_+\psi(x) = \psi_R(x), \quad P_-\psi(x) = \psi_L(x). \tag{2.32}$$

With this decomposition of the quark fields, one can rephrase the vector and axial $\mathrm{SU}(N_f)$ symmetries as independent symmetries of the left- and right-handed quark fields

$$\psi_L(x) \to \mathrm{e}^{i\frac{\tau_a}{2}\theta_{L,a}}\psi_L(x), \quad \psi_R(x) \to \mathrm{e}^{i\frac{\tau_a}{2}\theta_{R,a}}\psi_R(x). \tag{2.33}$$

These have the conserved currents

$$j^\mu_{L/R,a}(x) = \overline{\psi}_{L/R}(x)\,\gamma^\mu\frac{\tau_a}{2}\,\psi_{L/R}(x), \tag{2.34}$$

which are related to the vector and axial currents via the relation

$$\begin{aligned} j^\mu_{\mathrm{SU}(N_f)_V,\,a} &= j^\mu_{R,a} + j^\mu_{L,a} \\ j^\mu_{\mathrm{SU}(N_f)_A,\,a} &= j^\mu_{R,a} - j^\mu_{L,a}. \end{aligned} \tag{2.35}$$

While chiral symmetry is a fine symmetry of the (massless) QCD Lagrangian and free of anomalies [161], it is spontaneously broken by the QCD vacuum. Since this has important implications on both the phenomenology of light meson spectroscopy and the theoretical tools we use within this work, an entire section is dedicated to this phenomenon.

2.3. Spontaneous chiral symmetry breaking

In this section, we discuss the concept of spontaneous (aka. dynamical) chiral symmetry breaking (DχSB) in the context of QCD and its most important consequences for the spectrum of light mesons. For a treatment of DχSB in the context of QED_{2+1} see [169], and for a thorough treatment of DχSB in a general context, Ref. [170] may be consulted.

In Section 2.2.4 we have seen, that the QCD Lagrangian is invariant under an axial $\mathrm{SU}(N_f)$ transformation, where N_f is the number of massless quarks in the theory. This symmetry has an associated conserved current $Q_{\mathrm{SU}(N_f)_A,\,a}$ as defined in (2.30), meaning that if one were to repackage the QCD Lagrangian into a Hamiltonian $\hat{H}$, these two operators would commute

$$\left[\hat{H}, \hat{Q}_{\mathrm{SU}(N_f)_A,\,a}\right]_- = 0. \tag{2.36}$$

However, it turns out, that the expectation value of this charge is non-zero in the QCD vacuum, i.e.

$$\hat{H}\left|0\right\rangle = E_0\left|0\right\rangle, \quad \hat{Q}_{\mathrm{SU}(N_f)_A,\,a}\left|0\right\rangle = \left|\Omega\right\rangle_a \neq 0. \tag{2.37}$$

In other words, while the Lagrangian[3] of the theory is invariant under an axial transformation, the ground state of the theory is not. This is what is known as spontaneous chiral symmetry breaking.

Classical analogon: Ferromagnet

An often cited example for spontaneous symmetry breaking in a different context is a ferromagnetic system in three dimensions. While the Hamiltonian of such a system is usually invariant under SO(3) transformations, the ground state of the system, i.e. the system at zero temperature, lies below the critical temperature T_c. As a consequence, the system will have a non-zero magnetization $\vec{M}$ along some axis. Therefore, the SO(3) symmetry of the Hamiltonian is broken and the system is only invariant under SO(2) transformations around the axis of magnetization. Notably, the magnetization has a non-zero expectation value in the vacuum, just like the axial charge in QCD, i.e.

$$\left\langle 0\right|\vec{M}\left|0\right\rangle \neq 0. \tag{2.38}$$

2.3.1. Goldstone's theorem

A very important consequence of DχSB is Goldstone's theorem. It states that for every spontaneously broken continuous symmetry of a theory, massless bosons will emerge in the spectrum of that theory [171]. To see how this happens, consider the energy of the quantum state obtained by acting onto the vacuum with the charge operator

$$\hat{H}\left|\Omega\right\rangle_a = \hat{H}\hat{Q}_{\mathrm{SU}(N_f)_A,\,a}\left|0\right\rangle = E_{\Omega_a}\left|\Omega\right\rangle_a. \tag{2.39}$$

Due to the commutator (2.36) of the Hamiltonian and the conserved charge vanishing, the above expression is equal to

$$\hat{H}\left|\Omega\right\rangle_a = \hat{Q}_{\mathrm{SU}(N)_A,\,a}\hat{H}\left|0\right\rangle = \hat{Q}_{\mathrm{SU}(N)_A,\,a}E_0\left|0\right\rangle = E_0\left|\Omega\right\rangle_a. \tag{2.40}$$

By comparing equations (2.39) and (2.40) one finds $E_{\Omega_a} = E_0$. In other words, acting upon the vacuum with the conserved charge modifies the state, but this state has the same energy as the vacuum, i.e. the state of lowest energy. This degeneracy of the vacuum state implies, that the theory must contain massless particles, as the existence of a mass gap would imply that every eigenstate of the Hamiltonian

[3] Or equivalently the Hamiltonian or the classical action

besides the vacuum would have a higher energy. In the case of the spontaneously broken axial SU(N_f) symmetry of QCD, the conserved charge operator has the quantum numbers $J^P = 0^-$, indicating that the massless Goldstone particles of that symmetry are pseudoscalar bosons. In particular, in the case of $N_f = 2$ massless quarks (up and down quarks), one would expect $N_f^2 - 1 = 3$ massless pseudoscalar bosons, in the case of $N_f = 3$ (including massless strange quarks), one expects $N_f^2 - 1 = 8$ of them. In other words, in the $N_f = 2$ chiral limit the pions should become massless while in the $N_f = 3$ chiral limit additionally the kaons and η_8 meson should be massless.[4]

In fact, this is an important cross-check for theoretical calculations of meson spectra. By setting the current quark masses to zero and computing the masses of pions, kaons and η_8 meson, one can check whether a framework implements DχSB properly. Thus, if these particles stay massive in the chiral limit, it is a clear indication, that the calculations do not respect DχSB.

2.3.2. The chiral quark condensate

As a consequence of the action of the conserved SU$(N_f)_A$ charge on the QCD vacuum being non-zero in a theory of massless quarks and the ground state being degenerate, the energy required to create a new quark-antiquark pair is zero. Because of this, we expect the QCD vacuum to contain a condensate of quark-antiquark pairs. These pairs have zero net momentum and angular momentum, so they must have a non-zero net chiral charge, pairing left-handed quarks and right-handed antiquarks and vice versa. This condensate is characterized by a finite vacuum expectation value of the operator [128]

$$\left\langle \overline{\psi}\psi \right\rangle \coloneqq \left\langle 0 \right| \overline{\psi}\psi \left| 0 \right\rangle = \left\langle 0 \right| \overline{\psi}_L \psi_R + \overline{\psi}_R \psi_L \left| 0 \right\rangle \neq 0. \tag{2.41}$$

This expectation value is known as the chiral quark condensate. A non-zero quark condensate is a clear indicator of a spontaneously broken chiral symmetry. In a Green's function description, it can be calculated as an integral over the trace of the chiral quark propagator [45]

$$\left\langle \overline{\psi}\psi \right\rangle = -Z_2 Z_m N_c \int đ^4 q \, \mathrm{tr}\left(S(q)\right) = -4 Z_2 Z_m N_c \int đ^4 q \frac{Z_f(q^2) M(q^2)}{q^2 + M^2(q^2)}. \tag{2.42}$$

In the last step, we expressed the quark propagator in terms of its effective mass function $M(p^2)$ and wave function $Z_f(p^2)$, for details see Appendix A.5. From this relation one can read off, that a non-zero chiral quark condensate requires the effective mass function to not be equal to zero, i.e. $M \not\equiv 0$. This means, that DχSB

[4]The η_1 meson would still carry a topological mass from the U$(1)_A$ anomaly.

necessarily leads to the quark having a finite effective mass, even in the chiral limit, where the current quark mass is zero. We will further investigate this behaviour later in Chapter 5, when calculating the quark propagator numerically.

2.3.3. Gell-Mann-Oakes-Renner relation

In the real world, the masses of the lightest quarks are not exactly zero, but are on the order of a few MeV [4]. The existence of this quark mass explicitly breaks chiral symmetry, since a mass term in the QCD Lagrangian is not invariant under the transformation (2.29). Since chiral symmetry is broken dynamically due to interactions between quarks and gluons, if the masses are relatively small compared to the characteristic scale of those interactions Λ_{QCD}, some effects of DχSB are still noticeable. In particular, the masses of up and down quarks and, to a lesser extent, the strange quark mass are small compared to Λ_{QCD}. This means, that they should have an effective mass function, that is enhanced from their current quark masses. Additionally, in the presence of a small current quark mass m_c, the mass of the lightest pseudoscalar mesons, i.e. the pions in the case of up and down quarks, follows the Gell-Mann-Oakes-Renner (GMOR) relation [172]

$$f_\pi^2 m_\pi^2 = -2m_c \left\langle \overline{\psi}\psi \right\rangle / N_f + O(m_c^2). \tag{2.43}$$

In practical calculations, one can vary the value of m_c and observe how the calculated pion mass responds to see, if the GMOR relation is fulfilled. We will do so explicitly in Section 6.2.

2.3.4. Partially conserved axial current relation

If we take another look at the divergence of the conserved current (2.30) of the axial SU(N_f) symmetry of QCD, we see that in the presence of non-zero but equal quark masses m_c it equates to

$$\partial_\mu j^\mu_{\mathrm{SU}(N_f)_A,\,a}(x) = m_c \overline{\psi}\gamma_5 \tau_a \psi(x). \tag{2.44}$$

To get to this equation, we made use of the Dirac equation of the fermion field $(\not{\partial} + m)\psi = 0$. The right-hand side of this equation is proportional to the pseudoscalar density, while the current on the left-hand side is the axialvector density. One can thus also express this relation in shorthand notation as

$$\partial_\mu\, j^\mu_{5,a} = 2m_c\, j_{5,a}, \tag{2.45}$$

where the index 5 denotes the γ_5 matrices appearing in both currents. This relation is known as the Partially-Conserved-Axial-Current (PCAC) relation. In a full quantum field theory, the conservation of the vector current (2.21) and the PCAC relation are realized through Ward-Takahashi identities [173, 174]. In the context of functional methods, they lead to consistency relations between the quark self-energy and the quark-antiquark scattering kernel. Any practical calculation of light meson properties has to fulfill these identities in order to correctly produce the pion's properties. Due to this importance, we will take a more detailed look at those identities when discussing truncation schemes in sections 4.3.1 and 4.3.2.

3. Dyson-Schwinger equations and functional methods

In this chapter we will take a look at two different methods of deriving equations of motion for Green's functions of QCD.[1] The former is the formalism of Dyson-Schwinger equations (DSEs), the latter is the formalism of n-particle irreducible effective actions. The resulting equations of motion obtained from both methods tend to have subtle differences between them. The solution techniques however are mostly the same, thus we will call the equations derived by the latter formalism DSEs as well.

In Section 3.1 we will cover the Dyson-Schwinger formalism and in Section 3.2 we go over the formalism of n-particle irreducible effective actions. In sections 3.3 through 3.5, we go into more detail on the specific equations derived with the latter approach and sketch solution strategies, which we will use to obtain numerical results for these quantities.

3.1. Dyson-Schwinger equations

3.1.1. Generating functional end effective action

In Section 2.1.1 we have introduced the QCD Lagrangian and the corresponding classical action in equation (2.1). In order to quantize the theory, we introduced the partition function via the path integral formalism in equation (2.7) and derived its gauge-fixed version in eq. (2.11). We can Generalize this expression by introducing source terms for each of the fields to the QCD Lagrangian

$$\begin{aligned} Z\left[j,\eta,\overline{\eta},\sigma,\overline{\sigma}\right] = \int \mathscr{D}\left\{A,\psi,\overline{\psi},c,\overline{c}\right\} \\ \exp\Bigg(- S_{\mathrm{QCD}}[A,\psi,\overline{\psi}] - S_{\mathrm{GF}}[A,c,\overline{c}] \\ + \int \mathrm{d}^4x \left(A_a^\mu j_{a,\mu} + \overline{\eta}_i\psi_i + \overline{\psi}_i\eta_i + \overline{\sigma}c + \overline{c}\sigma\right)\Bigg)\,, \end{aligned} \tag{3.1}$$

[1] These methods can also be generalized to other quantum field theories, but since our goal is to apply them to hadron spectroscopy, we will solely focus on QCD.

where $S_{\mathrm{GF}}[A, c, \overline{c}]$ is the gauge fixing part of the action. By setting the sources $\eta, \overline{\eta}, \sigma, \overline{\sigma}, j$ to zero, this expression becomes equivalent to eq. (2.11) again. This source-dependent version of the partition function is called the generating functional of correlation functions. Since the path integral in equation (3.1) integrates over all possible configurations of the fields, the generating functional contains information about the full quantum field theory, including all kinds of Feynman-diagrams and correlation functions of the theory. It is thus convenient to work with the generating functional of connected correlation functions via the relation

$$\mathrm{e}^{W[J]} \coloneqq Z\left[J\right] \quad \Leftrightarrow \quad W\left[J\right] = \ln Z\left[J\right], \tag{3.2}$$

where J is a shorthand for the set of all sources introduced in eq. (3.1). Additionally, we perform a Legendre transformation of $W[J]$ to remove the explicit dependence on the sources J and go to a dependence on functional derivatives of $W[J]$. For that, we introduce the notation

$$\Phi_i \equiv \langle \phi_i \rangle_J \coloneqq \frac{\delta W[J]}{\delta J_i} = \frac{1}{Z[J]} \int \mathscr{D}\left\{\phi\right\} \phi_i \, \mathrm{e}^{-S + \sum\!\!\!\!\!\!\int_j \phi_j J_j}, \tag{3.3}$$

where ϕ_i can be any field of the theory, i.e. gluon, (anti-)quark or (anti-)ghost, J_i is the corresponding source term, $\mathscr{D}\left\{\phi\right\}$ is a shorthand for the full path integral measure appearing in eq. (3.1) and $\langle \phi_i \rangle_J$ is the expectation value of the field in the presence of non-zero source terms. The combined summation and integration symbol appearing in the argument of the exponential is to be understood as the sum over all fields and all appearing indices, as well as an integration over all position arguments. This explicitly reads for a quark field ψ_i

$$\Psi_i \equiv \langle \psi_i \rangle_J \coloneqq \frac{\delta W[J]}{\delta \overline{\eta}_i} = \frac{1}{Z[J]} \int \mathscr{D}\left\{\phi\right\} \psi_i \, \mathrm{e}^{-S + \sum\!\!\!\!\!\!\int_j \phi_j J_j} \tag{3.4}$$

with similar expressions for the other fields. With this notation at hand, we can perform a Legendre transformation, which leads us to the effective action

$$\Gamma[\Phi] \coloneqq \sup_J \left(-W[J] + \sum_i J_i \Phi_i \right), \tag{3.5}$$

where the explicit dependence on the source terms has been transformed to a dependence on Φ, which is again to be understood as the set of Φ_i for all fields in the theory. Note, that setting the source terms to zero in eq. (3.3) leads to the physical expectation value of the field, i.e. $\Phi_{\mathrm{phys}} \coloneqq \langle \phi \rangle_{J=0}$. This means, that in the following derivations evaluating Φ at the physical point $\Phi = \Phi_{\mathrm{phys}}$ is equivalent to setting the source terms to zero.

The effective action $\Gamma[\Phi]$ is the generating functional for one-particle irreducible (1PI) correlation functions and is thus also known as 1PI effective action. By repackaging the initial generating functional into the 1PI effective action we have lost no information about the full quantum field theory, since every disconnected and one-particle reducible Feynman diagram can be reconstructed by combining connected 1PI diagrams together [128].

3.1.2. N-point functions and propagators

By taking functional derivatives with respect to the fields of the gauge-fixed Lagrangian, one can obtain Green's functions of QCD. This however only yields tree level Green's functions. This is to be expected, since the Lagrangian and the classical action do not contain information about the quantization of the theory and thus cannot produce fully dressed Green's functions containing quantum effects. Instead, one has to resort to quantities derived from the path integral of QCD to obtain fully dressed correlation functions. From the 1PI effective action one can compute 1PI correlation functions, also known as N-point functions, by taking the N-th functional derivative with respect to the fields. Doing so, one ends up with source dependent N-point functions

$$\Gamma^J_{i_1 \dots i_N} = (-1)^\kappa \frac{\delta^N \Gamma[\Phi]}{\delta \Phi_{i_1} \dots \delta \Phi_{i_N}} \tag{3.6}$$

with $\kappa = 0$ for $N = 2$ and $\kappa = 1$ for $N > 2$ being chosen to cancel minus signs appearing in further derivations. The sources can again be set to zero by evaluating the fields at the physical point

$$\Gamma_{i_1 \dots i_N} = \Gamma^{J=0}_{i_1 \dots i_N} = (-1)^\kappa \left. \frac{\delta^N \Gamma[\Phi]}{\delta \Phi_{i_1} \dots \delta \Phi_{i_N}} \right|_{\Phi = \Phi_{\text{phys}}} . \tag{3.7}$$

Propagators are then the inverse of two-point functions

$$D_{ij} \coloneqq \left. \left(\Gamma^{-1}_{ij} \right) \right|_{\Phi = \Phi_{\text{phys}}} . \tag{3.8}$$

Similarly, one can also define field-dependent propagators as the inverse of field-dependent two-point functions $D^J_{ij} = (\Gamma^J_{ij})^{-1}$.

Thus far, we have kept the derivation rather general and worked with shorthand notations for fields. If we reintroduce explicit terms for quark and gluon fields, the quark and gluon propagators and the quark-gluon vertex, a three-point function with two (anti-)quark legs and one gluon leg, can be computed in position space as[2]

[2] We explicitly write out the flavour indices for all quark fields here. When computing these quantities, they will be diagonal in flavour-space, i.e. $S_{ij}(x, y) = \delta_{ij} S(x, y)$. More complicated

$$
\begin{aligned}
S_{ij}^{-1}(x,y) &= \left. \frac{\delta^2 \Gamma\left[A,\psi,\overline{\psi},c,\overline{c}\right]}{\delta\overline{\psi}_i(x)\delta\psi_j(y)} \right|_{\overline{\psi}=\psi=0} \\
D_{\mu\nu}^{-1}(x,y) &= \left. \frac{\delta^2 \Gamma\left[A,\psi,\overline{\psi},c,\overline{c}\right]}{\delta A^\mu(x)\delta A^\nu(y)} \right|_{A_\mu=0} \\
\Gamma^\mu_{\mathrm{qg},ij}(x,y,z) &= \left. \frac{\delta^3 \Gamma\left[A,\psi,\overline{\psi},c,\overline{c}\right]}{\delta\overline{\psi}_i(x)\delta A_\mu(y)\delta\psi_j(z)} \right|_{A_\mu=\overline{\psi}=\psi=0} .
\end{aligned}
\tag{3.9}
$$

Further N-point functions, such as ghost propagators or interaction vertices between only gluons, can be obtained analogously. Even functions with no corresponding tree-level term in the classical action, such as a two-ghost-two-gluon vertex, can be calculated and have a non-zero value in the full quantum field theory [137].

3.1.3. Equations of motion

In the previous section we derived a method to obtained propagators and other N-point functions from the 1PI effective action of QCD by means of functional derivatives. In practice, one does not know the exact expression for the effective action, which makes evaluating the right-hand side of equations (3.7) or specifically (3.9) directly not feasible. Instead, we will in this section take a look at the Dyson-Schwinger framework. It can be used to derive equations for the N-point functions of a theory, in which the explicit functional derivatives of the effective action are replaced with expressions only dependent on other N-point functions. This leads to a set of coupled integral equations for the N-point functions of the theory.

As a first step, it is helpful to realize, that first order functional derivatives of the 1PI effective action with respect to the fields yield the corresponding sources, while derivatives of the generating functional of connected correlation functions with respect to the sources yield the fields [175]

$$
\begin{aligned}
&\frac{\delta W}{\delta j_\mu} = A^\mu, \quad \frac{\delta W}{\delta \eta_i} = \overline{\psi}_i, \quad \frac{\delta W}{\delta \overline{\eta}_i} = \psi_i, \quad \frac{\delta W}{\delta \sigma} = \overline{c}, \quad \frac{\delta W}{\delta \overline{\sigma}} = c \\
&\frac{\delta \Gamma}{\delta A_\mu} = j^\mu, \quad \frac{\delta \Gamma}{\delta \psi_i} = \overline{\eta}_i, \quad \frac{\delta \Gamma}{\delta \overline{\psi}_i} = \eta_i, \quad \frac{\delta \Gamma}{\delta c} = \overline{\sigma}, \quad \frac{\delta \Gamma}{\delta \overline{c}} = \sigma.
\end{aligned}
\tag{3.10}
$$

To derive the Dyson-Schwinger equations, we have to assume, that the path integral formulation of the generating functional (3.1) is well-defined and the

N-point functions may have less trivial flavour structure though, so it can be useful to explicitly take it into consideration.

integral measure is invariant under field transformations $\phi(x) \to \phi(x) + \Lambda(x)$. The DSEs then follow from the observation that the integral of any total derivative vanishes [47]

$$\begin{aligned} 0 &= \int \mathscr{D}\{\phi\} \frac{\delta}{\delta \phi_k} \mathrm{e}^{-S+\not{\int}_j \phi_j J_j} \\ &= \int \mathscr{D}\{\phi\} \left(\frac{\delta}{\delta \phi_k} S[\phi] - J_k \right) \mathrm{e}^{-S+\not{\int}_j \phi_j J_j} \\ &= \left\langle \left(\frac{\delta}{\delta \phi_k} S[\phi] - J_k \right) \right\rangle_J . \end{aligned} \tag{3.11}$$

The last line in this equation is the expectation value of the term in brackets in the presence of the source terms. We can further rewrite this with this term pulled in front of the integral and then evaluated at $\phi_k = \delta/\delta J_k$

$$\left(\frac{\delta}{\delta \phi_k} S[\phi] \Big|_{\phi_k = \delta/\delta J_k} - J_k \right) Z[J] = 0. \tag{3.12}$$

By inserting the relations between S, Z, W and Γ and rewriting the source terms as functional derivatives of Γ as in eq. (3.10), one can further derive the relations [47]

$$\frac{\delta}{\delta \phi_k} S[\phi] \Big|_{\phi_k = \frac{\delta W}{\delta j_k} + \frac{\delta}{\delta j_k}} - J_k = 0 \tag{3.13}$$

$$\frac{\delta}{\delta \phi'_k} S[\phi'] \Big|_{\phi'_k = \phi_k + D^J_{kj} \frac{\delta}{\delta \phi_j}} - \frac{\Gamma[\phi]}{\delta \phi_k} = 0. \tag{3.14}$$

To get from (3.13) to (3.14), one uses that the second derivatives of W and Γ are reciprocal as well as relation (3.8). Equation (3.14) is the so-called "Master DSE", which relates functional derivatives of the 1PI effective action to functional derivatives of the classical action and propagators of the theory. We can use this to obtain explicit expressions for the right-hand side of equation (3.7).

To see how this works out in practice, we apply this to the equation for the quark propagator in Appendix B.2, as this is the most important DSE for this work. In position space[3] the quark DSE explicitly reads

$$S^{-1}_{ik}(x,y) = S^{-1}_{0,ik}(x,y) + g^2 C_F \int \mathrm{d}^4 x' \int \mathrm{d}^4 y' \gamma^\nu S_{il}(x,y') D^{\mu\nu}(x,x') \Gamma^\mu_{\mathrm{qg},lk}(x',y',y). \tag{3.15}$$

[3]In practice, we will later work in momentum space. The DSE in momentum space can be obtained by performing a Fourier transformation of equation (3.15) to obtain (3.29).

Since explicitly working out the functional derivatives can quickly become very tedious, one can resort to diagrammatic descriptions of the DSE formalism, see e.g. [176] for an explanation. The diagrammatic procedure can also be done algorithmically with the help of computer software, cf. [177, 178].

3.1.4. Truncation schemes

By using the Master DSE, we successfully constructed an equation for the fully dressed quark propagator of Landau gauge QCD in equation (3.15). It relates the quark propagator S to the gluon propagator D and the quark-gluon vertex Γ_{qg}. When applying the DSE formalism to derive equations of motion for the gluon propagator and quark-gluon vertex, they will in turn depend on higher order N-point functions and contributions from Faddeev-Popov ghosts. In fact, this is a general theme of Dyson-Schwinger equations; equations of motion for higher order N-point functions will in turn introduce even higher order N-point functions leading to an infinite tower of coupled integral equations [47].

As a consequence, the full set of DSEs in general cannot be solved in closed form. In practical calculations, one thus has to truncate the tower of equations at some point. Those N-point functions, which appear in the equations but have their own equations of motion truncated, have to be approximated, either by modelling them from phenomenological arguments or via systematic schemes, such as nPI effective actions or skeleton expansions[4]. The choice of where and how to truncate the tower is highly non-trivial and depends very much on the concrete problem one wants to apply the DSE formalism to. For example, in hadron spectroscopy, it is of utmost importance to preserve the effects of DχSB discussed in Section 2.3. The truncation of the DSE has therefore be chosen in accordance with the equation used to describe bound states, which we will discuss in detail in Section 4.3.1. For applications related to electromagnetic properties of hadrons, such as form factors, the truncation additionally has to preserve gauge symmetry. The corresponding constraint on the truncation scheme is discussed in Section 4.3.2. Applications to the phase diagram of QCD require their own set of truncations as well, see e.g. [136, 179].

While each truncation scheme has its own set of advantages and disadvantages, a common pitfall all truncation schemes have in common is the fact, that it is nearly impossible to correctly estimate the systematic error introduced through the omission of higher order equations. Recent studies suggest that there is apparent convergence in the Yang-Mills sector at a certain point [180], but there is neither a rigorous proof, that contributions from higher order N-point functions eventually

[4] A skeleton expansion is similar to a perturbative expansion, but uses fully dressed propagators and vertices to implement non-perturbative effects as well.

become negligible, nor is there a way to properly quantify the truncation error. There are ways to infer leading versus subleading contributions to some equations, a few of which we will even apply later in this work, but the lack of a concrete error estimate remains as the biggest drawback of the DSE framework.

We will now give a brief overview over some truncation schemes, which have been applied to several problems in the past. The truncations, which will be applied throughout this work, namely the three-loop 3PI truncation, the rainbow-ladder truncation and the kernel-first truncation will have their own dedicated sections in 3.2.4, 4.3.3 and 4.3.4.

NJL-type models

In the past, many hadron physics studies have been conducted using truncations based on simple models, such as the ones proposed by Nambu and Jona-Lasinio [181, 182] (NJL model) or a similar model by Munczek and Nemirovsky [183, 184]. The NJL model is a simplified low-energy effective theory constructed to describe interactions between nucleons and mesons and exhibits chiral symmetry. It is based on a tree-level four-fermion interaction and thus cannot be renormalized. However, it is useful for exploratory studies, since in the framework of functional methods, it leads to much simpler equations than full QCD. At the level of propagators and vertices, it amounts to replacing the quark-gluon vertex in the quark DSE by a bare vertex $\Gamma^{\mu}_{\mathrm{qg}} \sim \gamma^{\mu}$ as well as contracting the gluon-propagator to a contact interaction $D^{\mu\nu} \sim \delta^{\mu\nu}$. This can be regarded as a more severe simplification of the interaction than the rainbow-ladder truncation (see Section 4.3.3), leading to simpler equations at the cost of loosing information about the momentum dependence of quark and meson properties. The simplicity of the resulting equations has made it a popular and well-explored model for many years now. For reviews, cf. [45, 185]

Beyond the rainbow-ladder truncation

Over the years, many approaches to go beyond the rainbow-ladder truncation have been employed. One drawback of simple truncations of the DSE tower, especially in applications to hadron physics, is that they can obscure information about decays. For instance, within the rainbow-ladder truncation all mesons are stable bound states with real mass poles. Decay thresholds and dynamically generated decay widths are absent in such types of truncations. Nevertheless, for states with a decay width (imaginary part of the pole position) much smaller than the real part of the pole position, the real part can be extracted and decay constants can be calculated reliably via triangle diagrams, see, e.g., [186] for corresponding results for the ρ-meson. More advanced kernels including $\pi\pi$ intermediate states have been employed in Refs. [33, 187, 188] and have been shown to produce the two-pion right-hand cut in the iso-vector and iso-scalar channels.

Other approaches to go beyond rainbow-ladder have been to unquench the quark loops in the Yang-Mills sector [135]. Also, different efforts have been made to include effects of the quark-gluon vertex dressing, including [189–194]. Lately, progress has also been made in explicitly solving quark-gluon vertex equations of motion in different frameworks, such as the 3PI framework [195] and the functional renormalization group framework [61] and applying the results to hadron physics.

Scaling and decoupling solutions

While the infinite set of coupled DSEs cannot be solved in general, there are methods to obtain asymptotic solutions to the full tower of equations in the deep infrared limit. The first discovered solution associates the asymptotic behaviour for $p^2 \ll \Lambda^2_{\mathrm{QCD}}$ of each N-point function of Yang-Mills theory with a power law [44, 196–198]

$$\Gamma^{(n,m)}\left(p^2\right) \sim \left(p^2\right)^{(n-m)\kappa+(1-n)(d/2-2)}, \tag{3.16}$$

where d is the space-time dimension, m is the number of external gluon legs and $2n$ is the number of external ghost legs. These solutions are fittingly called scaling solutions. Obtaining a scaling solution for Green's functions involving quarks is much more complicated due to the quark masses introducing another scale into the theory, leading to much more complicated expressions [146].

There exists however another set of solutions known as decoupling solutions, which associates different asymptotic behaviour to the N-point functions of Yang-Mills theory [199–202]. In fact, there is an entire one-parameter family of asymptotic solutions, which link scaling and decoupling solutions together [137, 203]. The appearance of this one-parameter family has been discussed to be a consequence of the Gribov problem discussed in Section 2.1.3 [44, 204]. Consequentially, physical observables should be the same for all solutions of this family.

However, previous research suggests, that the differences between these solutions have no noticeable impact on hadron physics.[5] For hadron physics involving quarks, the dynamically generated effective quark mass caused by DχSB is much larger than the region of momenta in which scaling and decoupling solutions come into play [205]. Recent Bethe-Salpeter studies of glueballs also suggest, that the glueball spectrum is also approximately invariant for the whole one-parameter family [39]. This is particularly interesting, since the glueball spectrum is dominated by Yang-Mills contributions and has no mass scale in its classical action that could shield it from the infrared behaviour of the Yang-Mills N-point functions.

[5]Note, that the mass gap between the η and η' mesons due to the $\mathrm{U}(1)_{\mathrm{A}}$ anomaly has been explained in the framework of functional methods before using the scaling solution [167], but

There has been a lot of work on scaling and decoupling solutions of Yang-Mills theories in the past decades, which we can only cover superficially in the scope of this work. For more information on this topic, see e.g. [50, 53, 54, 196–198, 206, 207] and references therein.

3.2. n-particle irreducible effective action

In this section we will introduce the formalism of n-particle irreducible (nPI) effective actions. It is not only a generalization of the 1PI effective action (3.5), but it also serves as a means to truncate the tower of DSEs by doing a loop expansion on the level of the effective action.

We will start by constructing the nPI effective action as a generalization of the 1PI case in Section 3.2.1. Next we will take a look at a method to derive equations of motion for N-point functions from nPI actions in an analytic way in Section 3.2.2. Then, we will talk about loop expansions of the nPI effective action as truncation scheme in Section 3.2.3. Lastly, in Section 3.2.4 we will focus on the specific case of the 3PI effective action of QCD to three-loop order and highlight a diagrammatic way of deriving the equations of motion.

3.2.1. Definition of the nPI effective action

The idea behind the nPI formalism is to introduce higher order source terms into the generating functional (3.1) and then perform additional Legendre transformations of the generating functional of connected correlation functions to shift the dependence on higher order source terms to a dependence on n-point functions. For the sake of readability, we will again resort to a compact notation for now, in which (3.1) reads

$$Z[J] = \int \mathscr{D}\{\phi\} \exp\left(-S_{\text{QCD}}[\phi] - S_{\text{GF}}[\phi] + \sum\!\!\!\!\!\!\!\int_j \phi_j J_j\right), \tag{3.17}$$

We can now introduce source terms for products of n fields, which we call $J^{(n)}$, and define a version of the generating functional dependent on those sources as

no corresponding study has been published yet using decoupling solutions. This is still a topic of ongoing research.

$$
\begin{aligned}
Z[J, J^{(2)}, \dots, J^{(n)}] &:= \int \mathscr{D}\{\phi\} \exp\Bigg(-S_{\mathrm{QCD}}[\phi] - S_{\mathrm{GF}}[\phi] + \sum_j \phi_j J_j + \frac{1}{2!}\sum_{ij} \phi_i \phi_j J^{(2)}_{ij} \\
&\qquad + \frac{1}{3!}\sum_{ijk} \phi_i \phi_j \phi_k J^{(3)}_{ijk} + \dots \Bigg) \\
&= \int \mathscr{D}\{\phi\} \exp\left(-S_{\mathrm{QCD}}[\phi] - S_{\mathrm{GF}}[\phi] + \sum_{a=1}^{n} \frac{1}{a!}\left(\prod_{b=1}^{a} \phi_{i_b}\right) J^{(a)}_{i_1 i_2 \dots i_a}\right).
\end{aligned}
\tag{3.18}
$$

In the last line, a sum over repeating indices i_b together with the corresponding spacetime integral is implied. We can again obtain the nPI generating functional of connected Green's functions $W[J, J^{(2)}, \dots, J^{(n)}]$ analogously to eq. (3.2). The first order functional derivative of that quantity with respect to the source J again produces the expectation value of the corresponding field for non-zero sources, akin to eq. (3.3). But now we can also take functional derivatives with respect to higher order sources to obtain N-point functions [176]

$$
\begin{aligned}
&\frac{\delta W}{\delta J_i} = \langle \phi_i \rangle_J = \Phi_i, \qquad \frac{\delta W}{\delta J^{(2)}_{ij}} = \frac{1}{2!}\left(D^J_{ij} + \Phi_i \Phi_j\right), \\
&\frac{\delta W}{\delta J^{(3)}_{ijk}} = \frac{1}{3!}\left(D^{(3),J}_{ijk} + D^J_{ij}\Phi_k + D^J_{ki}\Phi_j + D^J_{jk}\Phi_i + \Phi_i\Phi_j\Phi_k\right), \quad \dots,
\end{aligned}
\tag{3.19}
$$

where $D^{(3),J}_{ijk}$ is the third derivative of W with respect to J. Now we can perform a Legendre transformation analogous to eq. 3.5 to obtain the n-particle irreducible effective action

$$
\Gamma_n \equiv \Gamma[\Phi, D, \Gamma^{(3)}, \dots, \Gamma^{(n)}] = -W + \frac{\delta W}{\delta J_i} J_i + \frac{\delta W}{\delta J^{(2)}_{ij}} J^{(2)}_{ij} + \dots + \frac{\delta W}{\delta J^{(n)}_{i_1 i_2 \dots i_n}} J^{(n)}_{i_1 i_2 \dots i_n}.
\tag{3.20}
$$

In the context of Feynman diagrams, the term n-particle irreducible usually means, that a diagram cannot be separated into disconnected loop diagrams by cutting at most n propagator lines. In the context of nPI effective actions this is only the case for $n \leq 4$ [208]. Instead, n can be interpreted as the highest dynamically included n-point function [209]. In the case of the 3PI effective action of QCD this implies, that the quark-gluon, three-gluon and ghost-gluon vertices are dynamically included and appear fully dressed in a loop expansion, while the four-gluon vertex only appears in its tree-level form.

3.2.2. Equations of motion

To see how equations of motion are obtained from the nPI effective action, note, that functional derivatives of eq. (3.20) with respect to fields and N-point functions yield expressions linear in the source terms

$$\frac{\delta\Gamma_n}{\delta\Phi_i} = J_i, \quad \frac{\delta\Gamma_n}{\delta D^{(2)}_{ij}} = \frac{1}{2!}J^{(2)}_{ij}, \quad \frac{\delta\Gamma_n}{\delta\Gamma^{(3)}_{ijk}} = \frac{1}{3!}D_{ai}D_{bj}D_{ck}J^{(3)}_{abc}, \quad \dots . \tag{3.21}$$

As a consequence, setting the sources to zero to obtain physical values leads to the stationarity conditions

$$\left.\frac{\delta\Gamma_n}{\delta\Phi_i}\right|_{J=J^{(2)}=\dots=J^{(n)}=0} = \left.\frac{\delta\Gamma_n}{\delta D^{(2)}_{ij}}\right|_{J=J^{(2)}=\dots=J^{(n)}=0} = \left.\frac{\delta\Gamma_n}{\delta\Gamma^{(3)}_{ijk}}\right|_{J=J^{(2)}=\dots=J^{(n)}=0} = 0, \dots . \tag{3.22}$$

Using the stationarity condition for the derivative with respect to the propagator, i.e. the inverse two-point function, one obtains for the equation of motion for the fermion propagator [210]

$$-S^{-1}_{ik}(x,y) + S^{-1}_{0,ik}(x,y) + i\left.\left(\frac{\delta\Gamma_n}{\delta S}\right)_{ik}\right|_{J=J^{(2)}=\dots=J^{(n)}=0} = 0. \tag{3.23}$$

This equation has the same structure as the equation of motion obtained from the Dyson-Schwinger mechanism (3.15) with the derivative of Γ_n with respect to the propagator being the self-energy. In practice, one usually works with a diagrammatic representation of the effective action, in which functional derivatives can conveniently be performed by "cutting out" propagator lines or vertices from the diagrams. An exemplary demonstration of that for the quark propagator's equation of motion will be given in Section 3.2.4.

3.2.3. Loop expansions

Thus far, by performing Legendre transformations to get from the 1PI effective action to the nPI effective action, we only performed a change in variables. The nPI effective action still formally contains an infinite amount of terms, which necessitates the need for truncation.

A common way of truncating the nPI effective action equations of motion is by performing a loop expansion. The idea behind an l-loop truncation is to only include vacuum diagrams in the nPI effective action, which have no more than l loops in them. For $l \geq n$, the equations of motion for m-point functions derived from the nPI effective action with $m \leq n-2$ agree with their corresponding DSEs [176, 211]. The results of the coupled system of equations will differ though, since higher order correlation functions differ in their equations of motion. These similarities and differences in the equations of motion obtained via different formalisms can lead to synergies when investigating certain N-point functions. For instance, the quark-gluon vertex satisfies a one-loop equation when calculated in a three-loop truncated 3PI effective action framework, while in the DSE framework it satisfies a two-loop equation. Still, the results of both equations agree very well [138]. We will go into more detail on the 3PI equation of motion of the quark-gluon vertex in Section 3.5.

3.2.4. 3PI effective action of QCD to three-loop order

In the following, we will work with a three-loop expansion of the 3-particle irreducible effective action of QCD. The reason for choosing this particular truncation are twofold.

Firstly, going to three loops and 3PI means that all three point vertices of QCD, namely the quark-gluon vertex, three-gluon vertex and ghost-gluon vertex are dynamically included in the system. This is of particular importance, since the quark-gluon vertex is the key quantity that links the quark sector of QCD to the Yang-Mills sector, and the three-gluon vertex is the leading vertex in the dynamics of the Yang-Mills sector [176]. Similarly, from the argumentation given above, the equations for propagators will be identical to their DSEs, which makes comparison with DSE results possible.

Secondly, previous research has shown, that going beyond this truncation has negligible effects in certain applications [180]. This phenomenon, that the effect on observable hadron spectra gets smaller for higher order truncations, is known as apparent convergence. In Ref. [180], apparent convergence was shown to happen in glueball spectra obtained from the 3PI effective action in three-loop truncation. Since the only vertex which appears in tree-level QCD, that is not dynamically included in the 3PI effective action is the four-gluon vertex, one would expect effects beyond the 3PI three-loop setup to become noticeable in the Yang-Mills sector first. The glueball spectrum apparently converging is thus a good indication, that this setup is also a good truncation for pure quark hadron spectroscopy, such as meson spectroscopy.[6]

The 3PI effective action of QCD in three-loop truncation is diagrammatically depicted in Fig. 3.1. To see, how equations of motion can be obtained from these diagrams, we will explicitly work through the derivation of the quark self-energy and the equation for the quark-gluon vertex. All other equations of motion can be

[6]There are still benefits to going to 4PI effective actions and possibly beyond, since it allows for investigation of resonances and decays by computing the time-like properties of N-point functions. Since the 4PI effective action is a much more complicated object than the 3PI one, this is still topic of ongoing research.

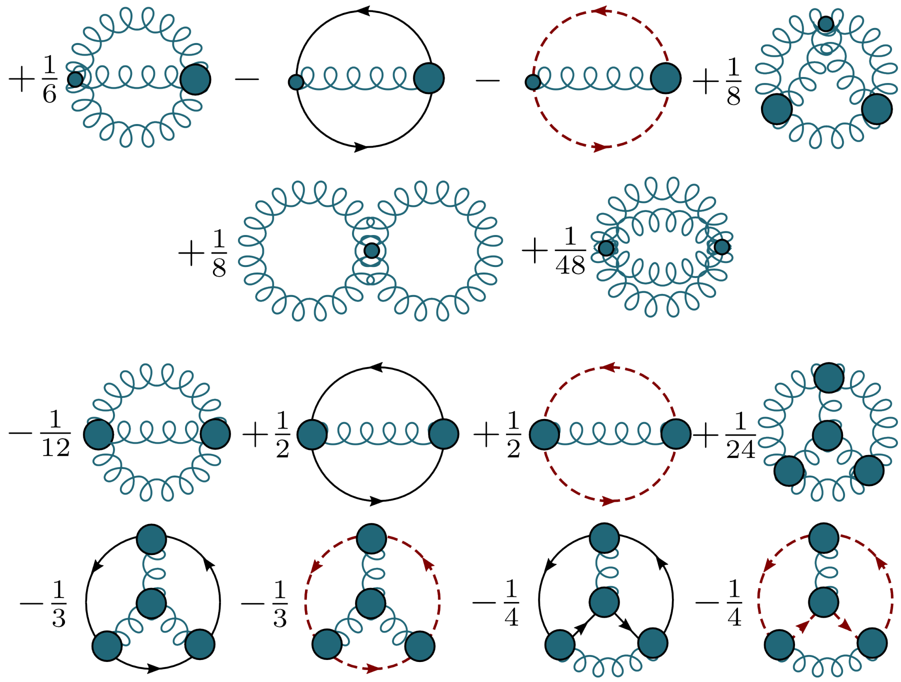

Figure 3.1.: Top two rows: Non-interacting part of the 3PI effective action. Bottom two rows: Interacting part of the 3PI effective action. Solid lines with arrows correspond to quark propagators, dashed lines are ghost propagators and springy lines are gluon propagators. All internal propagators are fully dressed. Small circles stand for tree level vertices, large circles are fully dressed vertices. Taken from [195].

obtained analogously, so we will only show the results of those derivations later in this chapter.

Recall from eq. (3.23), that the quark self-energy is obtained from the effective action by taking the functional derivative with respect to the quark propagator. On the level of Feynman diagrams, taking the functional derivative with respect to a propagator is equivalent to cutting through a corresponding propagator line in the diagram. There are only four diagrams containing quark propagators in the effective action in Fig. 3.1, the diagrams containing only gluon and ghost propagators do not contribute. The derivative is thus equal to

$$\frac{\delta\Gamma^{3l}_{3PI}}{\delta S} = \frac{\delta}{\delta S}$$

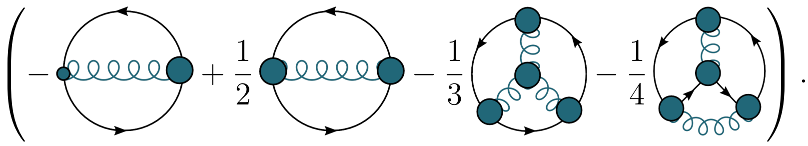

(3.24)

By cutting a propagator line for each derivative and using the product rule, this equates to

$$\frac{\delta\Gamma^{3l}_{3PI}}{\delta S} =$$

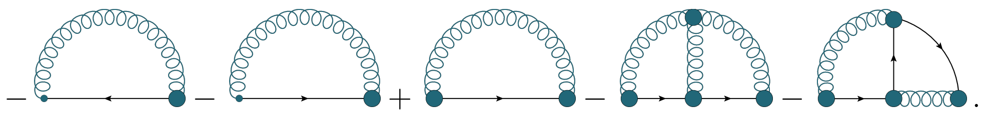

(3.25)

This expression does not yet resemble the quark self-energy in the quark DSE (3.15). To see how the two are equal, we use the stationarity condition (3.22) to get an equation for the quark-gluon vertex. Taking functional derivatives of the effective action with respect to the quark-gluon vertex is again equivalent to cutting out dressed vertices from the diagrams. Doing so leads to the equation

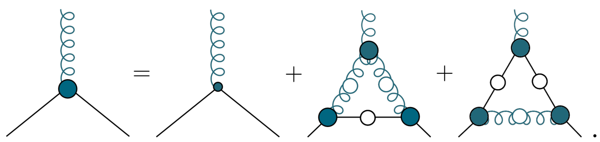

(3.26)

Inserting this for the left dressed quark-gluon vertices in the third diagram in equation (3.25) leads to

$$\frac{\delta\Gamma^{3l}_{3PI}}{\delta S} =$$

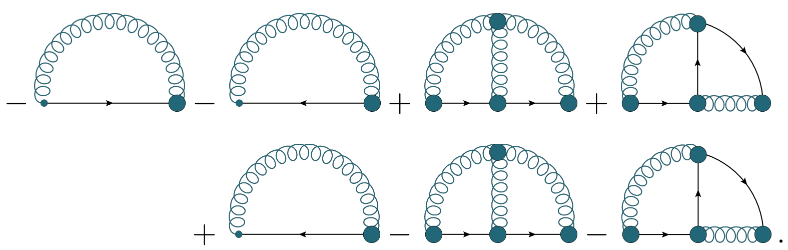

(3.27)

Now one sees, that all but the first diagram cancel, leading to the same self-energy as from the Dyson-Schwinger mechanism. Similar cancellations happen in the derivations for other propagator- and vertex equations. We will present the resulting equations and their most important features in the following sections.

3.3. Dyson-Schwinger equations of the Yang-Mills sector

Applying the methodology outlined in the previous section to the gluon propagator, ghost propagator, three-gluon vertex and ghost-gluon vertex leads to the equations of motion diagrammatically shown in Fig. 3.2. These equations have not been solved by the author of this work, but by Markus Q. Huber. Still, they will be briefly discussed, since they serve as important input for calculations beyond the rainbow-ladder truncation later on in this work. For details on the calculations, cf. [137, 138, 180, 212] and references therein.

The Yang-Mills N-point function most important for our work is the gluon propagator. It is important for this work, because it directly enters not only the equation of motion for the quark-gluon vertex, but also the bound state equations discussed in Chapter 4. In Landau gauge, it consists of a single tensor structure, namely a transverse projector to the gluon's momentum, with a single dressing function

$$D^{\mu\nu}(k) = \left(\eta^{\mu\nu} - \frac{k^\mu k^\nu}{k^2}\right)\frac{Z(k^2)}{k^2}. \tag{3.28}$$

In the form the Yang-Mills equations of motion are depicted in Fig. 3.2, they do not quite form a closed set of coupled equations yet. Instead, they still contain loops of quark propagators in the equations for the gluon propagator and the three-gluon vertex. For the sake of simplicity, a further simplification has been done to them by neglecting all diagrams containing closed quark loops. This is analogous to setting the fermion determinant in lattice QCD calculations to one, which is an approximation known as quenched QCD. Without the quark loops, the Yang-Mills sector can be solved fully self-contained and the results for the gluon propagator and three-gluon vertex are further used as input for the equation of motion of the quark-gluon vertex, see Sec. 3.5.

In principle our framework allows for inclusion of the quark loops, which is equivalent to unquenching the fermion determinant. This would then lead to the Yang-Mills sector N-point functions being directly coupled to the quark sector. In practice, this amounts to numerically solving a coupled set of integral equations with six different N-point functions containing a total of 17 one-loop and two-

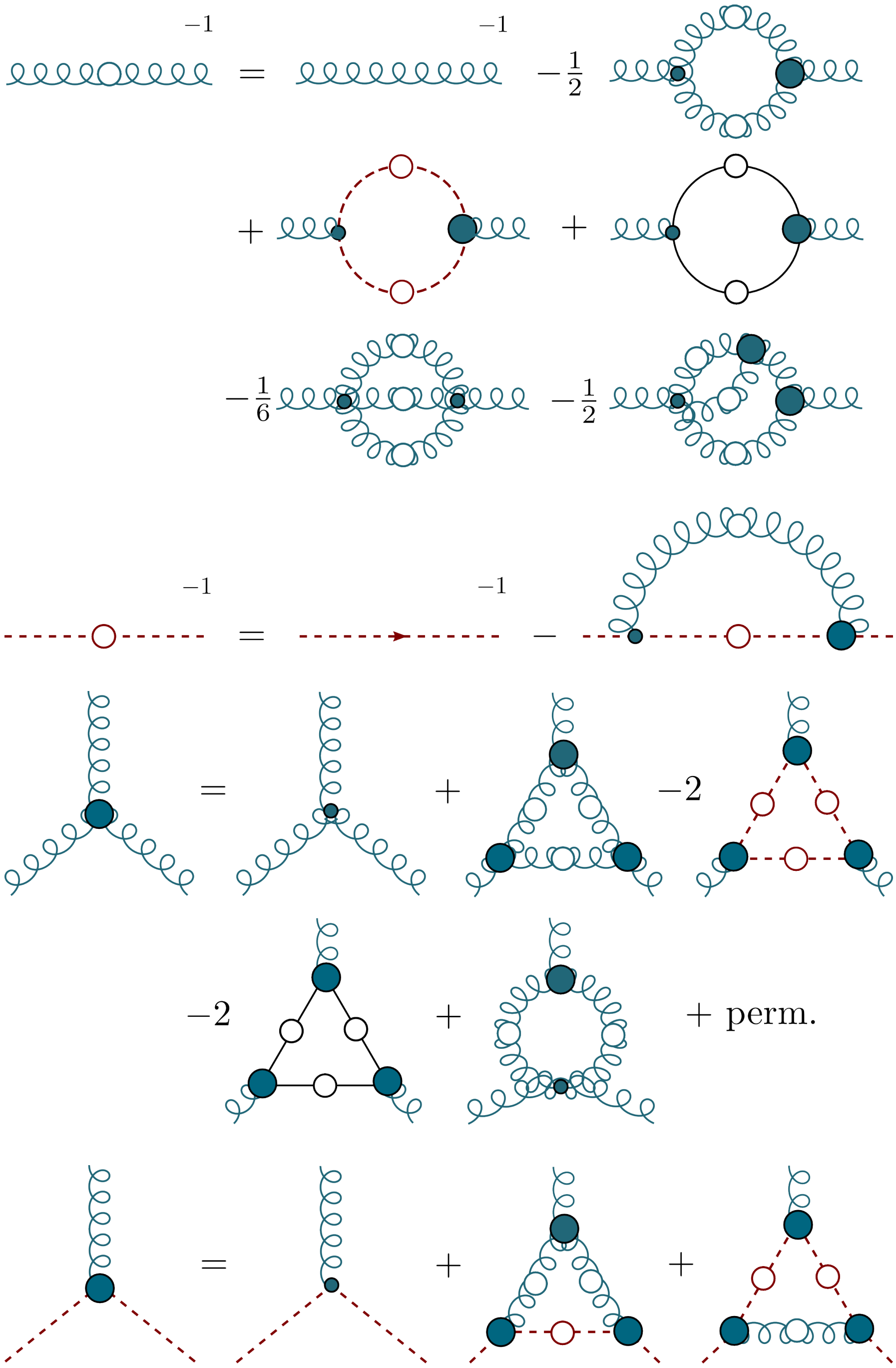

Figure 3.2.: Equations of motion for the Yang-Mills sector N-point functions. Top to bottom: Gluon propagator, ghost propagator, three-gluon vertex, ghost-gluon vertex. In the 3PI three loop truncation the four-gluon vertex does not become dressed.

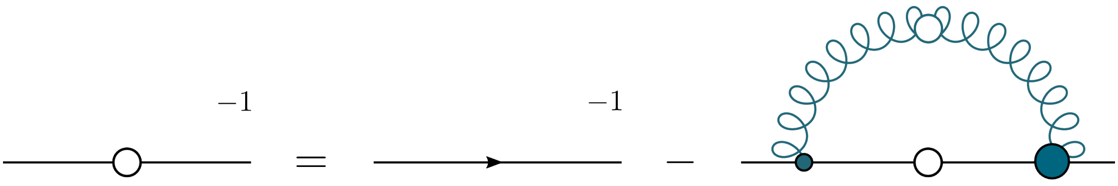

Figure 3.3.: Dyson-Schwinger equation of the quark propagator. Lines with arrows correspond to bare propagators, lines with a white circle represent dressed propagators.

loop diagrams[7] to be solved. This is both technically and computationally very demanding and has thus been delegated to future work.

3.4. Dyson-Schwinger equation of the quark propagator

In this section, we will discuss the equation of motion of the quark propagator. In practice, the quark self-energy $\Sigma(p)$ appearing in this equation or quantities appearing inside $\Sigma(p)$ need to be truncated in some way in order to render the set of equations of motion finite. We will go into detail on two truncation schemes used within this work in Section 4.3. In this section, we will focus on the general solution strategy of the quark DSE.

Using the Dyson-Schwinger formalism as well as the 3PI effective action procedure produces the exact same equation of motion for the quark two point function, i.e. the inverse quark propagator. Diagrammatically, it can be seen in Fig. 3.3. Using the Feynman rules of QCD, one can translate this into a symbolic equation, which reads

$$S^{-1}(p) = S_0^{-1}(p) - \Sigma(p) = S_0^{-1}(p) - Z_{1f} g^2 C_F \int đ^4 q \, i\gamma^\mu S(q) \Gamma^\mu_{\mathrm{qg}}(k; -p, q) D^{\mu\nu}(k). \tag{3.29}$$

$S_0^{-1}(p) = Z_2(i\not{p} + Z_m m_c)$ is the bare inverse quark propagator, C_F is a Casimir factor from the colour trace and is equal to $4/3$ for $N_c = 3$, Z_2 and Z_{1f} are renormalization constants introduced in Section 2.1.4, g^2 is the coupling constant of QCD, $D^{\mu\nu}(k)$ is the gluon propagator discussed in Section 3.3 and $\Gamma^\mu_{\mathrm{qg}}(k; p, q)$ is the quark-gluon vertex, which will also be discussed in detail in Section 3.5. Alternatively, one can perform a Fourier transform on the position space DSE (3.15) to obtain the same equation.

[7]Assuming no further approximations are made and no diagrams left out

The common way to solve the quark DSE is by decomposing the inverse propagator's tensor structure into a vector and a scalar part

$$S^{-1}(p) = i\not{p}A(p^2) + B(p^2). \tag{3.30}$$

There are also other possible ways to write the quark propagator in terms of tensor structures and dressing functions. Some common ones are listed and explained in Appendix A.5. With this decomposition in place, one can project onto the dressing functions $A(p^2)$ and $B(p^2)$ to obtain coupled integral equations for the two functions. In particular, we use the projection properties

$$A(p^2) = \frac{-i}{4p^2}\,\mathrm{tr}\left(\not{p}\,S^{-1}(p)\right), \quad B(p^2) = \frac{1}{4}\,\mathrm{tr}\left(S^{-1}(p)\right). \tag{3.31}$$

Inserting the right-hand side of equation (3.29) into the traces leads to coupled equations for both dressing functions, which read

$$\begin{aligned} A(p^2) &= Z_2 + \frac{i}{4p^2}\,\mathrm{tr}\left(\not{p}\,\Sigma(p)\right) \equiv Z_2 + \Sigma_A(p^2) \\ B(p^2) &= Z_2 Z_m m_c - \frac{1}{4}\,\mathrm{tr}\left(\Sigma(p)\right) \equiv Z_2 Z_m m_c + \Sigma_B(p^2). \end{aligned} \tag{3.32}$$

To solve these equations, one typically follows these four steps:

- Perform the traces $\mathrm{tr}\left(\not{p}\,\Sigma(p)\right)$ and $\mathrm{tr}\left(\Sigma(p)\right)$ to obtain expressions for $\Sigma_A(p^2)$ and $\Sigma_B(p^2)$.
- Initialize $A_0(P^2)$ and $B_0(p^2)$ on a logarithmic grid in p^2 with an initial guess. A common choice is $A_0(p^2) \equiv 1$ and $B_0(p^2) \equiv m_c + \varepsilon_m$, where ε_m is a small shift to prevent running into the $B(p^2) \equiv 0$ fix-point in the chiral limit.
- Recursively calculate $A_n(p^2)$ and $B_n(p^2)$ by inserting $A_{n-1}(p^2)$ and $B_{n-1}(p^2)$ into the right-hand side of equations (3.32) and evaluating the integrals.
- Check for convergence by testing, whether the change in $A_n(p^2)$ and $B_n(p^2)$ during the step $(n-1) \to n$ was smaller than a predefined small threshold.

Once the results have converged, they may be used as input for bound state calculations or continued into the complex plane. Details on how to do the latter can be found in Appendix C.2.

Note, that these instructions are specific to truncations, where other than the quark propagator all inputs for $\Sigma(p)$ are fixed. In the calculations we will perform later in this work this is the case, since all quantities appearing in $\Sigma(p)$, such as the quark propagator and the quark-gluon vertex, are either modelled or taken as input from previous calculations. In a full-fledged calculation of the coupled system between quark- and Yang-Mills sectors, iteration steps of different Green's functions need to be intertwined to propagate changes in one function to the others. The numerical details of these iterations can become quite involved and are highly non-trivial. For details on how this can be done in the Yang-Mills sector, cf. [138] and references therein.

Renormalization

In addition to updating the dressing functions $A(p^2)$ and $B(p^2)$ in each iteration step, one also needs to calculate the renormalization constants Z_2 and Z_m. To do this, one needs to specify a renormalization scale μ and renormalization conditions for $A(p^2)$ and $B(p^2)$. A canonical choice is

$$A(\mu^2) \stackrel{!}{=} 1, \quad B(\mu^2) \stackrel{!}{=} m_c. \tag{3.33}$$

Using these relations, one can calculate Z_2 and Z_m in each iteration step via[8]

$$Z_2 = 1 - \Sigma_A(\mu^2), \quad Z_m = \frac{1}{Z_2}\left(1 - \frac{\Sigma_B(p^2)}{m_c}\right). \tag{3.34}$$

It is important to note, that in the chiral limit the above formula for Z_m breaks down. Since $Z_2 Z_m m_c$ is zero in the chiral limit anyways, one can just extrapolate a value for Z_m obtained at finite m_c to the chiral limit.

Within the chiral limit, one can also calculate the chiral quark condensate $\left\langle\overline{\psi}\psi\right\rangle$ using equation (2.42). A non-zero value of it hints at chiral symmetry being broken spontaneously. Away from the chiral limit, when the current quark masses are still small, we still expect an enhancement in the effective quark mass $M(p^2) = B(p^2)/A(p^2)$ to appear, which also signals DχSB. We will investigate in how far this is the case in Chapter 5, when we discuss numerical results of the quark DSE in different truncations.

3.5. Dyson-Schwinger equation of the quark-gluon-vertex

Lastly, we will take a look at the equation of motion for the quark-gluon vertex. It is not only a central ingredient in the quark DSE, but it also serves as the central piece that links the quark sector of QCD and the Yang-Mills sector together. Its equation

[8] Within some truncations schemes, including the rainbow-ladder truncation with the Maris-Tandy effective running coupling, there is another way to calculate Z_2 via $Z_{2,n} = 1/(1 + Z_{2,n-1}\Sigma_A(\mu^2))$. This is, however, very much truncation dependent, while equation (3.34) is more universal.

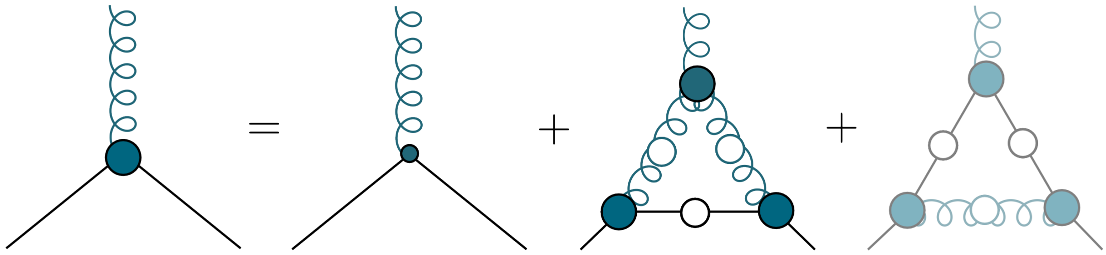

Figure 3.4.: Equation of motion for the quark-gluon vertex. The non-Abelian diagram has been omitted in calculations relevant to this work.

of motion derived from the 3PI effective action is depicted diagrammatically in Fig. 3.4. Note, that the appearance of only fully dressed vertices in the loop diagrams is an effect of the 3PI formalism, since in the DSE formalism each loop diagram will always contain one bare vertex [137]. The equation has the general structure

$$\Gamma^{\mu}_{\text{qg}} = \Gamma^{\mu}_{\text{bare}} + \Gamma^{\mu}_{\text{non-Abelian}} + \Gamma^{\mu}_{\text{Abelian}}. \tag{3.35}$$

The bare term is simply proportional to γ^{μ}. The non-Abelian term is used for the diagram containing two quark-gluon vertices and one three-gluon vertex, while the Abelian term corresponds to the diagram containing three quark-gluon vertices and no three-gluon vertex. The reason for this nomenclature is that the Abelian diagram also appears in calculations of fermion-gauge-boson vertices in Abelian gauge theories, such as the electron-photon vertex in quantum electrodynamics, while the non-Abelian diagram is only present in non-Abelian gauge theories where the gauge bosons interact with each other.

In this work, we will neglect the Abelian diagram in the quark-gluon vertex equation. The reason for this is twofold; firstly, the contribution of the Abelian diagram is suppressed compared to the non-Abelian one. When computing the colour trace of both diagrams, one finds that the Abelian one has a prefactor of g^2/N_c, while the non-Abelian diagram has a prefactor of $g^2 N_c$ [195]. Thus, from the colour structure alone, the Abelian diagram is suppressed by a factor of $N_c^2 = 9$. Additionally, direct calculations in the past have shown, that the contribution of the Abelian diagram is in fact small, on the level of few percent [195]. Secondly, if we were to include the Abelian diagram in the equation for the quark-gluon vertex, a consistent derivation of the scattering kernel used in the meson Bethe-Salpeter equation would introduce a two loop diagram with a crossed gluon exchange. We will see how this would arise in Section 4.3.4. Since such a diagram would result in considerable additional computational cost, it is also practical to omit it.

3.5.1. Kinematics of the quark-gluon vertex

In general, the quark-gluon vertex depends on three momenta. Taking the momentum of each of the legs as incoming, these are the quark momentum q, the anti-quark momentum p and the gluon momentum k. From these, one can construct a total of six Lorentz invariants by taking all combinations of scalar products. Conservation of four-momentum reduces the momentum dependence down to two independent momenta, which we take to be the gluon momentum $k = q + p$ and the relative quark momentum $l = (q - p)/2$. This means only three independent Lorentz invariants remain, which can be chosen to be k^2, l^2 and $(l \cdot k)$, or other linear combinations of them, such as q^2, p^2 and k^2.

In numerical calculations, the choice of parametrization by choosing a set of independent Lorentz invariants plays an important role, because discretization of the momentum variables can cause different kinematic regions to be probed in more or less detail. The question, which parametrization of the quark-gluon vertex is optimal for which application, still poses an open problem, as not a lot is know about the full momentum dependence of the quark-gluon vertex, especially in the complex plane. Studies done in the past by different groups have opted to choose different parametrizations [195, 213, 214].

In this work, we opt for a parametrization via S_3 variables. These have successfully been used in studies of the three-gluon vertex, where the symmetry between the gluon legs makes them the natural choice [138]. They have also been applied to quark-gluon vertex studies before [195]. The S_3 variables are defined via a singlet variable S_0 and two doublet variables a and s

$$\begin{aligned} S_0 &= \frac{p^2+q^2+k^2}{6} & & p^2 = S_0\left(1+\sqrt{3}\,a+s\right) \\ a &= \frac{\sqrt{3}\,(p^2-k^2)}{p^2+q^2+k^2} & \Leftrightarrow \quad & q^2 = 2S_0\,(1-s) \\ s &= \frac{p^2+k^2-2q^2}{p^2+q^2+k^2} & & k^2 = S_0\left(1-\sqrt{3}\,a+s\right). \end{aligned} \tag{3.36}$$

Additionally, we employ polar coordinates in the (a, s)-plane

$$\begin{aligned} \rho &= \sqrt{a^2+s^2} \\ \eta &= \operatorname{atan2}(s, a), \end{aligned} \tag{3.37}$$

such that $a = \rho\cos\eta$ and $s = \rho\sin\eta$. The choice of (S_0, ρ, η) as parametrization of the momentum dependence of the quark-gluon vertex brings some practical advantages. In numerical treatments of the quark DSE and the meson BSE involving the quark-gluon vertex, one has to interpolate the dressing functions of the vertex as a function of the momentum parametrization. In the (S_0, ρ, η) parametrization, the S_0 dependence dominates the dynamics of the vertex. Thus, a larger number of abscissas can be used in the (logarithmic) S_0-grid together with a cubic spline interpolation for improved accuracy. The ρ dependence is comparatively small, which makes a linear interpolation on a relatively small ρ-grid sufficient. Lastly, by definition, the variable η is periodic with a period of 2π, such that a trigonometric interpolation can be used, which removes the need of extrapolation ambiguities for values beyond the grid. This three-dimensional interpolation scheme, while being conceptually more complex, is computationally more efficient than employing a tri-cubic interpolation on relatively large grids for q^2, p^2 and k^2.

3.5.2. Tensor basis of the quark-gluon vertex

In general, the Dirac structure of the quark-gluon vertex can be decomposed into twelve basis elements, which are all possible combinations of

$$\Gamma^{\mu}_{\mathrm{qg}}(k;p,q) \sim \left\{\mathbb{1}, \not{p}\right\} \otimes \left\{\mathbb{1}, \not{q}\right\} \otimes \left\{\gamma^{\mu}, p^{\mu}, q^{\mu}\right\}. \tag{3.38}$$

In practice, the basis elements can also be chosen to be linear combinations of those quantities and the base can be constructed to suit the needs of the application at hand. Since the quark-gluon vertex in the quark DSE and the meson BSE always appears alongside a gluon propagator, which in Landau gauge equates to a dressed transverse propagator, it is sufficient to consider the vertex that is transverse to the gluon momentum. Throughout this work, we use a re-ordered version of the used in Ref. [213], which in compact form reads

$$\begin{aligned} T^{\mu\nu}(k)\Gamma^{\nu}_{\mathrm{qg}}(k;p,q) &= \sum_{i=1}^{8} h_i(k;p,q)\lambda_i^{\mu}(k;p,q) \\ &= \quad h_1\gamma^{\mu}_{\perp} + h_2\frac{1}{6}\left[\gamma^{\mu}_{\perp}, \not{l}, \not{k}\right] + h_3 l^{\mu}_{\perp}\not{l} + h_4 t^{\mu\nu}_{(kl)}\gamma^{\nu} \\ &\quad + h_5 i l_{\perp^{\mu}} + h_6\frac{i}{2}\left[\gamma^{\mu}_{\perp}, \not{k}\right] + h_7\frac{i}{2}\left[\gamma^{\mu}_{\perp}, \not{l}\right] + h_8 t^{\mu\nu}_{(kl)}\frac{i}{2}\left[\gamma^{\nu}, \not{l}\right], \end{aligned} \tag{3.39}$$

with gluon momentum $k = p+q$, relative quark momentum $l = (q-p)/2$, dressing functions $h_i = h_i(k;p,q) \equiv h_i(k,l)$, transverse projectors $t^{\mu\nu}_{(kl)} = (l\cdot k)\,\eta^{\mu\nu} - l^{\mu}k^{\nu}$ and $T^{\mu\nu} = t^{\mu\nu}_{(kk)}/k^2$. We also use the shorthand notation $[A,B,C] = [A,B]C + [B,C]A + [C,A]B$ for a cyclic sum of commutators. This basis is the same as the one used in refs. [37, 195, 215] except for a factor of $(l\cdot k)$ for $i = 4, 7$, which leads to kinematic problems at the symmetric point, where $(p^2 - q^2) = 2\,(l\cdot k) = 0$. As a consequence, all dressings are symmetric under charge conjugation with the exception of h_4 and h_7, which are antisymmetric. In this basis, the first four tensor structures contain an odd number of gamma matrices and are thus odd under chiral transformations, while the last four contain an even number of gammas and are thus chirally even. Additionally, the structures are roughly in order of how big their dressing functions are in the infrared momentum region as we will see in section 5.1.

Rescaling of the coupling and fixing of parameters

Whenever vertices appear in the equations of motion of N-point functions which have a tree level equivalent in the classical QCD action, the QCD coupling g, or equivalently $\alpha = g^2/4\pi$ appears as well. If one were to rescale the coupling consistently across all equations, this would be equivalent to a shift in renormalization point according to the running coupling of QCD discussed in Section 2.1.5.

In the calculations done for this work, a slightly different rescaling has been performed. The equations of motion of the quenched Yang-Mills sector have been solved self-consistently with a fixed coupling constant α_{YM}. The resulting gluon propagator and three-gluon vertex have been used as input for the quark-gluon vertex DSE. However, in the calculations of the quark-gluon vertex and quark propagator, the coupling α_{QG} has been rescaled. This is done in order to correctly produce the pion's electroweak decay constant, which is calculated in Section 6.3. The current quark mass m_c of the light up and down quarks are fixed by fitting the pion mass, and the strange quark mass is fixed via the pseudoscalar kaon mass. All other hadronic properties calculated with the resulting quark-gluon vertex as input are predictions of our framework.

3.5.3. Going to time-like quark momenta

As explained in detail in Appendix C.2, evaluating a meson bound state equation on-shell requires an evaluation of the quark propagator and quark-gluon vertex for time-like momenta, i.e. in the complex momentum plane. While there are methods to circumvent this for light enough mesons, see Appendix C.1, studies of mesons containing heavy quarks cannot be performed without knowledge about the quark propagator in the complex plane. Continuing all momentum arguments of the quark-gluon vertex into the complex plane would require knowing the gluon propagator and three-gluon vertex for complex momenta as well, which in turn would necessitate computations of the entire coupled Yang-Mills system in the complex plane. With many different momenta appearing in this system, which will be probed in different regions of the complex momentum plane and the tensor bases of the Green's functions having kinematic singularities for certain momenta, this would complicate the calculations significantly.

Fortunately, by carefully choosing a momentum routing, a subset of momenta can be evaluated in the time-like region while all other momenta stay space-like [195].

In particular, one can choose the (anti-)quark momenta appearing in the vertex to be complex valued, while the gluon momentum stays real. By routing the complex momentum through the quark propagator appearing in the non-Abelian diagram in Eq. (3.35) and also routing the complex momentum through only the quark propagator and (anti-)quark legs of the vertex in the quark DSE (3.29), one gets a closed set of equations for the quark propagator and quark-gluon vertex in the time-like region. All appearing Yang-Mills N-point functions stay space-like in this choice of routing. Additionally, one can choose a routing in the meson bound-state equation, such that again only the (anti-)quark legs of the vertex become complex while the gluon momentum stays real, see eq. (4.67).

In this work, we will focus on space-like momenta though and use the method explained in Appendix C.1 to access on-shell properties of mesons.

4. QCD bound states and the Bethe-Salpeter equation

In this section, we will first talk about bound states and resonances of quantum field theories in general, then we will go into some more detail on bound states and resonance in QCD. Next, in Section 4.2, we will focus our attention on the Bethe-Salpeter equation, which describes bound states in the functional approach used throughout this thesis. Numerical solutions to the Bethe-Salpeter equation of various mesons will be presented in chapter 6. Lastly, we will go into detail on truncations of functional equations in Section 4.3.

4.1. Bound states and resonances

The spectrum of any quantum field theory with a set of particles described by quantized fields ϕ_i naturally contains discrete states with one particle of any kind and a fixed energy of $E^2 = m^2$, as well as a continuous spectrum of multi-particle scattering states with energy $E^2 = \sum_i m_i^2 + \vec{p}_i^{\,2}$. If the dynamics of the theory allow for it, the spectrum can also exhibit additional states, known as bound states and resonances. In the following sections we will talk about what defines bound states and resonances and go over bound states and resonances of QCD in particular.

4.1.1. Bound states

The appearance of bound states in the spectrum of a theory is not an exclusive feature of relativistic quantum field theories. In fact, bound states can also appear in non-relativistic quantum mechanics with many of the observations being analogous to relativistic theories. We will thus start by taking a look at the non-relativistic picture.

In the lingo of scattering theory, the wave function of a particle with mass m and energy E scattering off a potential $V(\vec{r})$ is described by a wavefunction[1]

$$\psi(\vec{r}) = \frac{1}{r}\left(A(E)\,\mathrm{e}^{-ikr} + B(E)\,\mathrm{e}^{ikr}\right) \tag{4.1}$$

[1]The considerations below are for S-wave scattering, i.e. states with angular momentum $l = 0$. The observations made in this chapter can also be generalized to $l > 0$.

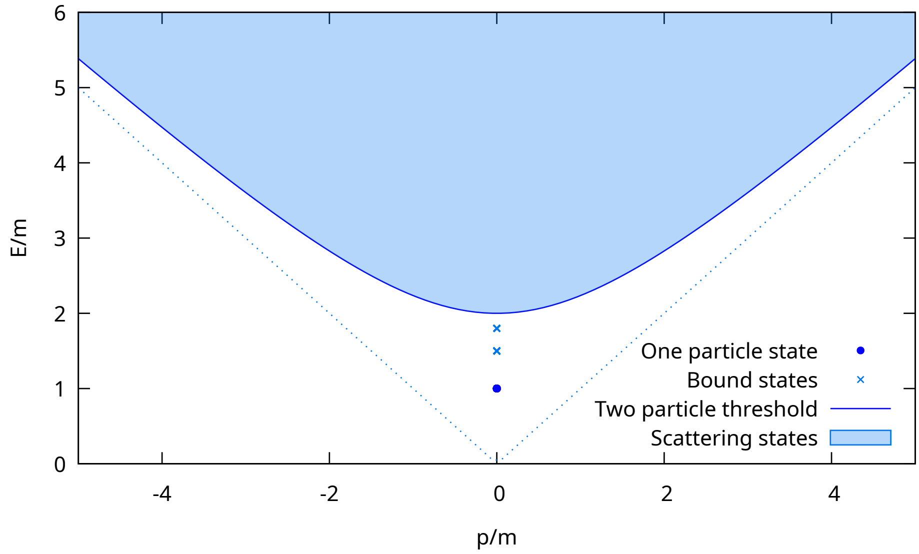

Figure 4.1.: Example spectrum for a theory with one particle type and bound states.

with wavenumber $k = \sqrt{2mE}$. $A(E)$ and $B(E)$ are generally complex valued functions for $E \in \mathbb{C}$ which can be obtained by solving the Schrödinger equation together with a normalization condition. Depending on the form of the potential $V(\vec{r})$, there might be solutions to the Schrödinger equation with energy eigenvalue $0 > E_0 \in \mathbb{R}$, such that $B(E_0) = 0$. The wavefunction of such solutions vanishes as $r \to \infty$, since the second term in eq. (4.1) is zero. The energy levels of these states are discrete, and they are unique zeroes in $B(E)$ if the potential $V(\vec{r})$ vanishes fast enough for $r \to \infty$ [216]. Furthermore, the S-wave scattering amplitude

$$f_0(E) = \frac{1}{2ik}\left(\mathrm{e}^{2i\delta_0} - 1\right) = \frac{1}{2\sqrt{-2mE}}\left(\frac{A(E)}{B(E)} + 1\right) \tag{4.2}$$

has a pole for those energies. These poles also manifest themselves in other quantities, such as the S-matrix and Green's functions of the theory [217]. The latter of those will be the starting point for deriving the Bethe-Salpeter equation in Section 4.2.1.

Example: Positronium

It is instructive to take a look at a simpler example of a system with bound states before going over to bound states in QCD. Consider a theory of electrons with charge $-e$ and positrons with charge $+e$ interacting via a Coulomb potential $V(\vec{r}) = q_1 q_2 / r$ with $\vec{r} = \vec{r}_1 - \vec{r}_2$ being the separation between two particles with charges q_1 and q_2. A single particle in this theory would have the (relativistic) energy $E = m_e$ in its restframe. For an electron-positron pair in such a theory, there are two possibilities.

Either, the particles have sufficiently large restframe momenta $\vec{p}_1 = -\vec{p}_2 \equiv \vec{p}$, such that their total kinetic energy $T = p^2/m_e + O(p^4/m^3)$ is larger than the binding energy from the potential. In this case, the total energy is larger than $2m_e$ and the particles can be separated indefinitely. Such states are called scattering states and the allowed momenta of the particles are a continuum.

In the other case, the kinetic energy is smaller than the binding energy from the potential. As a consequence, the total energy is less than $2m_e$ and it can only take on discrete values. In the case of a non-relativistic Coulomb potential, the binding energies for $l = 0$ can easily be calculated and are proportional to $-1/n^2$ with a quantum number $n \in \mathbb{N}$ [218]. A graphical depiction of such a theory can be seen in Fig. 4.1.

4.1.2. Resonances

If the dynamics of a theory permit, there can also be unstable states, which behave similar to bound states but have some key differences. They also express themselves through poles in Green's functions, but these poles do not lie on the negative real axis of the complex energy plane, but instead lie on the second Riemann sheet in the complex plane. This can be seen by observing the partial-wave scattering amplitude of a non-relativistic metastable state with energy E_0 [118]

$$f_l(E) \propto \frac{1}{E - E_0 + i\Gamma/2}. \tag{4.3}$$

This scattering amplitude has a pole at $E = E_0 - i\Gamma/2$, where Γ is the so-called Breit-Wigner width of the state. By calculating the convolution of this amplitude with a wave packet, we can compute the time dependence of such a state

$$\psi(t) \sim \int \mathrm{d}E \frac{1}{E - E_0 + i\Gamma/2}\, \tilde{\psi}(E)\, \mathrm{e}^{iEt} \sim \mathrm{e}^{-iE_0 t - \Gamma t/2}. \tag{4.4}$$

Thus, the absolute value squared of the state behaves as $|\psi(t)|^2 \sim \exp(-\Gamma t)$. This means that the state decays with Γ being its inverse lifetime.

In relativistic case, similar behaviour can arise, if the theory contains particles, that can decay into each other. For example, consider a theory with two massive, scalar fields ϕ_1 and ϕ_2 with masses m_1 and m_2, where $m_2 > 2m_1$ and a tree level vertex of the form $\phi_1^2\phi_2$. The kinematics of this theory allow for a decay of one ϕ_2 particle into two ϕ_1 particles. One can then show, that for center of mass energies $\sqrt{s}$ close to m_2, the scattering process of $\phi_1\phi_1 \to \phi_1\phi_1$, described by a four-point function, is dominated by a single s-channel ϕ_2-exchange [118]. The corresponding

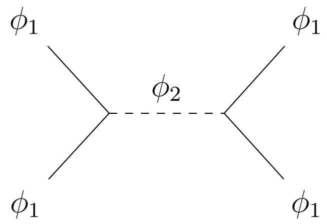

Figure 4.2.: The leading diagram for the $\phi_1\phi_1 \to \phi_1\phi_1$ process near the ϕ_2 pole.

Feynman-diagram is depicted in Fig. 4.2. Such unstable states with poles in the complex plane on the second Riemann sheet are known as resonances In practice, they are much more common than truly stable states. While there are a number of stable bound states within pure QCD, in the full standard model many more particles can decay via the weak force.

Additionally, there is a third option for where the pole of a bound state can lie. If the pole lies on the negative real axis below the two-particle threshold, but on the second Riemann sheet, it is called a virtual bound state.

4.1.3. Bound states in QCD

As discussed in Section 2.1.6, the quarks and gluons, which are the fundamental degrees of freedom of QCD, cannot be observed as asymptotic final states due to gauge symmetry and confinement. Thus, bound states and resonances play a hugely important role in the study of QCD, especially at low energies. Since gauge-invariance demands an observable state to be colourless, the options for how quarks and gluons can combine to form observable bound states are quite limited. As listed in Section 1.2, the valid options are mesons ($q\bar{q}$), (anti-)baryons ($qqq/\overline{qqq}$), glueballs (gg, ggg, $\ldots$), hybrids ($q\bar{q}g$) and combinations of those.

Hadron multiplets

The discovery of many new particles in the first half of the 20th century led to the question, whether these particles are elementary or not [217] and how to classify them. The solution proposed by Gell-Mann [219], that the fundamental particles are quarks and gluons and hadrons are composite states, is what gave rise to the theory of QCD. An important piece of this eightfold way proposed by Gell-Mann is, that hadrons are sorted into multiplets of the theory's underlying symmetry groups. For baryons, this lead to the grouping of ground state baryons with light and strange quarks into the baryon octet. Similarly, baryons with angular momentum of 3/2 are grouped into a baryon decouplet.

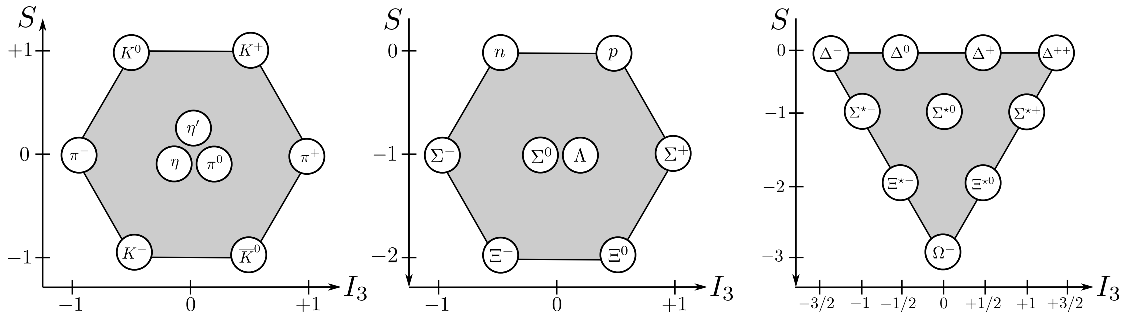

Figure 4.3.: Pseudoscalar meson nonet, baryon octet and baryon decouplet for three light quarks. Illustration taken from [45].

Ground state mesons made up of light and strange quarks that share quantum numbers can also be grouped into an octet and a singlet state. The reason behind this is the underlying SU(3) vector symmetry discussed in section 2.2.3. The quarks of the theory lie in the fundamental representation, called **3** or triplet, of SU(3), while the antiquarks are in the complex conjugate representation $\overline{\mathbf{3}}$. Using the group theoretical decomposition [220]

$$\mathbf{3} \otimes \overline{\mathbf{3}} = \mathbf{8} \oplus \mathbf{1}, \tag{4.5}$$

one sees that a quark-antiquark bound state can lie either in the singlet trivial representation **1** or the octet adjoint representation **8**. The resulting multiplets for mesons and baryons are illustrated in Fig. 4.3.

The effective potential of QCD

In a holistic picture of QCD, bound states and resonances are formed by the full complex dynamics between quarks and gluons encoded in the QCD Lagrangian (2.1). Heavy quarkonia and other states consisting of heavy quarks can approximately be described as bound states of non-relativistic particles held together by an effective potential $V(\vec{r})$. In the meson sector, this is a good approximation for bottomonium states, i.e. states containing two bottom (anti-)quarks. To a lesser extent this approximation can also be used for charmonium ($c\overline{c}$) states, but for states involving strange or light (up/down) quarks, this approximation breaks down. The reason for this is that the mass of even the lightest mesons is very large compared to the bare mass of light and strange quarks, which entails that the kinetic energy of the constituent quarks must be very large. As a consequence, the effective velocity of the quarks is very close to the speed of light, demanding a relativistic treatment.

As an example, consider the back-of-the-envelope calculation for a ρ meson, which is the lightest $q\overline{q}$ state that is not a pseudo Goldstone boson. It has a mass of roughly 775 MeV, while a down quark, the heavier of the two light quarks, has a mass of roughly 4.7 MeV. If we assume, that the mass of the ρ meson is evenly split as kinetic energy between two (anti-)down quarks, they each have a total energy of

$$E = \gamma\, m_d \approx 387.5\,\text{MeV} \approx 82.4\, m_d, \tag{4.6}$$

corresponding to a Lorentz factor of $\gamma = 82.4$ or equivalently a velocity of $v \sim 0.9999\,c$, which definitely demands a relativistic treatment.

As mentioned in section 2.1.6, we expect a confining static quark potential to exhibit a linearly rising part akin to the Cornell potential 2.19. More complex modelled potentials including spin and angular momentum dependent terms have been applied to heavy meson studies in the past, see e.g. [221] for a review. Such potentials are routinely used in non-relativistic QCD (NRQCD) [222, 223] and have also been investigated in lattice QCD [223–225].

Regge behaviour

If we approximate a meson to be a pair of quarks connected by a flux tube rotating with angular momentum J around the z-axis with the quarks lying in the xy-plane, we can derive a relation between angular momentum and rotational energy. For a classical, non-relativistic spinning stick with homogeneous mass distribution, the rotational energy is given by

$$E_{\text{rot}} = \frac{J^2}{2L}, \tag{4.7}$$

where L is the moment of inertia with respect to the rotational axis. For a flux tube between two quarks bound by a linearly rising Cornell-potential, the relation between E and J shifts though. We can express the angular momentum via the moment of inertia and rotational frequency ω as $J = L\omega$. For an object of mass M and length scale l, we can further write the moment of inertia as $L \sim Ml^2$, leading to $J \sim Ml^2\omega$. Furthermore, we can write mass, length and frequency of the rotating flux tube as powers of E [226]

$$M \sim E, \quad l \sim E, \quad w \sim 1/E. \tag{4.8}$$

Combining these relations, we obtain that for a spinning flux tube the angular momentum scales with the energy squared, i.e. $J \sim E^2$. By doing a more involved string theoretical derivation for quantized angular momenta, one obtains [226]

$$J = \alpha' E^2 + \beta' \quad \Leftrightarrow \quad M^2 = M_0^2 + \beta J. \tag{4.9}$$

Note that in the above derivation we used the fact that $l \sim E$, or in other words that the potential between two quarks is linearly rising, akin to a confining potential like the Cornell potential (2.19).

While the picture of gluon fields between static quarks forming a fluxtube and linearly rising potentials makes intuitive sense in the heavy quark sector, a surprising result of meson spectroscopy is the emergence of linear Regge trajectories also in the light meson sector [4, 227]. With the interactions between quarks bound inside light mesons being much more dynamic, this is a highly non-trivial result worth investigating in a sophisticated theoretical framework.

In particular, we expect the mass of mesons with increasing total angular momentum and alternating parity [228] to behave according to eq. (4.9). We will use the nomenclature, that states with $J^P = 1^-, 2^+, 3^- \ldots$ have "natural" parity, while states with $J^P = 1^+, 2^-, 3^+ \ldots$ have "unnatural" parity. We will explicitly observe, whether this behaviour is present in our results in Chapter 6 and try to find a justification for it.

4.2. The Bethe-Salpeter equation

Within the framework of functional methods, bound states and resonances are described by Bethe-Salpeter amplitudes (BSAs), which satisfy the Bethe-Salpeter equation (BSE), a homogeneous eigenvalue equation. In this section we will sketch a derivation of the BSE and talk about its solutions in general as well as strategies to solve it.

4.2.1. Derivation

Since bound states and resonances manifest themselves as poles in N-point functions of a theory, we derive the meson BSE from equations for those N-point functions. For even values of N, the full N-point function $\mathbf{G}$ satisfies a Dyson equation [45]

$$\mathbf{G} = \mathbf{G}_0 + \mathbf{G}_0 \mathbf{K} \mathbf{G}. \tag{4.10}$$

Here we used a compact notation with suppressed Dirac indices, momentum arguments and integrations.[2] $\mathbf{G}_0$ is the disconnected product of dressed propagators with the same number of external legs as $\mathbf{G}$, e.g. one quark propagator and one antiquark propagators in the case of a 4-point function with two external quark- and antiquark-legs. $\mathbf{K}$ denotes the scattering kernel, which encodes all possible two-particle irreducible interactions. Using $\mathbf{G}$ and $\mathbf{G}_0$ we can construct the scattering matrix $\mathbf{T}$, which contains only amputated and connected diagrams via

$$\mathbf{G} = \mathbf{G}_0 + \mathbf{G}_0 \mathbf{T}\, \mathbf{G}_0. \tag{4.11}$$

[2]We use bold-face letters to indicate such a notation and will use non bold-face letters with explicit indices and arguments later on when going into detail on the equations.

Combining equations (4.10) and (4.11) yields a Dyson equation for the scattering matrix

$$\mathbf{T} = \mathbf{K} + \mathbf{K}\mathbf{G}_0\mathbf{T}. \tag{4.12}$$

If the theory exhibits a bound state or resonance in the channel corresponding to the N-point function $\mathbf{G}$, both the N-point function and the scattering matrix $\mathbf{T}$ have a pole when the complex total momentum has an on-shell pole at $P^2 = -m^2$. Around those poles, one can express $\mathbf{G}$ and $\mathbf{T}$ in terms of their residue and a divergent denominator as

$$\mathbf{G} \xrightarrow{P^2 \to -m^2} \frac{\mathbf{\Psi}\overline{\mathbf{\Psi}}}{P^2 + m^2}, \quad \mathbf{T} \xrightarrow{P^2 \to -m^2} \frac{\mathbf{\Gamma}\overline{\mathbf{\Gamma}}}{P^2 + m^2}. \tag{4.13}$$

The quantity $\mathbf{\Psi}$ is the amputated wave function of the bound state/resonance and $\mathbf{\Gamma}$ is its Bethe-Salpeter amplitude (BSA). They are related via $\mathbf{\Psi} = \mathbf{G}_0\mathbf{\Gamma}$. Since they can easily be converted into each other, knowledge of one quantity plus the position of the mass pole is sufficient to fully describe the bound state/resonance. Throughout this work will we thus focus on obtaining knowledge about the BSA $\mathbf{\Gamma}$. By inserting equation (4.13) into the Dyson equation (4.12) and multiplying both sides by $(P^2 + m^2)$ one obtains

$$\mathbf{\Gamma}\overline{\mathbf{\Gamma}} = \left(P^2 + m^2\right)\mathbf{K} + \mathbf{K}\mathbf{G}_0\mathbf{\Gamma}\overline{\mathbf{\Gamma}}. \tag{4.14}$$

At the on-shell mass pole, where $P^2 = -m^2$, the first term on the right-hand side vanishes. One can then multiply the equation with the inverse of $\overline{\mathbf{\Gamma}}$ from the right side to arrive at the homogeneous Bethe-Salpeter equation[3] for $\mathbf{\Gamma}$

$$\mathbf{\Gamma} = \mathbf{K}\mathbf{G}_0\mathbf{\Gamma}. \tag{4.15}$$

This is the central equation used in the functional approach to extract properties of bound states and resonances. It can be seen in diagrammatic form in Fig. 4.4. Due to its significance, we will now go over several important properties of this equation and talk about solution strategies.

4.2.2. Structure of the Bethe-Salpeter equation

Thus far, we used a shorthand notation for the quantities that appear in the BSE, suppressing indices, sums, integrals etc. In full gory, the Bethe-Salpeter equation for a meson with total angular momentum J reads [186]

[3] Depending on the specific N-point function in question, this equation describes states with different constituents. While in most cases it is known as Bethe-Salpeter equation, in the case of Baryons as bound states in quark 6-point functions, the resulting equation is known as Faddeev equation [45].

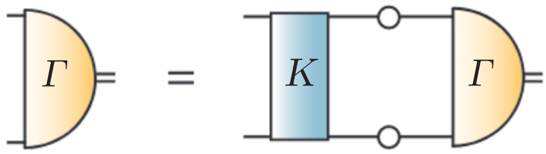

Figure 4.4.: The meson Bethe-Salpeter equation in diagrammatic form. Lines with a white circle represent fully dressed quark propagators.

$$\left[\Gamma^{\mu_1\mu_2\ldots\mu_J}\left(p,P\right)\right]_{ad} = \int đ^4 q \, K_{ab,cd}\left(q,p,P\right)\left[S\left(q_+\right)\Gamma^{\mu_1\mu_2\ldots\mu_J}\left(q,P\right)S\left(q_-\right)\right]_{bc}. \quad (4.16)$$

The momenta p, q and P are the relative quark momentum, loop momentum and total meson momentum. Indices with Greek letters are Lorentz indices and ones with Latin letters are Dirac indices. We use the notation $q_+ = q + \xi P$ and $q_- = q + (\xi - 1)P$ with a momentum routing parameter $\xi \in [0, 1]$. For equal mass quark constituents and also for kaons, where the constituents have similar, small mass, a sensible choice for this parameter is $\eta = \frac{1}{2}$, i.e. $q_\pm = q \pm \frac{1}{2}P$. The Dirac and Lorentz structure of the Bethe-Salpeter amplitude has to be constructed to fit the quantum numbers of the state under investigation. We will discuss this construction in detail in Section 4.2.4. For the tree level 4-point function $\mathbf{G}_0$ two dressed quark propagators $S(q_\pm)$ have been plugged in.

The general form of the Bethe-Salpeter equation is that of a homogeneous eigenvalue equation with the eigenvalue being equal to one

$$(\mathbf{K}\mathbf{G}_0) \cdot \mathbf{\Gamma} = \lambda \cdot \mathbf{\Gamma}, \quad \lambda = 1. \quad (4.17)$$

In practice, this eigenvalue is a function of total momentum P^2 and to find the mass pole of the state of interest one varies P^2 to find $\lambda(P^2 = -m^2) = 1$. We will go into more detail on the solution strategy of the BSE in Section 4.2.5.

4.2.3. Normalization

Since the BSE is a homogeneous equation, its solutions are only determined up to a constant factor. Thus, another condition is needed in order to fix this factor. The canonical normalization condition can be obtained by taking the derivative of $\mathbf{G}$ at the mass pole and comparing the most singular terms, which leads to [45]

$$\overline{\mathbf{\Gamma}}\left(\frac{\mathrm{d}\mathbf{G}_0}{\mathrm{d}P^2}+\mathbf{G}_0\frac{\mathrm{d}\mathbf{K}}{\mathrm{d}P^2}\mathbf{G}_0\right)\mathbf{\Gamma}\Bigg|_{P^2=-m^2}\stackrel{!}{=}1. \tag{4.18}$$

In practice, this condition is not handy to work with in truncation schemes, where the derivative of the kernel is non-zero. Instead, the normalization condition proposed by Nakanishi yields equivalent results and is easier to implement in practice [229, 230]

$$\left(\frac{\mathrm{d}\ln\lambda(P^2)}{\mathrm{d}P^2}\right)^{-1}=2N_c\,\mathrm{tr}\int đ^4q\,\overline{\Gamma}(q,-P)S(q_+)\Gamma(q,P)S(q_-). \tag{4.19}$$

The left-hand side contains the derivative of the logarithm of the momentum dependent eigenvalue appearing in the BSE (4.17) and can be rewritten as

$$\left(\frac{\mathrm{d}\ln\lambda(P^2)}{\mathrm{d}P^2}\right)^{-1}=\left(\frac{1}{\lambda(P^2)}\frac{\mathrm{d}\lambda(P^2)}{\mathrm{d}P^2}\right)^{-1} \tag{4.20}$$

such that one only needs to compute the derivative of the eigenvalue itself. One may be tempted to drop the factor of $1/\lambda$ appearing on the right-hand side, since on-shell it is equal to one. However, it can be useful to normalize an amplitude that has been calculated off-shell, as we will later see. In those cases, this factor is crucial to keep, since omitting it would lead to wrong results.

4.2.4. Constructing the Bethe-Salpeter amplitude

When solving the Bethe-Salpeter equation for mesons, their quantum numbers are reflected by their Bethe-Salpeter amplitudes. Thus, if one wants to solve the BSE for arbitrary quantum numbers, one needs a way to construct a tensor basis with the corresponding quantum numbers. While for states with $J=0$ and $J=1$ these bases can be constructed rather easily, see for example [186, 230, 231], higher angular momenta are best handled with a systematic approach, which is outlined in [45, 232–236] and will be explained in detail here. The explicit bases obtained with this procedure are given in Appendix C.7.

Constraints on the Bethe-Salpeter amplitude

In order to represent a unique physical state, a Bethe-Salpeter amplitude $\Gamma^{\mu_1\mu_2\cdots\mu_J}(p,P)$ has to satisfy a number of constraints [236]:

1. The amplitude has to be transverse with respect to the meson's momentum, i.e. $P_{\mu_1}\Gamma^{\mu_1\mu_2\cdots\mu_J}(p,P)=0$.

2. The number of Lorentz indices of the amplitude has to equal the total angular momentum J of the state.

3. The amplitude has to be symmetric in its Lorentz indices, i.e. $\Gamma^{\mu_1\mu_2\cdots\mu_J}(p,P) = \Gamma^{\Pi(\mu_1\mu_2\cdots\mu_J)}(p,P)$ where $\Pi \in \mathrm{S}_J$ is an arbitrary permutation of the Lorentz indices.

4. The Lorentz trace $\Gamma^{\mu_1}{}_{\mu_1}{}^{\cdots\mu_J}$ of the amplitude has to be zero.

5. It has to have the correct behaviour under a parity transformation.

Note, that due to the third requirement the amplitude is in fact transverse and traceless in all of its Lorentz indices. Our goal is now to find a set of linearly independent tensors $\{\tau_i^{\mu_1\mu_2\cdots\mu_J}\}$ which form a basis of the vector space of the amplitude such that we can express the amplitude as

$$\Gamma^{\mu_1\mu_2\cdots\mu_J}(p,P) = \sum_{i=1}^{n} f_i(p^2, P^2, p\cdot P)\, \tau_i^{\mu_1\mu_2\cdots\mu_J}(p,P), \tag{4.21}$$

where the dressing functions f_i only depend on Lorentz invariant combinations of p and P. It is then sufficient to construct the τ_i in a way to fulfill the aforementioned constraints for the entire amplitude to fulfill them as well. Additionally, in practice, it is extremely beneficial if the chosen basis is orthonormal, as this makes projection onto the dressing functions trivial and speeds up numerical computations. We will now go over each criterion and outline a procedure to construct a basis for arbitrary values of J.

Transversality

The canonical choice of building blocks for the tensor basis are the unit matrix $\mathbb{1}$, the relative and absolute four-momenta p^μ and P^μ as well as their contractions with the gamma matrix four vector, i.e. $\not{p} = \gamma^\mu p^\mu$ and $\not{P} = \gamma^\mu P^\mu$, and the gamma matrix four vector γ^μ itself. These are, however, neither normalized nor transverse to the total momentum P^μ. It is thus more convenient to work with the normalized and transverse versions of these quantities, i.e.

$$\begin{aligned} \hat{P}^\mu &= \frac{P^\mu}{\|P\|}, \\ p_\perp^\mu &= p^\mu - (p\cdot\hat{P})\,\hat{P}^\mu, \\ n^\mu &= \widehat{p_\perp}^\mu = \frac{\hat{p}^\mu - z\,\hat{P}^\mu}{\sqrt{1-z^2}}\,, \end{aligned} \tag{4.22}$$

where $z = \hat{p} \cdot \hat{P}$. Note, that this allows for a choice of coordinates in which $\hat{P}^\mu = (0,0,0,1)$ and $n^\mu = (0,0,1,0)$. These quantities have the convenient properties that $n^2 = \hat{P}^2 = 1$ and $n \cdot \hat{P} = 0$. Alongside these definitions, one can define gamma matrices which are transverse with respect to both n and $\hat{P}$ via

$$\begin{aligned} \gamma_\perp^\mu &= T_P^{\mu\nu}\,\gamma^\nu = \gamma^\mu - \hat{P}^\mu \hat{\not{P}} \\ \gamma_{\perp\perp}^\mu &= T_n^{\mu\nu}\,\gamma_\perp^\nu = \gamma^\mu - n^\mu \not{n} - \hat{P}^\mu \hat{\not{P}}\,, \end{aligned} \tag{4.23}$$

where $T_P^{\mu\nu} = \delta^{\mu\nu} - \hat{P}^\mu \hat{P}^\nu$ is the transverse projector with respect to P^μ and $T_n^{\mu\nu}$ is the transverse projector with respect to n. By construction, these transverse gamma matrices anticommute with both $\not{n}$ and $\hat{\not{P}}$.

Angular momentum

With these building blocks at hand, one can construct the basis of a state with total angular momentum J as

$$\begin{aligned} J = 0: &\quad \{\,\mathbb{1},\ \hat{\not{P}}\,\} \otimes \{\,\mathbb{1},\ \not{n}\,\}\,, \\ J > 0: &\quad \{\,\mathbb{1},\ \hat{\not{P}}\,\} \otimes \{\,\mathbb{1},\ \not{n}\,\} \otimes \{\,N^{\mu_1\mu_2\cdots\mu_J},\ \ M^{\mu_1\mu_2\cdots\mu_J}\,\}\,. \end{aligned} \tag{4.24}$$

The tensor $N^{\mu_1\mu_2\cdots\mu_J}$ can contain all possible combinations of n^μ and $T_P^{\mu\nu}$ while being transverse to the total momentum P^μ:

$$n^{\mu_1} n^{\mu_2} \cdots n^{\mu_J}, \quad T_P^{\mu_1\mu_2} n^{\mu_3} \cdots n^{\mu_J}, \quad \ldots, \quad T_P^{\mu_1\mu_2} T_P^{\mu_3\mu_4} \cdots T_P^{\mu_{J-1}\mu_J}. \tag{4.25}$$

Note that for odd values of J there is one more term containing $(J-1)/2$ copies of T_P and a single n. The tensor $M^{\mu_1\mu_2\cdots\mu_J}$, on the other hand, contains in addition a single factor of $\gamma_{\perp\perp}^\mu$ in every term:

$$\gamma_{\perp\perp}^{\mu_1} n^{\mu_2} \cdots n^{\mu_J},\ \gamma_{\perp\perp}^{\mu_1} T_P^{\mu_2\mu_3} n^{\mu_4} \cdots n^{\mu_J},\ \ldots,\ \gamma_{\perp\perp}^{\mu_1} T_P^{\mu_2\mu_3} T_P^{\mu_4\mu_5} \ldots T_P^{\mu_{J-2}\mu_{J-1}} n^{\mu_J}. \tag{4.26}$$

The last term is only present for even values of J.

Symmetry

To make the tensor basis symmetric in all its Lorentz indices, we sum up all permutations of indices for each term. This leaves us with the following general form of $N^{\mu_1\mu_2\cdots\mu_J}$ and $M^{\mu_1\mu_2\cdots\mu_J}$ for even J

$$\begin{aligned}
N^{\mu_1\mu_2\cdots\mu_J} =& N_{J,0}\Big(n^{\mu_1}n^{\mu_2}\cdots n^{\mu_J} \\
&+ N_{J,1}\ T_P^{[\mu_1\mu_2}n^{\mu_3}\cdots n^{\mu_J]} \\
&+ \dots \\
&+ N_{J,J/2}\ T_P^{[\mu_1\mu_2}T_P^{\mu_3\mu_4}\cdots T_P^{\mu_{J-1}\mu_J]}\Big) \\
M^{\mu_1\mu_2\cdots\mu_J} =& M_{J,0}\Big(\gamma_{\perp\perp}^{[\mu_1}n^{\mu_2}\cdots n^{\mu_J]} \\
&+ M_{J,1}\ \gamma_{\perp\perp}^{[\mu_1}T_P^{\mu_2\mu_3}n^{\mu_4}\cdots n^{\mu_J]} \\
&+ \dots \\
&+ M_{J,(J-2)/2}\ \gamma_{\perp\perp}^{[\mu_1}T_P^{\mu_2\mu_3}T_P^{\mu_4\mu_5}\dots T_P^{\mu_{J-2}\mu_{J-1}}n^{\mu_J]}\Big)\,.
\end{aligned} \tag{4.27}$$

The brackets around the Lorentz indices indicate a sum over all unique permutations of the indices. The coefficients $N_{J,i}$ and $M_{J,i}$ have to be chosen such that the final basis is traceless and normalized. In practice, the symmetrization is a bottleneck for going to arbitrarily large angular momenta since the number of terms needed for symmetrization grows very rapidly for increasing J. To see this, we can find a lower bound for the number of terms needed by just considering even J and only the term

$$T_P^{[\mu_1\mu_2}T_P^{\mu_3\mu_4}\cdots T_P^{\mu_{J-1}\mu_J]}. \tag{4.28}$$

There is a total of $J!$ possible permutations of indices in that term alone, but due to the symmetry of $T_P^{\mu\nu}$, the number of unique permutations of this term is $J!/2^J$, which still grows faster than exponentially for sufficiently large J. In this work, we go up to $J = 5$, since there are experimental candidate states for a light meson and a kaon with $J = 5$ [10, 11]. With proper computational methods, one could most likely also construct a base for $J = 6$ and potentially $J = 7$, but the lack of experimental candidates in those channels at present, especially in the heavy quark sector, makes predictions for such quantum numbers not interesting enough to justify the required effort.

Tracelessness

Since the expressions for $N^{\mu_1\mu_2\cdots\mu_J}$ and $M^{\mu_1\mu_2\cdots\mu_J}$ are constructed to be symmetric under permutation of Lorentz indices, one can rather easily derive expressions for the coefficients $N_{J,i}$ and $M_{J,i}$ with $i \geq 1$ such that the Lorentz trace of N and M vanishes. A straightforward way of determining them is to evaluate their traces with respect to μ_1 and μ_2 or any other pair of indices and tune $N_{J,i}$ and $M_{J,i}$ via comparison of coefficients to set the traces to zero. Some helpful relations for this derivation are

$$
\begin{aligned}
n^\mu n_\mu =& 1, \quad T_P^{\mu\nu} n_\nu = n^\mu, \quad T_P{}^\nu{}_\nu = 3, \\
\gamma_{\perp\perp}^\mu n_\mu =& 0, \quad T_P^{\mu\nu} T_{P\nu}{}^\rho = T_P^{\mu\rho}, \quad T_P^{\mu\nu} \gamma_{\perp\perp\,\nu} = \gamma_{\perp\perp}^\mu .
\end{aligned}
$$

For example, in the case of $J = 3$ one can construct the coefficients $N_{J,i}$ by first writing down all relevant terms

$$
\frac{1}{N_{3,0}} N^{\mu\nu\rho} = n^\mu n^\nu n^\rho + N_{3,1} \left(T_P^{\mu\nu} n^\rho + T_P^{\nu\rho} n^\mu + T_P^{\rho\mu} n^\nu \right). \tag{4.29}
$$

Taking the Lorentz trace with respect to μ and ν yields

$$
\begin{aligned}
\frac{1}{N_{3,0}} N^\mu{}_\mu{}^\rho &= n^\mu n_\mu n^\rho + N_{3,1} \left(T_P{}^\mu{}_\mu n^\rho + 2 T_P^{\rho\mu} n_\mu \right) \\
&= n^\rho + N_{3,1} \left(3 n^\rho + 2 n^\rho \right) = \left(1 + 5 N_{3,1} \right) n^\rho \stackrel{!}{=} 0,
\end{aligned}
$$

which entails that $N_{3,1} = -\frac{1}{5}$.

Parity

With the construction outlined above, the parity of the tensor basis will be determined by the total angular momentum via the relation $P = (-1)^J$. If one wants to construct a basis with the opposite parity, one simply needs to multiply the basis elements by a factor of γ_5 from the left.

Orthonormality

It is practical to work with a basis that is orthonormalized, i.e. that each pair of basis vectors $\tau_i^{\mu_1\mu_2\ldots\mu_J}$, $\tau_j^{\mu_1\mu_2\ldots\mu_J}$ obeys the orthonormality relation

$$
\mathrm{tr}(\overline{\tau}_i^{\mu_1\mu_2\ldots\mu_J} \tau_j^{\mu_1\mu_2\ldots\mu_J}) = \delta_{ij}, \tag{4.30}
$$

with projectors $\overline{\tau}_i^{\mu_1\mu_2\ldots\mu_J} = \pm \tau_i^{\mu_1\mu_2\ldots\mu_J}$; see Tables C.1 to C.6 for the specific signs in front of the projectors. Orthogonality is already achieved by construction since we only used orthogonal building blocks in our basis. Normalization is obtained by tuning $N_{J,0}$ and $M_{J,0}$ accordingly. Finally, by adding factors of i at appropriate places one can make all dressing functions $f_i(p^2, P^2, p \cdot P)$ real valued.

Applying this construction to mesons with $J = 0 \ldots 5$ and $P = \pm$ gives the orthonormal bases shown in Tables C.1 to C.6 in Appendix C.7.

Other basis conventions

While this approach to constructing a tensor basis for the meson BSA can systematically be applied to arbitrary values of J, some previous studies of mesons with $J = 0, 1$ have opted to use different bases, cf. [186, 230, 231]. A particular historically important convention is the basis for the pion BSA directly constructed in terms of the momentum vectors

$$\Gamma_\pi(p, P) = \gamma_5 \left(E(p, P) - i\not{P}F(p, P) - i\not{p}(p \cdot P)G(p, P) + \left[\not{p}, \not{P}\right] H(p, P)\right) . \tag{4.31}$$

Thus, we will resort to using this choice of base as well when investigating properties of the pion specifically.

4.2.5. Solution strategy

As stated in Section 4.2.2, the Bethe-Salpeter equation in general form is an eigenvalue equation of an operator. When formulated numerically, the BSE turns into an eigenvalue equation of a finite dimensional matrix. To see this, we plug the tensor structure decomposition from equation (4.21) into the BSE (4.16) to obtain

$$\begin{aligned} &\sum_{i=1}^{n} f_i(p^2, P^2, p \cdot P)\, \tau_i^{\mu_1\mu_2\ldots\mu_J}(p, P) = \\ &\sum_{i=1}^{n} \int đ^4 q\, K_{ab,cd}\,(q, p, P) \left[S\,(q_+)\, f_i(q^2, P^2, q \cdot P)\, \tau_i^{\mu_1\mu_2\ldots\mu_J}(q, P)\, S\,(q_-)\right]_{bc} . \end{aligned} \tag{4.32}$$

By further using the orthonormality relation of the tensor basis (4.30), we can project onto the dressing functions of the BSA by multiplying with the projectors of the base and taking the trace over Dirac indices

$$\begin{aligned} &\mathrm{tr}\left(\overline{\tau}_j^{\mu_1\mu_2\ldots\mu_J}(p, P) \sum_{i=1}^{n} f_i(p^2, P^2, p \cdot P)\tau_i^{\mu_1\mu_2\ldots\mu_J}(p, P)\right) = f_j(p^2, P^2, p \cdot P) = \\ &\mathrm{tr}\Bigg(\overline{\tau}_{j,\,da}^{\mu_1\mu_2\ldots\mu_J}(p, P) \sum_{i=1}^{n} \int đ^4 q\, K_{ab,cd}\,(q, p, P) \\ &\qquad\qquad \left[S\,(q_+)\, \tau_i^{\mu_1\mu_2\ldots\mu_J}(q, P)\, S\,(q_-)\right]_{bc}\Bigg)\, f_i(q^2, P^2, q \cdot P). \end{aligned} \tag{4.33}$$

Of the four integrals appearing on the right-hand side, one trivially equates to 2π, while the other three generally have to be solved numerically.[4] The numerical treatment of the integrals requires the values of p^2, q^2 and the angles between pairs of momenta to be discretized onto finite grids

$$\begin{aligned} p^2 &\to p_i^2, & q^2 &\to q_i^2 \\ z &\to z_i, & \beta &\to \beta_i. \end{aligned} \tag{4.34}$$

Using this discretization, we can express the dressing function appearing in eq. (4.33) as components of a vector with radial index k, angular index l and Dirac index i

$$f_i(p^2, P^2, p \cdot P) \to f_{i,k,l}(P^2). \tag{4.35}$$

The integrals appearing on the right-hand side of the projected BSE (4.33) turn into sums upon discretization, as discussed in detail in Appendix D.1. By combining the result of the dirac trace together with the Jacobians and integration weights of all the integrals, the BSE turns into

$$f_{i,k,l}(P^2) = \sum_{j=1}^{n} \sum_{\tilde{k}=1}^{N_p} \sum_{\tilde{l}=1}^{N_z} \mathcal{M}_{i,k,l,j,\tilde{k},\tilde{l}}(P^2) f_{j,\tilde{k},\tilde{l}}(P^2), \tag{4.36}$$

where N_p and N_z are the number of points in the radial and angular grids respectively. Furthermore, we can introduce a superindex s, which combines Dirac, radial and angular indices with a one-to-one correspondence[5]

$$s := k + N_p z + N_z N_p i \quad \Leftrightarrow \quad \begin{cases} k = s \mod N_p \\ z = \left\lfloor \frac{s}{N_p} \right\rfloor \mod N_z \\ i = \left\lfloor \frac{s}{N_p N_z} \right\rfloor \end{cases} \tag{4.37}$$

with which the projected BSE becomes

$$f_s(P^2) = \sum_{\tilde{s}=1}^{n N_z N_p} \mathcal{M}_{s\tilde{s}}(P^2) f_{\tilde{s}}(P^2). \tag{4.38}$$

This now obviously resembles the form of a finite dimensional eigenvalue equation of a matrix $\mathcal{M}$. We will call this matrix the Mother-matrix. It is a matrix of

[4] For more information on the hyperspherical coordinates used, Appendix A.4 can be consulted.

[5] The mapping between indices and superindex is not unique though, as the order of indices in the definition can be permuted. In practice, choosing a consistent mapping that fits the order of operations in the numerical implementation can improve cache locality on modern CPUs and thus have a significant impact on runtime performance of the computations.

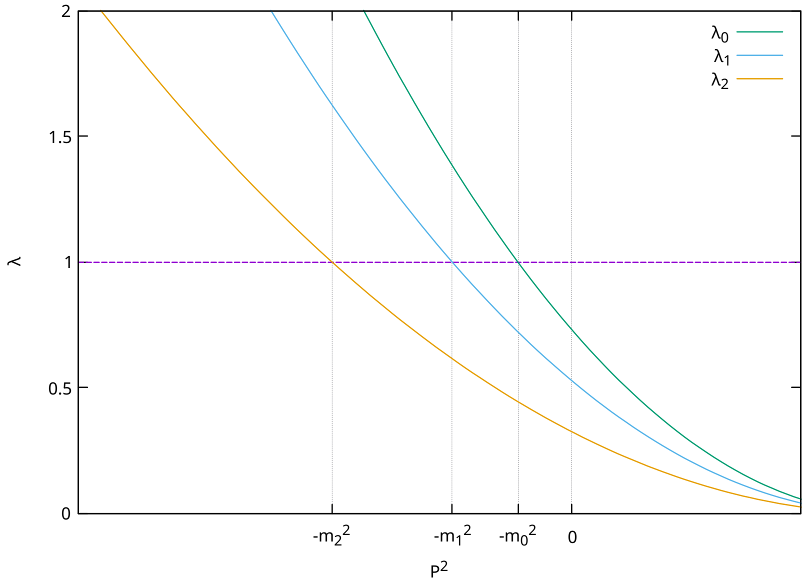

Figure 4.5.: Sketch of a BSE eigenvalue spectrum and mass pole positions.

dimension $(n \cdot N_z \cdot N_p) \times (n \cdot N_z \cdot N_p)$, where $n \cdot N_z \cdot N_p$ is typically of the order $10^3 \sim 10^4$. Thus, efficient numerical eigensolvers are necessary to tackle a numerical treatment of the BSE. We will talk about the eigensolvers used in this work in Appendix E.2.1.

In general, the eigenvalues of $\mathcal{M}(P^2)$ need not be equal to one for a given P^2. At the physical point, where $P^2 = -m^2$, the BSE (4.17) demands that the eigenvalue of $\mathcal{M}$ is equal to one. Thus, it is practical to calculate the eigenvalues of $\mathcal{M}$ as a function of squared meson momentum $\lambda(P^2)$, known as the eigenvalue curve, and find the point, where it intersects $\lambda(P^2 = m^2) = 1$. In practice, this can be done by finding the zeroes of the function $\lambda(P^2) - 1$ or the poles of the function $1/\ln(\lambda(P^2))$. Since calculating the components and eigenvalues of $\mathcal{M}$ can be computationally costly, using efficient root finding algorithms is recommended, see Appendix D.2 for details.

Additionally, one will find not only one, but multiple solutions to the equation $\lambda(P^2 = -m_i^2) = 1$, where the index i labels those solutions, where the subleading eigenvalues of $\mathcal{M}$ are equal to one. These extra solutions correspond to radial excitations of the meson with given quantum numbers. For example, for the pion the first solution is the ground state and corresponds to the $\pi(139)$, while the next solution with correct charge-parity corresponds to the $\pi(1300)$ and so on. This is sketched graphically in Fig. 4.5.

When computing the eigenvalue spectrum of the Mother-matrix, sometimes unphysical eigenvalues can appear, such as complex conjugate eigenvalue pairs. These typically arise from negative eigenvalue modes in the propagator matrix **G**, which is part of the Mother-matrix. By removing those modes from the propagator matrix, one can construct a modified Mother-matrix without complex eigenvalues [237]. Additionally, the eigenvalue curves can sometimes intersect, making extrapolation problematic. A numerical method to remove these crossings is explained in Appendix C.3.

The eigenvectors obtained from numerically solving this eigenvalue equation do contain results for each of the dressing functions of the meson at each point in the momentum and angular grids with the ordering depending on the choice of index ordering made in equation (4.37). They still have to be normalized according to one of the schemes outlined in section 4.2.3 before they can be used for calculating further mesonic properties, such as decay constants or form factors.

4.2.6. C-parity and symmetry

If the constituent quarks of a meson have the same flavour, a charge conjugation leaves the quark content invariant. As a consequence, the Bethe-Salpeter amplitude is an eigenstate of the charge-conjugation operation

$$\overline{\Gamma}^{\mu_1\mu_2\ldots\mu_J}(p,P) = \left[C\,\Gamma^{\mu_1\mu_2\ldots\mu_J}(-p,P)\,C^{-1}\right]^T = \eta_C\,\Gamma^{\mu_1\mu_2\ldots\mu_J}(p,P) \tag{4.39}$$

with $C = \gamma_2\gamma_4$ being the charge-conjugation matrix and η_C being the eigenvalue of the charge-conjugation operation. Since applying charge conjugation twice in a row leaves the initial amplitude invariant, the only possible values for the eigenvalue are $\eta_C = \pm 1$, which gives rise to another quantum number for mesons with equal constituent flavours.

If the tensor base of the Bethe-Salpeter amplitude is constructed in a way, such that the basis elements τ_i have a definite C-parity, the C-parity manifests itself in the symmetry of the dressing functions with respect to the scalar product between the relative quark momentum and the total meson momentum, i.e. $p \cdot P$ [238]. Equivalently, if one computes the BSA of a meson on-shell as a function of p and the cosine of that angle $z = \cos\psi$, the dressing functions are either odd or even in the z argument.

When computing the dressing functions of the BSA as eigenvectors of the Mother-matrix, solutions that are both even and odd in z will appear, indicating that states with both charge-parities are eigenvectors of the same matrix. There are multiple ways to deal with this issue in order to separate between states with positive and negative C-parity.

One way is by expanding the angular dependence of the dressing functions into a series of Chebyshev polynomials when calculating the elements of the Mother-matrix [186, 231]. This has the advantage, that only states with a certain C-parity appear as solutions in the first place. Additionally, the Chebyshev series tends to converge quite quickly, which means that one only has to compute the leading few terms in the series instead of having to calculate the full angular dependence. In order for this to work, the basis elements of the Bethe-Salpeter amplitude all have to have the same definite C-parity, which can be achieved by multiplying basis elements with diverging C-parity by a factor of $p \cdot P$.

Another method, which is used throughout this work, is to calculate the BSA with its full angular dependence[6] and later differentiate the obtained solutions by their symmetry in the z argument. The advantage of this method is, that by only calculating the Mother-matrix once, one obtains results for states with both C-parities at once. Since calculating the elements of the Mother-matrix is computationally much more expensive than calculating the leading eigenpairs, this can save a lot of computational work. Also, the obtained solutions are not expanded in a series but instead contain the full angular dependence.

A reliable way to perform the latter method has been to calculate the overlap between the obtained solution and Chebyshev polynomials of the second kind $U_n(x)$

$$O_{i,n}(p^2) := \int_{-1}^{1} \mathrm{d}z \sqrt{1-z^2}\, U_n(z) f_i(p^2, z) \equiv \sum_{k=1}^{N_z} w_k\, U_n(z_k) f_i(p^2, z_k), \tag{4.40}$$

where we transformed the $p \cdot P$ dependence of the dressing function f_i to a z dependence and w_k are Chebyshev integration weights, see Appendix D.1 for details. If the dressing function f_i is even (odd) in the z argument, the overlap with Chebyshev polynomials of even (odd) order n is non-zero, while the overlap with odd (even) order polynomials is zero. Since the values of f_i and thus the value of $O_{i,n}(p^2)$ can become quite small and deceptively close to zero, it is helpful to also integrate over p^2 to improve sensitivity to zero/non-zero results

$$\tilde{O}_{i,n} = \int \mathrm{d}p^2 \sum_{k=1}^{N_z} w_k U_n(z_k) f_i(p^2, z_k). \tag{4.41}$$

An example of this being applied to the pion can be seen in Fig. 4.6. One can see, that the eigenvector corresponding to the leading eigenvalue only has non-zero contributions of even order Chebyshev polynomials, while only polynomials of odd order contribute to the second eigenstate. This indicates, that the quantum

[6] Albeit on a finite grid of points in z.

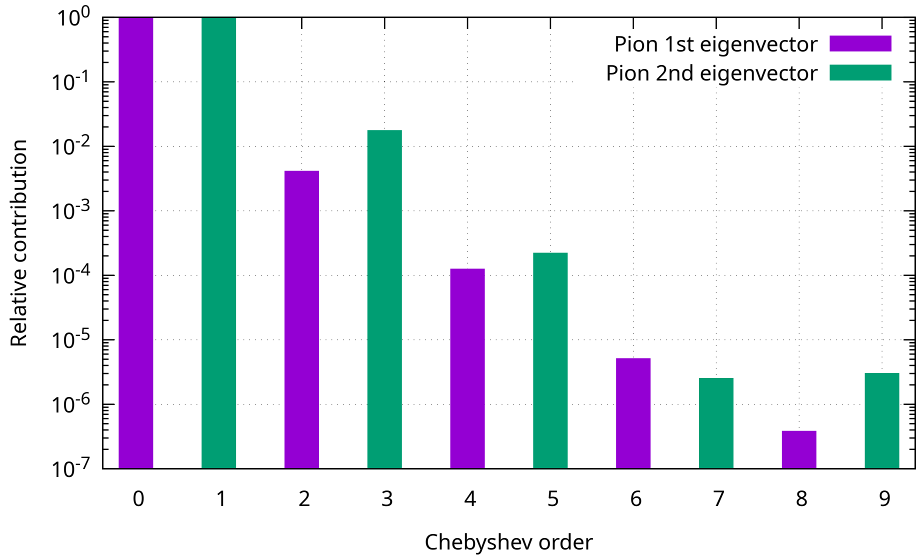

Figure 4.6.: Chebyshev expansion of the leading tensor structure's dressing function in the $J^P = 0^-$ channel akin to eq. (4.41). The results have been scaled, such that the leading order term has a contribution of 1. This calculation has been performed using the rainbow-ladder truncation.

numbers of the lowest lying state are $J^{PC} = 0^{-+}$, while the second-lowest state has quantum numbers 0^{--}, which are typically classified as exotic.

In Fig. 4.6 one can also see, that the third non-zero contribution in both states is already on the order of 10^{-4} in comparison to the leading contribution, indicating that an expansion of the full solution in Chebyshev polynomials converges quite rapidly.

4.3. Truncation schemes

As mentioned in Chapter 3, the equations of motion of QCD obtained from functional methods generally form an infinite tower of coupled equations and thus cannot be solved exactly. Instead, one has to truncate the coupled system of equations at some point. In practice, such a truncation cannot be done arbitrarily, but certain constraints have to be fulfilled. In this section we will talk about these constraints in detail and what they imply in sections 4.3.1 and 4.3.2. Then, we will go into detail on two truncation schemes important for this work in sections 4.3.3 and 4.3.4. Explicit results obtained in these two truncation schemes will be presented in Chapters 5 and 6.

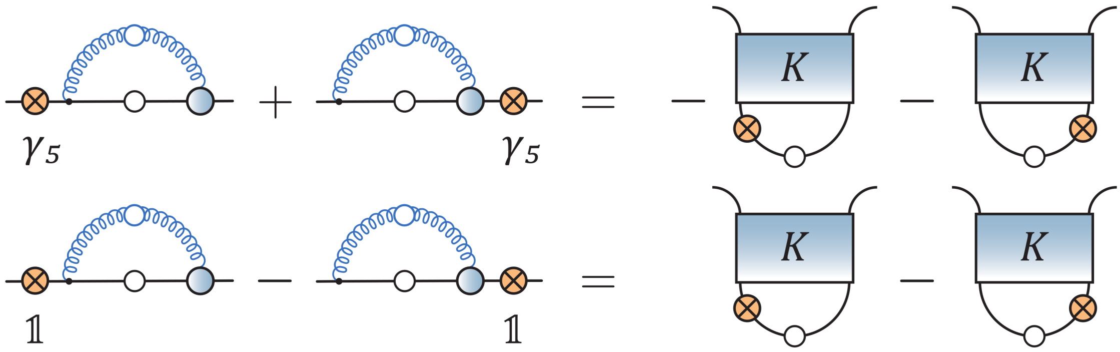

Figure 4.7.: Consistency relations between the quark self-energy and the Bethe-Salpeter kernel imposed by the axialvector Ward-Takahashi identity (top) and the vector Ward-Takahashi identity (bottom). The crossed boxes represent an insertion of an external on-shell momentum P^μ and a corresponding Dirac matrix [45].

4.3.1. The axialvector Ward-Takahashi identity

As mentioned in Section 2.3, it is of utmost importance for any practical calculation done in hadron physics to preserve the effects of DχSB, such as a non-vanishing chiral quark condensate (2.41) and the Gell-Mann-Oakes-Renner relation (2.43). In terms of currents, DχSB is characterized by the PCAC relation (2.45). At the quantum level, this leads to the axialvector Ward-Takahashi identity (axWTI), which relates axialvector and pseudoscalar vertices to the fully dressed quark propagator [45]

$$P_\mu \Gamma_5^\mu(p,P) + 2m_c\Gamma_5(p,P) = S^{-1}(p_+)i\gamma_5 + i\gamma_5 S^{-1}(p_-). \tag{4.42}$$

The momenta $p_\pm$ follow the same notation as the momenta $q_\pm$ introduced earlier. At the level of the quark self-energy Σ and the Bethe-Salpeter kernel K, the axWTI reads [190]

$$\Sigma(p_+)\gamma_5 + \gamma_5\Sigma(p_-) = -\int đ^4q\, K(q,p,P)\left(\gamma_5 S(q_-) + S(q_+)\gamma_5\right). \tag{4.43}$$

In diagrammatical form this can be seen in the top half of Fig. 4.7. The fact, that the axWTI relates the quark self-energy and the quark-antiquark scattering kernel to each other makes truncating the set of DSEs and the meson BSE a highly non-trivial task. While equation (4.43) looks deceptively simple, it implies, that the DSE tower and the meson BSE cannot be truncated independently of each other, but each truncation scheme has to consistently truncate both equations. In practice, this limits the choices of truncation schemes drastically as it can be difficult to find consistent truncation schemes. The two truncation schemes we will focus on in our meson studies do in fact both satisfy the axWTI though, making them well-suited for applications to light meson spectroscopy.

4.3.2. The vector Ward-Takahashi identity

Just like the axWTI encodes the PCAC relation and thus the effects of DχSB on the quantum level, the conservation of the vector U(1) current (2.21) is encoded in the vector Ward-Takahashi identity (vecWTI). It relates the (vector) quark-photon vertex $\Gamma^\mu_{\mathrm{q}\gamma}$ to the fully dressed quark propagator [45]

$$P_\mu \Gamma^\mu_{\mathrm{q}\gamma}(p,P) = S^{-1}(p_+) - S^{-1}(p_-). \tag{4.44}$$

The vecWTI states, that the longitudinal part of the quark-photon vertex is completely determined by the quark propagator. Fig. 4.7 shows the vecWTI in diagrammatical form. If we decompose the tensor structure of the quark-photon vertex into a longitudinal and a transverse part with respect to the photon momentum P, we can write it as

$$\Gamma^\mu_{\mathrm{q}\gamma}(p,P) = \sum_{j=1}^{4} g_j(p^2, P^2, p\cdot P)\, iG^\mu_j(p,P) + \sum_{j=1}^{8} f_j(p^2, P^2, p\cdot P)\, iT^\mu_j(p,P), \tag{4.45}$$

with dressing functions g_j and f_j which depend on all possible Lorentz invariant combinations of p and P. A canonical choice for the basis of the longitudinal part is

$$G^\mu_1 = \gamma^\mu, \quad G^\mu_2 = p^\mu \not{p}, \quad G^\mu_3 = ip^\mu, \quad G^\mu_4 = (p\cdot P)\,\frac{i}{2}\,[\gamma^\mu, \not{k}]\,. \tag{4.46}$$

The vecWTI now implies, that the dressing functions g_j formally have the Ball-Chiu solution [239, 240]

$$g_1 = \Sigma_A, \quad g_2 = 2\Delta_A, \quad g_3 = -2\Delta_B, \quad g_4 = 0, \tag{4.47}$$

where

$$\Sigma_A = \frac{A(p_+^2) + A(p_-^2)}{2}, \quad \Delta_A = \frac{A(p_+^2) - A(p_-^2)}{p_+^2 - p_-^2} \tag{4.48}$$

and an analogous expression for Δ_B, where $A(p^2)$ and $B(p^2)$ are again the dressing functions of the inverse quark propagator. The identities (4.47) give the possibility to test the vecWTI numerically by independently calculating the dressing functions of the longitudinal part of the quark-photon vertex and the linear combinations of quark propagator dressing functions appearing on the right-hand side of equation (4.47) and comparing them against each other. For more details on how the quark-photon vertex is obtained numerically, Appendix C.4 can be consulted.

Since the vector Ward-Takahashi identity is not only related to the conservation of the U(1) vector current, but also to gauge symmetry and the interaction between quarks and photons, any truncation used for calculations of electromagnetic properties of quarks and hadrons, such as hadronic formfactors, has to fulfill the vecWTI to ensure the results are physically meaningful.

4.3.3. The rainbow-ladder truncation

One truncation scheme, which is known to preserve both the vector and axialvector Ward-Takahashi identities, is the so-called rainbow-ladder truncation. It has been applied to a wide range of problems in hadron physics over the past decades. For reviews, cf. [45–47, 49] and references therein.

The idea behind the rainbow-ladder truncation is to replace the quark-gluon vertex appearing in the quark DSE by its leading, tree-level tensor structure and to combine its dressing function with the gluon propagator's dressing function into an effective one-gluon exchange. Simultaneously, the quark-antiquark scattering kernel appearing in the BSE is replaced with a single effective gluon exchange using the exact same effective gluon as in the quark DSE. In particular, the combination of quark-gluon vertex and gluon propagator is replaced by

$$D^{\mu\nu}(k)\Gamma^{\mu}_{\text{qg}}(k;p,q) = \frac{Z(k^2)}{k^2}\sum_{i=1}^{8} h_i(k;p,q)\lambda_i^{\mu}(k;p,q) \rightarrow Z_{1F}\frac{Z(k^2)}{k^2}\gamma_{\perp}^{\mu}h_1(k;p,q). \tag{4.49}$$

One further simplifies the momentum dependence of $h_1(k;p,q)$ to only depend on the squared gluon momentum, i.e. $h_1(k^2)$, such that one can combine $Z(k^2)$ and $h_1(k^2)$ into an effective running coupling

$$\alpha(k^2) = \left(\frac{\tilde{Z}_1}{\tilde{Z}_3}\right)^2 \frac{g^2}{4\pi} Z(k^2)h_1(k^2). \tag{4.50}$$

Finally, one can combine the appearing renormalization constants using the Slavnov-Taylor identities (2.14)

$$Z_{1F}^2 = Z_2^2\left(\frac{\tilde{Z}_1}{\tilde{Z}_3}\right)^2. \tag{4.51}$$

Thus, the truncated quark self energy becomes

$$\Sigma(p) = -C_f Z_2^2 4\pi \int đ^4 q \, \gamma^\mu S(q) \gamma_\perp^\mu \frac{\alpha(k^2)}{k^2}. \tag{4.52}$$

In order to fulfill the axialvector and vector WTIs, one has to choose the quark-antiquark scattering kernel to be

$$K_{ab,cd}(q,p,P) = -C_f Z_2^2 4\pi \gamma_{ab}^\mu T_{\mu\nu}(k) \gamma_{cd}^\nu \frac{\alpha(k^2)}{k^2}, \tag{4.53}$$

where $\alpha(k^2)$ is the exact same effective running coupling as in the truncated quark DSE. One can show, that even a light deviation between the effective running couplings used in the quark DSE and pion BSE leads to the pion obtaining a significant mass in the chiral limit [241]. A short analytic proof, that this choice of truncation indeed satisfies the axWTI, can be found in Appendix C.5.

As for the choice of effective running coupling, one typically composes an explicit form by combining an ultraviolet part, which is motivated by perturbation theory, with an infrared part, which is modelled using phenomenological arguments. This leads to the effective running coupling having the general form

$$\alpha_{\text{eff}}(k^2) = \alpha_{\text{IR}}(k^2) + \frac{\pi \gamma_m \left(1 - \mathrm{e}^{-k^2/\Lambda_0^2}\right)}{\ln \sqrt{\mathrm{e}^2 - 1 + \left(1 + k^2/\Lambda_{\text{QCD}}^2\right)^2}}, \tag{4.54}$$

with scales $\Lambda_0 = 1\,\text{GeV}$ and $\Lambda_{\text{QCD}} = 0.234\,\text{GeV}$, and the anomalous mass dimension being $\gamma_m = 12/(11N_c - 2N_f) = 12/25$ for $N_c = 3$ and $N_f = 4$. For the infrared part, several models have been used in the past with different arguments for their usefulness. During this work, we will investigate some properties of the models proposed by Maris and Tandy [186] and by Qin, Chang et al. [242][7]

$$\alpha_{\text{IR,MT}}(k^2) = \pi \eta^7 \, \frac{k^4}{\Lambda^4} \, \mathrm{e}^{-\eta^2 k^2/\Lambda^2} \tag{4.55}$$

$$\alpha_{\text{IR,QC}}(k^2) = \pi \eta_{\text{QC}}^7 \, \frac{k^2}{\Lambda_{\text{QC}}^2} \, \mathrm{e}^{-\eta_{\text{QC}}^2 k^2/\Lambda_{\text{QC}}^2}. \tag{4.56}$$

We will refer to the former effective running coupling as Maris-Tandy model and the latter as Qin-Chang model. We will investigate and compare some of the properties and results of both models throughout this work, but we will put a stronger emphasis on the Maris-Tandy model.

[7] The original works, in which these models have been proposed use a different parametrization in terms of parameters D and ω. Here, we opt for a different parametrization, which is used in [1, 45] and other works. We will later give explicit values for the parameters used in Section 6.4.

4.3.4. The kernel-first truncation

In this section, we will investigate another truncation scheme, which preserves the axWTI, called kernel-first truncation. It has first been developed by Richard Williams, Christian Fischer and Walter Heupel in an unpublished paper [3] and the derivation is reproduced here with permission by the authors. It has been applied to the light meson spectrum in another paper by these authors within a similar 3PI setup to the one used in this work [195]. Some exploratory work with simple model interactions based on the construction laid out in this section has been done in my master's thesis [241]. In this work, we will apply it to the more general framework introduced in sections 3.2 through 3.5.

Motivation - Problems of the rainbow-ladder truncation

While the rainbow-ladder truncation has been applied to a wide range of problems in the past, it has been done so with varying success. For instance, we will later see in Section 6.4, that rainbow-ladder is a good tool for describing ground state masses of mesons with quantum numbers on the natural Regge trajectory, while failing at reproducing and predicting ground state masses of other quantum numbers. Similar results have been observed in baryon spectra as well [45]. As a consequence, only some possible configurations of tetraquarks become reasonably accessible in rainbow-ladder [42]. Furthermore, the rainbow-ladder truncation generally does not do a good job at producing excited meson masses, which we will also see in practice later. Lastly, the drastic simplifications done to the quark-gluon vertex and gluon propagator make it impossible to access the analytic structure of Yang-Mills Green's functions or access exotic states beyond the quark sector, such as glueballs and hybrid mesons, in a consistent way.

Introducing the kernel-first truncation

In section 3.2.2 we have seen, how taking the first order functional derivative of an nPI effective action with respect to the quark propagator produces a term for the quark self-energy. Similarly, taking the second order functional derivative with respect to the quark propagator gives rise to the quark-antiquark scattering kernel [210]. One can use this approach to derive consistent equations of motion for the propagators and vertices of the truncated theory as well as a corresponding scattering kernel.

However, it is not always clear, whether the kernel and quark self-energy satisfy the Ward-Takahashi identities (4.43) and (4.44). This is especially the case, if further approximations are done in the process, such as kinematic simplifications, leaving out entire diagrams in equations or quenching the quark loops in the Yang-Mills sector. It is also not straight-forward to only consider certain tensor structures of objects appearing in the kernel, especially the quark-gluon vertex, to investigate their impact on computed quantities while still preserving the axWTI.

Note, that going from a truncated quark self-energy to a scattering kernel is not trivial either. Obtaining the quark self-energy entails evaluation at the physical point, i.e. setting the source terms to zero. One can thus not just take the functional derivative of the self-energy to get a scattering kernel, since setting the sources to zero would happen at the wrong step, leading to a wrong order of operations

$$\begin{aligned}\Sigma &\sim \left.\frac{\delta\Gamma^{3\mathrm{l}}_{3\mathrm{PI}}}{\delta S}\right|_{J=0}\\ K &\sim \left.\frac{\delta^2\Gamma^{3\mathrm{l}}_{3\mathrm{PI}}}{\delta S\delta S}\right|_{J=0} \neq \frac{\delta\Sigma}{\delta S}.\end{aligned} \tag{4.57}$$

If one were to calculate the functional derivative of the quark self-energy, the chain rule would have to be respected, leading to derivatives of the quark-gluon vertex appearing, which in turn introduces a four-quark-one-gluon vertex with its own coupled integral equation [3].

Thus, we will introduce the kernel-first truncation, which works the other way around compared to the usual procedure. The idea is to start with an expression for the quark-antiquark scattering kernel and derive an expression for the quark self-energy from there. The benefit of the kernel-first truncation is, that it automatically satisfies the axWTI by construction. This implies, that the effects of DχSB are automatically included in the calculations, especially the (pseudo) Goldstone nature of the pion. We will numerically verify this in section 6.2.

Constructing the quark self-energy

To construct a quark self-energy from a given scattering kernel K, we start with Goldstone's theorem in the form [3, 210]

$$\frac{\delta^2\Gamma}{\delta S\delta S}\left\{\gamma_5, S\right\} = 0. \tag{4.58}$$

The first term is the Bethe-Salpeter operator $S^{-1}_{ab}\otimes S^{-1}_{cd} - K_{ab,cd}$, while the second term is the analog of the Bethe-Salpeter wave function in the chiral limit. Using this expression for the Bethe-Salpeter operator we find

$$\left[S^{-1}(p)\right]_{ab}\left\{\gamma_5, S(p)\right\}_{bc}\left[S^{-1}(p)\right]_{cd} = \int đ^4 q\, K_{ab,cd}(p,q,P)\left\{\gamma_5, S(q)\right\}_{bc}. \tag{4.59}$$

We can now again decompose the inverse quark propagator into a vector and a scalar part according to (3.30). Using the fact that the vector part anticommutes with all occurrences of γ_5 we get

$$2\gamma_{5,ad}B(p^2) = \int đ^4q\, K_{ab,cd}(p,q,P)\,\{\gamma_5, S(q)\}_{bc}\,. \tag{4.60}$$

If we further multiply this expression by γ_5 from the left and take the trace over the uncontracted dirac indices, we can insolate $B(p^2)$ on the left-hand side of this equation. Doing so yields an equation for $B(p^2)$

$$B(p^2) = \frac{1}{8}\,\mathrm{tr}\left(\gamma_{5,ab}\int đ^4q\, K_{bc,de}(p,q,P)\,\{\gamma_5, S(q)\}_{cd}\right), \tag{4.61}$$

which replaces, as the consequence of introducing a constraint equation, the usual result for the scalar dressing function from the equations of motion. Technically, this derivation is only exact in the chiral limit, where the pion is massless and thus $P^2 = -m_\pi^2 = 0$. The kernel we will use for our practical calculations does not explicitly depend on the total meson momentum P though, which makes it possible to extend equation (4.61) to finite current quark masses m_c. Doing so does not change the fact that the equation remains in satisfaction of the axWTI. Therefore, the scalar part of the quark DSE becomes

$$B(p^2) = Z_2 Z_m m_c - \frac{1}{4}\,\mathrm{tr}\left[\int đ^4q\,\gamma_{5,ab}K_{bc,de}(q,p,P)\gamma_{5,cd}\frac{B(q^2)}{q^2A(q^2)+B(q^2)}\right]. \tag{4.62}$$

This construction bears some similarities to the Dirac-Brueckner scheme used in transport theory of nuclear reactions [243, 244]. In this scheme, the self energy term in the Dyson-Schwinger equation for the nucleon Green's function is also constructed from a four-nucleon vertex function, but without the insertions of γ_5 matrices to account for chirality and without the insertion of the anticommutator $\{\gamma_5, S\}$.

Equation for $A(p^2)$

It is important to note, that this construction, which uses the axWTI as basis, only constrains the equation for $B(p^2)$. It does not pose any constrains on the equation for the vector dressing function $A(p^2)$. Naively, this leaves us with a choice of equation for $A(p^2)$. However, the axWTI is not the only symmetry constraint we have to fulfill. Ideally, one would construct the equation for $A(p^2)$, such that the vector WTI is also fulfilled alongside the axialvector WTI.

Throughout this work, three different constructions for an A-equation have been investigated. The first is to derive the A-equation using the unmodified

3PI formalism outlined in Chapter 3. This means, that the equation for $A(p^2)$ is obtained by projecting the quark self-energy derived from the effective action onto the vector part and taking the trace, i.e.

$$A(p^2) = Z_2 - Z_{1f} g^2 C_F \operatorname{tr}\left(\frac{-i\not{p}}{4p^2} \int đ^4 q \, i\gamma^\mu S(q) \Gamma^\mu(k; -p, q) D^{\mu\nu}(k)\right). \tag{4.63}$$

This has the advantage of having a clear motivation for the choice of A-equation, as it is the "natural" equation derived from QCD.[8] On the other hand, its disadvantage is, that this makes it impossible to write down one self-energy in closed form from which the equations for both $A(p^2)$ and $B(p^2)$ can be derived via projection and tracing. This makes it impossible to reason about whether this setup fulfills the vecWTI using transformation properties of the self-energy, as is done in [210].

Thus, another construction for the A-equation investigated in this work is one first proposed by von Smekal in [245]. It uses an equation with a structure similar to eq. (4.62)

$$A(p^2) = Z_2 - \frac{1}{4} \operatorname{tr}\left[\frac{-i\not{p}}{p^2} \int đ^4 q \, \gamma_{5,ab} K_{bc,de}(q, p, P) \gamma_{5,cd} \frac{\not{q} A(q^2)}{q^2 A(q^2) + B(q^2)}\right]. \tag{4.64}$$

Lastly, since the right-hand side of equation (4.62) has clear similarities to the diagrams appearing on the right-hand side of the axWTI in Fig. 4.7, one can also try to construct an equation for $A(p^2)$ in analogy to the right-hand side of the vecWTI in Fig. 4.7. This leads to an A-equation of the form

$$A(p^2) = Z_2 - \frac{1}{4} \operatorname{tr}\left[\frac{-i\not{p}}{p^2} \int đ^4 q \, \mathbb{1}_{ab} K_{bc,de}(q, p, P) \mathbb{1}_{cd} \frac{\not{q} A(q^2)}{q^2 A(q^2) + B(q^2)}\right]. \tag{4.65}$$

We will investigate the impact of different A-equations on the vecWTI in Section 5.3. Unfortunately, none of the approaches presented here satisfy the axWTI and the vecWTI simultaneously. This might be a general problem of the truncated nPI approach [246, 247]. For the kernel-first truncation, this still poses an open problem.

Choosing a kernel

As a first consistency check, it is instructive to use the rainbow-ladder scattering kernel (4.53) in the kernel-first construction (4.62). One can easily verify, that

[8] The word "natural" is put in quotation marks, since the equations for the scalar and vector dressing functions are coupled and thus any modification done to one dressing function's equation will always affect both functions.

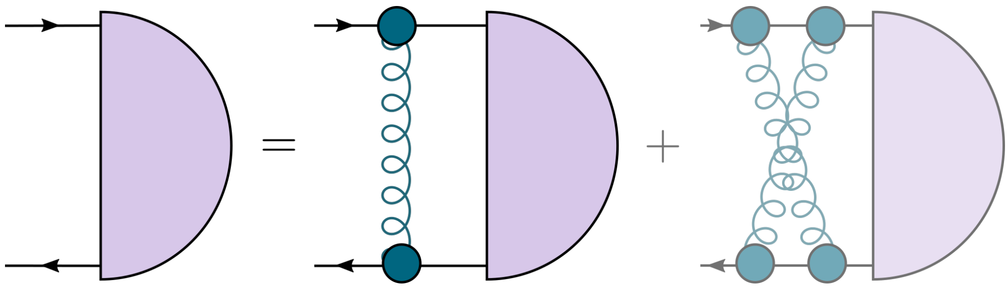

Figure 4.8.: Meson BSE derived from the three loop 3PI effective action. The crossed gluon exchange is being neglected, as it corresponds to the Abelian diagram in the quark-gluon vertex equation (3.35).

doing so results in the same equation for $B(p^2)$ as one obtains by using the quark self-energy (4.52) in the quark DSE [241].

For our calculations beyond the rainbow-ladder truncation, we will use a more sophisticated kernel. In fact, we will use the kernel, that is derived from the three particle irreducible effective action of QCD at three loop level. As mentioned at the beginning of this section, the kernel is obtained by performing the second order functional derivative with respect to the quark propagator and evaluating at the physical point [210]

$$K_{ab,cd} = 2 \frac{\delta^2 \Gamma^{3l}_{3PI}}{\delta S_{ab} \delta S_{cd}} \bigg|_{J=J^{(2)}=J^{(3)}=0} . \tag{4.66}$$

For the 3PI effective action at three-loop order this results in two terms, one being a dressed single gluon exchange between two dressed quark-gluon vertices, the other being a crossed two gluon exchange [195]. The meson BSE with the resulting scattering kernel is depicted diagrammatically in Fig. 4.8.

In our calculations we will neglect the crossed gluon exchange diagram. The reasoning behind it is twofold. Firstly, it introduces a two loop diagram into the meson BSE, which leads to significantly more computational effort when solving the BSE numerically. Secondly, when deriving this kernel from the 3PI effective action, this diagram corresponds to the Abelian diagram in the quark-gluon vertex equation (3.35). In other words, if one neglects the Abelian diagram in the quark-gluon vertex equation, the derivation of the kernel automatically only contains the single dressed gluon exchange [195]. The 3PI kernel we use thus has the explicit form

$$K_{ab,cd}(q,p,P) = -g^2 C_F D_{\mu\nu}(k) \left[\Gamma^{\mu}_{\mathrm{qg}}(k,-q_+,p_+)\right]_{ab} \left[\Gamma^{\nu}_{\mathrm{qg}}(k,-p_-,q_-)\right]_{cd} \tag{4.67}$$

One might assume, that inserting a kernel with two dressed quark-gluon vertices into the quark DSE might result in double counting of some diagrams. However, due to the kernel-first construction introducing γ_5 matrices into the quark self-energy, this problem is automatically mitigated. When one inserts the kernel (4.67) into equation (4.62), it will contain a term of the form

$$\tilde{\Gamma}^{\mu}_{\mathrm{qg}} := \gamma_5 \Gamma^{\mu}_{\mathrm{qg}} \gamma_5 \tag{4.68}$$

which is a chiral transformation of the quark-gluon vertex. While the chirally even tensor structures of the quark-gluon vertex do not change under this transformation, the chirally odd ones obtain a relative minus sign compared to the even ones. Thus, the two vertices appearing in the final equation are not equal after all.

5. Results - QCD correlation functions

5.1. Quark-gluon vertex

The results shown in this section have been calculated by Markus Q. Huber and are still preliminary. Once they are finalized, they will be published in a separate paper [2]. They are shown here, since they serve as input for quark and meson calculations within the kernel-first truncation later in this work.

Fig. 5.1 shows numerical results for the quark-gluon vertex dressing functions in the setup explained throughout Chapter 3. The top panel shows results for the light quark-gluon vertex. One immediately sees, that the leading, tree-level structure of the vertex is the dominant one. Its dressing function h_1 becomes constant in the infrared and exhibits logarithmic behaviour for large momenta as one would expect from perturbation theory. All other dressing functions go to zero in the ultraviolet, which is also in agreement with perturbation theory and asymptotic freedom. Besides the tree-level tensor structure, the structures with dressing functions h_2, h_5, h_6 and to a lesser extent h_3 also have a sizeable contribution, while the dressing functions h_4, h_7 and h_8 are close to zero. This general ordering is in accordance with Ref. [195], where a similar setup and tensor basis have been used. The fact, that the subleading tensor structures do contribute significantly to the results and their dressing functions are comparable in size to the tree level structure, indicates, that a more sophisticated treatment of the quark-gluon vertex beyond the simple rainbow-ladder truncation is necessary to fully grasp the dynamics of QCD.

The width of the bands in Fig. 5.1 shows the angular dependence of the dressing functions. In particular, the solid lines mark the largest and smallest values the dressing function takes on for fixed singlet variable S_0 when varying the doublet variables a and s, see Section 3.5.1 for details. From this one can see, that the quark-gluon vertex does have a sizeable angular dependence. For instance, around $S_0 = 1\,\mathrm{GeV}^2$ the largest and smallest value of the leading dressing function h_1 differ by a factor of roughly 1.65. The quark gluon vertex having a sizeable angular dependence is also in accordance with previous studies, cf. [215, 248].

Lastly, Fig. 5.1 also shows results for the strange quark-gluon vertex in the lower

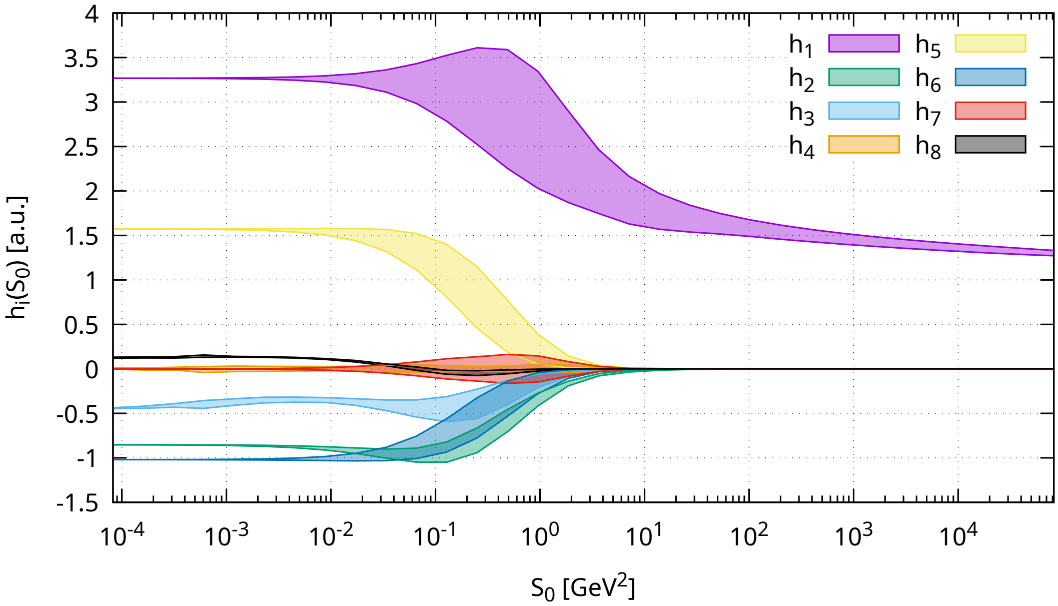

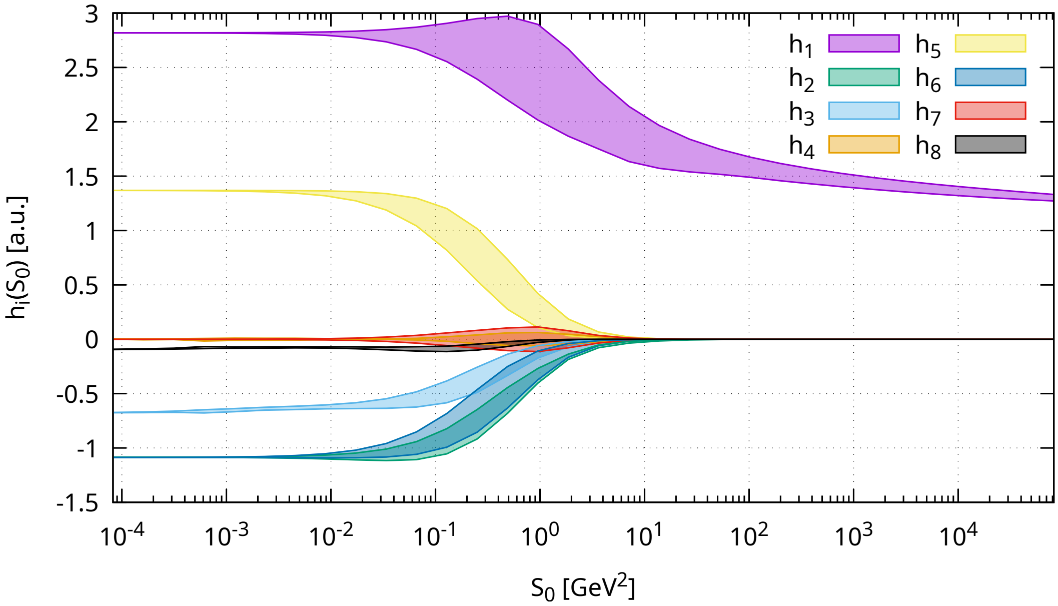

Figure 5.1.: Preliminary results for the quark-gluon vertex dressing functions. The width of the plots indicate the angular dependence of the dressing functions. Top panel: Light quarks ($m_c = 2.2\,\mathrm{MeV}$), bottom panel: Strange quarks ($m_c = 58\,\mathrm{MeV}$)

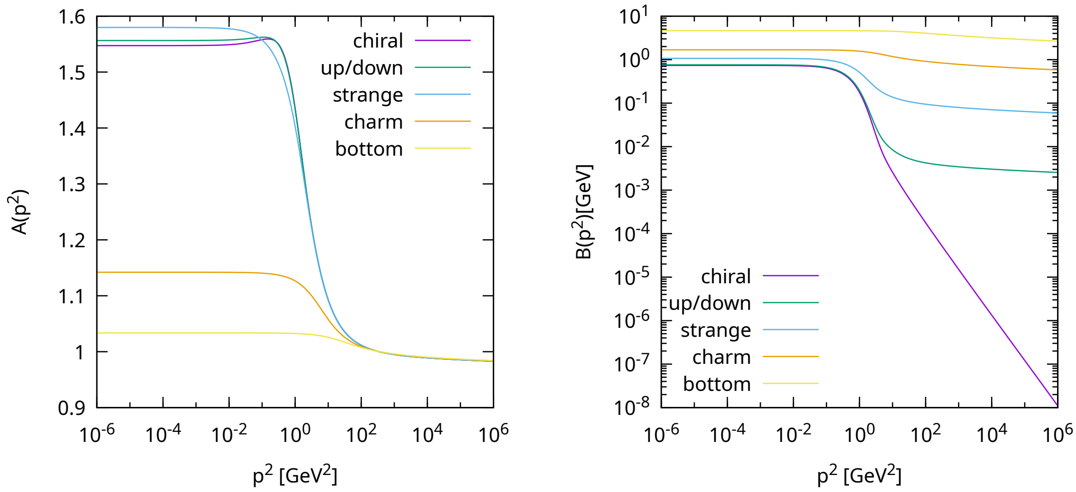

Figure 5.2.: Results for the dressing functions of the inverse quark propagator calculated in the rainbow-ladder truncation. The equations have been renormalized at $\mu = 19\,\text{GeV}$.

panel. The qualitative behaviour of the dressing functions stays the same, but the concrete values of them change noticeably. One feature visible here is that the leading dressing function h_1 becomes less dominant for strange quarks than it is for light quarks. Previous work done in [215] investigating the flavour dependence of the quark-gluon vertex for charm and bottom quarks has shown similar behaviour.

5.2. Quark propagator

The Landau gauge quark propagator has been thoroughly studied in the past using functional methods in several truncations. For reviews, see [45, 47–50, 249] and references therein. Since this quantity has already been studied extensively, we will only briefly sketch its most important features here, especially in regard to DχSB.

5.2.1. Rainbow-ladder truncation

Fig. 5.2 shows results for the dressing functions of the inverse quark propagator calculated in the rainbow-ladder truncation for several quark masses. The left plot shows the vector dressing function $A(p^2)$, the right plot shows the scalar dressing function $B(p^2)$ on a logarithmic plot. For the former, one can see, that it tends towards 1 in the ultraviolet[1] while it is enhanced in the infrared. Consequently, the wave function dressing $Z_f(p^2) = 1/A(p^2)$ tends towards 1 in the ultraviolet as well, while being suppressed in the infrared. Superficially, this can be seen as a representation of asymptotic freedom, with the quarks being tightly bound at small energies, while being asymptotically free at high energies.

For the scalar dressing function $B(p^2)$ we can see a qualitatively similar behaviour. In the ultraviolet, the dressing function tends towards the bare quark mass m_c, while also being enhanced in the infrared. For massless quarks, $B(p^2)$ does not decay logarithmically, but falls off with a power law. This happens, because in general $B(p^2)$ has two asymptotic terms in the ultraviolet, one decaying logarithmically and one decaying as a power law. The logarithmic term however is proportional to the bare quark mass, which leads to it being dominant for large values of p^2 for finite m_c while being absent in the chiral limit [175].

Similarly, the quark's effective mass function $M(p^2) = B(p^2)/A(p^2)$ is also enhanced in the infrared. This indicates, that even the truncated dynamics of the rainbow-ladder truncation lead to an effective quark mass being generated dynamically. Even in the chiral limit the effective quark mass becomes finite in the infrared. The larger the value of the bare quark mass, the less strong the effects of dynamical mass generation become in relation to the bare mass. In concrete numbers, the effective mass generated in the chiral limit is $M(0) = 476\,\mathrm{MeV}$. For light quarks it is $M(0) = 488\,\mathrm{MeV}$, which is larger than expected in a constituent quark picture. The chiral quark condensate has a value of $\left\langle\overline{\psi}\psi\right\rangle = -(272.8\,\mathrm{MeV})^3$.

5.2.2. Kernel-first truncation

Fig. 5.3 shows results for the dressing functions of the inverse quark propagator calculated in the kernel-first truncation for chiral, light and strange quarks.[2] For these calculations, we used the unmodified equation for $A(p^2)$ with a single dressed quark-gluon vertex. Generally speaking, these results share many similarities with the rainbow-ladder results. Both dressing functions are enhanced in the infrared and fall off in the ultraviolet, an effective mass is generated dynamically and the ordering of the results is generally also compatible with the rainbow-ladder case. It is noteworthy though, that the dynamically generated mass is smaller compared to the rainbow-ladder case. The chiral quark has an effective mass of $M(0) = 162\,\mathrm{MeV}$ and the light quark with $m_c = 2.2\,\mathrm{MeV}$ has an effective mass of $M(0) = 199\,\mathrm{MeV}$, which is smaller than one would expect in a constituent quark picture. Interestingly, the value of the chiral quark condensate barely changes compared to the rainbow-ladder truncation and comes out to be $\left\langle\overline{\psi}\psi\right\rangle = -(264.8\,\mathrm{MeV})^3$.

[1] In fact, $A(p^2) = 1$ at the renormalization point due to the renormalization condition (3.33). If we were to renormalize at ultraviolet cutoff, A would go to 1 at the cutoff.

[2] Charm and bottom quarks are not included in this study, since charmonium and bottomonium meson mass poles lie too far inside the complex plane to be accessible in our current setup, see Appendices C.2 and C.1 for details. While we technically could still calculate the quark

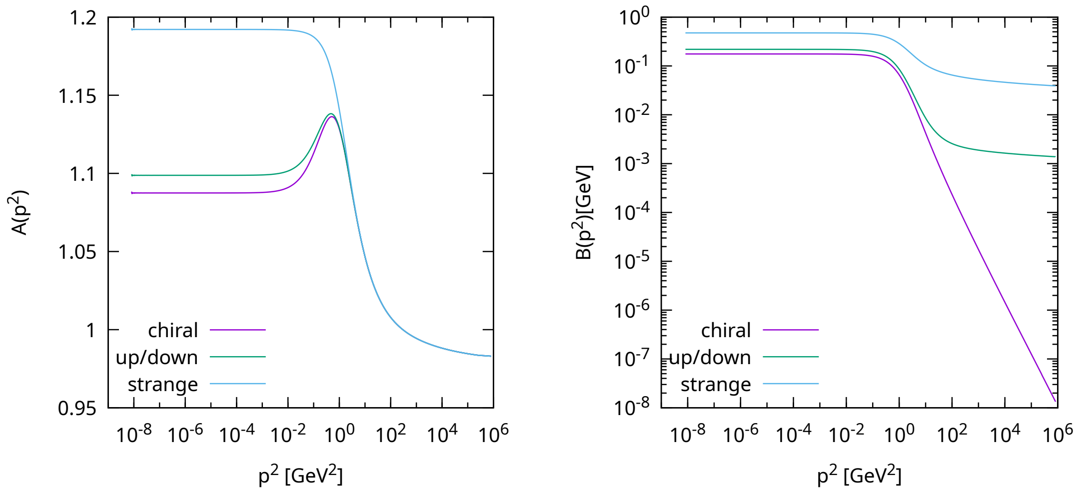

Figure 5.3.: Results for the dressing functions of the inverse quark propagator calculated in the kernel-first truncation. The equations have been renormalized at $\mu \approx 17.234\,\mathrm{GeV}$.

5.3. Quark-photon vertex

In this section, we will investigate numerical results for the longitudinal part of the quark-photon vertex and compare them to the Ball-Chiu solution (4.47). The purpose of that is to numerically investigate, whether the vecWTI is satisfied by the rainbow-ladder and kernel-first truncation schemes. Details on the numerical treatment of the quark-photon vertex BSE and results for the transverse part of the vertex can be found in Appendix C.4.

5.3.1. Rainbow-ladder truncation

The results obtained in the rainbow-ladder truncation are depicted in Fig. 5.4. They are compared to the Ball-Chiu vertex, which is the solution obtained from the vecWTI. For g_1 through g_3, the rainbow-ladder and Ball-Chiu solutions are nearly indistinguishable with only slight deviations at the edges of the z grid in g_1, where $z = (\hat{p} \cdot \hat{P}) \approx \pm 1$. At a first glance it looks like g_4 deviates significantly from the Ball-Chiu solution, but these deviations are only on the order of 10^{-6} at most.

We can thus conclude, that the rainbow-ladder truncation does respect not only the axWTI, but also the vecWTI. It therefore respects gauge symmetry and is a suitable truncation for calculations of electromagnetic properties of hadrons.

propagator for spacelike momenta, we cannot reliably fix the current quark masses to the charmonium and bottomonium sector, making such calculations not very meaningful.

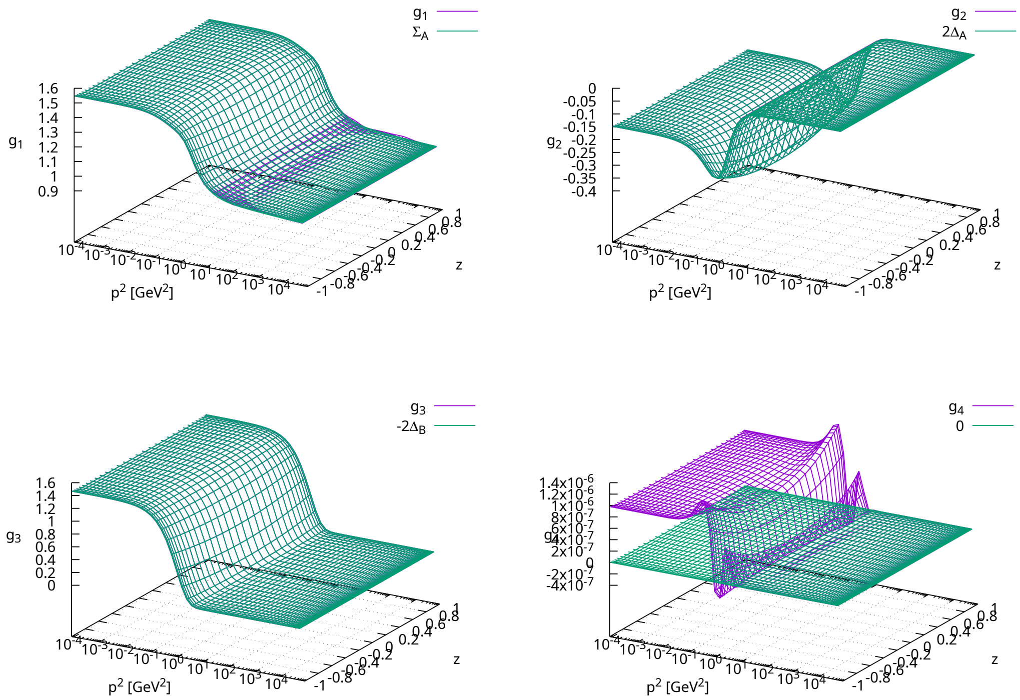

Figure 5.4.: Dressing functions of the longitudinal part of the quark-photon vertex calculated in the rainbow-ladder truncation with the Maris-Tandy model (purple) compared to the Ball-Chiu solution (green). The photon momentum has been fixed to $P^2 = 1\,\mathrm{GeV}^2$.

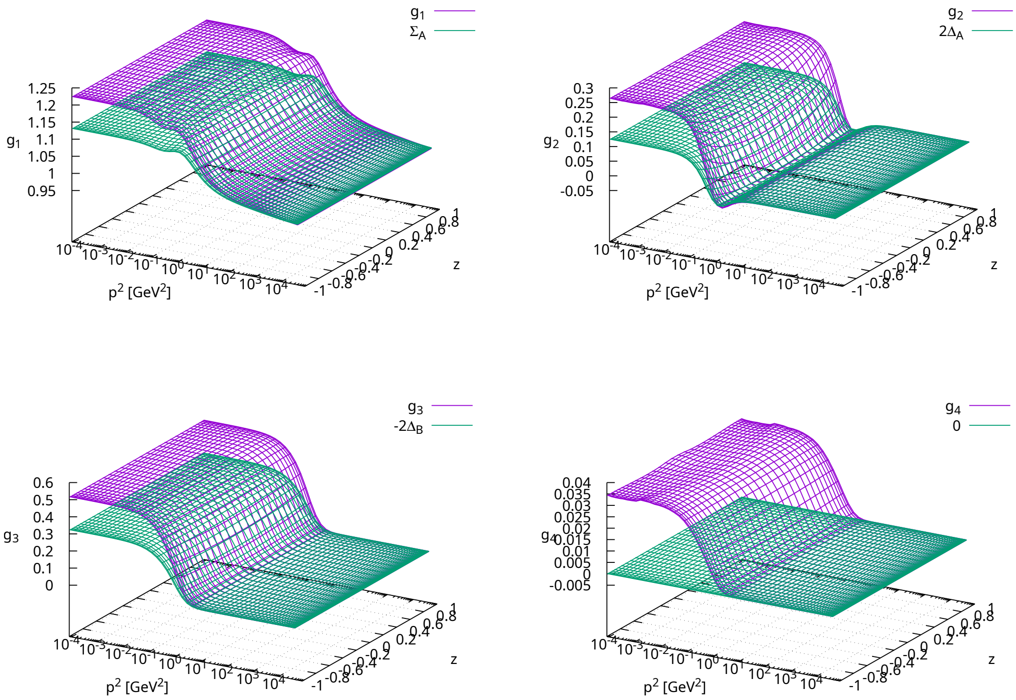

Figure 5.5.: Dressing functions of the longitudinal part of the quark-photon vertex calculated in the kernel-first truncation with a single dressed quark-gluon vertex (purple) compared to the Ball-Chiu solution (green). The photon momentum has been fixed to $P^2 = 0.822\,751\,\mathrm{GeV}^2$.

5.3.2. Kernel-first truncation

Fig. 5.5 shows results for the longitudinal part of the quark-photon vertex compared to the Ball-Chiu solution in the kernel-first truncation with a single dressed quark-gluon vertex in the equation for $A(p^2)$, see Eq. 4.63. In contrast to the rainbow-ladder results, we now see a clear discrepancy between the two solutions. While the ultraviolet behaviour of the numerical results does match up with the Ball-Chiu vertex, in the infrared all four dressing functions deviate substantially from the solution predicted by the vecWTI.

Unfortunately, none of the other approaches for the A-equation proposed in section 4.3.4 mitigate this problem. Results obtained with equation 4.64 used to determine $A(p^2)$ are shown in Figure 5.6.

Thus, we conclude, that the kernel-first truncation in its current form violates the vecWTI and is thus not well suited for calculations of electromagnetic properties

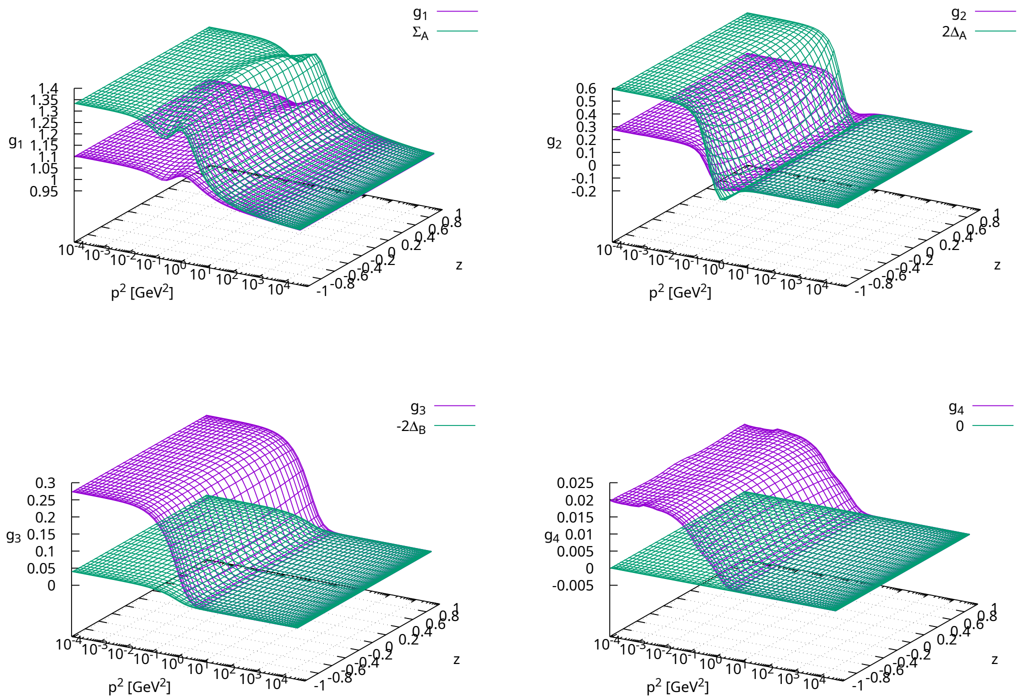

Figure 5.6.: Dressing functions of the longitudinal part of the quark-photon vertex calculated in the kernel-first truncation with the construction (4.64) used (purple) compared to the Ball-Chiu solution (green). The photon momentum has been fixed to $P^2 = 0.822\,751\,\mathrm{GeV}^2$.

of hadrons. For the sake of completeness, the results for the transverse part of the vertex are still given in Appendix C.4. Whether this problem can be solved by choice of a different equation for $A(p^2)$ still poses an open problem.

However, since the kernel-first truncation does satisfy the axWTI, which we will also explicitly verify in section 6.2, we will still apply it to calculations of light and strange meson spectra in Chapter 6. For these calculations, we will keep using the unmodified equation for $A(p^2)$ with a single dressed quark-gluon vertex.

6. Results - Meson properties

The results presented in sections 6.1 and 6.4 have partially been published in [1] and have been worked out in collaboration with the co-authors of that paper.

6.1. Interaction potentials

In section 2.1.6 we introduced the concept of an effective potential between a static quark-antiquark pair. In its simplest form, i.e. without spin and angular momentum dependent parts, such a potential can be parametrized by the Cornell ansatz (2.19). By choosing a constant string tension $\sigma(r) \approx \sigma_0$ for small values of r, while $\sigma(r) \to 1/r$ in the limit $r \to \infty$, one can implement a smoothed out version of the effects of string breaking [148].

As explained in Section 4.1.3, a striking feature of the QCD spectrum is the appearance of approximately linear Regge trajectories in Chew-Frautschi plots of squared mass vs. total angular momentum. While such a behaviour is very easily explained in simple models like a spinning stick or string picture, it has to emerge from the underlying complex dynamics of QCD [142]. Of course, the rainbow-ladder truncation with a modelled effective running coupling introduced in section 4.3.3 will hardly contribute fundamental insights into this issue. Nevertheless, as we will see, it is interesting to compare its corresponding heavy-quark interaction potential and the resulting meson spectra with these general expectations.

In order to obtain a potential from a running coupling, one has to perform a Fourier transformation with respect to the three-dimensional momentum of the truncated scattering kernel used in the BSE, see, e.g. [250]. Performing such a transformation on a bare (massive) single boson exchange kernel, one obtains a Yukawa potential

$$V(\vec{r}\,) = \int đ^3k\, \mathrm{e}^{-i\vec{k}\cdot\vec{r}} \frac{-4\pi g^2}{\vec{k}^2 + m^2} = -g^2 \frac{\mathrm{e}^{-mr}}{r} \tag{6.1}$$

which in the limit $m \to 0$ becomes a Coulomb potential. Applying the same procedure to the rainbow-ladder kernel (4.53) with any effective running coupling which only depends on the squared exchange momentum corresponds to evaluating the integral

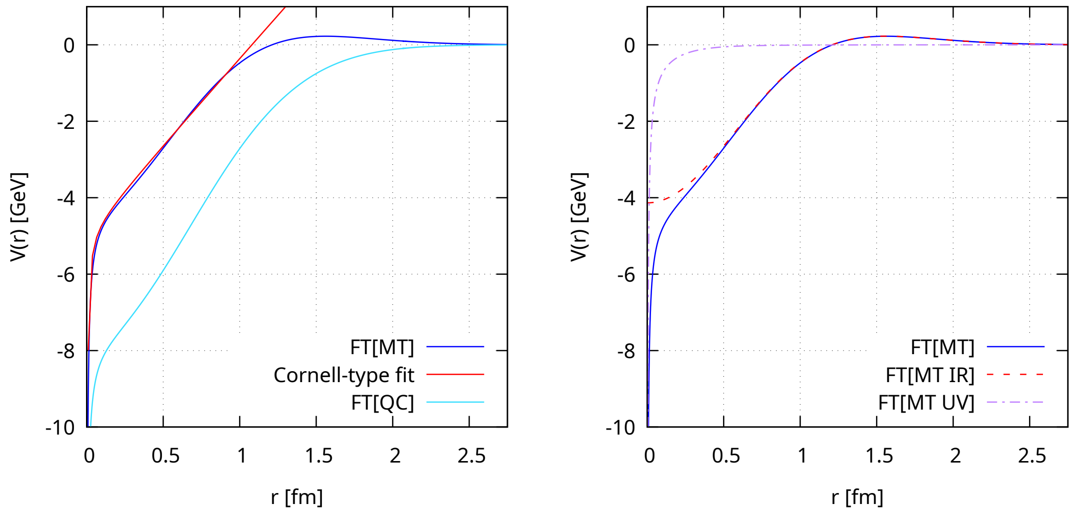

Figure 6.1.: **Left panel:** Interaction potentials obtained via Fourier transformation of effective running couplings. The MT potential has a (positive) maximum around $r = 1.6\,\mathrm{fm}$ and approaches zero from the positive side while the QC potential approaches zero monotonously. **Right panel:** The contributions of the infrared and ultraviolet parts of the effective running coupling to the MT potential.

$$V(\vec{r}) = -C_f 4\pi \int đ^3k\, \mathrm{e}^{-i\vec{k}\cdot\vec{r}}\, \frac{\alpha(\vec{k}^2)}{\vec{k}^2}. \tag{6.2}$$

In spherical coordinates, two of the integrals can be done analytically, the remaining one is performed numerically.

The resulting interaction potentials for the effective running couplings in Eq. (4.54) are displayed in the left diagram of Fig. 6.1 for the Maris-Tandy (MT) (4.55) and Qin-Chang (QC) (4.56) models. It is interesting to note, that the qualitative behaviour of both potentials follows the generic QCD form of a Coulomb term plus a linearly rising potential and includes a transition region to a constant long distance behaviour. Furthermore, in the right diagram of Fig. 6.1 we show that the ultraviolet logarithmic part of the effective running coupling is responsible for the short distance Coulomb type behaviour of the potentials, whereas the infrared exponential parts of the effective running couplings generate the non-trivial parts at intermediate distances.

In order to discuss the physics of these potentials, it is instructive to compare our results to the ones of Ref. [250], where a corresponding potential has been extracted from a quenched lattice gluon propagator (see their Fig. 2). The short distance behaviour in both approaches is generated by the perturbative one-gluon exchange modified with logarithmic corrections of the gluon (Ref. [250]) or the gluon combined with logarithmic corrections of the quark-gluon vertex (our potential). Both types of corrections do not modify the Coulomb part substantially, as expected. The large distance behaviour of both approaches, in particular when compared to our potential from the MT interaction, is also very similar. The underlying reason in both cases is that the dressing function of the gluon (Ref. [250]) as well as the effective running coupling (in our case) vanish at zero momentum. Consequently, the long range potential in both cases goes to zero. It has been noted in Ref. [250] that the physics of a long distance linear behaviour of the potential associated with confinement in pure Yang-Mills theory and the phenomenon of string breaking in QCD are not included in the simple one-gluon exchange picture. This is also true for our approach; the simple models for the effective running coupling as well as the severe truncations applied to the quark-gluon vertex in the rainbow-ladder truncation do not include this type of physics. Note, however, that in principle the combination of non-perturbative dressings of gluon and quark-gluon vertices in a fully non-perturbative calculation of the quark-antiquark potential may show these effects, as argued in Refs. [146, 152]. The dressing functions may conspire to generate an overall $1/k^4$-term, which suffices to create an asymptotic linearly rising part in the potential [251].

A significant difference between our potential and the one of Ref. [250] is the appearance of an approximately linearly rising part at intermediate distances for the potential from the Maris-Tandy model. Using the Cornell parametrization (2.19) with constant string tension, we obtain a good fit of our numerical data with $\alpha_S = 0.162$ for the strong coupling parameter, a string tension of $\sigma = 0.890\,\mathrm{GeV}^2$ and a constant offset of $V_0 = -4.84\,\mathrm{GeV}$. This is shown as "Cornell-type fit" in Fig. 6.1. The appearance of an almost linear region at intermediate distances has interesting implications for meson spectroscopy, since it could be a possible explanation for the appearance of (approximate) Regge trajectories in the calculated spectra. We will come back to this point in section 6.4. Also note, that the potential obtained from the Qin-Chang model shows a slight bend in the nearly linear region. Changing the linear term in our fit to be of the form $\sigma_0 r^n$ and using n as an additional fitting parameter, the fit prefers a clear deviation from linear behaviour with $n = 1.32$. For the MT potential, the best fit for n only deviates from 1 on the order of roughly $2\,\%$. It is thus not clear whether the QC model is similarly supportive of Regge behaviour as the MT model. This will also be discussed below.

We wish to emphasize that the potentials calculated in this section are for illustrational purposes only, and we do not use them to calculate mesonic properties. Instead, as described in chapters 3 and 4, we solve the fully relativistic Dyson-

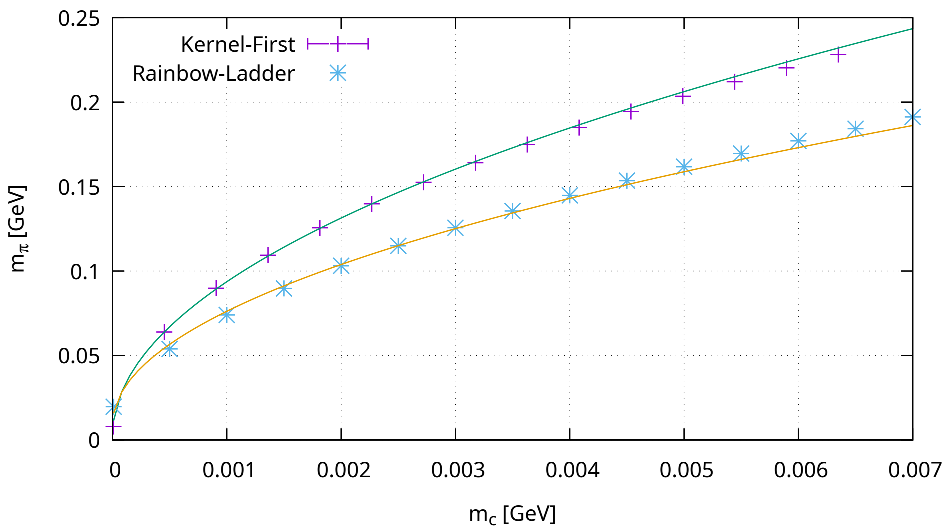

Figure 6.2.: Pion mass as a function of current quark mass calculated in rainbow-ladder and kernel-first truncations compared to the Gell-Mann-Oakes-Renner relation (2.43).

Schwinger and Bethe-Salpeter equations in momentum space and without recurse to any non-relativistic approximations.

6.2. Gell-Mann-Oakes-Renner relation

A critical test for any truncation, which is supposed to reproduce the effects of DχSB, is to numerically verify, whether the pion is indeed a Goldstone boson in the chiral limit and if the Gell-Mann-Oakes-Renner relation (2.43) can be reproduced. In order to test this, one simply needs to solve the BSE of the pion for varying current quark masses. The resulting pion masses can be fitted to a function of the form

$$m_\pi(m_c) = m_{\pi,0} + \alpha\sqrt{m_c}. \tag{6.3}$$

The resulting fits for the rainbow-ladder truncation with the Maris-Tandy effective interaction (4.55) and the kernel-first truncation are shown in Fig. 6.2, the corresponding fitting parameters are listed in Tab. 6.1. Note, that we used a rather narrow fitting window for m_c, since at larger values the curve is naturally going to deviate from a square-root like behaviour.

From the fits we can read of a few key features. Firstly, we see that the pion mass does in fact become vanishingly small at small current quark masses. Directly

Table 6.1.: Best fit parameters for fitting eq. (6.3) to the data presented in Fig. 6.2. All dimensional quantities are given in units of GeV and the given errors stem from fitting.

	Rainbow-ladder	Kernel-first
$m_{\pi,0}$	0.0094 ± 0.0018	0.0026 ± 0.0006
α	2.113 ± 0.040	2.878 ± 0.016

accessing the pion mass in the chiral limit is numerically very demanding, which is why we see a slight deviation from the expected result in the form of a finite fitted pion mass $m_{\pi,0}$. The numerical error is thus usually on the order of roughly 0.01 GeV, meaning the fitting error is negligible and the results are in agreement with a massless pion in the chiral limit. Secondly, we see that both truncations produce to a good approximation a square-root like behaviour of m_π as function of m_c. The concrete values of m_π are even similar between the two truncations. In particular, the physical pion mass of $m_\pi = 139\,\mathrm{MeV}$ is obtained at $m_c = 3.7\,\mathrm{MeV}$ in the rainbow-ladder truncation and at $m_c = 2.43\,\mathrm{MeV}$ in the kernel-first truncation. These values will be used henceforth to calculate physical meson properties. In a similar fashion, the value for the strange mass is obtained by fitting the pseudoscalar kaon ground state mass to its physical value of $m_K \approx 493.7\,\mathrm{MeV}$.

6.3. Pion decay constant

With the meson BSE solved and the BSA obtained and normalized, one can calculate the pion decay constant f_π by coupling its amplitude to an axialvector current of the form $\gamma_5 \not{P}$ [31, 230]

$$f_\pi = \frac{3Z_2}{P^2}\,\mathrm{tr}\int đ^4q\, i\gamma_5 \not{P} S(q_+)\Gamma_\pi(q,P)s(q_-). \tag{6.4}$$

Alternatively, one can use the fact, that in the chiral limit the dressing function of the scalar part of the inverse quark propagator $B(p^2)$ is proportional to the dressing function of the leading term of the pion BSA (4.31) with the proportionality constant being f_π [31][1]

$$E(p^2) = B(p^2)/f_\pi. \tag{6.5}$$

From this, one can derive an approximation for the pion decay constant, which only uses the quark propagator as input, known as the Pagels-Stokar relation [252]

[1]Since this relation is a very important consequence of DχSB, it is also derived analytically in Appendix B.1.

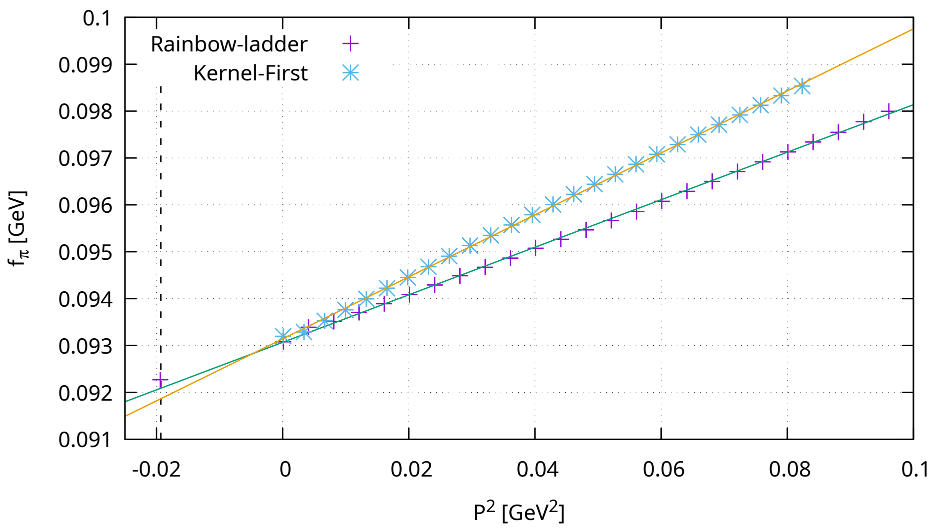

Figure 6.3.: Pion decay constant calculated off-shell and extrapolated linearly to the on-shell momentum in rainbow-ladder and kernel-first truncations. The dashed vertical line marks the on-shell momentum $P^2 = -m_\pi^2$.

Table 6.2.: Pion decay constant calculated directly, from extrapolation and via the Pagels-Stokar relation (6.6) in rainbow-ladder and kernel-first truncations.

	Pagels-Stokar	Direct calculation	Extrapolation
Rainbow-Ladder	0.0856	0.0923	0.0921 ± 0.0003
Kernel-First	0.0671	—	0.0919 ± 0.0003

$$f_\pi^2 = \frac{N_c}{(2\pi)^2} \int_0^\infty \mathrm{d}p^2\, p^2 \frac{M^2(p^2) - \frac{p^2}{2} M(p^2) M'(p^2)}{\left(p^2 + M^2(p^2)\right)^2}, \tag{6.6}$$

with $N_c = 3$. $M(p^2) = B(p^2)/A(p^2)$ is the effective mass function of the quark and $M'(p^2)$ is its derivative with respect to p^2.

The results for the pion decay constant obtained from direct calculation and the Pagels-Stokar formula within the rainbow-ladder truncation can be found in Tab. 6.2. One can see, that the direct calculation produces a value which matches the expected value of $f_\pi = 0.093\,\text{GeV}$ very well, while the Pagels-Stokar formula deviates from the direct calculation by roughly 8%.

Since we currently cannot access on-shell momenta in the BSE within the 3PI setup directly, we have to find another way to indirectly access the decay constant.

To do so, one can solve the BSE for off-shell momenta and use the normalized off-shell BSA to calculate f_π via eq. (6.4) and try to find a relation for $f_\pi(P^2)$. Doing so suggests, that a linear relation between f_π and P^2 is a good approximation, as can be seen in Fig. 6.3. By extrapolating a linear fit of the off-shell values for the decay constants to the pions mass pole, one can get an estimate of f_π.

Within the rainbow-ladder truncation, the extrapolated result matches the direct calculation near perfectly, while the kernel-first result lies only slightly below that, cf. Tab. 6.2. The Pagels-Stokar relation applied to the kernel-first truncation does not reproduce the decay constant well, predicting a value which is more than 27% lower than the extrapolated result.

To understand, why this is the case, one can use the fact, that eq. (6.4) is linear in Γ_π and thus can be decomposed into a sum of contributions from each tensor structure in Γ_π

$$f_\pi = \sum_{a=1}^{4} f_{\pi,a} \equiv \sum_{a\in\{E,F,G,H\}} f_{\pi,a}. \tag{6.7}$$

The results for the contributions of the dressing functions to f_π can be found in Fig. 6.4. The results within both the rainbow-ladder and kernel-first truncations follow a similar pattern; the leading contribution to f_π stems from the leading tensor structure in Γ_π, the second tensor structure has the second-largest contribution, the third tensor structure contributes with an opposite sign and the fourth tensor structure contributes only a small amount.

A key difference between the truncation schemes lies in the relative size of the contributions. Within the kernel-first truncation, the contribution of the second tensor structure $F(p^2)$ is much more prominent than within the rainbow-ladder truncation. The third and fourth tensor structures also contribute more within kernel-first, though not quite as much as the second. This difference in relative contribution to the total decay constant suggests, that employing eq. (6.5) outside the chiral limit is not a good approximation, which explains the discrepancy between the extrapolated result for f_π and the result obtained from the Pagels-Stokar formula (6.6).

6.4. Meson spectra

Numerical values for all results discussed throughout this section can be found explicitly in Tables C.7 through C.10 in Appendix C.8.

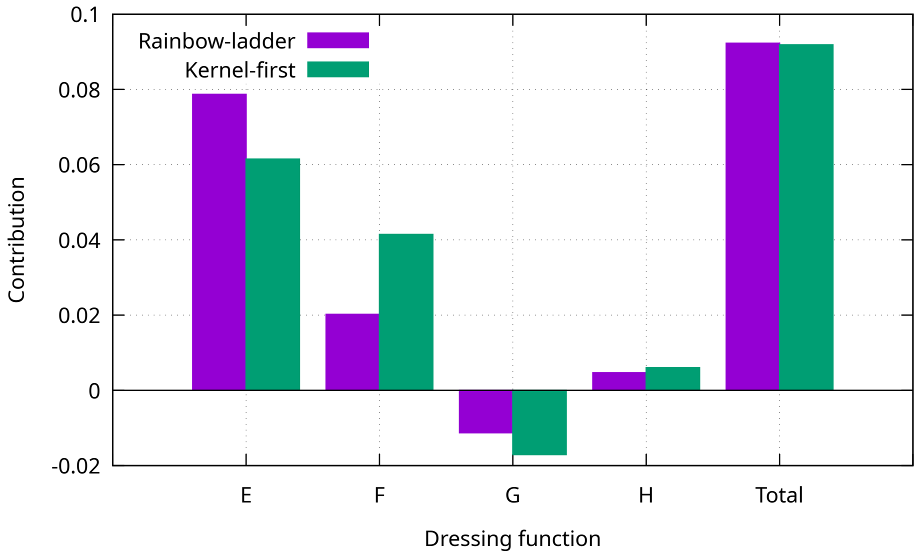

Figure 6.4.: Contributions from individual tensor structures to the pion decay constant in rainbow-ladder and kernel-first truncations.

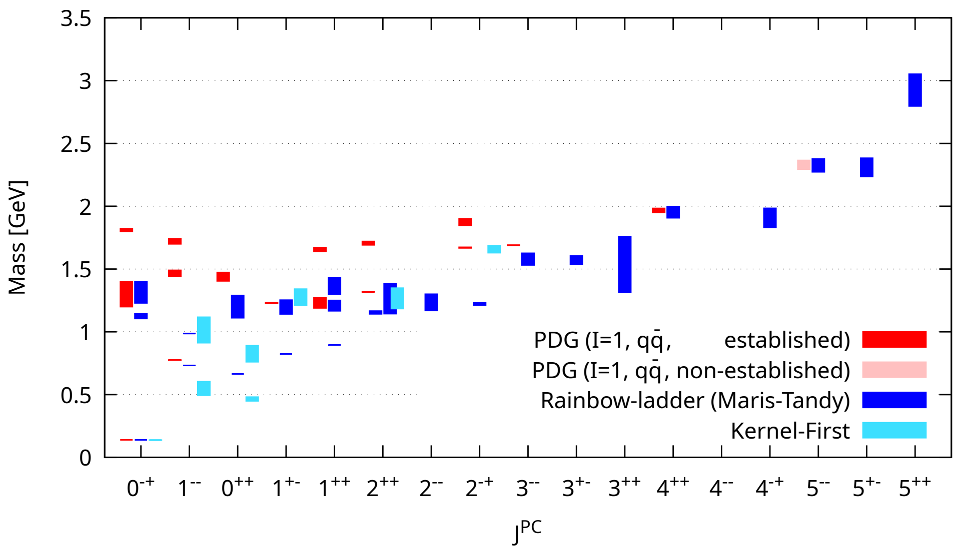

Figure 6.5.: Spectrum of $q\bar{q}$ states obtained from a rainbow-ladder truncation with the Maris-Tandy model and the kernel-first truncation compared to the experimental spectrum in the isovector channel [4].

6.4.1. Light mesons

The results for the spectrum of mesons composed of light quarks is shown in Fig. 6.5. The light meson rainbow-ladder spectrum has already been calculated up to $J = 3$ in previous work, see Refs. [253, 254] for details. Here, we reproduced those results and extended them up to $J = 5$ and focus our discussion on general aspects and in particular sequences including the new states with larger total angular momentum quantum numbers. Additionally, we will discuss some exploratory results obtained in the kernel-first truncation. Note, that these will be less complete and come with greater numerical uncertainty than the rainbow-ladder results due to the lack of access to the quark propagator and quark-gluon vertex for time-like momenta.

As described at the end of Section 6.2, the pion mass has been used as input to determine the light quark masses. The first non-trivial result is then the hyperfine splitting of pseudo-scalar and vector meson ground states, which comes out about right in rainbow-ladder [186]. In the kernel-first truncation, the calculated light vector meson ground state mass comes out too light compared to the $\rho(770)$. One potential explanation for this could be the comparatively low effective quark mass generated in our setup, see Section 5.2. While the effective quark mass can be increased by further rescaling the coupling in the quark-gluon vertex DSE, this would shift the scale of the theory too much and lead to an unphysical pion decay constant. In order to fully understand this discrepancy in the vector meson mass, a more complete treatment of the coupled Yang-Mills and quark sectors by unquenching the quark loops in the Yang-Mills sector is likely necessary [195]. Another possible reason might be the violation of the vecWTI seen in the kernel-first truncation, see Section 5.3 for details. Since the vector meson shares quantum numbers with the quark-photon vertex, a violation of the vecWTI might point at systematic issues of the truncation scheme in this particular channel.

The light scalar and axialvector channels are known to be not well represented in rainbow-ladder type kernels for different reasons. In the scalar channel, the ground state is not a conventional quark-antiquark state, but a four-quark state with a strong coupling to isoscalar $\pi\pi$ intermediate channels and only very small quark-antiquark contributions. This has been demonstrated by many approaches, see e.g. [7] for a review, but also in the DSE/BSE framework in a series of works [40, 187, 255–257]. Consequently, both the rainbow-ladder and kernel-first truncations predict a $q\bar{q}$ state around 400 $\sim$600 MeV. While initially this mass seems to match up well with the $f_0(500)$ state, a holistic treatment of the mesonic and tetraquark components of this state is required to produce meaningful results. In a similar vein, the mass region of 1 to 2 GeV in the scalar channel is where several calculations predict the lightest glueballs to appear [13, 14, 39, 258]. Thus, also the first excited state calculated in a $q\bar{q}$ picture in both rainbow-ladder and kernel-first truncations has to be taken with a grain of salt, since mixing effects between conventional mesons and glueballs might play a role for those states as well. The details behind this are still topic of ongoing research.

In the axialvector channel the rainbow-ladder masses for the ground state are too small, mainly due to the omission of the other tensor structures of the quark-gluon vertex. Previous research has shown, that their inclusion, improves the predictions of their masses [195, 259]. We observe the same behaviour in the kernel-first truncation, where the mass of the 1^{+-} ground state comes out about right. Unfortunately, no numerically stable result could be obtained in the 1^{++} channel.

For the other mesons with $J > 1$, no beyond rainbow-ladder calculations were available prior to this work. Comparing our results using the Maris-Tandy interaction with the available experimental data in these channels, it appears as if the sequence of ground states lying on the Regge trajectory with quantum numbers $J^{PC} = 1^{--}, 2^{++}, 3^{--}, 4^{++}, 5^{--}$ is in good agreement with experiment (with slight tensions in the 2^{++}-channel). This result has already been anticipated in Ref. [253] on the basis of states with $J \leq 3$. Our new result for the $J^{PC} = 4^{++}$ confirms this notion, and we predict a $J^{PC} = 5^{--}$ state in the mass region around 2325(52) MeV. This is in agreement with the $\rho_5(2350)$ state seen by [11], which still needs experimental confirmation though.

In contrast, states on the Regge trajectory with quantum numbers $J^{PC} = 1^{+\pm}, 2^{-\pm}, 3^{+\pm}, 4^{-\pm}, 5^{+\pm}$ are not well described within the rainbow-ladder truncation. We were able to compute two states with $J = 2$ within the kernel-first truncation, namely the 2^{++} and 2^{-+} ground states. The former matches the experimentally seen state even better than the rainbow-ladder result, being slightly more massive. The latter is a significant improvement from the rainbow-ladder result. While the rainbow-ladder result is about 400 MeV too light, the kernel-first result matches the experimentally seen $\pi_2(1670)$ state very well. This indicates further, that tensor structures beyond the rainbow-ladder truncation in the interaction kernel are mandatory to describe states with unnatural parity.

Another general aspect clearly visible in the spectrum is the poor description of radially excited states within the rainbow-ladder truncation. Previous work suggests, that going beyond the rainbow improves the situation drastically [259]. The limited amount of excited states in the light meson spectrum calculated in the kernel-first truncation makes it impossible to draw any conclusion on whether it is an improvement in that regard as well.

Finally, comparing results from the Maris-Tandy model with those obtained with the Qin-Chang interaction, see Tab. C.7, we find that both versions of the effective running coupling deliver qualitatively similar results with only slight advantages of MT in the 2^{++} tensor channel. Overall, the ground states in QC for larger quantum numbers are somewhat smaller in mass than the corresponding ones from the MT

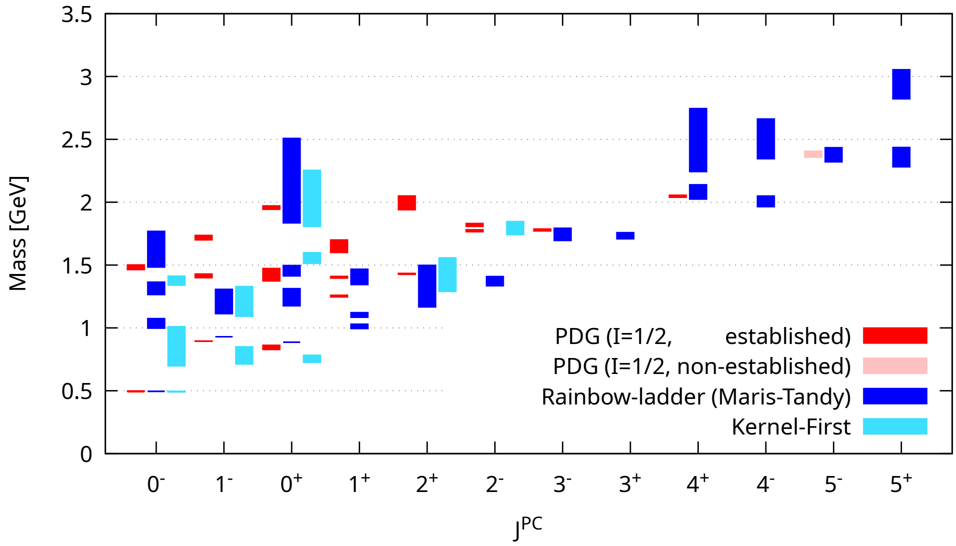

Figure 6.6.: Spectrum of states with one light and one strange (anti-)quark obtained from a rainbow-ladder truncation with the Maris-Tandy model and in the kernel-first truncation compared to the experimental kaon spectrum [4].

interaction. This effect may be understood by comparing the Fourier transforms of the effective running couplings, i.e. the interaction potentials depicted in Fig. 6.1. Higher mass states feel the (approximately) linearly rising parts of the potential. The QC potential is much broader which results in states that have a higher binding energy and thus lower masses compared to the MT potential. This interpretation has to be treated with care though, since the relativistic nature of light quarks in bound states makes interaction potential descriptions less applicable.

In our computations, we find that the MT coupling is numerically easier to handle. In fact, numerical problems with QC did prevent us from extracting a spectrum beyond $J = 2$. For rainbow-ladder, we therefore restrict ourselves to the MT interaction in the following.

6.4.2. Kaons

A qualitatively similar result to the one for the light mesons can be seen for the kaon spectrum in Fig. 6.6. Again, rainbow-ladder results for the ground states of the Regge trajectory[2] $J^P = 0^+, 1^-, 2^+, 3^-, 4^+, 5^-$ and the pseudoscalar ground state are in agreement with experiment (where experimental data are available), while other quantum numbers and excited states are not. Our new result 2082(57) MeV for the $J^{PC} = 4^{++}$ state agrees with the $K_4^*(2045)$ and we predict a $J^{PC} = 5^{--}$ state in the mass region around 2377(57) MeV. This is again in agreement with a not confirmed state seen in [10]. Notably, the kaonic state with quantum numbers $J^P = 0^+$ is described much better than the light quark state. This agreement may very well be accidental, since a corresponding four-quark state has already been identified as the ground state in this channel [187, 255, 256] with a mass corresponding to the experimental $K_0^*(700)$ shown in the plot. It is also possible that in the strange quark sector the mixing between two- and four-quark states is much stronger than in the light quark sector. This needs to be explored in future work.

The results for the kernel-first truncation in this channel mimic those in the light isovector channel. The vector kaon ground state comes out slightly too light, which we know is a problem of our current setup. However, the gap between the vector ground state and its first radial excitation is slightly larger than in rainbow-ladder, indicating, that in an improved setup the first excitation might come out right as well. In the scalar channel, we observe one less state in the mass region below 2 GeV than in rainbow-ladder, which brings the results to a 1-to-1 correspondence with experimentally seen states, albeit with the masses being slightly off. Additionally, we calculated two tensor kaons, one in the 2^+ and one in the 2^- channels, both in agreement with the experimental ground states of their respective channels.

6.4.3. $s\bar{s}$ spectrum

Numerical results for the $s\bar{s}$ spectrum are shown in Fig. 6.7. They look qualitatively similar to the light quark results. Here we do not compare to the experimental result for the η and η' mesons due to strong mixing in the pseudoscalar channel and the topological mass effect of the $U_A(1)$ anomaly which is not captured in the rainbow-ladder truncation.[3] In the other channels, mixing is much smaller and experimental states which are dominated by their $s\bar{s}$ component, such as the ϕ states, may be cleanly identified. Again, in the sequence $J^{PC} = 1^{--}, 2^{++}, 3^{--}, 4^{++}, 5^{--}$ the experimentally observed ground states are well reproduced within the rainbow-ladder truncation. Notably, the ground state in the 2^{++} channel is in better agreement with the experimentally seen but not confirmed $f_2(1430)$, see [260] among others, than with the confirmed $f_2'(1525)$ state. Since the $f_2(1430)$ has been observed in the D-wave of kaonic systems, it is reasonable to expect it to have a sizeable $s\bar{s}$ component. We further predict a state with $J^{PC} = 4^{++}$ at 2084(53) MeV and a state with $J^{PC} = 5^{--}$ in the mass region around 2418(64) MeV.

[2] Since $s\bar{q}$ states are not charge-conjugation eigenstates, the C-quantum number is not well-defined.

[3] For a way to include the anomaly in the DSE/BSE framework, [167] may be consulted.

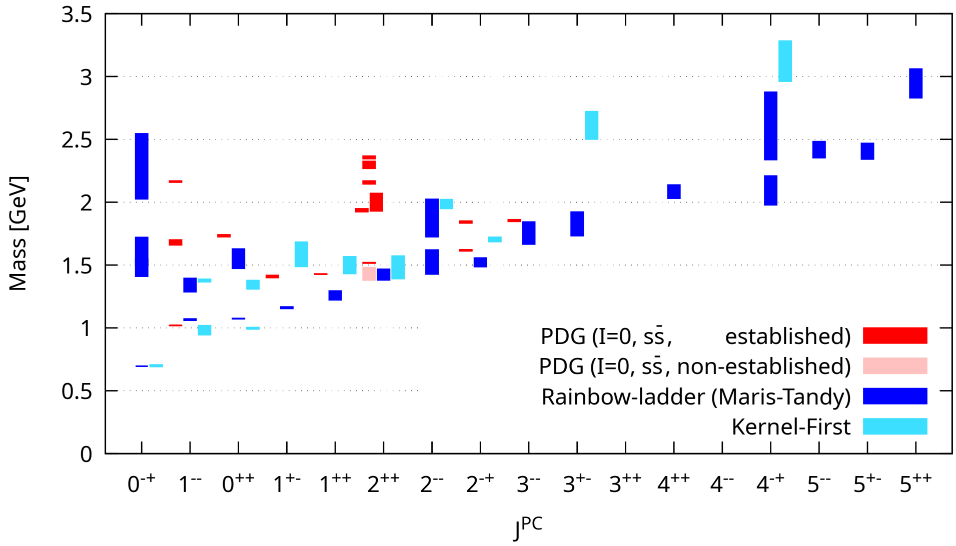

Figure 6.7.: Spectrum of $s\bar{s}$ states obtained from a rainbow-ladder truncation with the Maris-Tandy model and in the kernel-first truncation compared to the experimental spectrum of isoscalar states, which predominantly decay into strange mesons [4].

For the kernel-frist results in this spectrum, similar observations can be made as before. The pseudoscalar and vector ground states are in good agreement with rainbow-ladder and experiment. The gap between vector meson ground state and first radial excitation is again slightly larger than in rainbow-ladder, but still considerably smaller than in experiment. In the axialvector channel, the ground state masses are again enhanced compared to rainbow-ladder, with the 1^{++} state being in agreement with experiment and the 1^{+-} state coming out too heavy. The 2^{++} ground state is in agreement with the rainbow-ladder result, as well as both the $f_2(1430)$ and $f_2'(1525)$ states within our numerical uncertainty.

We also present results for ground states with quantum numbers $2^{-\pm}$, 3^{+-} and 4^{-+}. The 2^{-+} result is slightly heavier than the experimental ground state, similar to the axialvector channels. Overall, results in the light and strange meson spectrum have shown, that the kernel-first truncation produces better results for ground states with unnatural parity. Thus, we can treat our results for the 2^{--}, 3^{+-} and 4^{-+} channels as predictions with two caveats. The first is, that for $s\bar{s}$ states kernel-first produces slightly too massive states in other channels on that Regge trajectory. The second is, that we have no further results for $J \geq 3$ in the kernel-first truncation and can thus neither confirm nor refute whether our setup is well suited for treating states of such large angular momentum. The concrete

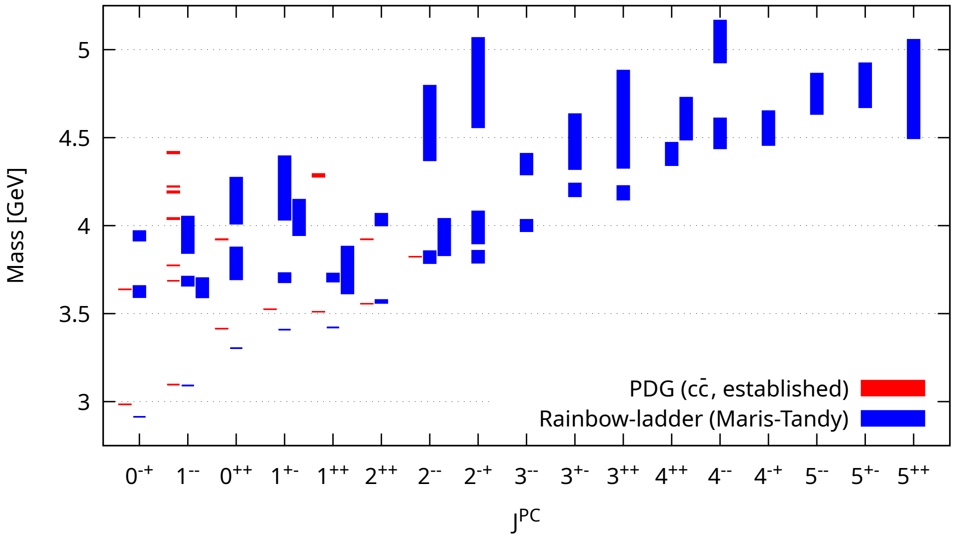

Figure 6.8.: Charmonium spectrum obtained from a rainbow-ladder truncation with the Maris-Tandy model and $\eta = 1.157$ compared to experimental data [4]. Note that potential tetraquark candidates such as the $\eta_{c1}(3872)$ are not included.

results for those channels are 1985(36) MeV for 2^{--}, 2611(110) MeV for 3^{+-} and 3122(160) MeV for the 4^{-+} channel.

6.4.4. Charmonium

Fig. 6.8 shows our results for the charmonium spectrum with the model parameter η fixed in Ref. [254]. For heavy quarks, i.e. charm and bottom, we need to evaluate the corresponding quark propagators deep in the time-like region which introduces additional numerical uncertainties. This also prevents us from calculating results in the heavy quark sector in the kernel-first truncation, since we currently do not have data for the quark-gluon vertex in the time-like region, see Section 3.5.3 for details. In turn, the momentum region where we can evaluate the Bethe-Salpeter equation safely does not exceed the lightest ground states and in general we have to extrapolate the eigenvalue of the Bethe-Salpeter matrix further towards larger masses. This leads to higher statistical uncertainties and larger error bars, see Appendices C.2 and C.1 for technical details. Nevertheless, we can again identify the same pattern as for the light and strange quark sector. In the Regge sequence $J^{PC} = 1^{--}, 2^{++}, 3^{--}, 4^{++}, 5^{--}$ the mass of the J/Ψ is used as input to fix our charm quark mass and the experimental mass of the $\chi_{c2}(1P)$ is well reproduced.

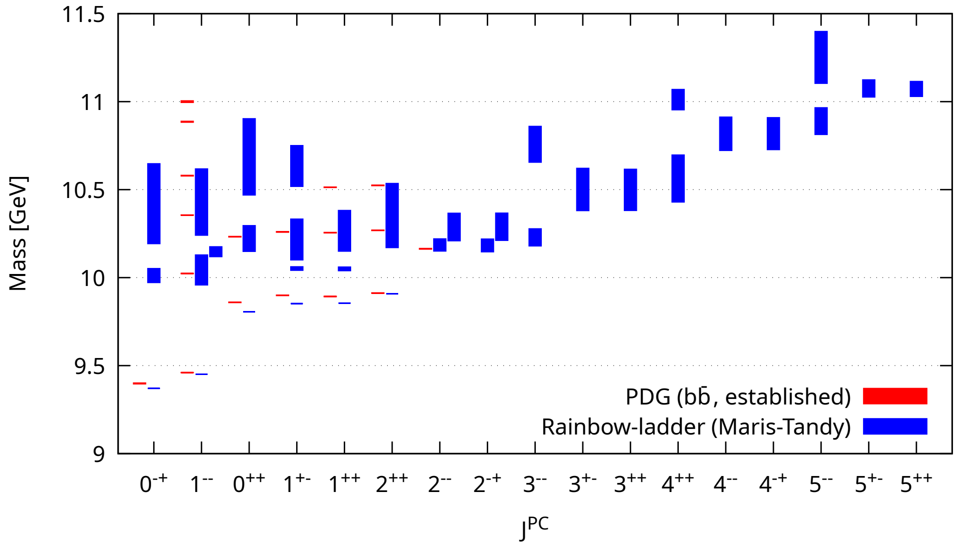

Figure 6.9.: Bottomonium spectrum obtained from a rainbow-ladder truncation with the Maris-Tandy model and $\eta = 1.357$ compared to experimental data [4].

We predict states with $J^{PC} = 3^{--}, 4^{++}, 5^{--}$ at 4001(33) MeV, 4407(64) MeV and 4749(115) MeV, respectively. Note that the PDG lists a $\psi_3(3842)$ state as potential 3^{--} candidate, with as yet unmeasured J^P, but reference to quark model predictions [4, 96]. Since our predicted mass for this state is much higher, this identification might be called into question.

6.4.5. Bottomonium

The same situation can be seen in the bottomonium spectrum, Fig. 6.9. In the Regge sequence $J^{PC} = 1^{--}, 2^{++}, 3^{--}, 4^{++}, 5^{--}$ the mass of the $\Upsilon(1S)$ is used as input to fix the bottom quark mass and the experimental mass of the $\chi_{b2}(1P)$ is well reproduced with our choice of model parameter η. Based on this identification, we predict states with $J^{PC} = 3^{--}, 4^{++}, 5^{--}$ at 10 229(48) MeV, 10 563(133) MeV and 10 889(75) MeV, respectively.

In general, when comparing results for the light, hidden strange, hidden charm and hidden bottom meson spectra, see Figs. 6.5, 6.7, 6.8, 6.9, it is notable that the rainbow-ladder results for channels not on this trajectory become better with heavier quark masses: As noted above, there are substantial discrepancies between our results and the experimental masses in the scalar and axialvector channels in the light and strange meson sector. In the charmonium energy region, this

	light	strange	charm	bottom
m_c	0.0037	0.085	0.83	3.79
η	1.8	1.8	1.157	1.357
Λ	0.72	0.72	0.72	0.72

Table 6.3.: Parameters used for rainbow-ladder calculations. All masses and the parameter Λ are given in units of GeV.

	$q\bar{q}$	$s\bar{q}$	$s\bar{s}$	$c\bar{c}$	$b\bar{b}$
M_0^2	-0.59 ± 0.06	-0.29 ± 0.03	-0.16 ± 0.18	6.35 ± 0.02	$82.466 \pm 9.8 \cdot 10^{-7}$
β	1.13 ± 0.06	1.15 ± 0.03	1.14 ± 0.07	3.20 ± 0.02	$7.501 \pm 6.3 \cdot 10^{-7}$

Table 6.4.: Parameters of Regge trajectories for $q\bar{q}$, $s\bar{q}$, $s\bar{s}$ and $c\bar{c}$ mesons with natural parity. All dimensional quantities are given in units of GeV, the errors stem from fitting only.

situation improves drastically and in the bottomonium region it improves further. The underlying reason is the suppression of dynamical effects in the quark-gluon vertex with quark mass, which becomes exact in the limit of infinite quark mass and entails dominance of the leading tensor structure $\Gamma_\mu \sim \gamma_\mu$ of the vertex. Since this is the (only) structure that is included in rainbow-ladder, truncations of this type improve in the heavy quark limit. In Coulomb gauge, this can even be shown analytically [261].

6.4.6. Regge trajectories

Compared to experiment, we obtain reasonable results in the rainbow-ladder truncation in channels on the natural Regge trajectories with quantum numbers $J^{PC} = 1^{--}, 2^{++}, 3^{--}, 4^{++}, 5^{--}$. Here, we collect these results and make a quantitative check for Regge behaviour. This is of particular interest in the light of the discussion in Section 6.1 on the linear part of the Maris-Tandy potential. The corresponding Chew-Frautschi plots are displayed in Fig. 6.10. For all of these plots, a linear fit of the form $M^2(J) = M_0^2 + \beta J$ has been performed. The resulting best fit parameters can be found in Tab. 6.4. The calculated masses are mostly in agreement with the linear fits within the numerical uncertainty.

While in the past similar results have been produced within the same framework [253], there was no obvious reason as to why Regge behaviour should arise from the truncation and the used effective running coupling. The emergence of a

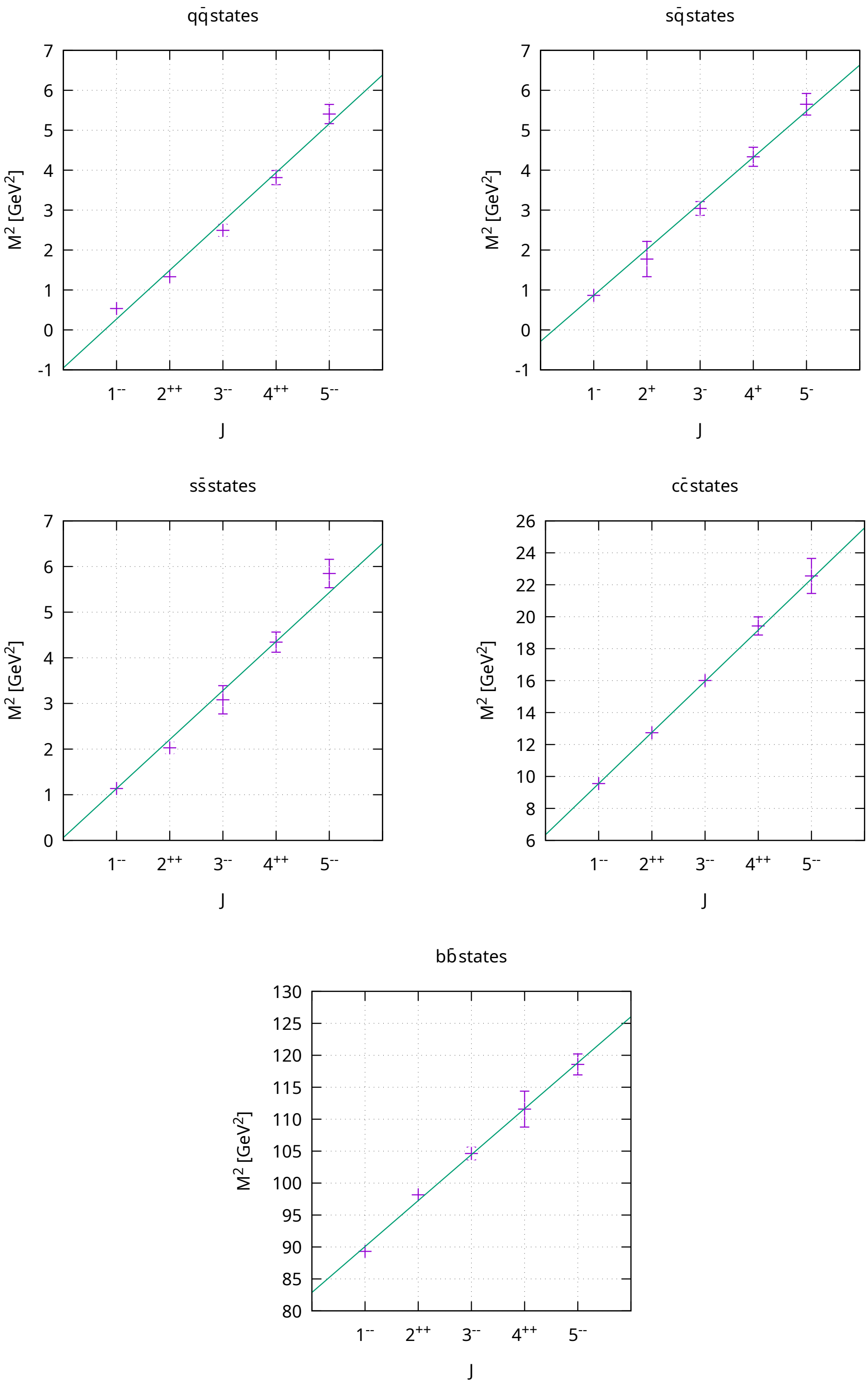

Figure 6.10.: Chew-Frautschi plots for different quark contents calculated in the rainbow-ladder truncation.

linearly rising term in the potential extracted from the running coupling provides some explanation of why Regge behaviour can be observed independent of quark flavour content. Notably, the heavy quark results are best described by a linear fit. This is in agreement with the notion that a non-relativistic description and an explanation in terms of an interaction potential should become valid only in the heavy quark sector.

Within the kernel-first truncation, we only have numerically reliable results for $J \leq 2$ except two states in the $s\bar{s}$ spectrum. Thus, it does not make much sense to talk about Regge behaviour for those states, since we lack the data to do a meaningful linear fit.

6.4.7. Exotic quantum numbers

Finally, we briefly want to touch on mesonic states with exotic quantum numbers. As mentioned in the motivation to this work in section 1.3, there are combinations of quantum numbers, which a non-relativistic constituent quark picture cannot produce, such as $J^{PC} = 1^{-+}$. In our fully relativistic functional framework, $q\bar{q}$ states with such quantum numbers can in principle exist, since the non-relativistic arguments are based on the notion of spin and orbital angular momentum, which are not good quantum numbers in a relativistic picture.

In section 4.2.6 we explained, how the symmetry properties of the mesonic Bethe-Salpeter amplitude relate to the charge-parity quantum number. Since we compute the full angular dependence of the amplitude in our calculations, we can also extract masses for $q\bar{q}$ states with exotic quantum numbers. Their eigenvalues and eigenfunctions naturally appear in our spectrum, and we can find them by searching for states with odd Chebyshev polynomial contributions to their wavefunctions.

Since there is only one experimentally confirmed state, with exotic quantum numbers, being the $\pi_1(1600)$ with quantum numbers $J^{PC} = 1^{-+}$, this state is the best way to gauge the usefulness of our $q\bar{q}$ approach to these quantum numbers.

In the rainbow-ladder truncation, the lowest lying state with quantum numbers 1^{-+} has a mass of 999 MeV, which is far too light compared to the $\pi_1(1600)$. For the lightest state with $J^{PC} = 0^{--}$, the rainbow-ladder truncation predicts a mass of 857 MeV and for 0^{+-} a mass of 1033(3) MeV. Since the result for the 1^{-+} state is far away from any experimental state, the $q\bar{q}$ picture in the rainbow-ladder truncation does not seem like a promising tool to predict exotic meson masses.

Our calculations for mesons with exotic quantum numbers within the kernel-first truncation did not produce any results with acceptable numerical precision. However, no eigenvalue curves could be found, which correspond to the quantum numbers 1^{-+} and that could be reasonably extrapolated to a mass of below 1 GeV, indicating that if such solutions exist, their mass is most likely bigger than the rainbow-ladder solutions. This is in agreement with a previous studies beyond the rainbow-ladder truncation, which found states with $J^{PC} = 1^{-+}$ to lie well above 1 GeV [45, 195].

7. Concluding remarks

In this work, we talked about meson spectroscopy and the structure of the strong interaction described by the theory of quantum chromodynamics (QCD) in the framework of functional methods. We introduced the main tools used throughout this work, namely the Dyson-Schwinger and Bethe-Salpeter equations and the nPI effective action formalism. We discussed the infinite nature of the resulting coupled equations of motion for Green's functions of the theory and discussed two truncation schemes in detail, namely the rainbow-ladder and kernel-first truncations. We explicitly verified numerically, that both satisfy the axialvector Ward-Takahashi identity and thus correctly produce the consequences of spontaneous chiral symmetry breaking. We have also seen, that the rainbow-ladder truncation does satisfy the vector Ward-Takahashi identity, while the kernel-first truncation, in the form we used it, violates it. We presented preliminary results for the quark propagator and quark-gluon vertex obtained from the 3PI effective action of QCD to three loop order with a kernel-first truncation. We used these as input for calculations of meson spectra in the light, open and hidden strange flavour sectors of QCD.

Furthermore, we calculated spectra in the hidden charm and hidden bottom sectors of QCD within the rainbow-ladder truncation. The rainbow-ladder truncation was suggested to work well for a sequence of states on the Regge trajectory with quantum numbers $J^{PC} = 1^{--}, 2^{++}, 3^{--}, 4^{++}, 5^{--}$ in previous works [253, 254]. We confirm this notion in all cases where experimental results for the $J^{PC} = 4^{++}$ channel are available and generate predictions for the ground state masses of states with $J^{PC} = 4^{++}, 5^{--}$ in all flavour sectors. In general, we also observe that the rainbow-ladder truncation gets better and better with increasing quark masses, confirming the notion of Ref. [261], although it uses a different gauge (Coulomb gauge) than the Landau gauge used in this work. We also verified, that we obtain straight lines in Chew-Frautschi plots on the "good" Regge trajectory. This behaviour may be tied to the specific momentum dependence of our interaction model which results in a linearly rising heavy-quark potential at intermediate distances. Let us emphasize again that this behaviour is accidental in the sense that the interaction model has not been chosen with this property in mind [31, 186, 231]. Nor does it in any intentional way reflect the underlying physics of an asymptotic string tension associated, e.g., with the physics of topologically non-trivial field configurations [142]. But it is, to our mind, a highly amusing property of an interaction model that has been successfully applied to many aspects of hadron physics in the past decades.

Finally, we have shown, that the kernel-first truncation leads to better agreement with experiment than the rainbow-ladder truncation for states with unnatural parity. In doing so we presented the - to our knowledge - first results for mesons with $J \geq 2$ beyond the rainbow-ladder truncation, including predictions for states with $J^{PC} = 2^{--}, 3^{+-}, 4^{-+}$ in the hidden strange sector. But, we have also shown, that the kernel-first truncation does still have problems producing certain results, such as the effective quark mass, the vector Ward-Takahashi identity and the light vector meson mass.

Nevertheless, we have shown where the strengths and limitations of the rainbow-ladder truncation within the meson sector of QCD lie. And we have shown that the kernel-first truncation is a promising tool to go beyond rainbow-ladder with potential improvements in many regards. Finally, it may be used to get a deeper understanding of the coupling between the Yang-Mills and quark sectors and of QCD interactions in hadrons in general.

A. Conventions

Throughout this thesis we mostly follow the conventions used in [241]. For completeness' sake we are going to quote some important ones here.

A.1. Euclidean conventions

In all the calculations in this thesis Euclidean conventions are applied, which means that the used metric is given by

$$\eta_{\mu\nu} = \eta_\mu{}^\nu = \eta^{\mu\nu} = \begin{pmatrix} 1 & 0 & 0 & 0 \\ 0 & 1 & 0 & 0 \\ 0 & 0 & 1 & 0 \\ 0 & 0 & 0 & 1 \end{pmatrix}. \tag{A.1}$$

With that, scalar products of four vectors can be written as

$$a \cdot b = \sum_{\mu=0}^{3} a_\mu b_\mu \equiv a_\mu b^\mu = a^\mu b_\mu. \tag{A.2}$$

Associated with the use of a Euclidean instead of a Minkowski metric the four momentum vector has been Wick rotated, such that

$$p^\mu := \begin{pmatrix} iE \\ \vec{p} \end{pmatrix}, \tag{A.3}$$

where $E = \sqrt{m^2 + |\vec{p}|^2}$ is the Energy and $\vec{p}$ is the three momentum vector. In this convention, a four vector $p \in \mathbb{C} \times \mathbb{R}^3$ is spacelike, if $p^2 > 0$. A free fermion propagator in this convention takes the form [262]

$$S_0(p) = (i\not{p} + m)^{-1}. \tag{A.4}$$

A.2. Gamma matrices

The gamma matrices γ_μ ($\mu \in \{0,1,2,3,5\}$), also sometimes called Dirac matrices, are a set of matrices, that obey a certain (anti-)commutator algebra. One possible representation of the matrices in Euclidean convention is via the Pauli matrices $\vec{\sigma}$:

$$\gamma_0 = \begin{pmatrix} \mathbb{1} & 0 \\ 0 & -\mathbb{1} \end{pmatrix}, \quad \gamma_j = \begin{pmatrix} 0 & -i\sigma_j \\ i\sigma_j & 0 \end{pmatrix}, \quad \gamma_5 = \begin{pmatrix} 0 & \mathbb{1} \\ \mathbb{1} & 0 \end{pmatrix}, \tag{A.5}$$

where $\mathbb{1} = \mathbb{1}_{2\times 2}$ and $j \in \{1,2,3\}$. In Euclidean metric the gamma matrices are hermitian

$$\gamma_\mu = (\gamma_\mu)^\dagger \tag{A.6}$$

and obey the anticommutator rules of a Clifford algebra

$$\{\gamma_\mu, \gamma_\nu\} = 2\delta_{\mu\nu}. \tag{A.7}$$

Helpful relations

In some derivations in this thesis traces of products of gamma matrices are evaluated. Therefore, the following relations for products and traces of gamma matrices are used frequently.

Products:

- $(\gamma_5)^2 = \mathbb{1}$
- $\{\gamma_\mu, \gamma_\nu\} = 2\delta_{\mu\nu}$
- $\gamma_j \gamma^j = 4 \cdot \mathbb{1}$
- $\gamma_\mu \gamma_\nu \gamma^\mu = -2\gamma_\nu$
- $\gamma_\mu \gamma_\nu \gamma_\rho \gamma^\mu = 4\delta_{\nu\rho} \cdot \mathbb{1}$
- $\gamma_\mu \gamma_\nu \gamma_\rho \gamma_\sigma \gamma^\mu = -2\gamma_\sigma \gamma_\rho \gamma_\nu$

Here again j and μ can take the value $\{1,2,3\}$ and $\{0,1,2,3\}$ respectively. Additionally, the anticommutator of γ_5 and every other gamma matrix vanishes.

Traces:

- $\mathrm{tr}(\gamma_\mu) = 0$
- $\mathrm{tr}(\gamma_\mu \gamma^\mu) = 16$
- $\mathrm{tr}(\gamma_\mu \gamma_\nu) = 4\delta_{\mu\nu}$
- $\mathrm{tr}(\gamma_\mu \gamma_\nu \gamma_\rho \gamma_\sigma) = 4(\delta_{\mu\nu}\delta_{\rho\sigma} + \delta_{\mu\sigma}\delta_{\nu\rho} - \delta_{\mu\rho}\delta_{\nu\sigma})$
- $\mathrm{tr}(\underbrace{\gamma_\alpha \gamma_\beta \ldots \gamma_\omega}_{\mathrm{odd}\#}) = 0$

A.2.1. Feynman slash notation

Another practical abbreviation is the so-called Feynman slash notation. It stands for a scalar product between a four vector and a four vector containing the gamma matrices γ_1 to γ_3,

$$\not{A} := \gamma_\mu A^\mu. \tag{A.8}$$

Due to the fact, that the gamma matrices' trace is zero, the trace of every slashed vector is zero as well,

$$\mathrm{tr}(\not{A}) = 0. \tag{A.9}$$

Since the gamma matrices form a Clifford algebra, see eq. (A.7), the product of two slashed vectors is the same as the scalar product of the vectors times a unity matrix

$$\not{A} \cdot \not{B} = (A \cdot B) \cdot \mathbb{1}_{4\times 4}. \tag{A.10}$$

Throughout this work, whenever objects with a Dirac structure, such as gamma matrices or slashed four vectors, appear next to each other in equations, a matrix product between them is implicitly performed. Whenever a matrix product between Dirac tensors which are not next to each other in an equation is to be performed, the Dirac indices are explicit written out in lower case Latin letters with repeated letters being summed over. For example in the expression

$$\gamma_{5,ab} K_{bc,de} \gamma_{5,cd} \tag{A.11}$$

the quantity K has four Dirac indices, the first of which is contracted with the latter Dirac index of the leftmost γ_5 matrix, while the second and third indices of K are contracted with the rightmost γ_5 matrix. The indices a and e only appear once and thus are not summed over.

A.3. Natural units

All equations and results in this thesis are calculated in a natural unit system. In this system we use the fact, that the speed of light c and the Planck constant $\hbar$ are finite value greater than zero, but the physics don't change qualitatively if they are exchanged for another value. So for convenience we set them to $\hbar = c = 1$. This also leads to the convenient situation that only powers of one unit, the unit of energy, are required to describe physical quantities. Some important examples for that are given in Tab. A.1. When converting back to SI units it is sufficient to multiply the value in natural units by a conversion factor, which is a power of $\hbar$ and c in SI units. For example to convert a distance r given in natural units to SI units, it needs to be multiplied by a factor of $\hbar c = 197.327\,\mathrm{MeVfm}$ to be given in units of femtometers.

Quantity	SI	N.u.	Conversion factor
Energy	J	eV^1	1
Momentum	$\mathrm{kg\,m\,s^{-1}}$	eV^1	c^{-1}
Mass	kg	eV^1	c^{-2}
Time	s	eV^{-1}	$\hbar$
Length	m	eV^{-1}	$\hbar c$
Energy density	$\mathrm{J\,m^{-3}}$	eV^4	$(\hbar c)^{-3}$

Table A.1.: Natural and SI units for some important quantities and the corresponding conversion factor f, such that $A_{\mathrm{SI}} = f A_{\mathrm{n.u.}}$

A.4. Hyperspherical coordinates

Throughout this thesis, there are several four-dimensional integrals to calculate. For convenience, they have been evaluated in hyperspherical coordinates, which are a generalization of three-dimensional spherical coordinates. A general, four-dimensional vector $x = (x_0, x_1, x_2, x_3)$ can be expressed as

$$x_0 = r\cos\psi \tag{A.12}$$

$$x_1 = r\sin\psi\cos\vartheta \tag{A.13}$$

$$x_2 = r\sin\psi\sin\vartheta\cos\varphi \tag{A.14}$$

$$x_3 = r\sin\psi\sin\vartheta\sin\varphi \tag{A.15}$$

Using this convention the Jacobi-determinant becomes

$$\mathrm{d}^4x = \mathrm{d}\varphi\,\mathrm{d}\vartheta\,\sin\vartheta\,\mathrm{d}\psi\,\sin^2\psi\,\mathrm{d}r\,r^3, \tag{A.16}$$

so that the integral of a function of x can be rewritten as

$$\int_{\mathbb{R}^4} \mathrm{d}^4x f(x) = \int_0^{2\pi} \mathrm{d}\varphi \int_0^{\pi} \mathrm{d}\vartheta \sin\vartheta \int_0^{\pi} \mathrm{d}\psi \sin^2\psi \int_0^{\infty} \mathrm{d}r r^3 f(r,\psi,\vartheta,\varphi). \tag{A.17}$$

Introducing the abbreviations, $y = \cos\vartheta$ and $z = \cos\psi$ we can express eq. (A.17) in terms of z and y

$$\int_{\mathbb{R}^4} f(x)\mathrm{d}^4x = \int_0^{2\pi} \mathrm{d}\varphi \int_{-1}^{1} \mathrm{d}y \int_{-1}^{1} \mathrm{d}z\sqrt{1-z^2} \int_0^{\infty} \mathrm{d}r r^3 f(r,z,y,\varphi). \tag{A.18}$$

Furthermore, most of the dressing functions appearing throughout this thesis typically depend only on a squared momentum p^2. It is thus convenient to further transform the integration variable from r to r^2. For a UV-regulated integral this means

$$\int_0^{\Lambda} \mathrm{d}r r^3 f(r) = \frac{1}{2}\int_0^{\Lambda^2} \mathrm{d}(r^2) r^2 f(r^2). \tag{A.19}$$

Additionally, most structure of the dressing functions lies in the infrared, i.e. momenta at or below 1 GeV. So, in order to improve the accuracy of our numerical integration, we can transform the integration variable to a logarithmic grid, enhancing the accuracy in the infrared. This results in an integral of the form

$$\frac{1}{2}\int_0^{\Lambda^2} \mathrm{d}(r^2) r^2 f(r^2) = \frac{1}{2}\int_0^{2\ln\Lambda} \mathrm{d}(\ln r)\, r^4 f(\ln r). \tag{A.20}$$

Lastly, when performing intergrals in momentum space we commonly use the shorthand notation

$$\int đ^n q\, f(q) \equiv \int \frac{\mathrm{d}^n q}{(2\pi)^n}\, f(q). \tag{A.21}$$

A.4.1. Scalar products

In the integrals appearing in the quark DSE and meson BSE a number of scalar products between different momenta appear. In practice, it is most convenient to choose the mesons restframe as frame of reference in the meson BSE. One can then rotate the frame in a way, that the relative momentum in the BSE only has two non-trivial components as well. This leads to the following explicit expressions for the momenta

$$P \propto (0,0,0,1) \tag{A.22}$$
$$p \propto (0,0,\sin\beta,\cos\beta) \tag{A.23}$$
$$q \propto (\sqrt{1-y^2}\sqrt{1-z^2}\cos\varphi, \sqrt{1-y^2}\sqrt{1-z^2}\sin\varphi, y\sqrt{1-z^2}, z), \tag{A.24}$$

where P is used to denote the total and p is the relative momentum of the meson. The variable q is the integration variable appearing in the integrals. z and y are the cosines of the angles ψ and ϑ respectively, defined analogously to eq. (A.18).

A.5. Quark propagator dressing functions

Throughout literature, several different notations are used for the dressing functions of the quark propagator. In this section we will not only restate the convention used within this work, but also show how it relates to other common notations.

In this work, we mostly use the convention where the two tensor structures of the inverse quark propagator are dressed independently with dressing functions labelled $A(p^2)$ and $B(p^2)$, i.e.

$$S^{-1}(p) = A(p^2)\cdot i\not{p} + B(p^2)\cdot \mathbb{1}. \tag{A.25}$$

Some older literature uses a similar convention, but with the letters A and B swapped [245]. Another common convention is to dress the inverse propagator with an effective mass function $M(p^2)$ and a wave function $Z_f(p^2)$[1]

$$S^{-1}(p) = Z^{-1}(p^2)\left(i\not{p} + M(p^2)\right). \tag{A.26}$$

One can convert between these two conventions via

$$\begin{aligned} Z_f(p^2) &= \frac{1}{A(p^2)}, \qquad & A(p^2) &= \frac{1}{Z_f(p^2)}, \\ M(p^2) &= \frac{B(p^2)}{A(p^2)}, \qquad & B(p^2) &= \frac{M(p^2)}{Z_f(p^2)}. \end{aligned} \tag{A.27}$$

[1] Ommitting the explicit $\mathbb{1}$.

Another approach is to dress the quark propagator itself instead of its inverse. The quark propagator also has a scalar and a vector tensor structure, which again can be dressed with their respective dressing functions

$$S(p) = \sigma_v(p^2) \cdot \big(-i\not{p}\big) + \sigma_s(p^2) \cdot \mathbb{1}. \tag{A.28}$$

In the previously mentioned conventions the quark propagator is dressed as

$$S(p) = \frac{A(p^2) \cdot (-i\not{p}) + B(p^2) \cdot \mathbb{1}}{A^2(p^2)p^2 + B^2(p^2)} = Z_f(p^2)\frac{-i\not{p} + M(p^2)}{p^2 + M^2(p^2)}, \tag{A.29}$$

which leads to the relations

$$\begin{aligned} \sigma_v(p^2) &= \frac{A(p^2)}{A^2(p^2)p^2 + B^2(p^2)} = \frac{Z_f(p^2)}{p^2 + M^2(p^2)} \\ \sigma_s(p^2) &= \frac{B(p^2)}{A^2(p^2)p^2 + B^2(p^2)} = \frac{Z_f(p^2)M(p^2)}{p^2 + M^2(p^2)}. \end{aligned} \tag{A.30}$$

B. Derivations

B.1. Chiral limit relations between dressing functions

In Section 6.3 we have used the fact, that in the chiral limit the scalar dressing function of the inverse quark propagator and the dressing function of the leading structure of the pion BSA are proportional to one another. We now want to derive that fact following the procedure outlined in [31, 241]. To begin with, recall the axWTI

$$P^\mu \Gamma_5^\mu(p,P) + 2m_c \Gamma_5(p,P) = S^{-1}(p_+) i\gamma_5 + i\gamma_5 S^{-1}(k_-). \tag{B.1}$$

We can again decompose the quark propagators appearing on the right-hand side into a scalar and a vector part. This leads to

$$P^\mu \Gamma_5^\mu(p,P) + 2m_c \Gamma_5(p,P) = i\gamma_5(B_+ + B_-) - (\not{p}_+ A_+ \gamma_5 + \gamma_5 \not{p}_- A_-). \tag{B.2}$$

Here we introduced the abbreviations $A_\pm = A(p_\pm^2)$ and $B_\pm = B(p_\pm^2)$. Furthermore, we can again use the anticommutator relation between gamma matrices and expand the shorthand notation $p_\pm = p \pm P/2$ to get

$$P^\mu \Gamma_5^\mu(p,P) + 2m_c \Gamma_5(p,P) = i\gamma_5(B_+ + B_-) + i\not{p}(A_- - A_+) - \frac{1}{2}\not{P}(A_+ + A_-). \tag{B.3}$$

We can evaluate this equation on-shell, where we can relate the axialvector amplitude to the pseudoscalar amplitude[1] via [45]

$$\Gamma_5^\mu(p,P) = P^\mu \frac{2if_\pi}{P^2 + m_\pi^2} \Gamma_\pi(p,P). \tag{B.4}$$

We can contract this equation with the total momentum P^μ to get

$$P_\mu \Gamma_5^\mu(p,P) = P^2 \frac{2if_\pi}{P^2 + m_\pi^2} \Gamma_\pi(p,P). \tag{B.5}$$

[1] Since the lightest pseudoscalar meson in nature is the pion, the subscript π is used to label pseudoscalar quantities.

Since the pion is a Goldstone boson in the chiral limit, evaluating this equation in the chiral limit yields

$$P_\mu \Gamma_5^\mu(p,0) = 2if_\pi \Gamma_\pi(p,0). \tag{B.6}$$

Since equation (B.3) still holds, we see that the pseudoscalar amplitude are related to the quark dressing functions via

$$2if_\pi \Gamma_\pi(p,0) = 2i\gamma_5 B(p^2). \tag{B.7}$$

Here we have already used to fact, that in the chiral limit $m_c = 0$ and $p_+ = p_- = p$. Furthermore, using the tensor basis (4.31), the only term in $\Gamma_\pi(p,0)$ that is not zero in the chiral limit is the leading tensor structure. Thus, the relation between $E(p^2)$ and $B(p^2)$ becomes

$$f_\pi \Gamma_\pi(p,0) = f_\pi \gamma^5 E(p,0) = \gamma^5 B(p^2). \tag{B.8}$$

By multiplying both sides with another γ_5 matrix, one obtains the wanted relation

$$E(p,0) = \frac{B(p^2)}{f_\pi}. \tag{B.9}$$

B.2. Derivation of the quark DSE

In this section, we sketch a derivation of the Dyson-Schwinger equation for the quark propagator using the method outlined in Section 3.1.3. Our goal is to obtain an expression for the functional derivative of the 1PI effective action as functional of N-point functions of QCD. As a starting point, we evaluate the functional derivative of the gauge-fixed classical action S, as it appears in the Master DSE (3.14)

$$\frac{\delta}{\delta\overline{\psi}_i(x)} S[A,\psi,\overline{\psi},c,\overline{c}] = \left(-\not{\partial} + m_i\right)\psi_i(x) + ig\gamma^\mu A_\mu(x)\psi_i(x). \tag{B.10}$$

We can insert this expression into equation (3.13) and evaluate the fields at the corresponding values to obtain

$$\begin{aligned}
\eta_i(x) &= \left(-\not{\partial} + m_i\right)\left(\frac{\delta W}{\delta\overline{\eta}_i(x)} + \frac{\delta}{\delta\overline{\eta}_i(x)}\right)\cdot 1 \\
&\quad + ig\gamma^\mu \left(\frac{\delta W}{\delta j^\mu(x)} + \frac{\delta}{\delta j^\mu(x)}\right)\left(\frac{\delta W}{\delta\overline{\eta}_i(x)} + \frac{\delta}{\delta\overline{\eta}_i(x)}\right)\cdot 1 \\
&= \left(-\not{\partial} + m_i\right)\frac{\delta W}{\delta\overline{\eta}_i(x)} + ig\gamma^\mu\left(\frac{\delta W}{\delta j^\mu(x)}\frac{\delta W}{\delta\overline{\eta}_i(x)} + \frac{\delta}{\delta j^\mu(x)}\frac{\delta W}{\delta\overline{\eta}_i(x)}\right).
\end{aligned} \tag{B.11}$$

We can furthermore apply a derivative with respect to $\eta_k(y)$ from the right[2] to this expression and set the sources to zero to get

$$\delta(x-y)\delta_{ik} = \left(-\not{\partial} + m_i\right) \frac{\delta}{\delta \overline{\eta}_i(x)} W \frac{\overleftarrow{\delta}}{\delta \eta_k(y)} + ig\gamma^\mu \frac{\delta}{\delta j^\mu(x)} \frac{\delta}{\delta \overline{\eta}_i(x)} W \frac{\overleftarrow{\delta}}{\delta \eta_k(y)}. \quad \text{(B.12)}$$

Here, we already used the fact, that the term proportional to $((\delta W/\delta j^\mu)(\delta W/\delta \overline{\eta}_i))\overleftarrow{\delta}/\delta\eta_k$ vanishes for $J \to 0$ due to appearing one-point functions equating to zero [179]. Using the relation for the derivative of an inverse operator

$$\delta M^{-1}_{ik}(x,y) = -\int \mathrm{d}^4x' \int \mathrm{d}^4y' M^{-1}_{il}(x,x') \left(\delta M_{lr}(x',y')\right) M^{-1}_{rk}(y',y), \quad \text{(B.13)}$$

where summation over repeated neighbouring indices is implied, we can express the third functional derivative of W in terms of QCD N-point functions

$$\begin{aligned}
\frac{\delta}{\delta j^\mu(x)} \frac{\delta}{\delta \overline{\eta}_i(x)} W \frac{\overleftarrow{\delta}}{\delta \eta_k(y)} &= \int \mathrm{d}^4z \frac{\delta A^\nu(z)}{\delta j^\mu(x)} \frac{\delta}{\delta A^\nu(z)} \left(\frac{\delta}{\delta \psi_i(x)} \Gamma \frac{\overleftarrow{\delta}}{\delta \overline{\psi}_k(y)} \right)^{-1} \\
= -\iiint \frac{\delta^2 W}{\delta j^\mu \delta j^\nu} \left(\frac{\delta}{\delta \psi_i} \Gamma \frac{\overleftarrow{\delta}}{\delta \overline{\psi}_l} \right)^{-1} &\left(\frac{\delta}{\delta A^\nu} \frac{\delta}{\delta \psi_l} \Gamma \frac{\overleftarrow{\delta}}{\delta \overline{\psi}_r} \right) \left(\frac{\delta}{\delta \psi_r} \Gamma \frac{\overleftarrow{\delta}}{\delta \overline{\psi}_k} \right)^{-1} \quad \text{(B.14)} \\
= -\int \mathrm{d}^4z \int \mathrm{d}^4x' \int \mathrm{d}^4y' D^\mu\nu(x,z) S_{il}(x,x') &\Gamma^\nu_{\mathrm{qg},lr}(z,x',y') S_{rk}(y',y).
\end{aligned}$$

Some position arguments have been suppressed for better readability. Lastly, we multiply both sides of equation (B.12) by the inverse quark propagator S^{-1}, perform an integration over one of the position arguments and a summation over one flavour index and rename some indices and position arguments to obtain the quark DSE in position space

$$S^{-1}_{ik}(x,y) = S^{-1}_{0,ik}(x,y) + g^2 C_F \int \mathrm{d}^4x' \int \mathrm{d}^4y' \gamma^\nu S_{il}(x,y') D^{\mu\nu}(x,x') \Gamma^\mu_{\mathrm{qg},lk}(x',y',y), \quad \text{(B.15)}$$

with $S^{-1}_{0,ik}(x,y) = (-\not{\partial} + m_i)\delta(x-y)\delta_{ik}$ being the bare quark propagator. By performing a Fourier transformation and inserting renormalization constants, we end up with the quark DSE in momentum space (3.29).

[2]Since the quark fields are Grassmann-valued, their sources and the corresponding functional derivatives have to be as well. As a consequence, one has to take care about the order of operations to not make any sign errors.

C. Technical details

C.1. Extrapolation of eigenvalue curves

When solving the meson BSE, one needs to evaluate the quark propagator's dressing functions at momenta, see Fig. C.1

$$q_\pm^2 = q^2 + \frac{1}{4}P^2 \pm q \cdot P = |q|^2 - \frac{1}{4}m^2 \pm i|q|m\cos\psi, \tag{C.1}$$

where ψ is the angle between q and P. This expression is valid in the centre of mass frame of the meson, where one can write the total on-shell momentum of the meson as $P = (\vec{0}, i\,m)$ with $m \in \mathbb{R}$. This necessitates an evaluation of the quark propagator within a parabolic region in the complex plane. However, the rainbow-ladder truncation is known to produce complex conjugate poles and other non-analytic structures in the complex quark propagator [249]. This gives rise to a limit P_0^2 on how small P^2 can get for a direct evaluation of the Bethe-Salpeter matrix. For $P^2 < P_0^2$ we have to fit the eigenvalue curve of the Mother-matrix as a function $\lambda = \lambda(P^2)$ and extrapolate to the value of P^2 where the fitted function is equal to one.

An approach, which has proven to work quite well for this purpose, is to calculate a number of eigenvalues on a grid of different values of P^2 and fit a rational function to them via the Schlessinger method [263]. The idea behind this method is to write the rational function as a continued fraction

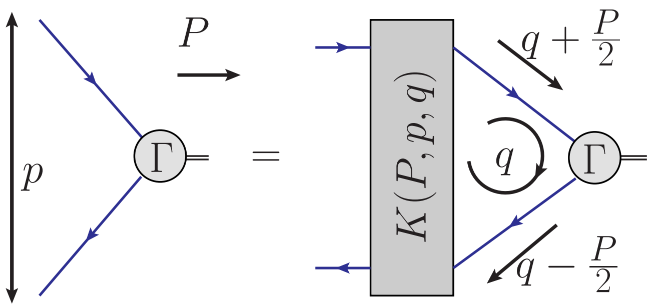

Figure C.1.: Momentum routing in the meson BSE. The total momentum P is split between the two internal quark legs.

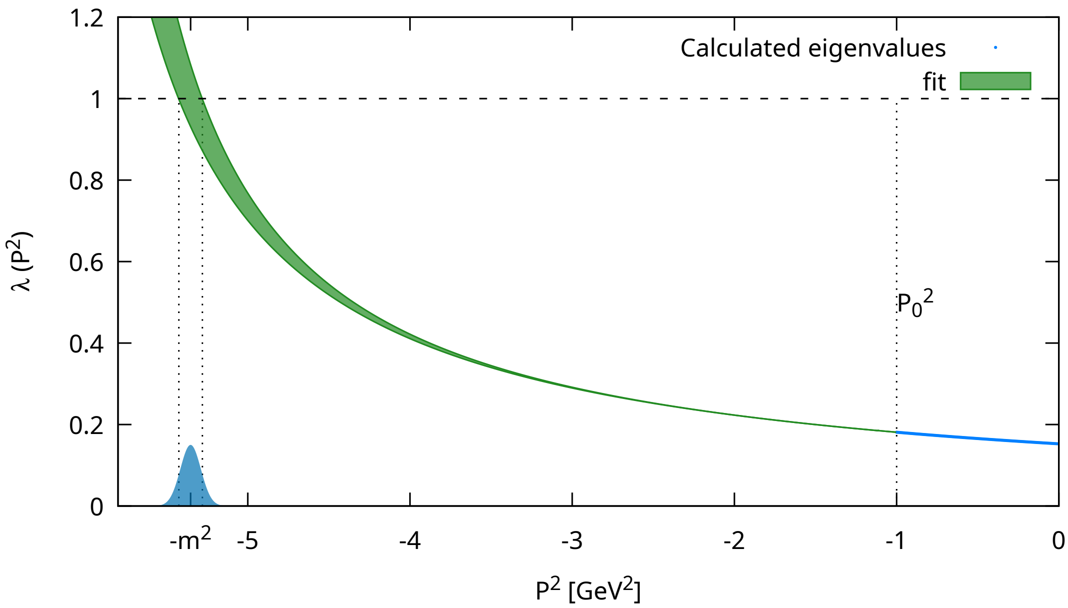

Figure C.2.: Extrapolation and resampling of an eigenvalue curve. The band of the fit represents a set of different fits.

$$C_N(x) = \frac{f_1}{1 + \frac{a_1(x-x_1)}{1+\frac{a_2(x-x_2)}{\vdots_{a_{N-1}(x-x_{N-1})}}}}, \tag{C.2}$$

where $x_1 \dots x_N \equiv P_1^2 \dots P_N^2$ are the points in the P^2 grid and $f_i = f(x_i) \equiv \lambda(P_i^2)$ are the explicitly calculated eigenvalues. The coefficients a_i can be calculated by initializing $a_1 = \frac{f_1/f_2 - 1}{x_2 - x_1}$ and then using the iterative formula

$$a_i = \frac{1}{x_i - x_{i+1}} \left(1 + \frac{a_{i-1}(x_{i+1} - x_{i-1})}{1 + \frac{a_{i-2}(x_{i+1}-x_{i-2})}{\vdots \frac{a_1(x_{i+1}-x_1)}{1-f_1/f_{i+1}}}} \right). \tag{C.3}$$

We estimate the numerical error introduced with this method via a resampling of the data points (x_i, f_i). This is done by taking a random subset of size $n < N$ of the original data and performing a Schlessinger fit on that subset to get an estimate of $P_j^2 = -m_j^2$ where $C_{n,j}(x_j \equiv P_j^2) = 1$. This sampling is repeated N_R times and the mean and standard deviation of the resulting set of values for $P^2 = -m^2$ are taken as the final result for the meson mass and its numerical error. This is sketched for a light meson with $J^{PC} = 5^{--}$ in Fig. C.2. This method is equivalent to a "delete d jackknife" procedure, where $d = N - n$. Using a bootstrapping method or even a n-out-of-N bootstrap is not possible here, since the grid points have to be distinct, as otherwise zeroes would appear in the denominators in the continued fractions.

C.2. Evaluating the quark propagator in the complex plane

As mentioned in the previous section, calculating on-shell properties of massive mesons requires the quark propagator to be evaluated at complex momenta inside a parabolic region of the form (C.1). While even in the rainbow-ladder truncation poles, branch cuts and other analytic structure of the quark propagator set a limit on how far one can venture into the complex plane, it is still possible to evaluate the quark propagator in the complex plane to a certain degree. The canonical way to parametrize the complex sampling region is in terms of two parameters q and z motivated by Eq. (C.1)

$$q_c^2 = q^2 - \frac{1}{4}M^2 + iqMz, \tag{C.4}$$

where q_c^2 is a complex squared momentum and M is a parameter, which determines how much of the complex plane gets sampled. The value of q is bounded above and below by the infrared and ultraviolet cutoffs and z is in the interval $(-1, 1)$. One then can choose how to route the complex momentum in the quark DSE. The easiest to implement way is to route it through the effective running coupling $\alpha(k^2)$

$$S(p_c) = S_0^{-1}(p_c) + C_f Z_2^2 4\pi \int đ^4 q\, \gamma^\mu S(q) \gamma_\perp^\mu \frac{\alpha((p_c - q)^2)}{(p_c - q)^2}. \tag{C.5}$$

The model running couplings used in this thesis, namely the Maris-Tandy and Qin-Chang models, Eqs. (4.55) and (4.56), do have lots of complex structure of their own and were not designed with complex momenta in mind. Thus, this way only allows evaluation in the complex plane for small values of M, such as $M \lesssim 1\,\text{GeV}$ for Maris-Tandy and even lower for Qin-Chang.

A better way to route the complex momentum, which we used for our Charmonium and Bottomonium calculations, is to route the complex momentum through the quark propagator appearing in the quark self-energy (4.52) and only evaluating the effective running coupling for real momenta

$$S(p_c) = S_0^{-1}(p_c) + C_f Z_2^2 4\pi \int đ^4 q\, \gamma^\mu S(p_c + q) \gamma_\perp^\mu \frac{\alpha(q^2)}{q^2}. \tag{C.6}$$

This removes the issues arising from the complex structure of the interaction models used. One can thus iterate the quark propagator using equation (C.6) inside the required region of the complex plane. The complex structure of the quark propagator remains problematic and still sets an upper limit, but this limit becomes larger for heavier quarks, allowing evaluation of the quark propagator much further into the complex plane for charm and bottom quarks.

Lastly, there is another way to parametrize the complex momenta other than Eq. (C.4). Instead, one can parametrize a complex squared momentum q_c^2 via two parameters k and Δ [40]

$$q_c^2 = k^2 - \Delta^2 + 2ik\Delta. \tag{C.7}$$

The parameter Δ labels parabolic momentum shells in the complex plane while k labels the points on those parabolas. One can then use the fact, that any point on a given momentum shell can be obtained using only information about momenta inside that shell [40]. This method is known as the shell-method and has successfully been used in the heavy quark sector before [40, 42, 264].

C.3. Level-crossing in eigenvalue curves

When evaluating the leading few eigenvalues of the Mother-matrix in the BSE as a function of total momentum squared, it can happen, that these eigenvalue curves have apparent intersections. In Hermitian matrices depending on k parameters, the von Neumann-Wigner theorem states, that level crossings can only appear on a manifold of dimension $k-2$ [216, 265]. As a result, if the Mother-matrix was Hermitian, no such intersections could appear, as it only depends on one parameter P^2.

An example of this can be seen in Fig. C.3. The left panel shows the largest three eigenvalues of the Mother-matrix in the $J^P = 2^+$ channel as a function of P^2 calculated within the rainbow-ladder truncation with the Maris-Tandy model with light constituent quarks. While the largest eigenvalue, which corresponds to the ground state of the system, as it crosses $\lambda(P^2) = 1$ for the smallest value of $m = \sqrt{-P^2}$, is smooth in the region of interest, the next two eigenvalue curves seem to be non-analytic at a critical momentum $P^2 = P_c^2 \approx -0.2\,\mathrm{GeV}^2$. Non-analytic points not only cause many numerical methods, like Newton's method for root finding or fits via the Schlessinger method, to fail or produce dubious results, but in some cases it can also lead to physically incorrect results. For instance, in the example shown in Fig. C.3, the eigenvectors corresponding to λ_1 and λ_2 swao their symmetry properties of their angular dependence and thus their charge-parity at the non-analytic point. Thus, it is evident, that a simple sorting of eigenvalues by size can lead to a wrong labelling of eigenvalue curves. Instead, a proper assignment

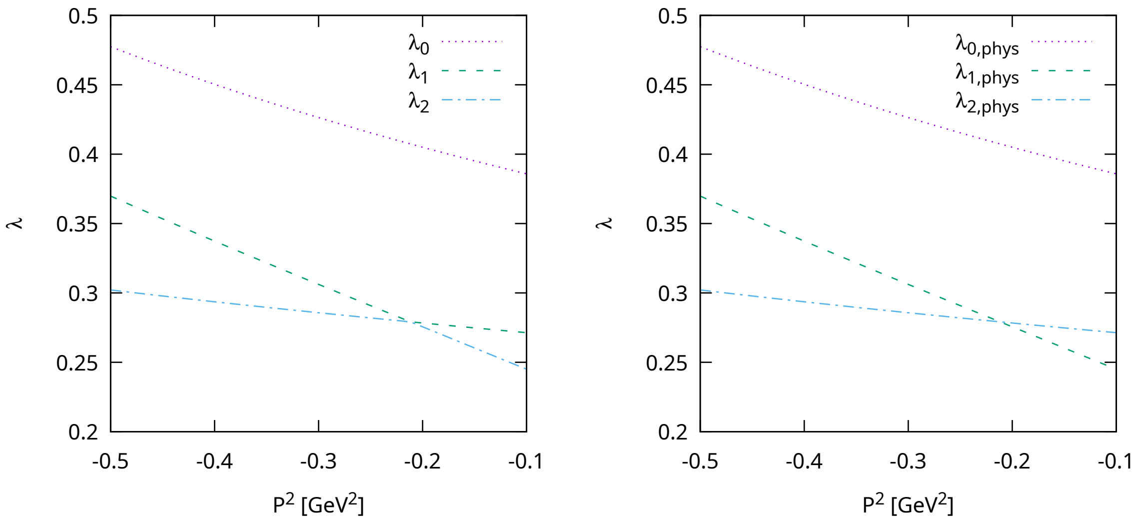

Figure C.3.: Left panel: Level crossing in the eigenvalue spectrum of the $J^P = 2^+$ channel in the rainbow-ladder truncation. Right panel: The corrected eigenvalue spectrum.

of eigenvalues to physical states would be according to the right panel in Fig. C.3 with the physical eigenvalue curves intersecting at P_c^2.

While in the aforementioned case one could identify such critical momenta P_c^2 by investigating the C-parity of the eigenvectors as a function of P^2, this method is not viable when searching for intersections between eigenvalue curves with equal C-parity. In order to derive a different method for finding and eliminating level crossings, consider the difference between λ_1 and λ_2. Since the eigenvalues are sorted by size in descending order by default, $\lambda_1(P^2) \geq \lambda_2(P^2)$ for all values of P^2. An intersection between them, i.e. a critical momentum with $\lambda_1(P_c^2) = \lambda_2(P_c^2)$, is therefore a zero of the function $\Delta\lambda(P^2) = \lambda_1(P^2) - \lambda_2(P^2)$. Due to the non-analytic nature of the eigenvalues, such a point would also be a minimum of $\Delta\lambda(P^2)$, with $\Delta\lambda(P^2)$ being not differentiable at P_c^2, which makes this almost impossible to find for most root finding algorithms.[1] We can use this property for our advantage though. To see how, consider the derivative of the function $\Delta\lambda(P^2)$

$$\Delta\lambda'(P^2) = \frac{\mathrm{d}}{\mathrm{d}P^2}\Delta\lambda(P^2) = \lim_{h\to 0}\frac{\Delta\lambda(P^2+h) - \Delta\lambda(P^2)}{h}. \tag{C.8}$$

At the critical momentum P_c^2, this function has a discontinuity, jumping from a

[1] In fact, the finite grid in P^2 used in the calculation and the precision of the plotting software used even make it difficult to properly visualize this behaviour.

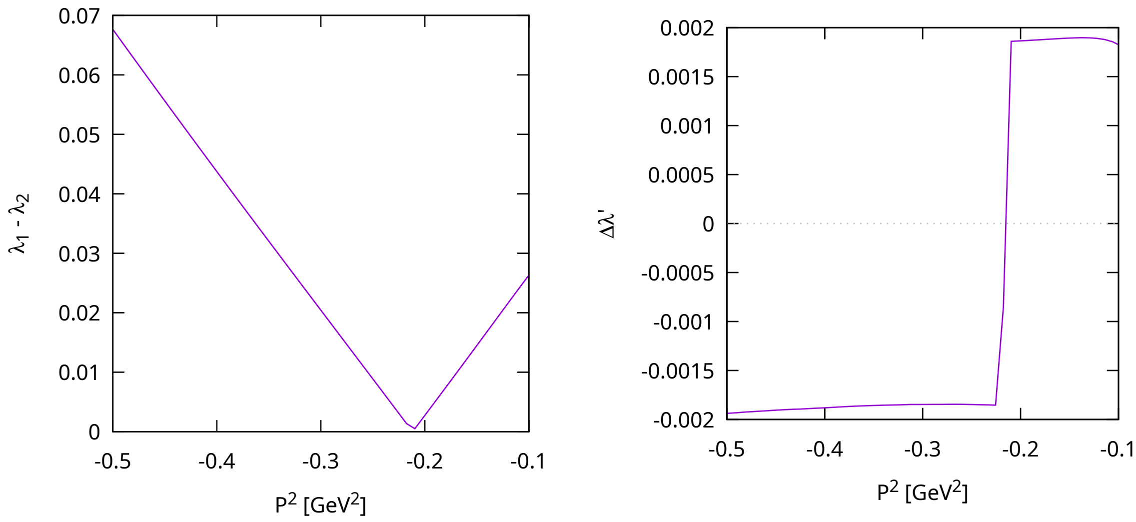

Figure C.4.: Left panel: Difference between two eigenvalues as a function of P^2. Right panel: Derivative of the difference shown in the left panel.

negative to a positive value, as can be seen in Fig. C.4. If we assume the spacing ΔP^2 of the momentum grid used to calculate the eigenvalue curves to be sufficiently small, we can approximate the derivative appearing in equation (C.8) as

$$\lim_{h\to 0} \frac{\Delta\lambda(P^2+h) - \Delta\lambda(P^2)}{h} \approx \frac{\Delta\lambda(P^2+\Delta P^2) - \Delta\lambda(P^2)}{\Delta P^2}. \tag{C.9}$$

Using the notation P_i^2 for the i-th discretized value of P^2, this further becomes.

$$\frac{\Delta\lambda(P^2+\Delta P^2) - \Delta\lambda(P^2)}{\Delta P^2} = \frac{\big(\lambda_1(P_{i+1}^2) - \lambda_2(P_{i+1}^2)\big) - (\lambda_1(P_i^2) - \lambda_2(P_i^2))}{\Delta P^2}. \tag{C.10}$$

Since we only look for a discontinuity and change of sign in $\Delta\lambda'$, we can furthermore focus on the numerator of this fraction

$$\lambda_1(P_{i+1}^2) - \lambda_2(P_{i+1}^2) - \lambda_1(P_i^2) + \lambda_2(P_i^2) \gtrless 0. \tag{C.11}$$

One can thus identify potential critical momenta by iterating over all momenta in the momentum grid, calculating the left-hand side of (C.11), and checking if the sign has flipped from the previous momentum. This criterion is not sufficient though. The derivative of the differences in eigenvalues can also cross zero if this difference is not monotonous. One thus needs to also check for at least one additional criterion for each candidate momentum. A possible additional criterion could be to check, if the zero crossing is continuous in nature or not. A continuous behaviour indicates a non-monotonous difference in eigenvalues, while a discontinuity indicates a crossing. Differentiating between a continuous zero crossing and a discontinuity can be difficult in practice though depending on how fine the grid in P^2 is. Alternatively, one can check, if the two eigenvalue curves are sufficiently close together, i.e.

$$\frac{\lambda_1(P^2) - \lambda_2(P^2)}{\lambda_1(P^2) + \lambda_2(P^2)} \ll 1. \tag{C.12}$$

By implementing at least one secondary check beyond (C.11), one can identify critical momenta quite reliably without checking every eigenvalue curve by hand. If a critical momentum has been identified, one can then reassign the eigenvalues to the corresponding states, resulting in what is depicted in the right panel in Fig. C.3.

C.4. Numerically solving the quark-photon vertex BSE

The quark-photon vertex $\Gamma_{q\gamma}$ satisfies an inhomogeneous Bethe-Salpeter equation

$$\Gamma^{\mu}_{q\gamma}(p,P) = Z_2 i\gamma^{\mu} + \int đ^4q\, K_{ab,cd}\,(q,p,P)\left[S\,(q_+)\,\Gamma^{\mu}_{q\gamma}\,(q,P)\,S\,(q_-)\right]_{bc}. \tag{C.13}$$

The integral in this equation has the exact same structure as the homogeneous BSE (4.16) for a meson with quantum numbers $J^{PC} = 1^{--}$. The appearance of the inhomogeneity demands a different numerical treatment than the eigenvalue method explained in Section 4.2.5 though. Instead, the equation has to be solved via iteration similarly to the quark DSE. The iteration method for the quark DSE is explained in section 3.4.

For the tensor basis of the quark-photon vertex one could in principle choose the Ball-Chiu base (4.46) with transverse part

$$\begin{aligned}
T_1^{\mu} &= P^2\gamma_{\perp}^{\mu}, & T_2^{\mu} &= P^2(p\cdot P)\frac{i}{2}\left[\gamma_{\perp}^{\mu}, \not{p}\right],\\
T_3^{\mu} &= \frac{i}{2}\left[\gamma^{\mu}, \not{P}\right], & T_4^{\mu} &= \frac{1}{6}\left[\gamma^{\mu}, \not{p}, \not{P}\right],\\
T_5^{\mu} &= iP^2 T_P^{\mu\nu} p^{\nu}, & T_6^{\mu} &= P^2 T_P^{\mu\nu} p^{\nu}\not{p},\\
T_7^{\mu} &= (p\cdot P)t_{Pp}^{\mu\nu}\gamma^{\nu}, & T_8^{\mu} &= t_{Pp}^{\mu\nu}\frac{i}{2}\left[\gamma^{\nu}, \not{p}\right].
\end{aligned} \tag{C.14}$$

In practice, it is computationally more efficient to work in an orthonormal base. For the transverse part, the same base as for the vector meson can be used, cf. Tab. C.2. For the longitudinal part, one can easily construct a base as well. Using the notation introduced in Sec. 4.2.4, it reads

$$\tau_9^\mu = \frac{1}{2}\hat{P}^\mu \mathbb{1}, \quad \tau_{10}^\mu = \frac{1}{2}\hat{P}^\mu \hat{\not{P}}, \quad \tau_{11}^\mu = \frac{1}{2}\hat{P}^\mu \not{n}, \quad \tau_{12}^\mu = \frac{1}{2}\hat{P}^\mu \hat{\not{P}}\not{n}. \tag{C.15}$$

Additionally, computations can be sped up by interweaving iteration steps of the quark-photon vertex itself with iteration steps of the vertex with external quark propagators attached

$$\Psi^\mu(p,P) = S(p_+)\Gamma^\mu_{q\gamma}(p,P)S(p_-). \tag{C.16}$$

For this quantity, we can employ the exact same orthonormal basis with another set of dressing functions b_i

$$\Psi^\mu(p,P) = \sum_{i=1}^{12} b_i(p,P) i\tau_i^\mu(p,P). \tag{C.17}$$

In this way, the BSE iteration can be split into a two-step process

$$\begin{aligned}\Gamma^\mu_{q\gamma}(p,P) &= Z_2 i\gamma^\mu + \int đ^4q\, K_{ab,cd}\,(q,p,P)\,\Psi^\mu_{bc}(q,P),\\ \Psi^\mu(p,P) &= S(p_+)\Gamma^\mu_{q\gamma}(p,P)S(p_-).\end{aligned} \tag{C.18}$$

This avoids the need to evaluate the quark propagators inside the momentum loop and thus saves some CPU time. If we now insert the tensor decomposition of the quark-photon vertex and project onto the dressing functions, we arrive at coupled equations for the dressing functions

$$\begin{aligned}a_i(p^2,z,P^2) &= Z_2 a_i^0 + \sum_{j=1}^{12}\int đ^4q\, \mathcal{K}_{ij}(q,p,P) b_j(q^2,z',P^2),\\ b_i(p^2,z,P^2) &= \sum_{j=1}^{12}\mathcal{G}_{ij}(p^2,z,P^2)a_j(p^2,z,P^2).\end{aligned} \tag{C.19}$$

The matrices $\mathcal{K}$ and $\mathcal{G}$ are the kernel and propagator matrices respectively and are given by

$$\begin{aligned}\mathcal{K}_{ij}(q,p,P) &= \mathrm{tr}\left(\overline{\tau}^\mu_{i,ab}(p,P)K_{bc,de}\tau^\mu_{j,cd}(q,P)\right),\\ \mathcal{G}_{ij}(p^2,z,P^2) &= \mathrm{tr}\left(\overline{\tau}^\mu_i S(p_+)\tau^\mu_j(p,P)S(p_-)\right).\end{aligned} \tag{C.20}$$

The advantage of the choice of orthonormal base is, that in this way the kernel and propagator matrices become block diagonal with the kernel matrix consisting of an 8×8 and a 4×4 block and the propagator matrix consisting of three 4×4

blocks. In the Ball-Chiu base the kernel matrix would be a complicated 12×12 matrix, requiring around 80 % more memory[2] and significantly more CPU time as well.

In Figs. C.5 through C.7 we show results for the transverse part of the quark-photon vertex in the Ball-Chiu base calculated in the rainbow-ladder and kernel-first truncations.

C.5. Axialvector WTI in the rainbow-ladder truncation

To verify, that the rainbow-ladder truncation indeed satisfies the axWTI, we start by plugging the expression (4.52) for $\Sigma(p)$ into the left-hand side of the axWTI of the form given in eq. (4.43). Ignoring factors, which both Σ and K have in common, such as C_f, Z_2^2 and 4π, the left-hand side now reads

$$\int đ^4q \; (\Delta_{\mu\nu}(p_+ - q)\gamma^\mu S(q)\gamma^\nu\gamma_5 + \Delta_{\mu\nu}(p_- - q)\gamma_5\gamma^\mu S(q)\gamma^\nu) \,. \tag{C.21}$$

Here we have introduced the abbreviation $\Delta_{\mu\nu}(p) = T_{\mu\nu}(p)\alpha(p)/p^2$. If we now plug the rainbow-ladder kernel (4.53) into the right-hand side of eq. (4.43), it reads

$$-\int đ^q \; \left(\Delta(p-q)\gamma^\mu\gamma^5 S(q_-)\gamma^\nu + \Delta(p-q)\gamma^\mu S(q_+)\gamma_5\gamma^\nu\right) . \tag{C.22}$$

Assuming, that all divergent integrals are regulated in a Lorentz invariant way, we can safely shift the integration variable on the right-hand side by a constant. In the first term of the integral we shift the integration variable by $q \to q + P/2$ and in the second term we shift it by $q \to q - P/2$. This leaves us with

$$-\int đ^4q \; \left(\Delta(p_- - q)\gamma^\mu\gamma^5 S(q)\gamma^\nu + \Delta(p_+ - q)\gamma^\mu S(q)\gamma_5\gamma^\nu\right) . \tag{C.23}$$

Since γ_5 anticommutes with all occurrences of γ^μ, we can change the order of each neighboring $\gamma^\mu\gamma_5$ pair at the cost of an additional minus sign. After doing this it is clear, that the left-hand side and the right-hand side of the equation are indeed equal. Therefore, the Rainbow-Ladder truncation does in fact satisfy the axWTI.

C.6. Transforming between different tensor bases

Throughout this thesis, we have used and referred to several different tensor bases for certain objects, like the quark-gluon and quark-photon vertices or meson Bethe-

[2]The exact numbers are of course implementation dependent.

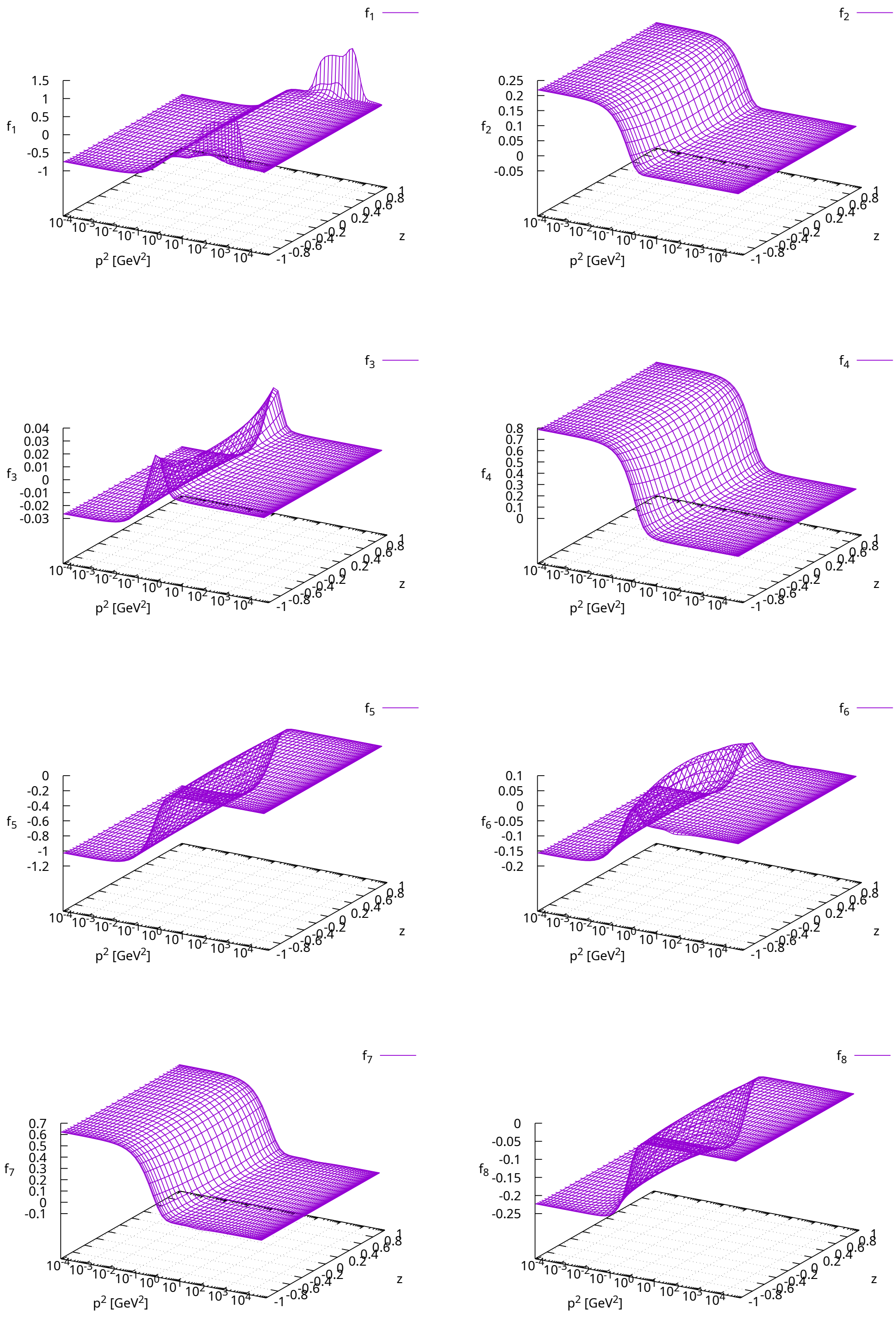

Figure C.5.: Dressing functions f_1 through f_8 of the transverse part of the quark-photon vertex calculated in the rainbow-ladder truncation.

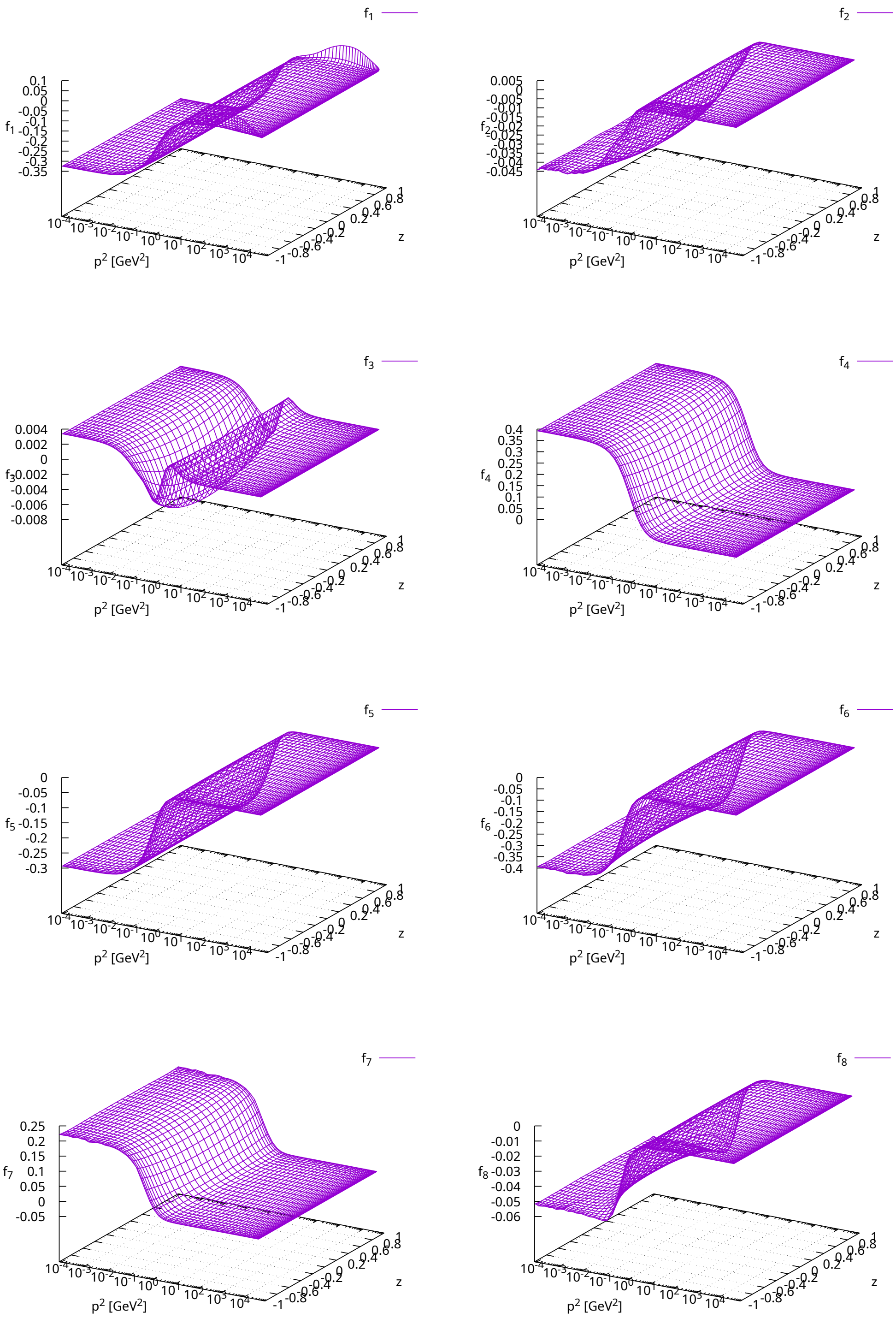

Figure C.6.: Dressing functions f_1 through f_8 of the transverse part of the quark-photon vertex calculated in the kernel-first truncation with A-equation (4.63).

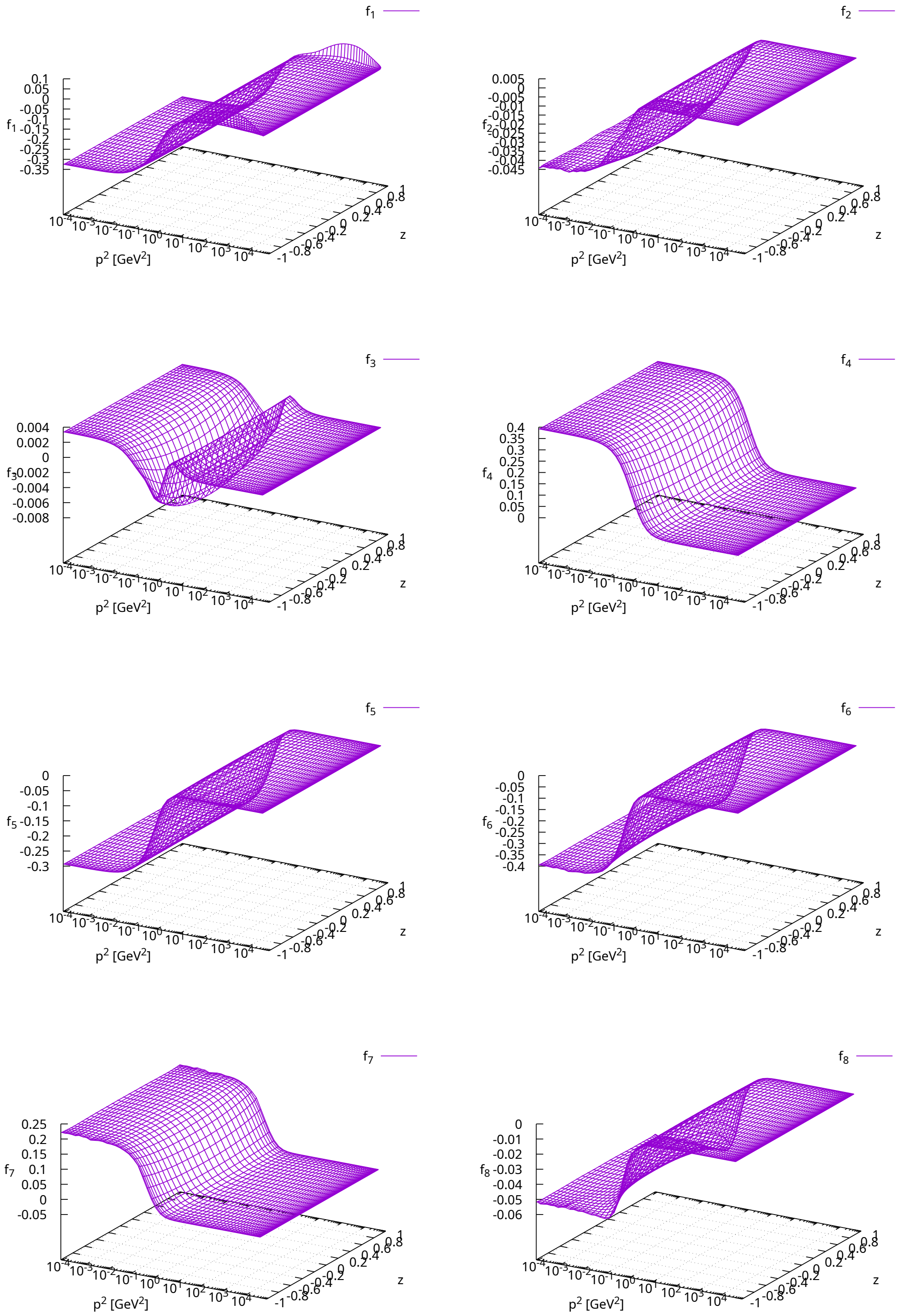

Figure C.7.: Dressing functions f_1 through f_8 of the transverse part of the quark-photon vertex calculated in the kernel-first truncation with A-equation (4.64).

Salpeter amplitudes. In order to compare results obtained in different bases, one must transform the results from one base to another. Assume we want to evaluate some quantity Γ, which has n tensor structures and can be expressed in two different sets of basis vectors $\{\tau_i\}$ and $\{\sigma_i\}$

$$\Gamma = \sum_{i=1}^{n} a_i \tau_i, \quad \Gamma = \sum_{i=1}^{n} b_i \sigma_i, \tag{C.24}$$

where a_i and b_i are the corresponding dressing functions. Since they span the same vector space, we can write each vector of one base as linear combination of the vectors of the other base

$$\tau_i = \sum_{i=1}^{n} M_{ij} \sigma_j. \tag{C.25}$$

The matrix M encodes the transformation between the bases and its elements can be obtained by multiplying Eq. (C.25) with the dual vector of the right-hand side base

$$\mathrm{tr}\left(\overline{\sigma}_k \sum_{i=1}^{n} M_{ij} \sigma_j\right) = \sum_{i=1}^{n} M_{ij} \delta_{kj} = M_{ik}. \tag{C.26}$$

Here, we used the identity $\mathrm{tr}(\overline{\sigma}_i \sigma_j) = \delta_{ij}$, where the trace over Dirac indices is performed. Since the total value of the quantity Γ in question is independent of the choice of representation, we can set both representations in Eq. (C.24) as equal and use relation (C.25) to obtain

$$\begin{gathered} \Gamma = \sum_{i=1}^{n} a_i \tau_i \stackrel{!}{=} \sum_{i=1}^{n} b_i \sigma_i = \Gamma \\ \sum_{i=1}^{n} a_i \sum_{j=1}^{n} \mathcal{M}_{ij} \sigma_j = \sum_{i=1}^{n} b_i \sigma_i \end{gathered} \tag{C.27}$$

After renaming the summation index on the right, one can easily see by comparison of coefficients, that the dressing functions follow the relation

$$b_i = \sum_{j=1}^{n} a_j \mathcal{M}_{ji} = \sum_{j=1}^{n} \mathcal{M}^T_{ij} a_j.$$

C.7. Explicit meson tensor bases

Using the procedure outlined in Section 4.2.4, one obtains the following explicit expressions for the tensor basis of mesons with $J \leq 5$. These results have already been published in [1].

i	τ_i	$\overline{\tau}_i$
1	$\frac{1}{2}\mathbb{1}$	τ_1
2	$\frac{1}{2}i\hat{\not{P}}$	$-\tau_2$
3	$\frac{1}{2}i\not{n}$	$-\tau_3$
4	$\frac{1}{2}i\hat{\not{P}}\not{n}$	τ_4

i	τ_i	$\overline{\tau}_i$
1	$\frac{1}{2}\gamma_5$	τ_1
2	$\frac{1}{2}\gamma_5\hat{\not{P}}$	$-\tau_2$
3	$\frac{1}{2}\gamma_5\not{n}$	$-\tau_3$
4	$\frac{1}{2}i\gamma_5\hat{\not{P}}\not{n}$	τ_4

Table C.1.: Tensor structures for mesons with quantum numbers (from left to right) $J^P = 0^+$, $J^P = 0^-$

i	τ_i	$\overline{\tau}_i$
1	$\frac{1}{2}i\mathbb{1}n^\mu$	$-\tau_1$
2	$\frac{1}{2}\hat{\not{P}}n^\mu$	τ_2
3	$\frac{1}{2}\not{n}n^\mu$	τ_3
4	$\frac{1}{2}\hat{\not{P}}\not{n}n^\mu$	$-\tau_4$
5	$\frac{\sqrt{2}}{4}\gamma^\mu_{\perp\perp}$	τ_5
6	$\frac{\sqrt{2}}{4}\hat{\not{P}}\gamma^\mu_{\perp\perp}$	$-\tau_6$
7	$\frac{\sqrt{2}}{4}\not{n}\gamma^\mu_{\perp\perp}$	$-\tau_7$
8	$\frac{\sqrt{2}}{4}i\hat{\not{P}}\not{n}\gamma^\mu_{\perp\perp}$	τ_8

i	τ_i	$\overline{\tau}_i$
1	$\frac{1}{2}\gamma_5 n^\mu$	τ_1
2	$\frac{1}{2}\gamma_5\hat{\not{P}}n^\mu$	$-\tau_2$
3	$\frac{1}{2}\gamma_5\not{n}n^\mu$	$-\tau_3$
4	$\frac{1}{2}i\gamma_5\hat{\not{P}}\not{n}n^\mu$	τ_4
5	$\frac{\sqrt{2}}{4}\gamma_5\gamma^\mu_{\perp\perp}$	$-\tau_5$
6	$\frac{\sqrt{2}}{4}i\gamma_5\hat{\not{P}}\gamma^\mu_{\perp\perp}$	τ_6
7	$\frac{\sqrt{2}}{4}i\gamma_5\not{n}\gamma^\mu_{\perp\perp}$	τ_7
8	$\frac{\sqrt{2}}{4}i\gamma_5\hat{\not{P}}\not{n}\gamma^\mu_{\perp\perp}$	$-\tau_8$

Table C.2.: Tensor structures for mesons with quantum numbers (from left to right) $J^P = 1^-$, $J^P = 1^+$

i	τ_i	$\overline{\tau}_i$	i	τ_i	$\overline{\tau}_i$
1	$\frac{\sqrt{6}}{4} i \mathbb{1} \left(n^\mu n^\nu - \frac{1}{3} T_P^{\mu\nu} \right)$	$-\tau_1$	1	$\frac{\sqrt{6}}{4} \gamma_5 \left(n^\mu n^\nu - \frac{1}{3} T_P^{\mu\nu} \right)$	τ_1
2	$\frac{\sqrt{6}}{4} \hat{\slashed{P}} \left(n^\mu n^\nu - \frac{1}{3} T_P^{\mu\nu} \right)$	τ_2	2	$\frac{\sqrt{6}}{4} \gamma_5 \hat{\slashed{P}} \left(n^\mu n^\nu - \frac{1}{3} T_P^{\mu\nu} \right)$	$-\tau_2$
3	$\frac{\sqrt{6}}{4} \slashed{n} \left(n^\mu n^\nu - \frac{1}{3} T_P^{\mu\nu} \right)$	τ_3	3	$\frac{\sqrt{6}}{4} \gamma_5 \slashed{n} \left(n^\mu n^\nu - \frac{1}{3} T_P^{\mu\nu} \right)$	$-\tau_3$
4	$\frac{\sqrt{6}}{4} \hat{\slashed{P}} \slashed{n} \left(n^\mu n^\nu - \frac{1}{3} T_P^{\mu\nu} \right)$	$-\tau_4$	4	$\frac{\sqrt{6}}{4} i \gamma_5 \hat{\slashed{P}} \slashed{n} \left(n^\mu n^\nu - \frac{1}{3} T_P^{\mu\nu} \right)$	τ_4
5	$\frac{1}{4} \left(\gamma_{\perp\perp}^\mu n^\nu + n^\mu \gamma_{\perp\perp}^\nu \right)$	τ_5	5	$\frac{1}{4} \gamma_5 \left(\gamma_{\perp\perp}^\mu n^\nu + n^\mu \gamma_{\perp\perp}^\nu \right)$	$-\tau_5$
6	$\frac{1}{4} \hat{\slashed{P}} \left(\gamma_{\perp\perp}^\mu n^\nu + n^\mu \gamma_{\perp\perp}^\nu \right)$	$-\tau_6$	6	$\frac{1}{4} i \gamma_5 \hat{\slashed{P}} \left(\gamma_{\perp\perp}^\mu n^\nu + n^\mu \gamma_{\perp\perp}^\nu \right)$	τ_6
7	$\frac{1}{4} \slashed{n} \left(\gamma_{\perp\perp}^\mu n^\nu + n^\mu \gamma_{\perp\perp}^\nu \right)$	$-\tau_7$	7	$\frac{1}{4} i \gamma_5 \slashed{n} \left(\gamma_{\perp\perp}^\mu n^\nu + n^\mu \gamma_{\perp\perp}^\nu \right)$	τ_7
8	$\frac{1}{4} i \hat{\slashed{P}} \slashed{n} \left(\gamma_{\perp\perp}^\mu n^\nu + n^\mu \gamma_{\perp\perp}^\nu \right)$	τ_8	8	$\frac{1}{4} i \gamma_5 \hat{\slashed{P}} \slashed{n} \left(\gamma_{\perp\perp}^\mu n^\nu + n^\mu \gamma_{\perp\perp}^\nu \right)$	$-\tau_8$

Table C.3.: Tensor structures for mesons with quantum numbers (from left to right) $J^P = 2^+$, $J^P = 2^-$

i	τ_i	$\overline{\tau}_i$	i	τ_i	$\overline{\tau}_i$
1	$\frac{\sqrt{10}}{4} i \mathbb{1} \left(n^\mu n^\nu n^\rho - \frac{1}{5} T_P^{[\mu\nu} n^{\rho]} \right)$	$-\tau_1$	1	$\frac{\sqrt{10}}{4} \gamma_5 \mathbb{1} \left(n^\mu n^\nu n^\rho - \frac{1}{5} T_P^{[\mu\nu} n^{\rho]} \right)$	τ_1
2	$\frac{\sqrt{10}}{4} \hat{\slashed{P}} \left(n^\mu n^\nu n^\rho - \frac{1}{5} T_P^{[\mu\nu} n^{\rho]} \right)$	τ_2	2	$\frac{\sqrt{10}}{4} \gamma_5 \hat{\slashed{P}} \left(n^\mu n^\nu n^\rho - \frac{1}{5} T_P^{[\mu\nu} n^{\rho]} \right)$	$-\tau_2$
3	$\frac{\sqrt{10}}{4} \slashed{n} \left(n^\mu n^\nu n^\rho - \frac{1}{5} T_P^{[\mu\nu} n^{\rho]} \right)$	τ_3	3	$\frac{\sqrt{10}}{4} \gamma_5 \slashed{n} \left(n^\mu n^\nu n^\rho - \frac{1}{5} T_P^{[\mu\nu} n^{\rho]} \right)$	$-\tau_3$
4	$\frac{\sqrt{10}}{4} \hat{\slashed{P}} \slashed{n} \left(n^\mu n^\nu n^\rho - \frac{1}{5} T_P^{[\mu\nu} n^{\rho]} \right)$	$-\tau_4$	4	$\frac{\sqrt{10}}{4} i \gamma_5 \hat{\slashed{P}} \slashed{n} \left(n^\mu n^\nu n^\rho - \frac{1}{5} T_P^{[\mu\nu} n^{\rho]} \right)$	τ_4
5	$\frac{\sqrt{30}}{24} \left(\gamma_{\perp\perp}^{[\mu} n^\nu n^{\rho]} - \frac{1}{5} \gamma_{\perp\perp}^{[\mu} T_P^{\nu\rho]} \right)$	τ_5	5	$\frac{\sqrt{30}}{24} \gamma_5 \left(\gamma_{\perp\perp}^{[\mu} n^\nu n^{\rho]} - \frac{1}{5} \gamma_{\perp\perp}^{[\mu} T_P^{\nu\rho]} \right)$	$-\tau_5$
6	$\frac{\sqrt{30}}{24} \hat{\slashed{P}} \left(\gamma_{\perp\perp}^{[\mu} n^\nu n^{\rho]} - \frac{1}{5} \gamma_{\perp\perp}^{[\mu} T_P^{\nu\rho]} \right)$	$-\tau_6$	6	$\frac{\sqrt{30}}{24} i \gamma_5 \hat{\slashed{P}} \left(\gamma_{\perp\perp}^{[\mu} n^\nu n^{\rho]} - \frac{1}{5} \gamma_{\perp\perp}^{[\mu} T_P^{\nu\rho]} \right)$	τ_6
7	$\frac{\sqrt{30}}{24} \slashed{n} \left(\gamma_{\perp\perp}^{[\mu} n^\nu n^{\rho]} - \frac{1}{5} \gamma_{\perp\perp}^{[\mu} T_P^{\nu\rho]} \right)$	$-\tau_7$	7	$\frac{\sqrt{30}}{24} i \gamma_5 \slashed{n} \left(\gamma_{\perp\perp}^{[\mu} n^\nu n^{\rho]} - \frac{1}{5} \gamma_{\perp\perp}^{[\mu} T_P^{\nu\rho]} \right)$	τ_7
8	$\frac{\sqrt{30}}{24} i \hat{\slashed{P}} \slashed{n} \left(\gamma_{\perp\perp}^{[\mu} n^\nu n^{\rho]} - \frac{1}{5} \gamma_{\perp\perp}^{[\mu} T_P^{\nu\rho]} \right)$	τ_8	8	$\frac{\sqrt{30}}{24} i \gamma_5 \hat{\slashed{P}} \slashed{n} \left(\gamma_{\perp\perp}^{[\mu} n^\nu n^{\rho]} - \frac{1}{5} \gamma_{\perp\perp}^{[\mu} T_P^{\nu\rho]} \right)$	$-\tau_8$

Table C.4.: Tensor structures for mesons with quantum numbers (from left to right) $J^P = 3^-$, $J^P = 3^+$

i	τ_i	$\overline{\tau}_i$
1	$\frac{\sqrt{70}}{8} i\mathbb{1}\left(n^\mu n^\nu n^\rho n^\sigma - \frac{1}{7}T_P^{[\mu\nu}n^\rho n^{\sigma]} + \frac{1}{35}T_P^{[\mu\nu}T_P^{\rho\sigma]}\right)$	$-\tau_1$
2	$\frac{\sqrt{70}}{8}\hat{\not{P}}\left(n^\mu n^\nu n^\rho n^\sigma - \frac{1}{7}T_P^{[\mu\nu}n^\rho n^{\sigma]} + \frac{1}{35}T_P^{[\mu\nu}T_P^{\rho\sigma]}\right)$	τ_2
3	$\frac{\sqrt{70}}{8}\not{n}\left(n^\mu n^\nu n^\rho n^\sigma - \frac{1}{7}T_P^{[\mu\nu}n^\rho n^{\sigma]} + \frac{1}{35}T_P^{[\mu\nu}T_P^{\rho\sigma]}\right)$	τ_3
4	$\frac{\sqrt{70}}{8}\hat{\not{P}}\not{n}\left(n^\mu n^\nu n^\rho n^\sigma - \frac{1}{7}T_P^{[\mu\nu}n^\rho n^{\sigma]} + \frac{1}{35}T_P^{[\mu\nu}T_P^{\rho\sigma]}\right)$	$-\tau_4$
5	$\frac{\sqrt{56}}{32}\left(\gamma_{\perp\perp}^{[\mu}n^\nu n^\rho n^{\sigma]} - \frac{1}{7}\gamma_{\perp\perp}^{[\mu}T_P^{\nu\rho}n^{\sigma]}\right)$	τ_5
6	$\frac{\sqrt{56}}{32}\hat{\not{P}}\left(\gamma_{\perp\perp}^{[\mu}n^\nu n^\rho n^{\sigma]} - \frac{1}{7}\gamma_{\perp\perp}^{[\mu}T_P^{\nu\rho}n^{\sigma]}\right)$	$-\tau_6$
7	$\frac{\sqrt{56}}{32}\not{n}\left(\gamma_{\perp\perp}^{[\mu}n^\nu n^\rho n^{\sigma]} - \frac{1}{7}\gamma_{\perp\perp}^{[\mu}T_P^{\nu\rho}n^{\sigma]}\right)$	$-\tau_7$
8	$\frac{\sqrt{56}}{32}i\hat{\not{P}}\not{n}\left(\gamma_{\perp\perp}^{[\mu}n^\nu n^\rho n^{\sigma]} - \frac{1}{7}\gamma_{\perp\perp}^{[\mu}T_P^{\nu\rho}n^{\sigma]}\right)$	τ_8

i	τ_i	$\overline{\tau}_i$
1	$\frac{\sqrt{70}}{8}\gamma_5\mathbb{1}\left(n^\mu n^\nu n^\rho n^\sigma - \frac{1}{7}T_P^{[\mu\nu}n^\rho n^{\sigma]} + \frac{1}{35}T_P^{[\mu\nu}T_P^{\rho\sigma]}\right)$	τ_1
2	$\frac{\sqrt{70}}{8}\gamma_5\hat{\not{P}}\left(n^\mu n^\nu n^\rho n^\sigma - \frac{1}{7}T_P^{[\mu\nu}n^\rho n^{\sigma]} + \frac{1}{35}T_P^{[\mu\nu}T_P^{\rho\sigma]}\right)$	$-\tau_2$
3	$\frac{\sqrt{70}}{8}\gamma_5\not{n}\left(n^\mu n^\nu n^\rho n^\sigma - \frac{1}{7}T_P^{[\mu\nu}n^\rho n^{\sigma]} + \frac{1}{35}T_P^{[\mu\nu}T_P^{\rho\sigma]}\right)$	$-\tau_3$
4	$\frac{\sqrt{70}}{8}i\gamma_5\hat{\not{P}}\not{n}\left(n^\mu n^\nu n^\rho n^\sigma - \frac{1}{7}T_P^{[\mu\nu}n^\rho n^{\sigma]} + \frac{1}{35}T_P^{[\mu\nu}T_P^{\rho\sigma]}\right)$	τ_4
5	$\frac{\sqrt{56}}{32}\gamma_5\left(\gamma_{\perp\perp}^{[\mu}n^\nu n^\rho n^{\sigma]} - \frac{1}{7}\gamma_{\perp\perp}^{[\mu}T_P^{\nu\rho}n^{\sigma]}\right)$	$-\tau_5$
6	$\frac{\sqrt{56}}{32}i\gamma_5\hat{\not{P}}\left(\gamma_{\perp\perp}^{[\mu}n^\nu n^\rho n^{\sigma]} - \frac{1}{7}\gamma_{\perp\perp}^{[\mu}T_P^{\nu\rho}n^{\sigma]}\right)$	τ_6
7	$\frac{\sqrt{56}}{32}i\gamma_5\not{n}\left(\gamma_{\perp\perp}^{[\mu}n^\nu n^\rho n^{\sigma]} - \frac{1}{7}\gamma_{\perp\perp}^{[\mu}T_P^{\nu\rho}n^{\sigma]}\right)$	τ_7
8	$\frac{\sqrt{56}}{32}i\gamma_5\hat{\not{P}}\not{n}\left(\gamma_{\perp\perp}^{[\mu}n^\nu n^\rho n^{\sigma]} - \frac{1}{7}\gamma_{\perp\perp}^{[\mu}T_P^{\nu\rho}n^{\sigma]}\right)$	$-\tau_8$

Table C.5.: Tensor structures for mesons with quantum numbers (from top to bottom) $J^P = 4^+$, $J^P = 4^-$

i	τ_i	$\overline{\tau}_i$
1	$\frac{3\sqrt{14}}{8} i\mathbb{1} \left(n^\mu n^\nu n^\rho n^\sigma n^\kappa - \frac{1}{9} T_P^{[\mu\nu} n^\rho n^\sigma n^{\kappa]} + \frac{1}{63} T_P^{[\mu\nu} T_P^{\rho\sigma} n^{\kappa]}\right)$	$-\tau_1$
2	$\frac{3\sqrt{14}}{8} \hat{\not{P}} \left(n^\mu n^\nu n^\rho n^\sigma n^\kappa - \frac{1}{9} T_P^{[\mu\nu} n^\rho n^\sigma n^{\kappa]} + \frac{1}{63} T_P^{[\mu\nu} T_P^{\rho\sigma} n^{\kappa]}\right)$	τ_2
3	$\frac{3\sqrt{14}}{8} \not{n} \left(n^\mu n^\nu n^\rho n^\sigma n^\kappa - \frac{1}{9} T_P^{[\mu\nu} n^\rho n^\sigma n^{\kappa]} + \frac{1}{63} T_P^{[\mu\nu} T_P^{\rho\sigma} n^{\kappa]}\right)$	τ_3
4	$\frac{3\sqrt{14}}{8} \hat{\not{P}}\not{n} \left(n^\mu n^\nu n^\rho n^\sigma n^\kappa - \frac{1}{9} T_P^{[\mu\nu} n^\rho n^\sigma n^{\kappa]} + \frac{1}{63} T_P^{[\mu\nu} T_P^{\rho\sigma} n^{\kappa]}\right)$	$-\tau_4$
5	$\frac{\sqrt{105}}{40} \left(\gamma_{\perp\perp}^{[\mu} n^\nu n^\rho n^\sigma n^{\kappa]} - \frac{1}{9} \gamma_{\perp\perp}^{[\mu} T_P^{\nu\rho} n^\sigma n^{\kappa]} + \frac{1}{63} \gamma_{\perp\perp}^{[\mu} T_P^{\nu\rho} T_P^{\sigma\kappa]}\right)$	τ_5
6	$\frac{\sqrt{105}}{40} \hat{\not{P}} \left(\gamma_{\perp\perp}^{[\mu} n^\nu n^\rho n^\sigma n^{\kappa]} - \frac{1}{9} \gamma_{\perp\perp}^{[\mu} T_P^{\nu\rho} n^\sigma n^{\kappa]} + \frac{1}{63} \gamma_{\perp\perp}^{[\mu} T_P^{\nu\rho} T_P^{\sigma\kappa]}\right)$	$-\tau_6$
7	$\frac{\sqrt{105}}{40} \not{n} \left(\gamma_{\perp\perp}^{[\mu} n^\nu n^\rho n^\sigma n^{\kappa]} - \frac{1}{9} \gamma_{\perp\perp}^{[\mu} T_P^{\nu\rho} n^\sigma n^{\kappa]} + \frac{1}{63} \gamma_{\perp\perp}^{[\mu} T_P^{\nu\rho} T_P^{\sigma\kappa]}\right)$	$-\tau_7$
8	$\frac{\sqrt{105}}{40} i\hat{\not{P}}\not{n} \left(\gamma_{\perp\perp}^{[\mu} n^\nu n^\rho n^\sigma n^{\kappa]} - \frac{1}{9} \gamma_{\perp\perp}^{[\mu} T_P^{\nu\rho} n^\sigma n^{\kappa]} + \frac{1}{63} \gamma_{\perp\perp}^{[\mu} T_P^{\nu\rho} T_P^{\sigma\kappa]}\right)$	τ_8

i	τ_i	$\overline{\tau}_i$
1	$\frac{3\sqrt{14}}{8} \gamma_5\mathbb{1} \left(n^\mu n^\nu n^\rho n^\sigma n^\kappa - \frac{1}{9} T_P^{[\mu\nu} n^\rho n^\sigma n^{\kappa]} + \frac{1}{63} T_P^{[\mu\nu} T_P^{\rho\sigma} n^{\kappa]}\right)$	τ_1
2	$\frac{3\sqrt{14}}{8} \gamma_5\hat{\not{P}} \left(n^\mu n^\nu n^\rho n^\sigma n^\kappa - \frac{1}{9} T_P^{[\mu\nu} n^\rho n^\sigma n^{\kappa]} + \frac{1}{63} T_P^{[\mu\nu} T_P^{\rho\sigma} n^{\kappa]}\right)$	$-\tau_2$
3	$\frac{3\sqrt{14}}{8} \gamma_5\not{n} \left(n^\mu n^\nu n^\rho n^\sigma n^\kappa - \frac{1}{9} T_P^{[\mu\nu} n^\rho n^\sigma n^{\kappa]} + \frac{1}{63} T_P^{[\mu\nu} T_P^{\rho\sigma} n^{\kappa]}\right)$	$-\tau_3$
4	$\frac{3\sqrt{14}}{8} i\gamma_5\hat{\not{P}}\not{n} \left(n^\mu n^\nu n^\rho n^\sigma n^\kappa - \frac{1}{9} T_P^{[\mu\nu} n^\rho n^\sigma n^{\kappa]} + \frac{1}{63} T_P^{[\mu\nu} T_P^{\rho\sigma} n^{\kappa]}\right)$	τ_4
5	$\frac{\sqrt{105}}{40} \gamma_5 \left(\gamma_{\perp\perp}^{[\mu} n^\nu n^\rho n^\sigma n^{\kappa]} - \frac{1}{9} \gamma_{\perp\perp}^{[\mu} T_P^{\nu\rho} n^\sigma n^{\kappa]} + \frac{1}{63} \gamma_{\perp\perp}^{[\mu} T_P^{\nu\rho} T_P^{\sigma\kappa]}\right)$	$-\tau_5$
6	$\frac{\sqrt{105}}{40} i\gamma_5\hat{\not{P}} \left(\gamma_{\perp\perp}^{[\mu} n^\nu n^\rho n^\sigma n^{\kappa]} - \frac{1}{9} \gamma_{\perp\perp}^{[\mu} T_P^{\nu\rho} n^\sigma n^{\kappa]} + \frac{1}{63} \gamma_{\perp\perp}^{[\mu} T_P^{\nu\rho} T_P^{\sigma\kappa]}\right)$	τ_6
7	$\frac{\sqrt{105}}{40} i\gamma_5\not{n} \left(\gamma_{\perp\perp}^{[\mu} n^\nu n^\rho n^\sigma n^{\kappa]} - \frac{1}{9} \gamma_{\perp\perp}^{[\mu} T_P^{\nu\rho} n^\sigma n^{\kappa]} + \frac{1}{63} \gamma_{\perp\perp}^{[\mu} T_P^{\nu\rho} T_P^{\sigma\kappa]}\right)$	τ_7
8	$\frac{\sqrt{105}}{40} i\gamma_5\hat{\not{P}}\not{n} \left(\gamma_{\perp\perp}^{[\mu} n^\nu n^\rho n^\sigma n^{\kappa]} - \frac{1}{9} \gamma_{\perp\perp}^{[\mu} T_P^{\nu\rho} n^\sigma n^{\kappa]} + \frac{1}{63} \gamma_{\perp\perp}^{[\mu} T_P^{\nu\rho} T_P^{\sigma\kappa]}\right)$	$-\tau_8$

Table C.6.: Tensor structures for mesons with quantum numbers (from top to bottom) $J^P = 5^-$, $J^P = 5^+$

C.8. Tabulated results for meson spectra

Tables C.7 through C.10 explicitly list the calculated meson masses, which are plotted and discussed in Section 6.4. All masses and uncertainties are given in units of MeV, all uncertainties are numerical uncertainties introduced by extrapolating eigenvalue curves and cells without an entry have either not been calculated or no numerically reliable result could be obtained.

J^{PC}	Excitation	Mass (RL, MT)	Mass (RL, QC)	Mass (KF)
0^{-+}	0	139	136	138
	1	1124 ± 19	1053 ± 155	—
	2	1315 ± 85	—	—
0^{++}	0	664	697 ± 23	465 ± 15
	1	1201 ± 89	—	826 ± 64
1^{--}	0	732	774 ± 37	549 ± 55
	1	986	—	1015 ± 102
1^{+-}	0	823	767 ± 30	1275 ± 65
	1	1197 ± 55	—	—
1^{++}	0	895	—	—
	1	1209 ± 42	—	—
	2	1367 ± 66	—	—
2^{++}	0	1154 ± 11	1065 ± 78	1266 ± 82
	1	1264 ± 120	—	—
2^{--}	0	1235 ± 65	1071 ± 102	—
2^{-+}	0	1222 ± 9	—	1657 ± 28
3^{--}	0	1579 ± 47	—	—
3^{+-}	0	1571 ± 33	—	—
3^{++}	0	1537 ± 222	—	—
4^{++}	0	1953 ± 45	—	—
4^{-+}	0	1908 ± 76	—	—
5^{--}	0	2325 ± 52	—	—
5^{+-}	0	2310 ± 73	—	—
5^{++}	0	2925 ± 127	—	—

Table C.7.: Light meson masses calculated in the rainbow-ladder (RL) truncation with the Maris-Tandy (MT) and Qin-Chang (QC) effective running couplings and in the kernel-first (KF) truncation.

J^P	Excitation	Mass (RL, MT)	Mass (RL, QC)	Mass (KF)
0^-	0	495	532 ± 9	493 ± 3
	1	1036 ± 39	—	854 ± 156
	2	1315 ± 50	—	1376 ± 36
	3	1626 ± 142	—	—
0^+	0	887	921 ± 83	754 ± 28
	1	1244 ± 69	—	1556 ± 43
	2	1455 ± 42	—	2031 ± 223
	3	2171 ± 336	—	—
1^-	0	930	965 ± 66	781 ± 69
	1	1210 ± 97	—	1211 ± 118
1^+	0	1012 ± 18	974 ± 93	—
	1	1103 ± 19	—	—
	2	1406 ± 61	—	—
2^+	0	1332 ± 166	1244 ± 170	1424 ± 134
2^-	0	1372 ± 37	1242 ± 195	1784 ± 52
3^-	0	1744 ± 49	—	—
3^+	0	1733 ± 25	—	—
4^+	0	2082 ± 57	—	—
	1	2494 ± 251	—	—
4^-	0	2007 ± 43	—	—
	1	2504 ± 158	—	—
5^-	0	2377 ± 57	—	—
5^+	0	2358 ± 77	—	—
	1	2938 ± 116	—	—

Table C.8.: Kaon masses calculated in the rainbow-ladder (RL) truncation with the Maris-Tandy (MT) and Qin-Chang (QC) effective running couplings and in the kernel-first (KF) truncation.

J^{PC}	Excitation	Mass (RL, MT)	Mass (RL, QC)	Mass (KF)
0^{-+}	0	696	769 ± 46	699 ± 7
	1	1480 ± 69	—	—
	2	1611 ± 109	—	—
	3	2285 ± 259	—	—
0^{++}	0	1074 ± 2	—	982 ± 36
	1	1551 ± 77	—	1377 ± 11
1^{--}	0	1066 ± 6	—	982 ± 36
	1	1341 ± 54	—	1377 ± 11
1^{+-}	0	1161 ± 7	1122 ± 222	1586 ± 97
1^{++}	0	1258 ± 36	—	1499 ± 67
2^{++}	0	1424 ± 43	—	1482 ± 90
2^{--}	0	1524 ± 96	—	1985 ± 36
	1	1874 ± 149	—	—
2^{-+}	0	1522 ± 35	—	1704 ± 18
3^{--}	0	1755 ± 88	—	—
3^{+-}	0	1827 ± 94	—	2611 ± 110
4^{++}	0	2084 ± 53	—	—
4^{-+}	0	2094 ± 115	—	3122 ± 160
	1	2607 ± 268	—	—
5^{--}	0	2418 ± 64	—	—
5^{+-}	0	2405 ± 63	—	—
5^{++}	0	2945 ± 115	—	—

Table C.9.: $s\bar{s}$ meson masses calculated in the rainbow-ladder (RL) truncation with the Maris-Tandy (MT) and Qin-Chang (QC) effective running couplings and in the kernel-first (KF) truncation.

J^{PC}	Excitation	Mass (RL, MT)
0^{-+}	0	2913
	1	3625 ± 32
	2	3942 ± 28
0^{++}	0	3304
	1	3785 ± 91
	2	4142 ± 131
1^{--}	0	3091
	1	3684 ± 27
	2	3647 ± 55
	3	3948 ± 104
1^{+-}	0	3409
	1	3704 ± 27
	2	4046 ± 102
	3	4214 ± 181
1^{++}	0	3421
	1	3705 ± 24
	2	3748 ± 134
2^{++}	0	3569 ± 9
	1	4034 ± 34
2^{--}	0	3821 ± 35
	1	3935 ± 104
	2	4583 ± 212
2^{-+}	0	3823 ± 35
	1	3990 ± 92
	2	4813 ± 255
3^{--}	0	4001 ± 33
	1	4350 ± 60
3^{+-}	0	4203 ± 37
	1	4477 ± 157
3^{++}	0	4186 ± 39
	1	4604 ± 277
4^{++}	0	4407 ± 64
	1	4608 ± 120
4^{--}	0	4524 ± 86
	1	5046 ± 120
4^{-+}	0	4554 ± 97
5^{--}	0	4749 ± 115
5^{+-}	0	4798 ± 126
5^{++}	0	4776 ± 281

J^{PC}	Excitation	Mass (RL, MT)
0^{-+}	0	9371
	1	10012 ± 39
	2	10420 ± 226
0^{++}	0	9805
	1	10222 ± 73
	2	10686 ± 216
1^{--}	0	9451
	1	10044 ± 85
	2	10147 ± 27
	3	10429 ± 188
1^{+-}	0	9852
	1	10052 ± 9
	2	10217 ± 115
	3	10634 ± 115
1^{++}	0	9855
	1	10050 ± 10
	2	10266 ± 115
2^{++}	0	9908
	1	10266 ± 115
2^{--}	0	10186 ± 34
	1	10288 ± 78
2^{-+}	0	10182 ± 36
	1	10289 ± 77
3^{--}	0	10229 ± 48
	1	10758 ± 101
3^{+-}	0	10501 ± 120
3^{++}	0	10499 ± 117
4^{++}	0	10563 ± 133
	1	11011 ± 57
4^{--}	0	10817 ± 94
4^{-+}	0	10818 ± 90
5^{--}	0	10889 ± 75
	1	11251 ± 147
5^{+-}	0	11075 ± 48
5^{++}	0	11072 ± 42

Table C.10.: Charmonium (left) and bottomonium (right) masses calculated in the rainbow-ladder (RL) truncation with the Maris-Tandy (MT) effective running coupling.

D. Numerical methods

In this chapter, we will briefly go over some of the numerical methods used throughout this work. More details on most of them can be found in Ref. [266], which also contains example implementations for those methods.

D.1. Numerical integration

Many of the integrals appearing in the quark DSE and meson BSE have been evaluated numerically. There are many ways to approach the task of numerical integration. The simplest is the bar method, which approximates the integral of a function f over a given interval (a, b) by approximating the area under the function with rectangles of equal width, and their height being the functions value at the centre of each rectangle's base. This can be written as the equation

$$\int_a^b f(x)\mathrm{d}x \approx \sum_{i=1}^{N} f(x_i) \cdot \Delta x, \tag{D.1}$$

with $x_i = a + \frac{2i-1}{2N}(b-a)$ and $\Delta x = \frac{b-a}{N}$. This method however is not very efficient as it only converges slowly for increasing N. A faster method is the Gaussian quadrature, where the function is no longer evaluated at equidistant points, but instead is only evaluated at a specific set of points x_i which all have their own weight factor w_i, so that we get

$$\int_a^b f(x)\mathrm{d}x \approx \sum_{i=1}^{N} f(x_i) \cdot w_i. \tag{D.2}$$

With the correct choice of the abscissas and weights this method converges much faster, even for small values of N. The quadrature method can even be generalized to integrals of the form

$$\int_a^b f(x)g(x)\mathrm{d}x \approx \sum_{i=1}^{N} f(x_i) \cdot w_i, \tag{D.3}$$

where the contribution of the function $g(x)$ gets absorbed into the weights. One particularly useful case of this is the GauSS-Chebyshev integration, where $g(x) = \sqrt{1-x^2}$ and the abscissas and weights are calculated using Chebyshev polynomials of the second kind. Integrals of that form frequently appear in angular integrals in both the DSE and BSE and we use this method whenever they appear.

In practice, the radial integrals in the DSE have been evaluated using 640 abscissas, while the angular integrals used 128 abscissas. The integrals appearing in the BSE required even fewer abscissas, being 32 for the ψ integration and 12 for the ϑ integration, with more or less points being used in some channels when appropriate. In and close to the chiral limit, twice as many abscissas have been used for the angular integrals in the BSE, as this region requires some higher precision in order to converge.

D.2. Root finding

To find the zeros of the function $f(P^2) = \lambda(P^2) - 1$, several root finding methods have been applied. In cases where no extrapolation of eigenvalue curves is required, cf. Sec. C.1, well-established root finding methods, such as the false position method, also known as regula falsi, or the Newton method are useful, since they minimize the number of eigenvalues that need to be calculated.

When the eigenvalue curve is extrapolated, a different method has been used to find the solutions to $\lambda = 1$. Since the rational function obtained by the Schlessinger method is not an expensive function to call and can be evaluated many times per second, even on standard desktop hardware, we no longer need to optimize for a minimum number of function calls. Instead, the problem shifts to different difficulties, since we no longer know beforehand, in which interval the root lies, which is a prerequisite for the false position method. The Newton method also does not work reliably on the kind of function we are solving. Instead, it often goes off towards infinity without converging.

The method that has proven to be the most reliable in our calculations is a tiny-step rootfinder. It works by starting at $P^2 = P_0^2$ and going towards more negative values of P^2 in tiny steps, evaluating $\lambda(P^2) - 1$ at each one and checking, if the function has switched signs, indicating a root lying between the two previous steps. These can then be used as upper and lower limits for a further false position root finding in order to improve accuracy. Additionally, one needs to set a maximum momentum $P^2_{\text{max}} \ll P_0^2$, at which the algorithm stops without converging.

While this method requires many function calls, easily going into the hundreds, it is the most reliable method to find roots of Schlessinger functions without prior input of search intervals, which would introduce a bias into our calculations.

E. Technical toolkit

E.1. Feynman diagrams

Some of the Feynman diagrams used in this work have been taken from prior publications of our working group with permission by Christian Fischer. In particular, Figures 3.1, 3.2, 3.3, 3.4 and 4.8 have been taken from [195]. Figures 4.4 and 4.7 have been taken from [45]. Other Feynman diagrams in the same colouring scheme have been created by me using the JaxoDraw software, version 2.1.0 [267].

E.2. The Rust programming language

The numerical calculations done for this work have been mostly programmed in the Rust programming language [268], a modern multi-paradigm programming language with a focus on memory safety, concurrency and performance. The code has been compiled using version 1.89 of the stable release Rust toolchain, including the rustc compiler and the cargo build system. Occasionally, compute kernels have been written in the C programming language [269] and embedded into the codebase using Rust's foreign function interface directly or via the cc crate. Most compute kernels, as well as all other code relevant for computations, have been written in Rust.

E.2.1. Krylov-Schur eigensolver

Since the Rust standard library is quite small compared to other languages, some functionality is relegated to third-party libraries, called crates. One of the most important dependencies of this work's codebase is the crate faer (version 0.23), which implements very performant state-of-the-art linear algebra algorithms, including Krylov-Schur eigensolver methods. It is published under an MIT licence at [270].

E.3. FORM

While some of the Dirac traces performed throughout this work are easy enough to be done by hand, some expressions become impractically large, demanding computational treatment. The tool of choice here was the FORM programming language [271], which can perform arbitrarily large symbolic manipulations and optimize the number of floating point operations needed, speeding up some computations drastically.

E.4. Plotting and Typesetting

Most plots of results shown throughout this work have been generated using gnuplot 6.0 [272], a free and open source data visualization and plotting program. The document itself has been typest in LaTeXand compiled using version 1.17.0 of the lualatex compiler. The bibliography has been generated using the biblatex package with the biber backend, version 2.19.

Bibliography

[1] Stephan Hagel et al. "Spectra of light and heavy mesons with $J \leq 5$ in a relativistic Bethe-Salpeter approach". In: (Oct. 2025). arXiv: 2510.27423 [hep-ph].

[2] Markus Q. Huber et al. In: *in preparation.* ().

[3] Richard Williams, Christian S. Fischer, and Walter Heupel. "Kernel-first truncations of the Dyson-Schwinger/Bethe-Salpeter equations". In: *unpublished work* ().

[4] S. Navas et al. "Review of particle physics". In: *Phys. Rev. D* 110.3 (2024), p. 030001. DOI: 10.1103/PhysRevD.110.030001.

[5] C. M. G. Lattes et al. "PROCESSES INVOLVING CHARGED MESONS". In: *Nature* 159 (1947), pp. 694–697. DOI: 10.1038/159694a0.

[6] RJ Jaffe. "Multiquark hadrons. I. Phenomenology of Q 2 Q 2 mesons". In: *Physical Review D* 15.1 (1977), p. 267.

[7] J. R. Pelaez. "From controversy to precision on the sigma meson: a review on the status of the non-ordinary $f_0(500)$ resonance". In: (2015). arXiv: 1510.00653 [hep-ph].

[8] M. Alekseev et al. "Observation of a J**PC = 1-+ exotic resonance in diffractive dissociation of 190-GeV/c pi- into pi- pi- pi+". In: *Phys. Rev. Lett.* 104 (2010), p. 241803. DOI: 10.1103/PhysRevLett.104.241803. arXiv: 0910.5842 [hep-ex].

[9] T. Skwarnicki et al. "Spin Analysis of the $\chi(b)$ States". In: *Phys. Rev. Lett.* 58 (1987), p. 972. DOI: 10.1103/PhysRevLett.58.972.

[10] D. Aston et al. "Observation of the Leading K^* L Excitation Series From JP = 1- Through 5- in the Reaction $K^-p \to K^-\pi^+n$ at 11 GeV/c". In: *Phys. Lett. B* 180 (1986). [Erratum: Phys.Lett.B 183, 434 (1987)], p. 308. DOI: 10.1016/0370-2693(86)90316-3.

[11] D. Alde et al. "Partial wave analysis of the omega pi0 system at high masses". In: *Nuovo Cim. A* 107 (1994), pp. 1867–1874. DOI: 10.1007/BF01556363.

[12] D. Alde et al. "Study of the pi0 pi0 system with the GAMS-4000 spectrometer at 100-GeV/c". In: *Eur. Phys. J. A* 3 (1998), pp. 361–371. DOI: 10.1007/s100500050190.

[13] Colin J. Morningstar and Mike J. Peardon. “The Glueball spectrum from an anisotropic lattice study”. In: *Phys. Rev. D* 60 (1999), p. 034509. DOI: 10.1103/PhysRevD.60.034509. arXiv: hep-lat/9901004 [hep-lat].

[14] Andreas Athenodorou and Michael Teper. “The glueball spectrum of SU(3) gauge theory in 3 + 1 dimensions”. In: *JHEP* 11 (2020), p. 172. DOI: 10.1007/JHEP11(2020)172. arXiv: 2007.06422 [hep-lat].

[15] Markus Q. Huber, Christian S. Fischer, and Helios Sanchis-Alepuz. “Higher spin glueballs from functional methods”. In: *Eur. Phys. J. C* 81.12 (2021). [Erratum: Eur.Phys.J.C 82, 38 (2022)], p. 1083. DOI: 10.1140/epjc/s10052-021-09864-5. arXiv: 2110.09180 [hep-ph].

[16] Eberhard Klempt and Alexander Zaitsev. “Glueballs, hybrids, multiquarks: Experimental facts versus QCD inspired concepts”. In: *Physics Reports* 454.1-4 (2007), pp. 1–202.

[17] Nora Brambilla et al. “The XYZ states: experimental and theoretical status and perspectives”. In: *Phys. Rept.* 873 (2020), pp. 1–154. DOI: 10.1016/j.physrep.2020.05.001. arXiv: 1907.07583 [hep-ex].

[18] Friederike Ihssen et al. “Towards quantitative precision in functional QCD I”. In: (Aug. 2024). arXiv: 2408.08413 [hep-ph].

[19] D. Horn and J. Mandula. “Model of mesons with constituent gluons”. In: *Phys. Rev. D* 17 (3 Feb. 1978), pp. 898–908. DOI: 10.1103/PhysRevD.17.898.

[20] L. Maiani et al. “Diquark-antidiquark states with hidden or open charm and the nature of $X(3872)$”. In: *Phys. Rev. D* 71 (1 Jan. 2005), p. 014028. DOI: 10.1103/PhysRevD.71.014028.

[21] Ying Cui et al. *The Possible Heavy Tetraquarks $qQ\bar{q}\overline{Q}$, $qq\overline{QQ}$ and $qQ\overline{QQ}$*. 2006. arXiv: hep-ph/0607226 [hep-ph].

[22] Pan-Pan Shi, Fei Huang, and Wen-Ling Wang. “Hidden charm tetraquark states in a diquark model”. In: *Phys. Rev. D* 103 (9 May 2021), p. 094038. DOI: 10.1103/PhysRevD.103.094038.

[23] Kenneth G. Wilson. “Confinement of Quarks”. In: *Phys. Rev.* D10 (8 Oct. 1974). [,45(1974)], pp. 2445–2459. DOI: 10.1103/PhysRevD.10.2445.

[24] Zoltan Fodor and Christian Hoelbling. “Light Hadron Masses from Lattice QCD”. In: *Rev. Mod. Phys.* 84 (2 Apr. 2012), p. 449. DOI: 10.1103/RevModPhys.84.449. arXiv: 1203.4789 [hep-lat].

[25] Sinya Aoki et al. “Review of Lattice Results Concerning Low-Energy Particle Physics”. In: *Eur. Phys. J. C* 74 (2014), p. 2890. DOI: 10.1140/epjc/s10052-014-2890-7. arXiv: 1310.8555 [hep-lat].

[26] Christof Gattringer and Christian Lang. *Quantum chromodynamics on the lattice: an introductory presentation*. Vol. 788. Springer Science & Business Media, 2009.

[27] Ronald Babich et al. "Scaling lattice QCD beyond 100 GPUs". In: *Proceedings of 2011 International Conference for High Performance Computing, Networking, Storage and Analysis*. 2011, pp. 1–11.

[28] Bálint Joó et al. "Status and Future Perspectives for Lattice Gauge Theory Calculations to the Exascale and Beyond". In: *Eur. Phys. J. A* 55.11 (2019), p. 199. DOI: `10.1140/epja/i2019-12919-7`. arXiv: `1904.09725 [hep-lat]`.

[29] Peter Boyle et al. "Lattice QCD and the computational frontier". In: *arXiv preprint arXiv:2204.00039* (2022).

[30] Gustavo Alonso Ramirez Hidalgo. "Multilevel Algorithms in Lattice QCD for Exascale Machines". PhD thesis. 2022.

[31] Pieter Maris, Craig D. Roberts, and Peter C. Tandy. "Pion mass and decay constant". In: *Phys. Lett.* B420.3-4 (1998), pp. 267–273. DOI: `10.1016/S0370-2693(97)01535-9`. arXiv: `nucl-th/9707003 [nucl-th]`.

[32] G. Eichmann et al. "Nucleon mass from a covariant three-quark Faddeev equation". In: *Phys. Rev. Lett.* 104 (20 May 2010), p. 201601. DOI: `10.1103/PhysRevLett.104.201601`. arXiv: `0912.2246 [hep-ph]`.

[33] Richard Williams. "Vector mesons as dynamical resonances in the BetheSalpeter framework". In: *Phys. Lett. B* 798 (2019), p. 134943. DOI: `10.1016/j.physletb.2019.134943`. arXiv: `1804.11161 [hep-ph]`.

[34] Pieter Maris and Peter C. Tandy. "The Quark photon vertex and the pion charge radius". In: *Phys. Rev.* C61 (4 Mar. 2000), p. 045202. DOI: `10.1103/PhysRevC.61.045202`. arXiv: `nucl-th/9910033 [nucl-th]`.

[35] Esther Weil et al. "Electromagnetic decays of the neutral pion". In: *Phys. Rev. D* 96.1 (1 July 2017), p. 014021. DOI: `10.1103/PhysRevD.96.014021`. arXiv: `1704.06046 [hep-ph]`.

[36] Gernot Eichmann et al. "On the large-Q^2 behavior of the pion transition form factor". In: *Phys. Lett. B* 774 (2017), pp. 425–429. DOI: `10.1016/j.physletb.2017.10.002`. arXiv: `1704.05774 [hep-ph]`.

[37] Gernot Eichmann and Christian S. Fischer. "Nucleon Compton scattering in the Dyson-Schwinger approach". In: *Phys.Rev.* D87.3 (3 Feb. 2013), p. 036006. DOI: `10.1103/PhysRevD.87.036006`. arXiv: `1212.1761 [hep-ph]`.

[38] Gernot Eichmann et al. “Axial-vector and scalar contributions to hadronic light-by-light scattering”. In: *Eur. Phys. J. C* 85.4 (2025), p. 445. DOI: 10.1140/epjc/s10052-025-14055-7. arXiv: 2411.05652 [hep-ph].

[39] Markus Q. Huber, Christian S. Fischer, and Hèlios Sanchis-Alepuz. “Spectrum of scalar and pseudoscalar glueballs from functional methods”. In: *Eur. Phys. J. C* 80.11 (2020), p. 1077. DOI: 10.1140/epjc/s10052-020-08649-6. arXiv: 2004.00415 [hep-ph].

[40] Nico Gideon Santowsky. “The Role of Four-Quark States in the Nature of Exotic Hadrons from Bethe-Salpeter Equations”. PhD thesis. Giessen U., 2021. DOI: 10.22029/JLUPUB-241.

[41] Gernot Eichmann et al. “Four-Quark States from Functional Methods”. In: *Few Body Syst.* 61.4 (2020), p. 38. DOI: 10.1007/s00601-020-01571-3. arXiv: 2008.10240 [hep-ph].

[42] Joshua Hoffer. “Properties Of Heavy-Light Four-Quark States From Functional Methods”. PhD thesis. JLU GieSSen, Jan. 2025. DOI: 10.22029/jlupub-19943.

[43] Gernot Eichmann, M. T. Peña, and Raul D. Torres. “Five-body systems with Bethe-Salpeter equations”. In: *Phys. Lett. B* 866 (2025), p. 139525. DOI: 10.1016/j.physletb.2025.139525. arXiv: 2502.17944 [hep-ph].

[44] Christian S. Fischer, Axel Maas, and Jan M. Pawlowski. “On the infrared behavior of Landau gauge Yang-Mills theory”. In: *Annals Phys.* 324 (2009), pp. 2408–2437. DOI: 10.1016/j.aop.2009.07.009. arXiv: 0810.1987 [hep-ph].

[45] Gernot Eichmann et al. “Baryons as relativistic three-quark bound states”. In: *Prog. Part. Nucl. Phys.* 91 (2016), pp. 1–100. DOI: 10.1016/j.ppnp.2016.07.001. arXiv: 1606.09602 [hep-ph].

[46] Craig D. Roberts and Anthony G. Williams. “Dyson-Schwinger equations and their application to hadronic physics”. In: *Prog. Part. Nucl. Phys.* 33 (1994), pp. 477–575. DOI: 10.1016/0146-6410(94)90049-3. arXiv: hep-ph/9403224 [hep-ph].

[47] Reinhard Alkofer and Lorenz von Smekal. “The Infrared behavior of QCD Green’s functions: Confinement dynamical symmetry breaking, and hadrons as relativistic bound states”. In: *Phys. Rept.* 353.5-6 (2001), pp. 281–465. DOI: 10.1016/S0370-1573(01)00010-2. arXiv: hep-ph/0007355 [hep-ph].

[48] Adnan Bashir et al. “Collective perspective on advances in Dyson-Schwinger Equation QCD”. In: *Commun. Theor. Phys.* 58 (2012), pp. 79–134. DOI: 10.1088/0253-6102/58/1/16. arXiv: 1201.3366 [nucl-th].

[49] Pieter Maris and Craig D. Roberts. "Dyson-Schwinger equations: A Tool for hadron physics". In: *Int. J. Mod. Phys. E* 12 (2003), pp. 297–365. DOI: 10.1142/S0218301303001326. arXiv: nucl-th/0301049 [nucl-th].

[50] Christian S. Fischer. "Infrared properties of QCD from Dyson-Schwinger equations". In: *J. Phys.* G32 (2006), R253–R291. DOI: 10.1088/0954-3899/32/8/R02. arXiv: hep-ph/0605173 [hep-ph].

[51] Christof Wetterich. "Exact evolution equation for the effective potential". In: *Phys. Lett. B* 301 (1993), pp. 90–94. DOI: 10.1016/0370-2693(93)90726-X. arXiv: 1710.05815 [hep-th].

[52] Christian Kellermann and Christian S. Fischer. "The Running coupling from the four-gluon vertex in Landau gauge Yang-Mills theory". In: *Phys. Rev. D* 78 (2008), p. 025015. DOI: 10.1103/PhysRevD.78.025015. arXiv: 0801.2697 [hep-ph].

[53] Christian S. Fischer and Jan M. Pawlowski. "Uniqueness of infrared asymptotics in Landau gauge Yang-Mills theory". In: *Phys. Rev. D* 75 (2007), p. 025012. DOI: 10.1103/PhysRevD.75.025012. arXiv: hep-th/0609009 [hep-th].

[54] Christian S. Fischer and Jan M. Pawlowski. "Uniqueness of infrared asymptotics in Landau gauge Yang-Mills theory II". In: *Phys. Rev. D* 80 (2009), p. 025023. DOI: 10.1103/PhysRevD.80.025023. arXiv: 0903.2193 [hep-th].

[55] Fei Gao and Jan M. Pawlowski. "QCD phase structure from functional methods". In: *Phys. Rev. D* 102.3 (2020), p. 034027. DOI: 10.1103/PhysRevD.102.034027. arXiv: 2002.07500 [hep-ph].

[56] Jan M. Pawlowski. "Aspects of the functional renormalisation group". In: *Annals Phys.* 322 (2007), pp. 2831–2915. DOI: 10.1016/j.aop.2007.01.007. arXiv: hep-th/0512261 [hep-th].

[57] N. Dupuis et al. "The nonperturbative functional renormalization group and its applications". In: *Phys. Rept.* 910 (2021), pp. 1–114. DOI: 10.1016/j.physrep.2021.01.001. arXiv: 2006.04853 [cond-mat.stat-mech].

[58] Wei-jie Fu. "QCD at finite temperature and density within the fRG approach: an overview". In: *Commun. Theor. Phys.* 74.9 (2022), p. 097304. DOI: 10.1088/1572-9494/ac86be. arXiv: 2205.00468 [hep-ph].

[59] Mario Mitter, Jan M. Pawlowski, and Nils Strodthoff. "Chiral symmetry breaking in continuum QCD". In: *Phys. Rev. D* 91 (2015), p. 054035. DOI: 10.1103/PhysRevD.91.054035. arXiv: 1411.7978 [hep-ph].

[60] Anton K. Cyrol et al. “Nonperturbative quark, gluon, and meson correlators of unquenched QCD”. In: *Phys. Rev. D* 97.5 (2018), p. 054006. DOI: 10.1103/PhysRevD.97.054006. arXiv: 1706.06326 [hep-ph].

[61] Fei Gao, Joannis Papavassiliou, and Jan M. Pawlowski. “Fully coupled functional equations for the quark sector of QCD”. In: *Phys. Rev. D* 103.9 (Feb. 2021), p. 094013. DOI: 10.1103/PhysRevD.103.094013. arXiv: 2102.13053 [hep-ph].

[62] Holger Gies and Christof Wetterich. “Renormalization flow of bound states”. In: *Phys. Rev. D* 65 (2002), p. 065001. DOI: 10.1103/PhysRevD.65.065001. arXiv: hep-th/0107221.

[63] Wei-jie Fu et al. “Four-quark scatterings in QCD III”. In: *Phys. Rev. D* 112.5 (2025), p. 054047. DOI: 10.1103/4sh5-w4yc. arXiv: 2502.14388 [hep-ph].

[64] Dao-yu Zhang, Chuang Huang, and Wei-jie Fu. “Quasiparton distributions of pions at large longitudinal momentum”. In: *Phys. Rev. D* 112.7 (2025), p. 074001. DOI: 10.1103/9k1c-kwvw. arXiv: 2502.15384 [hep-ph].

[65] Jens Braun et al. “From Quarks and Gluons to Hadrons: Chiral Symmetry Breaking in Dynamical QCD”. In: *Phys. Rev. D* 94.3 (2016), p. 034016. DOI: 10.1103/PhysRevD.94.034016. arXiv: 1412.1045 [hep-ph].

[66] Fabian Rennecke. “Vacuum structure of vector mesons in QCD”. In: *Phys. Rev. D* 92.7 (2015), p. 076012. DOI: 10.1103/PhysRevD.92.076012. arXiv: 1504.03585 [hep-ph].

[67] N. Brambilla et al. “QCD and Strongly Coupled Gauge Theories: Challenges and Perspectives”. In: *Eur. Phys. J. C* 74.10 (2014), p. 2981. DOI: 10.1140/epjc/s10052-014-2981-5. arXiv: 1404.3723 [hep-ph].

[68] Emi Kou et al. “The Belle II physics book”. In: *Progress of Theoretical and Experimental Physics* 2019.12 (2019), p. 123C01.

[69] S. K. Choi et al. “Observation of a narrow charmonium-like state in exclusive $B^\pm \to K^\pm \pi^+ \pi^- J/\psi$ decays”. In: *Phys. Rev. Lett.* 91.26 (Dec. 2003), p. 262001. DOI: 10.1103/PhysRevLett.91.262001. arXiv: hep-ex/0309032.

[70] Adrian Bevan et al. *The physics of the B factories*. Springer Nature, 2017.

[71] M. Aghasyan et al. “Light isovector resonances in $\pi^- p \to \pi^- \pi^- \pi^+ p$ at 190 GeV/c”. In: *Phys. Rev. D* 98.9 (2018), p. 092003. DOI: 10.1103/PhysRevD.98.092003. arXiv: 1802.05913 [hep-ex].

[72] Henri Clemens Pekeler. “Recent spectroscopy highlights from COMPASS”. In: *PoS* HQL2023 (2024), p. 041. DOI: 10.22323/1.462.0041.

[73] C. Adolph et al. "Odd and even partial waves of $\eta\pi^-$ and $\eta'\pi^-$ in $\pi^- p \to \eta^{(\prime)}\pi^- p$ at 191 GeV/c". In: *Phys. Lett. B* 740 (2015). [Erratum: Phys.Lett.B 811, 135913 (2020)], pp. 303–311. DOI: 10.1016/j.physletb.2014.11.058. arXiv: 1408.4286 [hep-ex].

[74] Jan Friedrich. "Chiral symmetry breaking: Current experimental status and prospects". In: *EPJ Web Conf.* 282 (2023), p. 01007. DOI: 10.1051/epjconf/202328201007.

[75] Julien Beckers and Philipp Haas. "Measuring Light-Meson Resonances in the $\omega\pi^-\pi^0$ and $K^0_S K^-$ Final States at COMPASS". In: *21st International Conference on Hadron Spectroscopy and Structure*. July 2025. arXiv: 2507.21936 [hep-ex].

[76] Stefan Wallner. "News from the light and strange meson sector". In: *Rev. Mex. Fis. Suppl.* 3.3 (2022), p. 0308004. DOI: 10.31349/SuplRevMexFis.3.0308004.

[77] Bernhard Ketzer, Boris Grube, and Dmitry Ryabchikov. "Light-meson spectroscopy with COMPASS". In: *Progress in Particle and Nuclear Physics* 113 (2020), p. 103755.

[78] Chang-Zheng Yuan and Stephen Lars Olsen. "The BESIII physics programme". In: *Nature Reviews Physics* 1.8 (2019), pp. 480–494.

[79] D. M. Asner et al. "Physics at BES-III". In: *Int. J. Mod. Phys.* A24 (2009), S1–794. arXiv: 0809.1869 [hep-ex].

[80] Medina Ablikim et al. "Observation of Structures in the Processes e+e- $\to\omega\chi$c1 and $\omega\chi$c2". In: *Phys. Rev. Lett.* 132.16 (2024), p. 161901. DOI: 10.1103/PhysRevLett.132.161901. arXiv: 2401.14720 [hep-ex].

[81] M. Ablikim et al. "Study of the Decay and Production Properties of Ds1(2536) and Ds2*(2573)". In: *Phys. Rev. Lett.* 133.17 (2024), p. 171903. DOI: 10.1103/PhysRevLett.133.171903. arXiv: 2407.07651 [hep-ex].

[82] M. Ablikim et al. "Partial-wave analysis of $J/\psi \to K^+K^-\pi^0$". In: *Phys. Rev. D* 100.3 (2019), p. 032004. DOI: 10.1103/PhysRevD.100.032004. arXiv: 1904.10630 [hep-ex].

[83] M. Ablikim et al. "Partial wave analysis of $\psi(3686) \to K^+K^-\eta$". In: *Phys. Rev. D* 101.3 (2020), p. 032008. DOI: 10.1103/PhysRevD.101.032008. arXiv: 1912.08566 [hep-ex].

[84] Yanping Huang, Shan Jin, and Peng Zhang. "Discovery of a glueball-like particle X(2370) at BESIII". In: *Int. J. Mod. Phys. A* 40.19 (2025), p. 2530007. DOI: 10.1142/S0217751X25300078. arXiv: 2503.13286 [hep-ex].

[85] Medina Ablikim et al. "Determination of Spin-Parity Quantum Numbers of X(2370) as 0-+ from J/$\psi\rightarrow\gamma$KS0KS0η"'. In: *Phys. Rev. Lett.* 132.18 (2024), p. 181901. DOI: `10.1103/PhysRevLett.132.181901`. arXiv: `2312.05324 [hep-ex]`.

[86] A Augusto Alves Jr et al. "The LHCb detector at the LHC". In: *Journal of instrumentation* 3.08 (2008), S08005.

[87] Roel Aaij et al. "Amplitude analysis of B+$\rightarrow$ J/ψ ϕ K+ decays". In: *Physical Review D* 95.1 (2017), p. 012002.

[88] Roel Aaij et al. "Observation of J/ψ ϕ Structures Consistent with Exotic States from Amplitude Analysis of B+$\rightarrow$ J/ψ ϕ K+ Decays". In: *Physical review letters* 118.2 (2017), p. 022003.

[89] Roel Aaij et al. "Model-independent study of structure in B+$\rightarrow$ D+ D-K+ decays". In: *Physical review letters* 125.24 (2020), p. 242001.

[90] Roel Aaij et al. "Amplitude analysis of the B+$\rightarrow$ D+ D-K+ decay". In: *Physical Review D* 102.11 (2020), p. 112003.

[91] Roel Aaij et al. "Observation of J/ψ p Resonances Consistent with Pentaquark States in Λ b 0$\rightarrow$ J/ψ K-p Decays". In: *Physical review letters* 115.7 (2015), p. 072001.

[92] R Aaij et al. "Determination of the X (3872) meson quantum numbers". In: *Physical review letters* 110.22 (2013), p. 222001.

[93] Roel Aaij et al. "Observation of CP violation in charm decays". In: *Physical review letters* 122.21 (2019), p. 211803.

[94] Roel Aaij et al. "Observation of CP violation in two-body $B^0_{(s)}$-meson decays to charged pions and kaons". In: *JHEP* 03 (2021), p. 075. DOI: `10.1007/JHEP03(2021)075`. arXiv: `2012.05319 [hep-ex]`.

[95] LHCb Collaboration et al. "Observation of charge–parity symmetry breaking in baryon decays". In: *Nature* 643 (2025), p. 1223.

[96] Roel Aaij et al. "Near-threshold $D\overline{D}$ spectroscopy and observation of a new charmonium state". In: *JHEP* 07 (2019), p. 035. DOI: `10.1007/JHEP07(2019)035`. arXiv: `1903.12240 [hep-ex]`.

[97] Alexander Austregesilo. "Light-meson spectroscopy with GlueX and beyond". In: *Nuovo Cim. C* 47.4 (2024), p. 151. DOI: `10.1393/ncc/i2024-24151-7`. arXiv: `2310.13122 [hep-ex]`.

[98] Volker Crede. "Baryon Spectroscopy at GlueX". In: *Few Body Syst.* 64.2 (2023), p. 32. DOI: `10.1007/s00601-023-01810-3`.

[99] William Imoehl. "Search for Hybrid Mesons at GlueX". In: *EPJ Web Conf.* 303 (2024), p. 01014. DOI: 10.1051/epjconf/202430301014.

[100] Peter Hurck. "Recent results from GlueX". In: *PoS* QCHSC24 (2025), p. 084. DOI: 10.22323/1.483.0084.

[101] B Adams et al. *COMPASS++/AMBER: Proposal for Measurements at the M2 beam line of the CERN SPS Phase-1: 2022-2024*. Tech. rep. 2019.

[102] Björn Seitz. "AMBER: a new QCD facility at the CERN SPS M2 beam line". In: *PoS* ICHEP2022 (2023), p. 839. DOI: 10.22323/1.414.0839.

[103] Jan M Friedrich. "The AMBER Experiment at CERN". In: *EPJ Web of Conferences*. Vol. 303. EDP Sciences. 2024, p. 06001.

[104] Klaus Peters et al. "PANDA: Strong interaction studies with antiprotons". In: *Nuclear Physics News* 27.3 (2017), pp. 24–28.

[105] W Erni et al. "Physics performance report for PANDA: strong interaction studies with antiprotons". In: *arXiv preprint arXiv:0903.3905* (2009).

[106] PANDA Collaboration, Nora Brambilla, and Ulf-G. MeiSSner. *Studies of Hadron Structure and Interactions with the* $\overline{\mathbf{P}}$*ANDA Experiment at FAIR*. 2015. arXiv: 1512.03299 [hep-ex].

[107] Panda Collaboration et al. "Precision resonance energy scans with the PANDA experiment at FAIR: Sensitivity study for width and line shape measurements of the X (3872)". In: *The European Physical Journal A* 55.3 (2019), p. 42.

[108] M Sudo et al. "Feasibility studies of the time-like proton electromagnetic form factor measurements with ANDA at FAIR". In: *The European Physical Journal A* 44.3 (2010), pp. 373–384.

[109] Miguel Albaladejo et al. "Snowmass white paper: Need for amplitude analysis in the discovery of new hadrons". In: *arXiv preprint arXiv:2203.08208* (2022).

[110] Peter Donald Bruce Collins. *An introduction to Regge theory and high energy physics*. Cambridge University Press, 1977.

[111] M. Jacob and G. C. Wick. "On the General Theory of Collisions for Particles with Spin". In: *Annals Phys.* 7 (1959). [Annals Phys.281,774(2000)], pp. 404–428. DOI: 10.1006/aphy.2000.6022.

[112] S. U. Chung. "Helicity coupling amplitudes in tensor formalism". In: *Phys. Rev. D* 48 (1993). [Erratum: Phys.Rev.D 56, 4419 (1997)], pp. 1225–1239. DOI: 10.1103/PhysRevD.56.4419.

[113] Suh-Urk Chung and Jan Michael Friedrich. "Covariant helicity-coupling amplitudes: A New formulation". In: *Physical Review D–Particles, Fields, Gravitation, and Cosmology* 78.7 (2008), p. 1225.

[114] V. Filippini, A. Fontana, and A. Rotondi. "Covariant spin tensors in meson spectroscopy". In: *Phys. Rev. D* 51 (1995), pp. 2247–2261. DOI: 10.1103/PhysRevD.51.2247.

[115] A. V. Anisovich and A. V. Sarantsev. "Partial decay widths of baryons in the spin-momentum operator expansion method". In: *Eur. Phys. J. A* 30 (2006), pp. 427–441. DOI: 10.1140/epja/i2006-10102-1. arXiv: hep-ph/0605135 [hep-ph].

[116] M. Mikhasenko et al. "What is the right formalism to search for resonances?" In: *Eur. Phys. J. C* 78.3 (2018), p. 229. DOI: 10.1140/epjc/s10052-018-5670-y. arXiv: 1712.02815 [hep-ph].

[117] A. Pilloni et al. "What is the right formalism to search for resonances? II. The pentaquark chain". In: *Eur. Phys. J. C* 78.9 (2018), p. 727. DOI: 10.1140/epjc/s10052-018-6177-2. arXiv: 1805.02113 [hep-ph].

[118] Mark Srednicki. *Quantum field theory*. Cambridge University Press, 2007.

[119] Matthew D. Schwartz. *Quantum Field Theory and the Standard Model*. Cambridge University Press, 2013.

[120] C. Abel et al. "Measurement of the Permanent Electric Dipole Moment of the Neutron". In: *Phys. Rev. Lett.* 124.8 (2020), p. 081803. DOI: 10.1103/PhysRevLett.124.081803. arXiv: 2001.11966 [hep-ex].

[121] R. D. Peccei and Helen R. Quinn. "CP Conservation in the Presence of Pseudoparticles". In: *Phys. Rev. Lett.* 38 (25 June 1977), pp. 1440–1443. DOI: 10.1103/PhysRevLett.38.1440.

[122] Roberto D. Peccei. "The Strong CP Problem and Axions". In: *Axions*. Springer Berlin Heidelberg, 2008. ISBN: 9783540735182. DOI: 10.1007/978-3-540-73518-2_1.

[123] Kiwoon Choi, Sang Hui Im, and Chang Sub Shin. "Recent Progress in the Physics of Axions and Axion-Like Particles". In: *Ann. Rev. Nucl. Part. Sci.* 71 (2021), pp. 225–252. DOI: 10.1146/annurev-nucl-120720-031147. arXiv: 2012.05029 [hep-ph].

[124] Ivana Batkovi et al. "Axion-Like Particle Searches with IACTs". In: *Universe* 7.6 (2021). [Erratum: Universe 8, 74 (2022)], p. 185. DOI: 10.3390/universe7060185. arXiv: 2106.03424 [astro-ph.HE].

[125] V.N. Gribov. "Quantization of non-Abelian gauge theories". In: *Nuclear Physics B* 139.1 (1978), pp. 1–19. ISSN: 0550-3213. DOI: https://doi.org/10.1016/0550-3213(78)90175-X.

[126] Mark Hamilton. "JD Mathematical Gauge Theory: With Applications to the Standard Model of Particle Physics. Universitext". In: *Springer International Publishing, Cham* 10 (2017), pp. 978–3.

[127] L. D. Faddeev and V. N. Popov. "Feynman Diagrams for the Yang-Mills Field". In: *Phys. Lett. B* 25 (1967). Ed. by Jong-Ping Hsu and D. Fine, pp. 29–30. DOI: 10.1016/0370-2693(67)90067-6.

[128] Michael E. Peskin and Daniel V. Schroeder. *An Introduction to quantum field theory*. Reading, USA: Addison-Wesley, 1995. ISBN: 978-0-201-50397-5, 978-0-429-50355-9, 978-0-429-49417-8. DOI: 10.1201/9780429503559.

[129] D. Dudal et al. "Aspects of the Gribov-Zwanziger framework". In: (2009). arXiv: 0911.0082 [hep-th].

[130] M.A.L. Capri et al. "An all-order proof of the equivalence between Gribovs no-pole and Zwanzigers horizon conditions". In: *Physics Letters B* 719.4 (2013), pp. 448–453. ISSN: 0370-2693. DOI: https://doi.org/10.1016/j.physletb.2013.01.039.

[131] N. Nakanishi and I. Ojima. *Covariant operator formalism of gauge theories and quantum gravity*. Vol. 27. 1990, pp. 1–434.

[132] P. J. Silva and O. Oliveira. "Gribov copies, lattice QCD and the gluon propagator". In: *Nucl. Phys. B* 690 (2004), pp. 177–198. DOI: 10.1016/j.nuclphysb.2004.04.020. arXiv: hep-lat/0403026 [hep-lat].

[133] A. Sternbeck et al. "Towards the infrared limit in SU(3) Landau gauge lattice gluodynamics". In: *Phys. Rev. D* 72 (2005), p. 014507. DOI: 10.1103/PhysRevD.72.014507. arXiv: hep-lat/0506007 [hep-lat].

[134] P. Pascual and R. Tarrach. *QCD: Renormalization for the practitioner*. Vol. 194. Lecture Notes in Physics. Heidelberg: Springer, 1984, pp. 1–277.

[135] C. S. Fischer, P. Watson, and W. Cassing. "Probing unquenching effects in the gluon polarisation in light mesons". In: *Phys. Rev. D* 72 (2005), p. 094025. DOI: 10.1103/PhysRevD.72.094025. arXiv: hep-ph/0509213 [hep-ph].

[136] Christian S. Fischer. "QCD at finite temperature and chemical potential from DysonSchwinger equations". In: *Prog. Part. Nucl. Phys.* 105 (2019), pp. 1–60. DOI: 10.1016/j.ppnp.2019.01.002. arXiv: 1810.12938 [hep-ph].

[137] Markus Q. Huber. "Nonperturbative properties of YangMills theories". In: *Phys. Rept.* 879 (2020), pp. 1–92. DOI: 10.1016/j.physrep.2020.04.004. arXiv: 1808.05227 [hep-ph].

[138] Markus Q. Huber. "Correlation functions of Landau gauge Yang-Mills theory". In: *Phys. Rev. D* 101.11 (2020), p. 114009. DOI: 10.1103/PhysRevD.101.114009. arXiv: 2003.13703 [hep-ph].

[139] Siegfried Bethke. *Look how it runs!* 2023. arXiv: 2310.01111 [hep-ph].

[140] Siegfried Bethke. "Experimental tests of asymptotic freedom". In: *Prog. Part. Nucl. Phys.* 58 (2007), pp. 351–386. DOI: 10.1016/j.ppnp.2006.06.001. arXiv: hep-ex/0606035.

[141] R. Alkofer et al. "Panel discussion: What don't we know about confinement?" In: *AIP Conference Proceedings*. AIP, 2011, pp. 17–24. DOI: 10.1063/1.3574936.

[142] Jeff Greensite. *An introduction to the confinement problem*. Vol. 821. 2011. DOI: 10.1007/978-3-642-14382-3.

[143] Taichiro Kugo. "The universal renormalization factors Z(1) / Z(3) and color confinement condition in non-Abelian gauge theory". In: (1995). Talk given at International Symposium on BRS Symmetry on the Occasion of Its 20th Anniversary, Kyoto, Japan, 18-22 Sep 1995. Published in *Kyoto 1995, BRS symmetry*107-119. arXiv: hep-th/9511033.

[144] H. Hata. "RESTORATION OF THE LOCAL GAUGE SYMMETRY AND COLOR CONFINEMENT IN NONABELIAN GAUGE THEORIES. II". In: *Prog. Theor. Phys.* 69 (1983), pp. 1524–1536. DOI: 10.1143/PTP.69.1524.

[145] Hideo Nakajima, Sadataka Furui, and Azusa Yamaguchi. "Numerical study of the Kugo-Ojima criterion and the Gribov problem in the Landau gauge". In: *30th International Conference on High-Energy Physics*. July 2000. arXiv: hep-lat/0007001.

[146] Reinhard Alkofer et al. "The Quark-gluon vertex in Landau gauge QCD: Its role in dynamical chiral symmetry breaking and quark confinement". In: *Annals Phys.* 324 (2009), pp. 106–172. DOI: 10.1016/j.aop.2008.07.001. arXiv: 0804.3042 [hep-ph].

[147] E. Eichten et al. "The Spectrum of Charmonium". In: *Phys. Rev. Lett.* 34 (1975). [Erratum: Phys.Rev.Lett. 36, 1276 (1976)], pp. 369–372. DOI: 10.1103/PhysRevLett.34.369.

[148] Gunnar S. Bali et al. "Observation of string breaking in QCD". In: *Phys. Rev. D* 71 (2005), p. 114513. DOI: 10.1103/PhysRevD.71.114513. arXiv: hep-lat/0505012.

[149] Nora Brambilla and Antonio Vairo. "Quark confinement and the hadron spectrum". In: *13th Annual HUGS AT CEBAF*. May 1999, pp. 151–220. arXiv: hep-ph/9904330.

[150] N. E. Mavromatos and J. Papavassiliou. *Novel Phases and Old Puzzles in QED3 and related models*. 2003. arXiv: cond-mat/0311421 [cond-mat.str-el].

[151] Jens Braun, Holger Gies, and Jan M. Pawlowski. “Quark confinement from colour confinement”. In: *Physics Letters B* 684.45 (Feb. 2010), pp. 262–267. ISSN: 0370-2693. DOI: 10.1016/j.physletb.2010.01.009. arXiv: 0708.2413 [hep-th].

[152] Reinhard Alkofer, Christian S. Fischer, and Felipe J. Llanes-Estrada. “Dynamically induced scalar quark confinement”. In: *Mod. Phys. Lett.* A23.15 (2008), pp. 1105–1113. ISSN: 1793-6632. DOI: 10.1142/s021773230802700x. arXiv: hep-ph/0607293.

[153] Nicola Cabibbo and Giorgio Parisi. “Exponential hadronic spectrum and quark liberation”. In: *Physics Letters B* 59.1 (1975), pp. 67–69.

[154] J Kogut et al. “Deconfinement and chiral symmetry restoration at finite temperatures in SU (2) and SU (3) gauge theories”. In: *Physical Review Letters* 50.6 (1983), p. 393.

[155] Robin Kehr, Dominik Smith, and Lorenz von Smekal. “QCD Anderson transition with overlap valence quarks on a twisted-mass sea”. In: *Phys. Rev. D* 109.7 (2024), p. 074512. DOI: 10.1103/PhysRevD.109.074512. arXiv: 2304.13617 [hep-lat].

[156] H. O. Back et al. “New limits on nucleon decays into invisible channels with the BOREXINO counting test facility”. In: *Phys. Lett. B* 563 (2003), pp. 23–34. DOI: 10.1016/S0370-2693(03)00636-1. arXiv: hep-ex/0302002.

[157] M. Agostini et al. “Searches for new physics below twice the electron mass with GERDA”. In: *Eur. Phys. J. C* 84.9 (2024), p. 940. DOI: 10.1140/epjc/s10052-024-13020-0. arXiv: 2405.15954 [nucl-ex].

[158] David B. Kaplan. *Chiral Symmetry and Lattice Fermions*. 2012. arXiv: 0912.2560 [hep-lat].

[159] David Griffiths. *Introduction to elementary particles*. John Wiley & Sons, 2020.

[160] Claude Amsler and Frank E Close. “Is f 0 (1500) a scalar glueball?” In: *Physical Review D* 53.1 (1996), p. 295.

[161] G. ’t Hooft. “Symmetry Breaking through Bell-Jackiw Anomalies”. In: *Phys. Rev. Lett.* 37 (1 July 1976), pp. 8–11. DOI: 10.1103/PhysRevLett.37.8.

[162] Edward Witten. “Current Algebra Theorems for the U(1) Goldstone Boson”. In: *Nucl. Phys. B* 156 (1979), pp. 269–283. DOI: 10.1016/0550-3213(79)90031-2.

[163] Gabriele Veneziano. “U(1) without instantons”. In: *Nucl. Phys. B* 159 (1979), pp. 213–224. DOI: 10.1016/0550-3213(79)90332-8.

[164] Luigi Del Debbio, Leonardo Giusti, and Claudio Pica. "Topological Susceptibility in SU(3) Gauge Theory". In: *Phys. Rev. Lett.* 94 (3 Jan. 2005), p. 032003. DOI: 10.1103/PhysRevLett.94.032003.

[165] Martin Lüscher and Filippo Palombi. "Universality of the topological susceptibility in the SU (3) gauge theory". In: *Journal of High Energy Physics* 2010.9 (2010), pp. 1–12.

[166] Marco Cè et al. "Testing the Witten-Veneziano mechanism with the Yang-Mills gradient flow on the lattice". In: *arXiv preprint arXiv:1410.8358* (2014).

[167] Reinhard Alkofer, Christian S. Fischer, and Richard Williams. "U(A)(1) anomaly and eta-prime mass from an infrared singular quark-gluon vertex". In: *Eur. Phys. J.* A38.1 (2008), pp. 53–60. DOI: 10.1140/epja/i2008-10646-x. arXiv: 0804.3478 [hep-ph].

[168] Marten Becker. "Reconstruction of the Σ^0 baryon in Ag+ Ag collisions at $\sqrt{s_{NN}} = 2.55$ GeV with HADES". PhD thesis. 2025. DOI: 10.22029/jlupub-20150.

[169] C. S. Fischer et al. "Dynamical chiral symmetry breaking in unquenched QED_3". In: *Physical Review D* 70.7 (Oct. 2004). ISSN: 1550-2368. DOI: 10.1103/physrevd.70.073007.

[170] Vladimir A Miransky. *Dynamical symmetry breaking in quantum field theories*. World Scientific, 1994.

[171] J. Goldstone. "Field Theories with Superconductor Solutions". In: *Nuovo Cim.* 19 (1961), pp. 154–164. DOI: 10.1007/BF02812722.

[172] Murray Gell-Mann, R. J. Oakes, and B. Renner. "Behavior of current divergences under SU(3) x SU(3)". In: *Phys. Rev.* 175 (1968), pp. 2195–2199. DOI: 10.1103/PhysRev.175.2195.

[173] John Clive Ward. "An Identity in Quantum Electrodynamics". In: *Phys. Rev.* 78 (1950), p. 182. DOI: 10.1103/PhysRev.78.182.

[174] Y. Takahashi. "On the generalized Ward identity". In: *Nuovo Cim.* 6 (1957), p. 371. DOI: 10.1007/BF02832514.

[175] Christian S. Fischer. "Nonperturbative propagators, running coupling and dynamical mass generation in ghost - anti-ghost symmetric gauges in QCD". PhD thesis, Eberhard-Karls-Universität zu Tübingen. 2003. arXiv: hep-ph/0304233.

[176] Markus Q. Huber. "A beginner's guide to functional methods in particle physics". In: (Oct. 2025). arXiv: 2510.18960 [hep-ph].

[177] Markus Q. Huber and Mario Mitter. “CrasyDSE: A Framework for solving Dyson-Schwinger equations”. In: *Comput.Phys.Commun.* 183 (2012), pp. 2441–2457. DOI: 10.1016/j.cpc.2012.05.019. arXiv: 1112.5622 [hep-th].

[178] Markus Q. Huber, Anton K. Cyrol, and Jan M. Pawlowski. “DoFun 3.0: Functional equations in Mathematica”. In: *Comput. Phys. Commun.* 248 (2020), p. 107058. DOI: 10.1016/j.cpc.2019.107058. arXiv: 1908.02760 [hep-ph].

[179] Julian Bernhardt. “Quark Mass and Volume Dependence of the QCD Phase Diagram with DSEs”. PhD thesis. Justus-Liebig-Universität GieSSen, 2023.

[180] Markus Q. Huber, Christian S. Fischer, and Hèlios Sanchis-Alepuz. “Apparent convergence in functional glueball calculations”. In: *Eur. Phys. J. C* 85.8 (2025), p. 859. DOI: 10.1140/epjc/s10052-025-14590-3. arXiv: 2503.03821 [hep-ph].

[181] Yoichiro Nambu and G. Jona-Lasinio. “Dynamical Model of Elementary Particles Based on an Analogy with Superconductivity. 1.” In: *Phys. Rev.* 122 (1961), pp. 345–358. DOI: 10.1103/PhysRev.122.345.

[182] Yoichiro Nambu and G. Jona-Lasinio. “Dynamical Model of Elementary Particles Based on an Analogy with Superconductivity. II”. In: *Phys. Rev.* 124 (1961), pp. 246–254. DOI: 10.1103/PhysRev.124.246.

[183] Herman J. Munczek and Adolfo M. Nemirovsky. “Regularization and Renormalization of Four - Fermion Theories”. In: *Phys. Rev.* D22 (1980), p. 2001. DOI: 10.1103/PhysRevD.22.2001.

[184] H. J. Munczek and A. M. Nemirovsky. “The Ground State $q\bar{q}$ Mass Spectrum in QCD”. In: *Phys. Rev.* D28 (1983), p. 181. DOI: 10.1103/PhysRevD.28.181.

[185] C. D. Roberts et al. “Aspects of hadron physics”. In: *Eur. Phys. J. ST* 140 (2007), pp. 53–116. DOI: 10.1140/epjst/e2007-00003-5. arXiv: 0802.0217 [nucl-th].

[186] Pieter Maris and Peter C. Tandy. “Bethe-Salpeter study of vector meson masses and decay constants”. In: *Phys. Rev.* C60.5 (1999), p. 055214. DOI: 10.1103/PhysRevC.60.055214. arXiv: nucl-th/9905056 [nucl-th].

[187] Nico Santowsky et al. “σ-meson: Four-quark versus two-quark components and decay width in a Bethe-Salpeter approach”. In: *Phys. Rev. D* 102.5 (2020), p. 056014. DOI: 10.1103/PhysRevD.102.056014. arXiv: 2007.06495 [hep-ph].

[188] Ángel S. Miramontes, Hèlios Sanchis Alepuz, and Reinhard Alkofer. "Elucidating the effect of intermediate resonances in the quark interaction kernel on the timelike electromagnetic pion form factor". In: *Phys. Rev. D* 103.11 (2021), p. 116006. DOI: 10.1103/PhysRevD.103.116006. arXiv: 2102.12541 [hep-ph].

[189] A. Bender, Craig D. Roberts, and L. Von Smekal. "Goldstone theorem and diquark confinement beyond rainbow ladder approximation". In: *Phys. Lett.* B380 (1996), pp. 7–12. DOI: 10.1016/0370-2693(96)00372-3. arXiv: nucl-th/9602012 [nucl-th].

[190] P. Watson, W. Cassing, and P. C. Tandy. "Bethe-Salpeter meson masses beyond ladder approximation". In: *Few Body Syst.* 35.3-4 (2004), pp. 129–153. DOI: 10.1007/s00601-004-0067-x. arXiv: hep-ph/0406340 [hep-ph].

[191] M. S. Bhagwat et al. "Aspects and consequences of a dressed quark gluon vertex". In: *Phys. Rev.* C70 (2004), p. 035205. DOI: 10.1103/PhysRevC.70.035205. arXiv: nucl-th/0403012 [nucl-th].

[192] P. Maris and P. C. Tandy. "QCD modeling of hadron physics". In: *Nucl. Phys. Proc. Suppl.* 161 (2006). [,136(2005)], pp. 136–152. DOI: 10.1016/j.nuclphysbps.2006.08.012. arXiv: nucl-th/0511017 [nucl-th].

[193] Hrayr H. Matevosyan, Anthony William Thomas, and Peter Charles Tandy. "Quark-gluon vertex dressing and meson masses beyond ladder-rainbow truncation". In: *Phys. Rev.* C75 (2007), p. 045201. DOI: 10.1103/PhysRevC.75.045201. arXiv: nucl-th/0605057 [nucl-th].

[194] Lei Chang and Craig D. Roberts. "Sketching the Bethe-Salpeter kernel". In: *Phys. Rev. Lett.* 103 (2009), p. 081601. DOI: 10.1103/PhysRevLett.103.081601. arXiv: 0903.5461 [nucl-th].

[195] Richard Williams, Christian S. Fischer, and Walter Heupel. "Light mesons in QCD and unquenching effects from the 3PI effective action". In: *Phys. Rev.* D93.3 (2016), p. 034026. DOI: 10.1103/PhysRevD.93.034026. arXiv: 1512.00455 [hep-ph].

[196] Lorenz von Smekal, Andreas Hauck, and Reinhard Alkofer. "A Solution to Coupled Dyson Schwinger Equations for Gluons and Ghosts in Landau Gauge". In: *Annals Phys.* 267 (1998). [Erratum: Annals Phys.269,182(1998)], pp. 1–60. DOI: 10.1006/aphy.1998.5806, 10.1006/aphy.1998.5864. arXiv: hep-ph/9707327 [hep-ph].

[197] Lorenz von Smekal, Reinhard Alkofer, and Andreas Hauck. "The infrared behavior of gluon and ghost propagators in Landau gauge QCD". In: *Phys. Rev. Lett.* 79 (1997), pp. 3591–3594. DOI: 10.1103/PhysRevLett.79.3591. arXiv: hep-ph/9705242.

[198] Christoph Lerche and Lorenz von Smekal. "On the infrared exponent for gluon and ghost propagation in Landau gauge QCD". In: *Phys.Rev.* D65 (2002), p. 125006. DOI: 10.1103/PhysRevD.65.125006. arXiv: hep-ph/0202194.

[199] John M. Cornwall. "Dynamical Mass Generation in Continuum QCD". In: *Phys. Rev.* D26 (1982), p. 1453. DOI: 10.1103/PhysRevD.26.1453.

[200] A. C. Aguilar, D. Binosi, and J. Papavassiliou. "Gluon and ghost propagators in the Landau gauge: Deriving lattice results from Schwinger-Dyson equations". In: *Phys. Rev.* D78 (2008), p. 025010. DOI: 10.1103/PhysRevD.78.025010. arXiv: 0802.1870 [hep-ph].

[201] Ph. Boucaud et al. "IR finiteness of the ghost dressing function from numerical resolution of the ghost SD equation". In: *JHEP* 06 (2008), p. 012. DOI: 10.1088/1126-6708/2008/06/012. arXiv: 0801.2721 [hep-ph].

[202] David Dudal et al. "A Refinement of the Gribov-Zwanziger approach in the Landau gauge: Infrared propagators in harmony with the lattice results". In: *Phys. Rev.* D78 (2008), p. 065047. DOI: 10.1103/PhysRevD.78.065047. arXiv: 0806.4348 [hep-th].

[203] André Sternbeck and Michael Müller-Preussker. "Lattice evidence for the family of decoupling solutions of Landau gauge Yang-Mills theory". In: *Phys.Lett.* B726 (2013), pp. 396–403. DOI: 10.1016/j.physletb.2013.08.017. arXiv: 1211.3057 [hep-lat].

[204] Axel Maas. "Constructing non-perturbative gauges using correlation functions". In: *Phys. Lett.* B689 (2010), pp. 107–111. DOI: 10.1016/j.physletb.2010.04.052. arXiv: 0907.5185 [hep-lat].

[205] Martina Blank, A. Krassnigg, and Axel Maas. "Rho-meson, Bethe-Salpeter equation, and the far infrared". In: *Phys. Rev.* D83 (2011), p. 034020. DOI: 10.1103/PhysRevD.83.034020. arXiv: 1007.3901 [hep-ph].

[206] Markus Q. Huber et al. "The infrared behavior of Landau gauge Yang-Mills theory in d=2, 3 and 4 dimensions". In: *Phys. Lett.* B659 (2008), pp. 434–440. DOI: 10.1016/j.physletb.2007.10.073. arXiv: 0705.3809 [hep-ph].

[207] Reinhard Alkofer, Christian S. Fischer, and Felipe J. Llanes-Estrada. "Vertex functions and infrared fixed point in Landau gauge SU(N) Yang-Mills theory". In: *Phys. Lett.* B611 (2005). [Erratum: Phys. Lett.670,460(2009)], pp. 279–288. DOI: 10.1016/j.physletb.2008.11.068,10.1016/j.physletb.2005.02.043. arXiv: hep-th/0412330 [hep-th].

[208] M. E. Carrington and Yun Guo. "Techniques for n-Particle Irreducible Effective Theories". In: *Phys. Rev.* D83 (2011), p. 016006. DOI: 10.1103/PhysRevD.83.016006. arXiv: 1010.2978 [hep-ph].

[209] Jurgen Berges. "n-PI effective action techniques for gauge theories". In: *Phys. Rev.* D70 (2004), p. 105010. DOI: 10.1103/PhysRevD.70.105010. arXiv: hep-ph/0401172.

[210] H. J. Munczek. "Dynamical chiral symmetry breaking, Goldstone's theorem and the consistency of the Schwinger-Dyson and Bethe-Salpeter Equations". In: *Phys. Rev.* D52.8 (1995), pp. 4736–4740. DOI: 10.1103/PhysRevD.52.4736. arXiv: hep-th/9411239 [hep-th].

[211] M.E. Carrington and E. Kovalchuk. "Next-to-Leading Order Transport Coefficients from the Four-Particle Irreducible Effective Action". In: *Phys.Rev.* D81 (2010), p. 065017. DOI: 10.1103/PhysRevD.81.065017. arXiv: 0912.3149 [hep-ph].

[212] Markus Q. Huber, Christian S. Fischer, and Hèlios Sanchis-Alepuz. "Glueballs from Dyson-Schwinger and Bethe-Salpeter equations". In: Dec. 2023. arXiv: 2312.12029 [hep-ph].

[213] Jonivar Skullerud and Ayse Kizilersu. "Quark gluon vertex from lattice QCD". In: *JHEP* 09 (2002), p. 013. DOI: 10.1088/1126-6708/2002/09/013. arXiv: hep-ph/0205318 [hep-ph].

[214] Andre Sternbeck et al. "Triple-gluon and quark-gluon vertex from lattice QCD in Landau gauge". In: *PoS* LATTICE2016 (2017), p. 349. DOI: 10.22323/1.256.0349. arXiv: 1702.00612 [hep-lat].

[215] Richard Williams. "The quark-gluon vertex in Landau gauge bound-state studies". In: *Eur. Phys. J. A* 51.5 (2015), p. 57. DOI: 10.1140/epja/i2015-15057-4. arXiv: 1404.2545 [hep-ph].

[216] Lev Davidovich Landau and E. M. Lifshitz. *Quantum Mechanics: Non-Relativistic Theory*. Vol. v.3. Course of Theoretical Physics. Oxford: Butterworth-Heinemann, 1991. ISBN: 978-0-7506-3539-4. DOI: 10.1016/C2013-0-02793-4.

[217] G. F. Chew and Steven C. Frautschi. "Principle of Equivalence for All Strongly Interacting Particles Within the S Matrix Framework". In: *Phys. Rev. Lett.* 7 (1961), pp. 394–397. DOI: 10.1103/PhysRevLett.7.394.

[218] David J Griffiths and Darrell F Schroeter. *Introduction to quantum mechanics*. Cambridge university press, 2018.

[219] Murray Gell-Mann. "The Eightfold Way: A Theory of strong interaction symmetry". In: (1961).

[220] Frank WK Firk. "Introduction to Groups, Invariants and Particles". In: (2000).

[221] Gunnar S. Bali. “QCD forces and heavy quark bound states”. In: *Phys. Rept.* 343 (2001), pp. 1–136. DOI: 10.1016/S0370-1573(00)00079-X. arXiv: hep-ph/0001312.

[222] Nora Brambilla et al. “Potential NRQCD: An Effective theory for heavy quarkonium”. In: *Nucl. Phys. B* 566 (2000), p. 275. DOI: 10.1016/S0550-3213(99)00693-8. arXiv: hep-ph/9907240.

[223] Yoshiaki Koma, Miho Koma, and Hartmut Wittig. “Nonperturbative determination of the QCD potential at O(1/m)”. In: *Phys. Rev. Lett.* 97 (2006), p. 122003. DOI: 10.1103/PhysRevLett.97.122003. arXiv: hep-lat/0607009 [hep-lat].

[224] Yoshiaki Koma and Miho Koma. “Spin-dependent potentials from lattice QCD”. In: *Nucl. Phys. B* 769 (2007), pp. 79–107. DOI: 10.1016/j.nuclphysb.2007.01.033. arXiv: hep-lat/0609078 [hep-lat].

[225] Michael Eichberg and Marc Wagner. “Computing $1/m_Q$ and $1/m_Q^2$ corrections to the static potential with lattice gauge theory using gradient flow”. In: *PoS* LATTICE2024 (2025), p. 117. DOI: 10.22323/1.466.0117. arXiv: 2411.11640 [hep-lat].

[226] Barton Zwiebach. *A first course in string theory.* Cambridge university press, 2004.

[227] Daniel Winney and Adam P. Szczepaniak. “Regge theory in hadron physics”. In: (Dec. 2025). arXiv: 2512.21805 [hep-ph].

[228] T. Regge. “Introduction to complex orbital momenta”. In: *Nuovo Cim.* 14 (1959), p. 951. DOI: 10.1007/BF02728177.

[229] Noboru Nakanishi. “Normalization Condition and Normal and Abnormal Solutions of the Bethe-Salpeter Equation”. In: *Physical Review* 138.5B (June 1965), B1182–B1192. DOI: 10.1103/physrev.138.b1182.

[230] R. Williams. “BetheSalpeter studies of mesons beyond rainbow-ladder”. In: *EPJ Web of Conferences* 3 (2010), p. 03005. DOI: 10.1051/epjconf/20100303005.

[231] Pieter Maris and Craig D. Roberts. “π-and K-meson Bethe-Salpeter amplitudes”. In: *Phys. Rev.* C56.6 (1997), pp. 3369–3383. DOI: 10.1103/PhysRevC.56.3369. arXiv: nucl-th/9708029 [nucl-th].

[232] A. Krassnigg and M. Blank. “A covariant study of tensor mesons”. In: *Phys. Rev. D* 83 (2011), p. 096006. DOI: 10.1103/PhysRevD.83.096006. arXiv: 1011.6650 [hep-ph].

[233] Helios Sanchis-Alepuz and Richard Williams. "Recent developments in bound-state calculations using the Dyson-Schwinger and Bethe-Salpeter equations". In: (2017). arXiv: 1710.04903 [hep-ph].

[234] Charles Zemach. "Determination of the Spins and Parities of Resonances". In: *Phys. Rev.* 140 (1965), B109–B124. DOI: 10.1103/PhysRev.140.B109.

[235] C. H. Llewellyn-Smith. "A relativistic formulation for the quark model for mesons". In: *Annals Phys.* 53 (1969), pp. 521–558. DOI: 10.1016/0003-4916(69)90035-9.

[236] M. Fierz. "Force-free particles with any spin". In: *Helv. Phys. Acta* 12 (1939), pp. 3–37.

[237] Gernot Eichmann. "More about the light baryon spectrum". In: *Few Body Syst.* 58.2 (Feb. 2017), p. 81. ISSN: 1432-5411. DOI: 10.1007/s00601-016-1200-3. arXiv: 1611.10118 [hep-ph].

[238] Martina Blank. "Properties of quarks and mesons in the Dyson-Schwinger/Bethe-Salpeter approach". PhD thesis. Graz U., 2011. arXiv: 1106.4843 [hep-ph].

[239] James S. Ball and Ting-Wai Chiu. "Analytic Properties of the Vertex Function in Gauge Theories. 1." In: *Phys. Rev.* D22 (1980), p. 2542. DOI: 10.1103/PhysRevD.22.2542.

[240] James S. Ball and Ting-Wai Chiu. "Analytic Properties of the Vertex Function in Gauge Theories. 2." In: *Phys. Rev.* D22 (1980). [Erratum: Phys. Rev.D23,3085(1981)], p. 2550. DOI: 10.1103/PhysRevD.22.2550,10.1103/PhysRevD.23.3085.

[241] Stephan Hagel. "Meson spectrum from functional methods beyond rainbow ladder". Master Thesis. Justus-Liebig-Universität Giessen, 2020.

[242] Si-xue Qin et al. "Interaction model for the gap equation". In: *Phys. Rev.* C84.4 (2011), p. 042202. DOI: 10.1103/PhysRevC.84.042202. arXiv: 1108.0603 [nucl-th].

[243] O. Buss et al. "Transport-theoretical Description of Nuclear Reactions". In: *Phys. Rept.* 512 (2012), pp. 1–124. DOI: 10.1016/j.physrep.2011.12.001. arXiv: 1106.1344 [hep-ph].

[244] Wim Botermans and Rudi Malfliet. "Quantum transport theory of nuclear matter". In: *Phys. Rept.* 198 (1990), pp. 115–194. DOI: 10.1016/0370-1573(90)90174-Z.

[245] Lorenz v. Smekal. "Ein kovariantes Modell zur chiralen Symmetriebrechung in der Quantenchromodynamik". Diplomarbeit. TU München, 1990.

[246] Hendrik van Hees and Joern Knoll. “Renormalization in selfconsistent approximation schemes at finite temperature. 3. Global symmetries”. In: *Phys. Rev. D* 66 (2002), p. 025028. DOI: 10.1103/PhysRevD.66.025028. arXiv: hep-ph/0203008.

[247] A. Arrizabalaga and J. Smit. “Gauge fixing dependence of Phi derivable approximations”. In: *Phys. Rev. D* 66 (2002), p. 065014. DOI: 10.1103/PhysRevD.66.065014. arXiv: hep-ph/0207044.

[248] Anton K. Cyrol. “Non-perturbative QCD Correlation Functions”. PhD thesis, Universität Heidelberg. 2017.

[249] Reinhard Alkofer et al. “Analytic properties of the Landau gauge gluon and quark propagators”. In: *Physical Review D* 70.1 (2004), p. 014014.

[250] Attilio Cucchieri, Tereza Mendes, and Willian M. Serenone. “Lattice Gluon Propagator and One-Gluon-Exchange Potential”. In: *Braz. J. Phys.* 49.4 (2019), pp. 548–563. DOI: 10.1007/s13538-019-00665-6. arXiv: 1704.08288 [hep-lat].

[251] Geoffrey B. West. “Confinement, the Wilson Loop and the Gluon Propagator”. In: *Phys. Lett. B* 115 (1982), pp. 468–472. DOI: 10.1016/0370-2693(82)90394-X.

[252] Heinz Pagels and Saul Stokar. “The Pion Decay Constant, Electromagnetic Form-Factor and Quark Electromagnetic Selfenergy in QCD”. In: *Phys. Rev. D* 20 (1979), p. 2947. DOI: 10.1103/PhysRevD.20.2947.

[253] Christian S. Fischer, Stanislav Kubrak, and Richard Williams. “Mass spectra and Regge trajectories of light mesons in the Bethe-Salpeter approach”. In: *Eur. Phys. J.* A50 (2014), p. 126. DOI: 10.1140/epja/i2014-14126-6. arXiv: 1406.4370 [hep-ph].

[254] Christian S. Fischer, Stanislav Kubrak, and Richard Williams. “Spectra of heavy mesons in the Bethe-Salpeter approach”. In: *Eur. Phys. J.* A51 (2015), p. 10. DOI: 10.1140/epja/i2015-15010-7. arXiv: 1409.5076 [hep-ph].

[255] Walter Heupel, Gernot Eichmann, and Christian S. Fischer. “Tetraquark Bound States in a Bethe-Salpeter Approach”. In: *Phys. Lett.* B718 (2012), pp. 545–549. DOI: 10.1016/j.physletb.2012.11.009. arXiv: 1206.5129 [hep-ph].

[256] Gernot Eichmann, Christian S. Fischer, and Walter Heupel. “The light scalar mesons as tetraquarks”. In: *Phys. Lett.* B753 (2016), pp. 282–287. DOI: 10.1016/j.physletb.2015.12.036. arXiv: 1508.07178 [hep-ph].

[257] Nico Santowsky and Christian S. Fischer. "Light scalars: Four-quark versus two-quark states in the complex energy plane from Bethe-Salpeter equations". In: *Phys. Rev. D* 105.3 (2022), p. 034025. DOI: 10.1103/PhysRevD.105.034025. arXiv: 2109.00755 [hep-ph].

[258] Markus Q. Huber, Christian S. Fischer, and Helios Sanchis-Alepuz. "Glueballs from bound state equations". In: *15th Conference on Quark Confinement and the Hadron Spectrum*. Nov. 2022. arXiv: 2211.09131 [hep-ph].

[259] Walter Heupel, Tobias Goecke, and Christian S. Fischer. "Beyond Rainbow-Ladder in bound state equations". In: *Eur. Phys. J.* A50 (2014), p. 85. DOI: 10.1140/epja/i2014-14085-x. arXiv: 1402.5042 [hep-ph].

[260] J. P. Lees et al. "Light meson spectroscopy from Dalitz plot analyses of η_c decays to $\eta' K^+ K^-$, $\eta' \pi^+ \pi^-$, and $\eta \pi^+ \pi^-$ produced in two-photon interactions". In: *Phys. Rev. D* 104.7 (2021), p. 072002. DOI: 10.1103/PhysRevD.104.072002. arXiv: 2106.05157 [hep-ex].

[261] Peter Watson and Hugo Reinhardt. "Bethe-Salpeter equation at leading order in Coulomb gauge". In: *Phys. Rev.* D86 (2012), p. 125030. DOI: 10.1103/PhysRevD.86.125030. arXiv: 1211.4507 [hep-ph].

[262] Cliff Burgess and Guy Moore. *The standard model: A primer*. Cambridge University Press, 2007.

[263] Leonard Schlessinger. "Use of analyticity in the calculation of nonrelativistic scattering amplitudes". In: *Physical Review* 167.5 (1968), p. 1411.

[264] Christian S. Fischer, Dominik Nickel, and Richard Williams. "On Gribov's supercriticality picture of quark confinement". In: *Eur. Phys. J.* C60 (2009), pp. 47–61. DOI: 10.1140/epjc/s10052-008-0821-1. arXiv: 0807.3486 [hep-ph].

[265] John Von Neumann and Eugene Wigner. "Über das Verhalten von Eigenwerten bei adiabatischen Prozessen". In: *Z. Phys* 30 (1929), pp. 467–470.

[266] William H. Press et al. *Numerical Recipes 3rd Edition: The Art of Scientific Computing*. Ed. by 3rd. Cambridge University Press, 2007.

[267] D. Binosi and L. Theussl. "JaxoDraw: A Graphical user interface for drawing Feynman diagrams". In: *Comput.Phys.Commun.* 161 (2004), pp. 76–86. DOI: 10.1016/j.cpc.2004.05.001. arXiv: hep-ph/0309015.

[268] Steve Klabnik and Carol Nichols. *The Rust programming language*. No Starch Press, 2023.

[269] Dennis M Ritchie et al. "The C programming language". In: *Bell Sys. Tech. J* 57.6 (1978), pp. 1991–2019.

[270] Sarah El Kazdadi. *faer-rs*. Version 0.23. https://codeberg.org/sarah-quinones/faers.

[271] Ben Ruijl, Takahiro Ueda, and Jos Vermaseren. "FORM version 4.2". In: (2017). arXiv: `1707.06453 [hep-ph]`.

[272] Thomas Williams, Colin Kelley, et al. *Gnuplot*. Version 6.0. http://gnuplot.info/. 2023.

Acknowledgements / Danksagungen

First and foremost, I want to sincerely thank my supervisor Prof. Dr. Christian Fischer for giving me the opportunity to work in his group over better part of the last decade and for always being very patient with me as well as a very helpful contact in all questions regarding physics and beyond. I also wish to thank Prof. Dr. Lorenz von Smekal for being my second referee and for bringing in some interesting insights to my work during our regular PhD committee meetings, which I would not have had without him. Furthermore, I want to thank my long time office mate PD Dr. Markus Huber for his collaborative work, without which this project would not have been possible, as well as his competent support and guidance whenever I needed help. I further wish to thank PD Dr. Richard Williams and Dr. Walter Heupel for laying the groundwork of important parts of the theory behind this work Beyond that, I wish to thank all the colleagues at the institute, who not only provided constructive help in my work, but also made the everyday life at the institute much more cheerful and enjoyable.[1] Additionally, I want to thank Dr. Marten Becker, Robin Kehr, Dr. Jonas Wessely, Jonathan Yigzaw and Christian Eichmann for proofreading parts of this manuscript. I also want to give special thanks to Jakub Bandola for introducing me to the Rust programming language and greatly helping me while learning, both of which has saved me from a lot of headache while programming.

I thank the Studienstiftung des Deutschen Volkes for their financial support throughout the most of my PhD project. I also thank the Helmholtz Graduate School for Hadron and Ion Research (HGS-HIRe) for providing access to helpful courses and financial support during the first months of this project. Furthermore, I want to thank Pieter Maris for providing me access to the Perlmutter high performance computing cluster at the National Energy Research Scientific Computing Center (NERSC).

Besides that, I want to thank my family and friends, especially my parents, for providing emotional and financial support throughout the past three decades. Finally, I want to express my deepest gratitude to my partner Antonia and my daughter Mina, who patiently went through the toughest and most stressful periods of the past few years with me and were always a reliable constant, without which I could have not come this far.

[1] I would list them all personally by name, but this margin is quite literally too small to hold the names of so many giants with big shoulders to stand on.

Selbstständigkeitserklärung

(gemäß §17 Absatz 2 der Promotionsordnung der naturwissenschaftlichen Fachbereiche vom 21.01.2016)

Ich erkläre: Ich habe die vorgelegte Dissertation selbstständig und ohne unerlaubte fremde Hilfe und nur mit den Hilfen angefertigt, die ich in der Dissertation angegeben habe. Alle Textstellen, die wörtlich oder sinngemäß aus veröffentlichten Schriften entnommen sind, und alle Angaben, die auf mündlichen Auskünften beruhen, sind als solche kenntlich gemacht. Ich stimme einer evtl. Überprüfung meiner Dissertation durch eine Antiplagiat-Software zu. Bei den von mir durchgeführten und in der Dissertation erwähnten Untersuchungen habe ich die Grundsätze guter wissenschaftlicher Praxis, wie sie in der "Satzung der Justus-Liebig-Universität Gießen zur Sicherung guter wissenschaftlicher Praxis" niedergelegt sind, eingehalten.

Gießen, den 23. April 2026

____

(Unterschrift)